Contributions to Microwave Passive Component Design

by

Petrie Meyer

Dissertation presented for the degree of Doctorate in Engineering in the Faculty of Engineering at Stellenbosch University

Supervisor: Prof. C. Fourie

December 2019

Declaration

By submitting this dissertation electronically, I declare that the entirety of the work contained therein is my own, original work, that I am the sole author thereof (save to the extent explicitly otherwise stated), that reproduction and publication thereof by Stellenbosch University will not infringe any third party rights and that I have not previously in its entirety or in part submitted it for obtaining any qualification.

Date: December 2019

Abstract

Contributions to Microwave Passive Component Design

P. Meyer

Dissertation: DEng

December 2019

The dissertation presents an overview of the publications of the candidate and his research group on design techniques and structures for microwave passive networks which have advanced the field in a number of aspects. They have also impacted materially on local industry. The work includes three main activities, namely numerical modelling and analysis of microwave structures, microwave filter applications, and microwave antenna applications.

A particular focus is placed on structures supporting multiple propagating modes, as this has been a recurring topic throughout the career of the author. Firstly applied to microwave waveguide filters, his most recent work extends multimodal concepts also to antennas. The modelling of these structures forms a crucial part of the design procedure, and also contributes largely to the ability of designers to exploit this behaviour to achieve added functionality and improved performance.

Uittreksel

Contributions to Microwave Passive Component Design

P. Meyer

Proefskrif: DIng

Desember 2019

Hierdie proefskrif bied ’n oorsig aan van die kandidaat en sy navorsingsgroep se publikasies in die veld van passiewe mikrogolf netwerke en antennas, wat ’n bydrae tot die veld gemaak het, en ’n impak in industrie gehad het. Drie hoof aktiwiteite word aangebied, naamlik numeriese modellering en analise, mikrogolffilter toepassings, en mikrogolfantennas.

’n Spesifieke fokus word geplaas op strukture wat die voortplanting van meer as een modus ondersteun, aangesien hierdie ’n deurlopende tema was in die kandidaat se hele loopbaan. Oorspronklik toegepas op filterstrukture, verskyn hierdie tema ook in die mees onlangse werk op antennas. The modellering van hierdie strukture vorm ’n integrale deel van die ontwerpsiklus, en dra beduidend by tot die vermoë van ontwerpers om hierdie tipe gedrag te benut, om sodoende ekstra funksionaliteit in te bou in die ontwerp, en werkverrigting te verhoog.

Acknowledgements

I would like to express my sincere gratitude to the following people and organisations ...

Contents

List of Figures

Chapter 1

Background

1.1 Introduction

Passive microwave component design has undergone huge changes over the past 30 years, but in some ways has also stayed much the same. In the 1980's, computer power and memory, especially that of personal computers, were very limited, and electromagnetic analysis was only possible on large mainframe computers. Designers of passive microwave components were therefore fully dependent on equivalent circuit models of distributed structures, with the values of the circuit elements expressed as functions of physical dimensions such as lengths and widths, and wavelength. Classical texts such as Marcuvitz's *Waveguide Handbook*, *Microwave Filters, Impedance-Matching Networks, and Coupling Structures* by Matthaei, Young and Jones, and Collin's *Field Theory of Guided Waves*, as well as a host of journal papers, provided graphs and formulas for equivalent circuit elements, and designers were effectively limited to these structures. Any new structures had to characterised with approximate (or self-written numerical) electromagnetic analysis, or measurements.

Since then, the capabilities of both personal computers and commercial electromagnetic software have grown exponentially, with the current state-of-the-art making the analysis of a typical planar or cavity filter possible on a laptop, and within a time frame of minutes. This has created an enormous amount of freedom for designers, as any geometrical shape can now be investigated for its electrical properties, and used in a design.

In addition, the application of microwave circuits have undergone a breathtaking change - three decades have essentially witnessed the whole mobile revolution. Where microwave components and sub-systems were the domain of expensive military and communications equipment, now even a simple cellphone contains up to eight microwave radios. The active parts of microwave systems have shrunk exponentially, and entire receiver-transmitter units are currently available on commercially available chips. For designers of passive subsystems, mobile applications have created a whole new set of very challenging design requirements, with form-factors, weight, size and most importantly cost, of equal or more importance than electrical performance. New developments in manufacturing techniques such as multi-layer stacking of microwave substrates, and inexpensive numerically controlled milling machines, have opened up the way for completely new ways of thinking about microwave design, resulting in three-dimensional technologies such as Surface Integrated Waveguide (SIW) and Low Temperature Co-fired Ceramic (LTCC).

While a lot has changed, the most important aspects of microwave design have however remained, and ironically even grown in importance. With essentially unlimited design variations possible these days, it has become imperative for present day designers to have a fundamental knowledge of how fields behave in structures, of the characteristics of a wide range of classical and modern solutions, and of the possibilities and cost of a host of manufacturing processes. Especially for an engineer trained in classical network synthesis and modelling, the current environment offers design opportunities never seen before.

The aim of the dissertation presented here, is to illustrate the contributions of myself and my research group to this exciting field of microwave passive circuits, including antennas. Viewed as a body of knowledge, I believe this work has made a significant contribution to the field in both the academic research community, and the commercial microwave industry in South Africa. This dissertation therefore describes my journey through three decades of microwave passive component design, up to the time of writing in 2018.

1.2 A Short Profile

My tertiary education commenced when I enrolled for my BEng degree in 1983 at the Department of Electronic Engineering at Stellenbosch University. I subsequently obtained all my degrees at the same department, with an MEng in 1986, a PhD in 1995, and quite dramatically different, a BA Honours degree in English Literature in 2012. The latter was started on a whim, but ended up being an immensely enriching experience. Whilst busy with my Master's degree, I also embarked on what turned out to be a lifelong academic career, first as a temporary, part-time, junior lecturer, and then stepwise through all the ranks. In 2003 I was appointed as a full professor, and most recently, in 2016, as a Distinguished Professor. Through the years I was involved with almost all levels of departmental management, including that of Head of Department.

Almost from the start of my career, I became active in the broader professional environment. Over the years, I have worked as contract designer for a host of local companies, primarily on microwave filter design. On the academic front, I started the first local newsletter of the South African branch of the IEEE in 1990, and filled various positions in the society until I became chairman of the local branch in 1996. I was general chair of three consecutive local IEEE AP/MTT conferences (2005-2009), and on the technical committee of various IEEE Region 8 africon conferences, including being chair of the technical programme committee of IEEE region 8 africon 1999. During this period, I was also a standing member of a THRIP panel (THRIP was one of the largest government funding programmes in South Africa).

Since 2000, I and my research group have been involved with a number of international cooperation programmes. Most important of these were a joint project under the South Africa-Flaanders agreement with KU Leuven on parameter extraction techniques to establish circuit models for microwave FET?s (2000-2006), a joint project under the South Africa-Flaanders agreement with Antwerp University on macro-modelling of microwave circuits (2002-2006), and a European Union FP7 project (Marie Curie) *Multiwaves*, on tunable and reconfigurable filters (2010-2014). This project included Novi-Sad University (Serbia), University of St Petersburg (Russia), and Herriot-Watt University (Scotland).

At present, I head the Microwave and Antenna Laboratory at Stellenbosch University, a research group funded by a number of local industrial partners, the National Research Foundation (NRF), and the South African SKA. The group currently consists of 10 staff members and in the region of 50 postgraduate students.

1.3 Contributions

My activities over the years have covered quite a wide spectrum of research. Starting from mainly defence orientated work on numerical electromagnetic analysis techniques and applications to microwave filter design, I spent a significant phase working on mathematical modelling (or meta-modelling) and optimisation of microwave structures. This branched out to other microwave devices such as combiners and switches. The most recent years saw a deep involvement in the South African efforts on the Square-Kilometre-Array (SKA) radio telescope which is currently under construction in the Karoo, including work on reflector antenna feeds, arrays, receiver front ends etc.

In terms of research outputs, my body of work at present includes more than 40 peer-reviewed journal papers, more than 80 conference papers and workshops, 2 book chapters and 2 patents. I have supervised more than 60 postgraduate students and post-doctoral fellows, including 2 DEng candidates - the highest degree awarded by the Faculty of Engineering at Stellenbosch University, based on a lifetime technical contribution. The first of these was by Prof Willem Perold on his contributions to the fields of superconductor devices and sensors [1], and the second by Prof David Davidson on his contributions to the field of electromagnetics [2]. A full list appears in Appendix A.

The main contributions of myself and my research group over the past three decades, can be summarised as follows:

- Advances in the design of devices using multiple propagating modes. This includes modelling and analysis algorithms, structural innovation, and measurement techniques. The range of devices includes filters, dividers and antennas.
- Advances in mathematical models (meta-models) of microwave devices, including multi-variate models, and optimisation techniques exploiting these models.
- Advances in microwave filter design. This includes a number of unpublished high-performance filters for industry which will be discussed here briefly.
- Advances in multi-modal antenna design, and work on the SKA reflector feed designs.

These topics will be discussed in detail in the body of the dissertation, with references to published work.

1.4 Layout

As the aim of this dissertation is purely to present contributions by myself and my research group, it differs markedly from standard dissertations in terms of referencing. For the purposes of the DEng, only references to work by the author himself are included. It goes without saying however that all the work presented here built on previous work by other authors not referenced here. In all cases, the reader should consult the specific papers for these references.

The dissertation is structured by topic and not chronologically, as many of the topics run throughout the whole of my career. Four main chapters make up the bulk of the work. Chapter 2 presents my work on numerical analysis, mathematical modelling and optimisation. Chapter 3 focuses on filters and devices utilising higher order propagating modes, except antennas. Chapter 4 discusses work on general passive devices. Finally, Chapter 5 presents the work on antennas.

1.5 Recognition

While the body of the dissertation provides a technical perspective on my research career, I have over the years received more general recognition on a number of occasions, which do not form part of the main dissertation text. At the completion of my Master's degree, I was awarded the Stellenbosch University Chancellor's medal, the highest award of the university to a student, partially based on my research for the degree. In 2009, I was elected as Fellow of the South African Academy of Engineering, and in 2015 I received the

Stellenbosch University Lifetime Award, for excellence over a career. This is the highest award of the university to a staff member. In 2012 the South African National Research Foundation (NRF) awarded me a B-rating (a B-rating indicates an "internationally recognized researcher"). Finally, in 2016 I was appointed as one of 40 Distinguished Professors at Stellenbosch University, the highest academic rank at the university.

Chapter 2

Modelling

2.1 Introduction

Numerical modelling is an integral part of microwave, antenna and electromagnetics research. Throughout a large part of my career, any analysis or design of a structure was done using circuit models, with element values in look-up tables or from equations, or self-written electromagnetic analysis code. Even for filter synthesis, self-written code was required if no standard tables could be used. The start of my career therefore focused very strongly on Computational Electromagnetics (CEM), and the creation of numerical software tools.

In the case of numerical electromagnetic analysis, especially in-house written code which can seldom be optimised for speed, execution times are often long. When there is a requirement for optimisation, such a code needs to execute multiple times, which often results in design cycles which are prohibitively slow. The late 1990's saw a surge in attention in so-called *meta-models* - typically sets of general mathematical equations, such as partial fraction expansions or polynomials, with coefficients calculated by a set of test points. As a result of a joint programme with Antwerp University, meta-modelling formed a large part of my research for almost a decade.

While meta-models proved extremely useful for passive structures, active components such as transistors are even today still best modelled by equivalent circuit models. To obtain the element values for such a circuit model, from for instance a set of measurements, is however challenging, as the sensitivity of any response to one of the elements can vary wildly between elements. So-called *parameter extraction* techniques thus also formed an important part of my research.

Finally, any device utilising multiple excitations, or multiple sets of electromagnetic fields, requires advanced network models. The development of network theory and models for thus type of device stretches back to the very start of my career, and has emerged again in my most recent work on multimode antennas. This is however discussed in chapter 5.

2.1.1 Accurate Filter Synthesis

In 1986, my final year project entailed the accurate exact design of filters using the insertion loss method combined with cascade synthesis. At that stage, the first personal computers typically had clock speeds of below 10MHz and typically 128kB of RAM, and floating point operations required a special co-processor. The problem with exact synthesis was (and is) that it is numerically ill-conditioned, in the sense that small rounding errors at each stage of the synthesis very quickly cause the synthesis to become unstable. In the cascade synthesis procedure, this takes the form of two element values which should be identical at each stage of the process, starting to diverge in numerical value. To combat this, synthesis could either be performed in a transformed frequency plane, known as z-plane synthesis, or by keeping all the polynomials in product form, i.e. as a list of roots. The latter was my project, and required a complex-valued numerical root-finding procedure at each step. No complex variable type however existed in any of the standard compiler languages, therefore I had to create a library of pointer-based algorithms to perform from the most basic of numerical operations, to fairly advanced two-variable Newton-Raphson algorithms.

This was my first taste of numerical work, and resulted in my first set of publications [3, 4]. It also initiated me into a field which would become one of my core research fields.

2.1.2 E-plane filters and the Mode-Matching method

Waveguide filters with thin metal inserts in the E-plane (therefore called *E-plane filters*), emerged as a very popular type of filter in the early eighties. All the inserts could be etched very accurately and inexpensively from a single thin metal sheet, resulting a filter with waveguide performance, yet requiring only very simple manufacturing techniques. An example is shown in Fig 2.1.

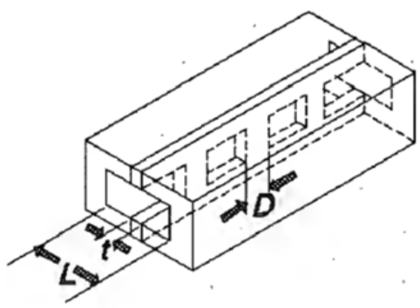

Figure 2.1: E-plane waveguide filter (from [5])

The goal of my Master's degree was to design such a filter. As full-wave optimisation of a three-dimensional structure was not possible, the design relied on creating equivalent circuit models of each vertical post, using numerical electromagnetic analysis of only one post. Thus resulted my first numerical code - an implementation of the Mode-Matching Method. This code ran on an Olivetti M24 personal computer, and could perform a narrow band frequency sweep of a second order filter in a few hours. At the time, the work was of significant interest to the local defence industry, as South Africa was under severe sanctions due to the political situation, and especially microwave components and subsystems were extremely hard to acquire on the open market. It was therefore published locally [5].

Due to the very long analysis times, the dependence on EM analysis in order to design these filters was problematic to local industry, and a set of equations was next derived to approximate the analysis accurately enough to design very narrow band filters [6, 7]. Finally, the work was extended to round pins in waveguide [8].

2.2 The Combined Mode-Matching and Method-of-Lines Technique

Both the technique for Mode-Matching analysis from my Master's degree work, and the complex root-finding technique from my undergraduate work, would prove to be building blocks of my first serious research effort, i.e. my PhD [9]. Again originating from industry, a serious local need had arisen for planar filters at the time of the start of my PhD. While the theory for the Finite-Element electromagnetic analysis (FEM) of planar circuits was well established at that stage, analysis of even a very simple structure, such as a single discontinuity, was a challenge in terms of both memory and execution time on a personal computer. Most compilers for personal computers (running Microsoft MS-DOS) had a maximum size limit of 64kB for any single variable, and for FEM analysis, quite complicated data structures were required which very quickly created single variable structures exceeding this limit. Even though various software techniques emerged to create larger variables by using more than one 64kB block, these were slow, clumpy and often failed.

For two-dimensional planar structures, a very efficient and accurate method of electromagnetic analysis was proposed by Pregla and Pascher in 1989. This method solved the two-dimensional Helmholtz equation in a transformed domain on a set of vertical lines, and was called the *Method-of-Lines (MOL)*. The basic structure for half of a symmetrical two-layer planar structure is shown in Fig. 2.2.

The MOL relied on the discretisation of the partial derivative with respect to the horizontal direction. With the z-directed electric field on line i described

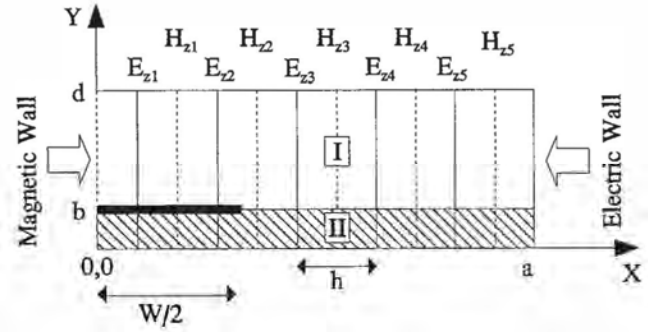

Figure 2.2: Discretisation for 2D Method-of-Lines(from [10])

by a set of equations

$$\frac{\partial^2 E_{zi}}{\partial x^2} + \frac{\partial^2 E_{zi}}{\partial y^2} + (\gamma^2 + k^2)E_{zi} = 0 \tag{2.1}$$

where $i = 1 \ldots N$, the finite difference derivatives with respect to x can be expressed in a matrix form as

$$\frac{\partial^2 [E_z]}{\partial x^2} = \frac{1}{h^2}[D_{xx}][E_z] \tag{2.2}$$

This allows the system to be diagonalised using standard matrix techniques and the diagonalisation matrix $[T]$, consisting of the eigenvectors of $[D_{xx}]$. In turn, this can be used to define the transformed field vector $[\tilde{E_z}] = [T]^t[E_z]$. When inserted back into a transformed Helmholtz equation, a set of one-dimensional, second order differential equations in y are obtained as

$$\frac{1}{h^2}[d][\tilde{E_z}] + \left(\frac{\partial^2}{\partial y^2} + \gamma^2 + k^2\right)[\tilde{E_z}] = 0 \tag{2.3}$$

where $[d]$ is the diagonal eigenvalue matrix of $[D_{xx}]$. Each of these equations can be solved separately by applying the correct, transformed boundary conditions and solving for values of γ.

The 2D-MOL is a very efficient numerical implementation, as only one dimension is discretised while the other is treated analytically, resulting in very small matrices. The extension to three-dimensional problems however proved to be difficult, as instead of $N \times N$-matrices (where N is the number of lines), sets of $N_xN_z \times N_xN_z$ matrices result (with N_x the number of lines in the x-direction and N_z the number of lines in the z-direction). For structures with large z-dimensions such as transmission-line filters, this proved fatal, as the matrices simply became too large.

For my PhD, I proposed a combination of the very memory-efficient 2D-MOL, and the equally memory-efficient *Mode-Matching Method*. The latter was one of the first numerical electromagnetic analysis techniques, and entails the matching of orthogonal expansions of fields on both sides of an abrupt discontinuity.

In order to do this, the work firstly developed closed-form analytical expressions for the transformed fields in the 2D-MOL [11], which at that point were not available in literature. This was then used to find solutions for the propagation constant γ for each cross-section of the structure. The process to calculate γ for high numbers of modes (up to 100) is completely non-trivial, and involves the finding of multiple imaginary and complex roots, in ascending order without skipping one, of a severely non-linear function which exhibits poles and zeros in random orders - such function not being available analytically, but only through a computer algorithm. The next step, i.e. the application of the Mode-Matching Method, required the solution of the generalised scattering matrix for each discontinuity, using the integrals of products of the fields. To implement this analytically, I developed a set of Mode-Matching equations in the transformed domain which yielded a full set of generalised S-parameters using only analytical diagonal matrices, of low order. This was the first formulation of this nature, and because of the diagonal nature and the low order of the matrices, had a very low memory requirement, and a fast execution speed [10]. The method was further extended to analyse whole structures by cascading the S-parameters of each discontinuity with section of multi-modal transmission lines.

The combined technique, called the *Combined Mode-Matching and Method-of-Lines Technique*, was tested on a variety of single microstrip discontinuities such as open and short-circuits, and gaps. As a final illustration, a small interdigital filter which exhibited an unexpected transmission zero, was analysed [12]. The filter, and its cross-sections, are shown in Figs. 2.3 and 2.4

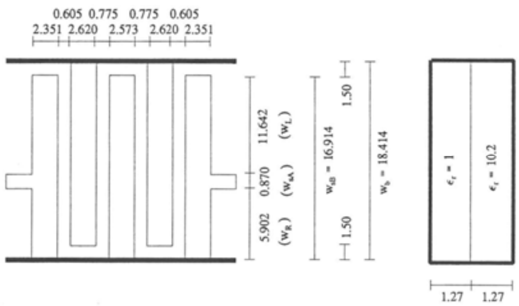

Figure 2.3: Interdigital filter top view (from [12])

The full filter response, shown in Fig. 2.5, clearly shows the transmission zero, and a filter response with a 5% error in centre frequency as compared to measurement.

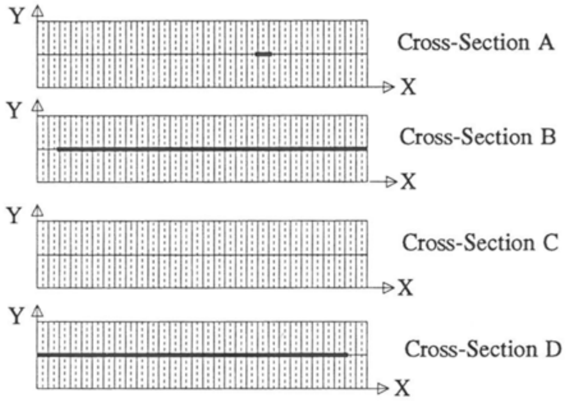

Figure 2.4: Interdigital filter cross-sections (from [12])

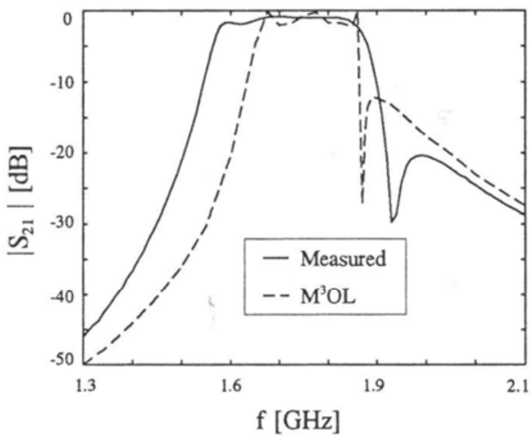

Figure 2.5: Interdigital filter response (from [12])

To assess this work after a twenty-five-year interval is complex. After two decades of rapid progress in computational electromagnetics, it is hard to envisage a scenario where no commercial tools were available to analyse even a small filter. For the example shown, this code was one of a very small number of methods at the time which could analyse such a filter on a small PC. The result in Fig. 2.5 indeed shows only a comparison with measured data, as no other software was available. As such, the work constituted a very useful tool for planar design, as it could show full-wave effects in addition to the normal circuit, or TEM-line analysis. It also extended the 2D-MOL significantly, as the 3D implementation would never become viable due to the very large data structures it required.

At the time, this approach had the following unique advantages over existing methods:

- Using the smallest data structures of any full-wave method.
- Having data structures independent of the longitudinal dimension of a structure. This was especially useful for planar filter structures having relatively few discontinuities along the longitudinal direction, but electrical lengths of a number of wavelengths.
- Having both memory requirement and execution time completely independent of the height of the structure, as that was treated analytically.
- Yielding modal information between every two successive discontinuities.

The enormous jumps in computer hardware and software would however, within a few years, remove the limits on variable size, and allow for huge data structures. This suited the methods utilising full three-dimensional discretisation, which could be used for much more general structures. Methods like the one proposed here therefore very quickly became redundant, and would indeed be replaced rapidly by commercial software such as CST, Ansoft HFSS, etc.

The impact of this first research project on my own work would however turn out to be significant and lasting, and a very important building block in my career. Especially the themes related to higher order electromagnetic modes would become a recurring theme in my work, and would appear in future work on microwave filters, modelling, and antennas.

2.3 Other Computational Work

Following the completion of my PhD, my work would mostly shift from direct CEM to that of modelling and structural design. However, a number of contributions on CEM were made over the years, mostly as part of various bigger projects.

The first of these was work on the so-called *hybrid methods* that were very popular in the early 90's. At this time, a large body of research focused on the combination of different numerical methods, exploiting the strong points of each. For this work, PhD student Dr Riana Geschke, with supervision from my colleague Prof David Davidson, Prof Ron Ferrari from Cambridge, and myself, implemented a method proposed by Prof Ferrari, the so-called *Extended Huygens' Method*, for waveguide problems [13]. The technique formed part of the class of hybrid Integral Equation and Finite Element techniques, as applied to general penetrable discontinuities, with the aim of treating the region exterior to waveguide discontinuity using the Surface Integral Formulation, and the discontinuity with the Finite Element Method. The method employed both the electric and magnetic waveguide Green dyadics in an integral equation that may be recognised to be of the form described as a formulation of Huygens' principle, here satisfying the particular field boundary conditions of a hollow waveguide [14, 15, 16, 17]. The method proved to be efficient in terms of memory, but again the rapid improvements in computers made the work essentially obsolete within a few years.

Other work, in the form of small niche solutions, were focused on improving the speed of standard methods for specific structures. The first of these was a technique for optimally selecting the modes to be used in a given Mode-Matching implementation, which emerged from the PhD work of my student Dr Chris Vale, during his research into multi-modal stopband filters [18]. For general cross-sections, an infinite set of modes, including all TE, TM, and hybrid modes need to be used to perfectly match fields at a boundary. However, the behaviour of scattering parameters are typically influenced by only a few dominant modes. For simple problems, it is straightforward to identify these dominant modes, but for more complex problems, this becomes more difficult. This work automated this process, and reduced the matrices to be solved dramatically by ignoring non-dominant modes.

A second very useful contribution in this area, was from the Master's degree work on Method-of-Moments implementations by my student Dr Marlize Schoeman [19], and took the form of a detailed analysis of the structure of the matrices generated by the Method-of-Moments' formulations utilising both magnetic and electric surface currents for apertures and metal sections respectively [20]. As for the work on Mode-Matching, this work was aimed at packing the matrices in ways that allow for a separation between dominant and non-dominant entries, resulting in smaller matrices. In addition, the work provided fascinating insights into the method itself.

As a final contribution of significance in this list, an algorithm for optimising the placement of sources in the 2D Method-of-Moments analysis of coupled line structures of arbitrary form, resulted from the undergraduate work on interdigital filter design by my student Dr Dirk de Villiers [21]. The method used straight-line shadows to calculate directly illuminated areas, with these areas then populated with a high density of sources. The 2D Method-of-Moments is very simple to implement, and the technique is still used widely for quick MATLAB programmes.

While general CEM software has become the default tool for designers over the last decade, such software is still very expensive, especially for industry. For standard structures, many of the classical techniques can be (and often still are) self-coded. The improvements referenced here are therefore still used in industry, even today. Open-source software such as Python has in fact created a small resurgence in the development of toolboxes which can analyse sets of very specific and limited structures.

2.4 Measurement

An important part of modelling is of course the verification of models. In the 1990's, this was mostly done using published results, or measurements using Vector Network Analysers. For the latter, calibration is of essence, and my modelling work at the time exposed me to the world of calibration and measurements. At the time, superconductors also formed part of my interests, and my very first postgraduate student, Mr Jakobus van Zyl, therefore worked on calibration procedures for measurements of superconducting passive devices [22]. This also resulted in the first international conference publication by one of my students, an important milestone in my career [23]. This work also brought me my first PhD student, Dr Cornel van Niekerk, who started his career on this subject [24].

2.5 Parameter Extraction of FET Circuit models

Starting in 1996, myself and Dr Cornell van Niekerk embarked on a project to extract circuit models for Field-Effect transistors (FET's) from measured S-parameters [25]. This work was in response to a need by the local RADAR industry to have a better first-pass design success for microwave amplifier designs. At the time, few good models were available from vendors, and designers had to rely on generic models, or measured data. The availability of a good circuit model offered significant design advantages in terms of noise matching, or gain optimisation over frequency.

The first step in this direction was a new procedure to calculate element values of a general small-signal FET circuit model which would fit a given set of small-signal S-parameters. This calls for a solution to the so-called *parameter extraction* problem, a very difficult process, as the standard FET-model shown in Fig. 2.6 has 13 circuit elements, while only four complex S-parameters, over a limited frequency range, are available to perform a fit.

The problem can be classified as an inversely ill-conditioned sensitivity problem, where a very small dependency of the S-parameters to some of the circuit elements translates into great difficulty in finding an accurate value for such an element from the S-parameters. Historically, it was approached using a single, global multivariate error function, with the error function consisting of a weighted sum of the differences between each of the four sets of predicted and measured S-parameters, in a 13-dimensional error landscape. This landscape is ill-conditioned, and exhibits large numbers of local minima with minimum values very close to that of the absolute minimum, and large variations in sensitivity to different variables. In the case of the FET-model, the extraction of element values for the resistive components is particularly difficult, and the

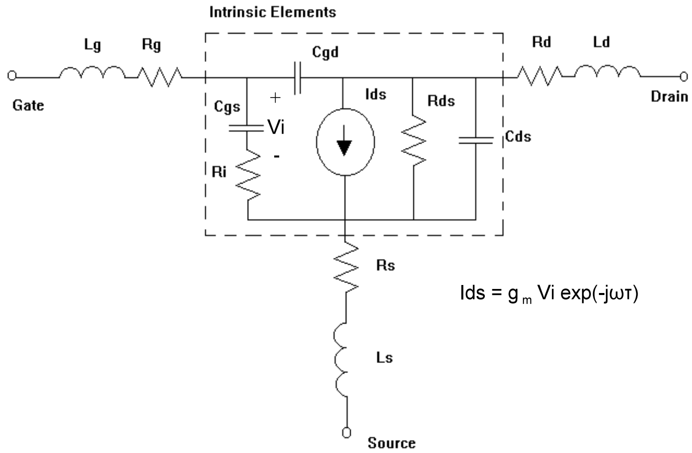

Figure 2.6: 13-Element small-signal FET-model (from [25])

state-of-the-art extraction techniques in 1996 produced very inaccurate results, with errors of up to a factor of 10, for these elements.

The proposed technique called for the separate, systematic minimisation of 13 univariate error functions - one for each circuit element - of the form

$$F_{(j,b)}(\bar{x}_i, z) = \sum_{k=1}^{M} |S_k(j,b)^{meas} - S_k(j,b)^{calc}(\bar{x}_i, z)|^2 \quad (2.4)$$

where $\bar{x}_i$ represent 12 fixed elements, k the frequency point, (j, b) the S-parameter index, and z the element to be extracted using the i-th error function. As the value obtained for any such single extraction (or minimisation) is dependent on the values of the other 12 elements, the 13 minimisation steps have to be executed multiple times, until the values have converged to within a pre-set error band. Such convergence is by no means guaranteed, as the minimisation problem is extremely ill-natured. To solve this problem, a global error function was formed by adding the error functions for all the S-parameters before each set of 13 minimisation steps, and a principle components sensitivity analysis was performed on this function. This analysis uses the eigenvalues of a Jacobian matrix, formed from the global error function, to determine the sensitivity of the global error function at the point in the parameter space, to each parameter. In this case, the parameters (elements) can then be ordered in terms of decreasing sensitivity, and the 13 error functions then minimised in this order. After each full iteration of 13 functions, a new sensitivity analysis is performed, and the order updated. Such an *adaptive* ordering of the univariate minimisation problems had never been used for this type of extraction at that stage, and proved to be the key to the convergence of the procedure to a global minimum.

The procedure, denoted as *Decomposition-Based Parameter Extraction*, was a significant step forward, and reduced the errors in extraction by orders of magnitude, as can be seen from the table in Fig. 2.7, which compared the new procedure with the state-of-the-art at that time, for a few transistors [26].

TABLE 2 The Percentage Error Made by Two Different Parameter-Extraction Routines

Model Elements	FLR016XV a	FLR016XV b	FSX51X a	FSX51X b	FLK052XV a	FLK052XV b
R_{ds}	0.003	0.316	0.210	2.078	0.067	2.282
C_{ds}	0.002	0.038	0.039	0.353	0.014	0.494
C_{gs}	0.004	0.352	0.244	2.349	0.075	2.650
C_{dg}	0.010	0.724	0.242	2.427	0.129	4.546
R_s	0.099	8.669	3.003	28.042	0.928	31.787
g_m	0.004	0.314	0.221	2.119	0.066	2.331
R_d	0.030	3.111	2.497	23.895	0.752	26.005
L_d	0.002	0.019	0.007	0.090	0.004	0.119
R_g	9.780	884.725	23.756	228.038	12.149	438.795
R_i	0.317	28.641	3.828	36.435	2.699	96.369
L_g	0.001	0.118	0.048	0.388	0.012	0.295
L_s	0.010	0.399	0.034	0.299	0.008	0.193
τ	0.002	0.272	0.155	1.489	0.053	1.847

[a] Results obtained with the new parameter-extraction procedure.
[b] Results obtained with the 10-step parameter-extraction procedure of Leong et al. [2].

Figure 2.7: Comparison of extraction errors (from [26])

The proposed extraction algorithm was evaluated rigorously in 1997 in a follow-up paper [27]. This paper again used simulated S-parameters, and provided an in-depth look at the performance and accuracy of the technique. Fig. 2.8 for example shows the robustness of the minimisation, with the global error function climbing for more than 70 iterations before converging rapidly.

Of considerable interest was the significant variations in the univariate landscapes of each minimisation problem as a function of the iteration cycle, as is shown in Fig. 2.9 for the variable C_{gs}. This gave previously undocumented insight into the convergence characteristics of this type of extraction, and would lead in future work to much more refined minimisation algorithms.

Finally, the paper introduced an innovative way of evaluating the robustness of such a technique visually, by plotting the start and end values of a variable against the extraction number, for a hundred extractions, each starting with a different set of element values. For perfect robustness, each extraction, irrespective of the starting value, should give the same end value - the end values thus forming a straight line. Fig. 2.10 shows such a plot for two of the most difficult elements. It is immediately clear that the algorithm is very robust for element R_i, but much less so for element R_g.

For the last phase of this work with which I was involved, Dr Van Niekerk teamed up with Dr Dominique Schreurs from KU Leuven, and Dr Peter Winson from Raytheon in Dallas, to expand the technique to multi-bias models [28], [29]. For this, each element is simply viewed as being bias-dependent, and

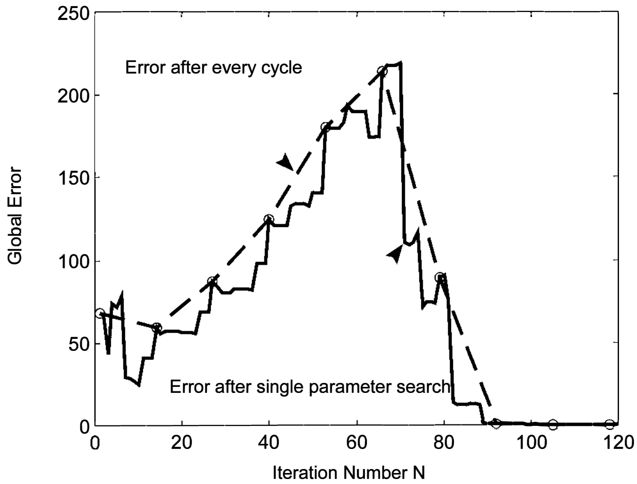

Figure 2.8: Global error function behaviour (from [27])

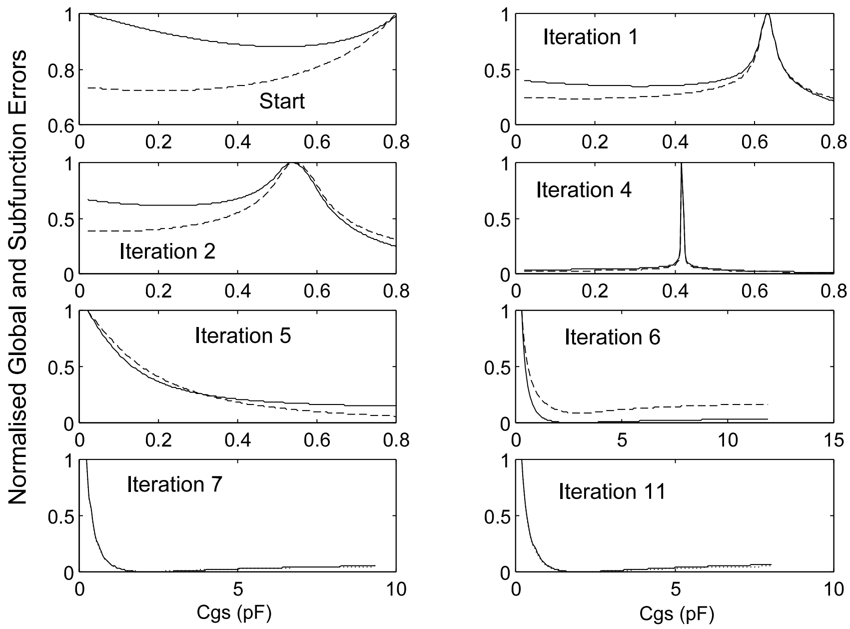

Figure 2.9: Global error function behaviour (from [27])

an extraction performed at each bias point. However, some elements are essentially bias independent, and taken together over all bias points, significant improvements can be obtained for these elements. The paper also introduced 'cold' measurements (or zero bias) into the pool of data , and improvements

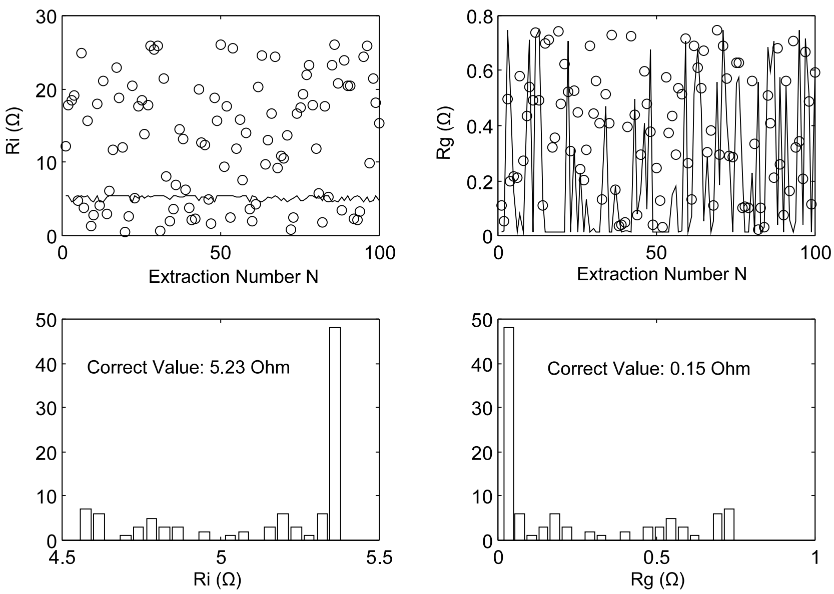

Figure 2.10: Robustness plots and histograms (from [27])

to handle measurement noise. Very accurate models could be obtained in this way, and fundamental insights into the circuit behaviour under different bias conditions.

The Decomposition-Based Extraction proved to have a number of significant advantages to other techniques at the time:

- It only made use of a single global error function for ordering the subproblems, not for the optimisation itself, making it more immune to local minima and the ill-conditioned nature of the problem than other methods.
- It determined all the elements with optimisation and proved itself to be resistant to the effect of measurement errors.
- It required no assumptions concerning the bias dependencies of the intrinsic elements.
- It was suitable for modelling commercial devices about which very little additional information was known.

The work was my first effort as a PhD supervisor, and proved to be very successful and long-lasting. In total, this set of papers has been cited more than 80 times, with the latest citations in 2010, or two decades after publication. In the most recent citations, the minimisation algorithms have changed, but the basic principles introduced by Dr Van Niekerk and myself are still being used. Dr Van Niekerk continued this work after completion of his PhD, and would make a distinct name for himself in the world of device modelling.

On a personal level, [27] became my first paper in the prestigious *IEEE Transactions on Microwave Theory and Techniques* - a very important milestone in my career.

2.6 Interpolation-Based Meta-Models of Microwave Components

2.6.1 Adaptively sampled interpolation models

For networks of which the internal structure is not known at all, circuit-based models are difficult to construct, and pure mathematical models, the so-called *meta-models*, offer a much more general set of models. These models use mathematical functions which describe one or more network outputs as a function of one or more variables, with a wide variety of mathematical functions having been proposed. In its most general sense, this forms part of the mature mathematical research area of *approximation functions*, but in the early 2000's, the application to microwave structures and electromagnetic analysis was quite new.

One of the most important goals for this class of applications, is to use the least possible amount of analysis points (or *support points*) in order to establish a model, as the generation of such points using computational electromagnetic analysis is very time-consuming. This problem is intimately connected to the exact type of mathematical function, as some functions naturally approximate typical passive network functions better than others.

In 1999, my PhD student Dr Robert Lehmensiek, myself, and Profs Tom Dhaene (then from Antwerp University, and since at Ghent University) and Annie Cuyt from Antwerp University, initiated a project on using rational interpolation functions to create meta-models for passive microwave structures [30]. Rational functions are particularly well-suited for this type of structure, as most passive structures can be modelled in terms of passive network functions, which are fundamentally of a rational polynomial nature. The project formed part of a larger activity of Prof Dhaene, who had for a number of years been active in the field.

The first phase of this project was the proposal of an algorithm to reduce the amount of support points for a single network function, dependent on one variable only, and to use it in the very popular *Space-Mapping* optimisation technique [31]. As approximation function, the rational polynomial in (2.5) was used, with both numerator and denominator in the form of the recursive partial fraction expansions in (2.6) and (2.7). Here, frequency (f) is the variable, and $R(f)$ represents a network function such as one S-parameter.

$$R(f) = \frac{\sum_{k=0}^{\zeta} p_k f^k}{\sum_{k=0}^{\nu} q_k f^k} = \frac{N_\zeta(f)}{D_\nu(f)} \tag{2.5}$$

where

$$\begin{aligned} N_k &= \psi(f_k, f_{k-1}, \ldots, f_0)N_{k-1} + (f - f_{k-1})N_{k-2} \\ D_k &= \psi(f_k, f_{k-1}, \ldots, f_0)D_{k-1} + (f - f_{k-1})D_{k-2} \end{aligned} \tag{2.6}$$

and

$$\psi_k(f_k, f_{k-1}, \ldots, f_0) = \frac{f_i - f_{k-1}}{\psi_{k-1}(f_i, f_{k-1}, \ldots, f_0) - \psi_{k-1}(f_{k-1}, f_{k-2}, \ldots, f_0)} \tag{2.7}$$

For such a function, the order determines the number of support points, with the location of these points not specified. The order of the function is however unknown, as the network function can be of any complexity. In addition, the location of the support points has a dramatic effect on the accuracy of the final function. The algorithm in [31] proposed the generation of a set of functions of systematically increasing order. The recursive partial fraction expansion form is very well-suited to such an algorithm, as a very natural error function can be found by simply subtracting two successive functions. To increase the order by one, a new support point is then chosen at the point where the two functions of highest order differ the most in the range of interest. The process thus yields an *adaptive sampling technique* for establishing a meta-model. This process is shown for two orders in Fig. 2.11, together with the resulting error function. At each support point, the error function becomes zero. The algorithm continues until the error function is smaller than some arbitrary value over the range of interest. The combination of adaptive sampling and the recursive partial fraction form, requires an order of magnitude smaller number of support points for a certain accuracy, as all the support points are optimally positioned.

To illustrate the power of the procedure, it was used in the Space-Mapping optimisation algorithm to reduce the number of sampling points in the return-loss function of a microwave filter [31]. The result of such an optimisation is shown in Fig. 2.12, together with the actual support points. It is clear that only a few points are required to very accurately model the return loss function.

From my previous work, a very obvious application of the adaptively sampled meta-model technique, was as an intermediate step in the calculation of the poles and zeros of functions, and specifically in the calculation of the propagation constants of higher order modes in guided-wave structures [32],[33]. Such propagation constants are typically numerically calculated by finding the solution to the so-called *characteristic function*, of the form

$$g(\gamma) = \det[Y(\gamma)] = 0 \tag{2.8}$$

6	9.66	3.4071	0.11554
7	8.82	0.15642	0.063557
8	9.30	1.5324	0.078406
9	8.88	3.2876	0.59799
10	11.20	0.89726	0.31784
11	8.42	50.271	0.54331
12	10.34	4.9408	0.0602
13	9.48	0.27409	0.048094
14	11.36	0.27793	0.017606
15	10.90	0.019483	0.0076628
16	8.22	0.038204	0.032795
17	8.54	0.032615	0.0083645
18	8.10	0.018352	0.0011104
19	10.68	0.0071846	3.4605e-5

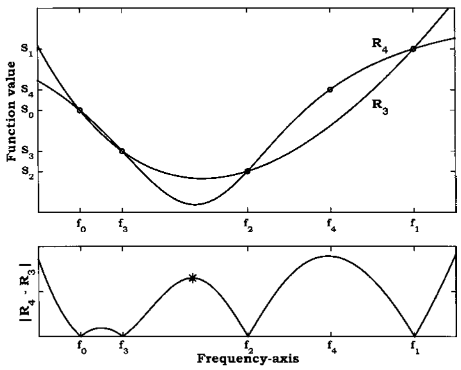

Figure 1 Illustration of the adaptive sampling technique. The interpolation functions $R_3(f)$, $R_4(f)$ and the residual $|R_4(f) - R_3(f)|$ are shown. The asterisk indicates the new sample point

Figure 2.11: Model responses of successive order (from [31])

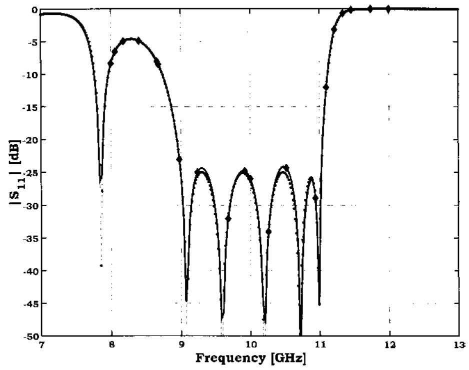

Figure 4 Fine model response (solid line) after the second ASM iteration determined by the adaptive sampling algorithm using the sample points indicated by diamonds. The dotted line represents the optimal response

Figure 2.12: Optimised response showing support points (from [31])

IV. USING ADAPTIVE SAMPLING IN ASM

The ASM technique [12] minimizes the number of fine model simulations in the design optimization by performing optimization of a coarse model instead of the actual EM model, and iteratively establishes a mapping between the spaces of the design parameters of the two models. Define the vectors $\mathbf{x}_{os}$ and $\mathbf{x}_{em}$ as the design parameters of the coarse and the fine models, respectively, and $\mathbf{R}_{os}(\mathbf{x}_{os})$ and $\mathbf{R}_{em}(\mathbf{x}_{em})$ as the corresponding model responses. Parameter extraction is used to determine $\mathbf{x}_{os}$, whose response matches the fine model response at $\mathbf{x}_{em}$ for every space mapping iteration. When applying the adaptive sampling algorithm, $\mathbf{R}_{em}(\mathbf{x}_{em})$ is replaced by the adaptively determined $R(f)$, where $R(f)$ is valid for a certain fine model input parameter vector $\mathbf{x}_{em}$ over the entire frequency band for all of the scattering parameters. Note that the ASM technique combined with the adaptive sampling algorithm requires the convergence of three iterative processes, i.e., 1) the adaptive sampling algorithm determining $R(f)$ which approximates $\mathbf{R}_{em}(\mathbf{x}_{em})$, 2) the parameter extraction step determining $\mathbf{x}_{os}$, whose response matches $R(f)$, and 3) finding $\mathbf{x}_{em}$ that produces the optimal response according to design specifications (space mapping). The adaptive algorithm uses the minimum number of frequency sample points [8] fine model simulations to determine $R(f)$. Given $R(f)$, an arbitrary large number of frequency points can be chosen to ensure the nonfailure of the parameter extraction step if $R(f)$ is determined for every ASM iteration. The adaptive sampling algorithm can also be applied to the response vector of the coarse model $\mathbf{R}_{os}(\mathbf{x}_{os})$.

The design of a rectangular waveguide filter with eight capacitive steps is considered. The design specification for the filter is $|S_{11}| \leq -15$ dB in the passband, where the passband lies in the range [9 GHz, 11 GHz]. The design is for a standard WR90 rectangular waveguide. The capacitive step lengths are all chosen 2 mm long. The filter is symmetric with eight optimization variables ($L_1, L_2, L_3, L_4, C_1, C_2, C_3, C_4$) as defined in Figure 2. The fine model is a mode-matching solution combined with the generalized scattering matrix [15]. With a TE_{10}-mode incident on a capacitive step in a rectangular waveguide only, TE^{x}_{1n}-modes (with n even) are necessary for a complete description of the fields [16]. The number of even modes considered on both sides of a waveguide junction was set to 15. Increasing the number of modes had no noticeable effect on the response of the filter. Because of the symmetry, the generalized scattering matrices of only four discontinuities need to be calculated with the mode-matching algorithm. The coarse model is a transmission-line model, as shown in Figure 2(b).

ASM assumes that $\mathbf{x}_{os}$ and $\mathbf{x}_{em}$ describe the same physical parameters, which is not the case here. We can calculate the capacitance and the transmission-line length for a waveguide step using the mode-matching technique for several values of the gap opening. Interpolation of these values establishes a mapping from the circuit model variables $\mathbf{x}_{em}$ to the physical waveguide dimensions. Since the ASM technique compares $\mathbf{R}_{os}(\mathbf{x}_{os})$ and $\mathbf{R}_{em}(\mathbf{x}_{em})$, this mapping is incorporated into the ASM.

The parameter extraction optimizations are driven by a BFGS quasi-Newton method [14] with a mixed quadratic and cubic line search procedure [14]. l_1 norm objectives are used throughout the ASM algorithm. The input parameter $\mathbf{x}^{*}_{os}$, which produces the optimal response, is determined by minimax optimization on the coarse model, also using the BFGS quasi-Newton method. The response of $\mathbf{x}^{*}_{os}$ is shown in Figure 3 (dotted line). The solid line shows the fine model response $\mathbf{R}_{em}(\mathbf{x}^{(1)}_{em})$ with $\mathbf{x}^{(1)}_{em} = \mathbf{x}^{*}_{os}$, which was determined by the adaptive sampling algorithm with only 12 frequency samples (diamonds) and interpolating for a smooth response. The two responses differ significantly due to the evanescent modes

where γ is the complex propagation constant, and $\det[Y(\gamma)]$ the determinant of a matrix produced by the specific numerical technique. This function is severely non-linear, with an infinite number of solutions, interspersed with an infinite number of poles and very sharp non-zero local minima. The function is also not known in closed form for most microwave structures, but only at discrete frequency points. A typical example is shown in Fig. 2.13.

Using the adaptively sampled meta-model technique, the characteristic function is found as separate denominator and numerator functions, both of which are polynomials (with only zeros), using the least number of analysis points [32]. As example, Fig. 2.13 also shows the support points, with Fig. 2.14 showing the numerator and denominator polynomials. Once the latter functions are accurately approximated, it becomes a trivial task to obtain the zeros of the numerator.

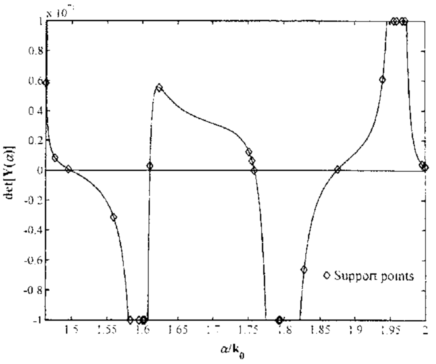

Figure 2.13: Typical characteristic function (from [32])

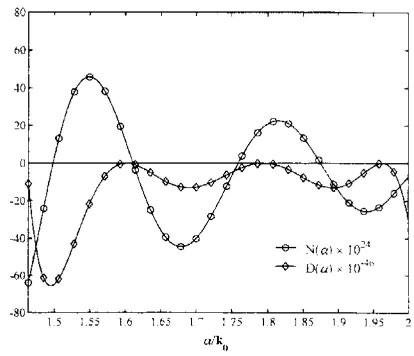

Figure 2.14: Characteristic function as numerator and denominator showing support points (from [32])

The propagation constants of two widely used structures were calculated in this way - one the microstrip structure shown in Fig. 2.15, and one the finline structure in Fig. 2.16. For the microstrip example, a set of higher-order modes both below and above cut-off is shown in Fig. 2.17, while the finline example shows the propation constant of the fundamental mode for different dimensions in Fig. 2.18. It should be noted that, even at the time of writing, it is a difficult task to obtain Fig. 2.17 without such an intermediate model.

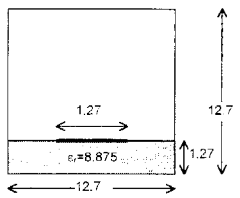

Figure 2.15: Microstrip line cross-section (from [32])

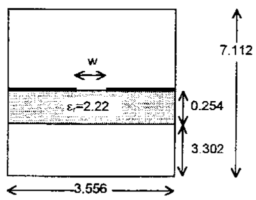

Figure 2.16: Finline cross-section (from [32])

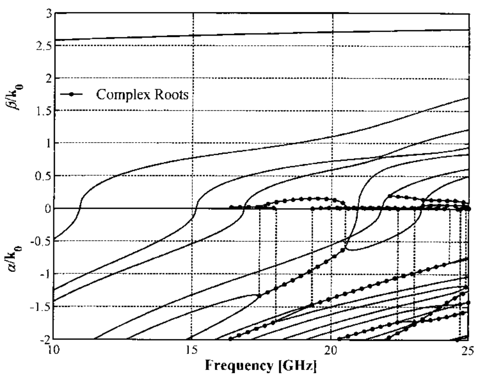

Figure 2.17: Microstrip modes (from [32])

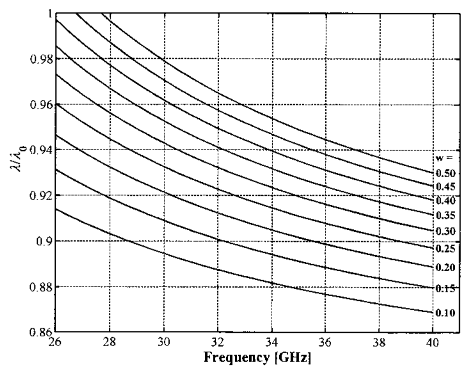

Figure 2.18: Finline modes (from [32])

The next phase of this project was to extend the algorithm to multi-variable and multiple output models. For the multi-variate case, each of the ψ-functions in (2.7) is replaced with a recursive set of functions, each recursion level containing one fewer variable. The mathematical equations for this are quite complex, and is not repeated here, but the reader is referred to [34], [35], and for even more detail, [30].

The adaptive sampling process also has to increase to an n-dimensional landscape, which calls for innovative sampling. In [34], samples were chosen in an increasing fashion along constant-valued lines in the n-dimensional variable space. Again, the reader is referred to the original texts.

An example of a two-dimensional problem ... plotted against the two variables ... error between the approximation ... Fig. 2.20 for the support ...

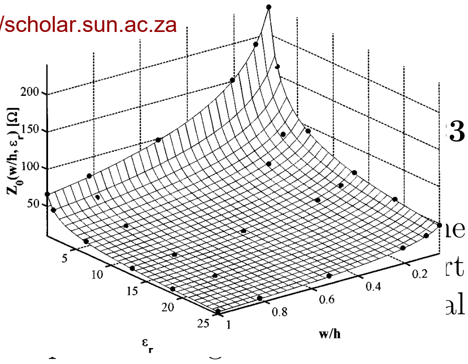

Fig. 5. ASA2: stripline example. Response of $\Re(w/h, \varepsilon_r)$ with 29 support points.

Figure 2.19: Two-variable function landscape shown ... (from [34]).

The multi-... of which are shown here, Fig. 2.21 and Fig. ... a waveguide, with the error for two frequency ... of support points ... a waveguide, ... three-variable c...

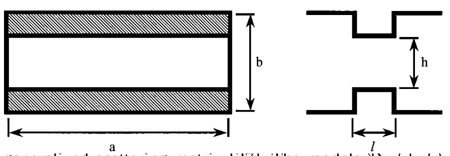

Figure 2.21: Step in waveguide (from [34]).

Figure 2.22: Model errors for step in waveguide (from [34]).

TABLE V
CONVERGENCE OF $\Re_{11}(f, w)$ DETERMINED BY ASA1 AND ASA2 FOR THE INDUCTIVE POSTS EXAMPLE

ASA1			ASA2		
Number of support points	E_{11}(f, w) [dB] Mean	Max	Number of support points	E_{11}(f, w) [dB] Mean	Max
18	−32.4	−16.8	18	−38.1	−23.7
36	−39.8	−13.8	28	−67.2	−49.2
48	−88.4	−73.8	53	−91.5	−73.7

TABLE VI
CONVERGENCE OF $\Re_{21}(f, w)$ DETERMINED BY ASA1 AND ASA2 FOR THE INDUCTIVE POSTS EXAMPLE

ASA1			ASA2		
Number of support points	E_{21}(f, w) [dB] Mean	Max	Number of support points	E_{21}(f, w) [dB] Mean	Max
18	−38.1	−25.1	23	−59.1	−41.6
36	−39.6	−9.2	30	−52.1	−27.4
48	−89.8	−68.6	51	−76.8	−51.3
56	−90.4	−64.9	57	−87.9	−72.5

TABLE VII
CONVERGENCE OF $\Re_{11}(f, h, l)$ DETERMINED BY ASA1 FOR THE CAPACITIVE STEP EXAMPLE

f ∈ [8 GHz, 12 GHz], h ∈ [3 mm, 7 mm], l ∈ [1 mm, 4 mm]			f ∈ [7 GHz, 13 GHz], h ∈ [2 mm, 8 mm], l ∈ [0.5 mm, 5 mm]		
Number of support points	E_{11}(f, h, l) [dB] Mean	Max	Number of support points	E_{11}(f, h, l) [dB] Mean	Max
64	−65.1	−49.5	150	−56.6	−31.1
180	−82.2	−55.5	294	−62.0	−30.1
294	−85.3	−59.5	576	−59.3	−15.1
512	−100.8	−63.1	1300	−81.0	−32.1
832	−108.2	−76.6	1716	−83.2	−35.0
936	−109.3	−96.8	2730	−70.0	−26.7

TABLE VIII
CONVERGENCE OF $\Re_{11}(f, h, l)$ DETERMINED BY ASA2 FOR THE CAPACITIVE STEP EXAMPLE

f ∈ [8 GHz, 12 GHz], h ∈ [3 mm, 7 mm], l ∈ [1 mm, 4 mm]			f ∈ [7 GHz, 13 GHz], h ∈ [2 mm, 8 mm], l ∈ [0.5 mm, 5 mm]		
Number of support points	E_{11}(f, h, l) [dB] Mean	Max	Number of support points	E_{11}(f, h, l) [dB] Mean	Max
115	−70.7	−21.9	343	−55.5	−15.3
164	−75.5	−46.7	593	−67.0	−31.4
300	−86.6	−57.8	737	−76.5	−40.0
379	−89.9	−75.8	871	−79.5	−47.0
496	−107.3	−86.0	1375	−91.7	−47.7
645	−108.3	−94.4	1758	−96.1	−54.7
917	−109.1	−97.5	2142	−97.2	−58.1

For many problems, more than one output function needs to be modelled, for instance S_{11} and S_{21} for a passive circuit. Normally, individual models will be built for such a problem, but in [36], the same set of support points, adaptively chosen to yield an optimum model for all output functions, was used. This resulted in a significant reduction in support points, as shown in Figs. 2.25, 2.26, 2.27 and 2.28 where a two-variable, two-output capacitive

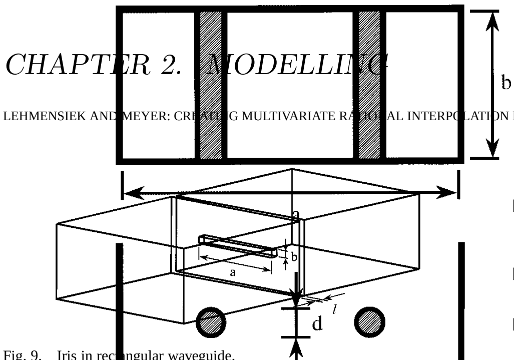

Figure 2.23: Iris in waveguide (from [34]).

step model, and a three-variable, three-output waveguide example are shown.

Figure 2.24: Model errors for iris in waveguide (from [34]).

Figure 2.25: Step in waveguide for multi-variate, multiple output problem (from [36]).

Figure 2.26: Model errors for the step in waveguide for multi-variate, multiple output problem (from [36]).

Figure 2.27: Slot in waveguide for multi-variate, multiple output problem (from [36]).

Figure 2.28: Model errors for slot in waveguide for multi-variate, multiple output problem (from [36]).

In terms of citations, the work in this section represents the research from the author with the highest impact. At the time, the algorithm required the least amount of support points for a multi-variate problem of any of the available techniques, was very stable numerically and produced a model that had many benefits due to its partial fraction nature. The paper in the *IEEE Transactions on Microwave Theory and Techniques* has turned out to be the most cited paper from my group, and is still cited every year a number of times. It provided a benchmark of sampled interpolation models for at least a decade, and is even today still a method to which new algorithms are compared.

2.6.2 Extended meta-models

Dr Lehmensiek's work was continued by another PhD student, Dr Marlize Schoeman, again in cooperation with Prof Dhaene and Prof Cuyt. For the follow-up work, we focused on the application of meta-models to microwave resonators [37]. The analysis of high-Q resonators is quite challenging, as most resonators exhibit multiple resonance modes, and the Q-factor of each of these modes, as well as their centre frequencies, are often of interest. The Q-factors are of special importance, as they determine the performance of any device which utilises a resonator, such as filters, oscillators, etc. Typical computational analysis of Q-values performs a loss-less eigenmode analysis to obtain the resonance frequencies and the field distributions at each frequency, and then uses the loss-less surface currents to calculate loss, and the loss-less fields to calculate stored energy. From these two values, the Q is obtained as a simple ratio. This approximated technique is used because the eigen-solution of a structure is much more difficult if lossy boundaries (or complex impedance boundaries) are included in the basic analysis.

For structures containing bulk loss mechanisms, such as dielectric, and radiation or surface-wave losses, such as open microstrip, the approximate technique does however not work, as loss has to be included in the basic formulation. This also means that eigenmode analysis is mostly not possible, except under very specific conditions. Instead, the calculation of resonant frequency and Q are typically done by analysing a structure which consists of a port, or two ports, coupling lightly to the resonator, and calculating the Q from an $|S_{21}|$ or $|S_{11}|$ sweep against frequency, as shown in Fig. 2.29. In principle, the resonance frequencies are simply read off from such a sweep, as the points of maximum transmission or minimum reflection, and the Q is calculated by the ratio of the magnitude at that point and the 3dB-bandwidth.

CHAPTER 4—CALCULATION OF RESONANT FREQUENCIES 43

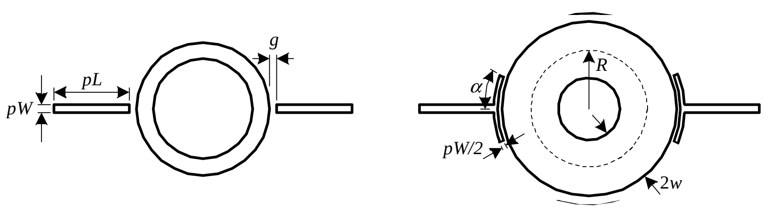

Fig. 4.7. Excitation used to construct ring resonators of normalised ring width $w/R = 0.1$ and $w/R = 0.6$.

Figure 2.29: Input and output coupled ring resonators (from [38])

and Vector Fitting) are compared with respect to their ability to predict the resonance frequencies of a loaded microwave ring resonator. The prediction of both fundamental and higher-order resonances are investigated and results are verified against predictions obtained from commercial software and measurement. In addition, a new algorithm for the extraction of the resonant frequencies from the rational approximation of the scattering parameter magnitude plot is proposed. The second study investigates the correctness of the interpolation function, by focusing on asymmetries in the discretisation causing unwanted mode splitting.

4.2.1 Study 1—Investigation of the Accuracy of Different Model Predictions

When a loaded microstrip ring resonator is loosely coupled to its feed lines, the coupling gap capacitances do not greatly affect the intrinsic resonant frequencies of the ring. Using this model

For high-Q resonators, this is however very difficult, as the calculation depend very strongly on both the exact position and the exact magnitude of a very sharp peak in either $|S_{21}|$ or $|S_{11}|$,. To find this position and magnitude accurately, the frequency sweep should include this exact point, within parts of one percent - however, this point is not known beforehand. Most commercial solvers therefore struggle to do this. This problem is even worse in measurements, as a measurement is always limited to fixed frequency points set up at the start of the measurement, during calibration, and to position a point at the exact resonance frequency is impossible.

In [37], the basic principle applied was to first approximate an $|S_{21}|$ or $|S_{11}|$ curve, using adaptive sampling and a meta-model, and then find the resonance point from the curve. In this way, the CEM analysis (or measurement sweep) need not include the exact point. The Q-value is then determined from the skirts of the curves in the vicinity of this point, and not from the exact value at the resonance point.

The first attempts at this exploited some of the characteristics of the Method-of-Moments (MoM) to fit models to computed data points for ring resonators specifically, across a frequency range which includes a number of resonance points [38],[39]. The advantage of this approach is clear in Fig. 2.30, where a interpolation-based curve is compared to one using equally spaced frequency points. It is evident that, in the case of discrete points, the accuracy of the resonant point will be completely determined by the frequency spacing, which quickly become prohibitive if accuracies better than 0.1% are required. In addition, some resonant points are inevitably completely invisible. The interpolated curve, on the other hand, naturally predicts this extremely accurately, using a small number of points.

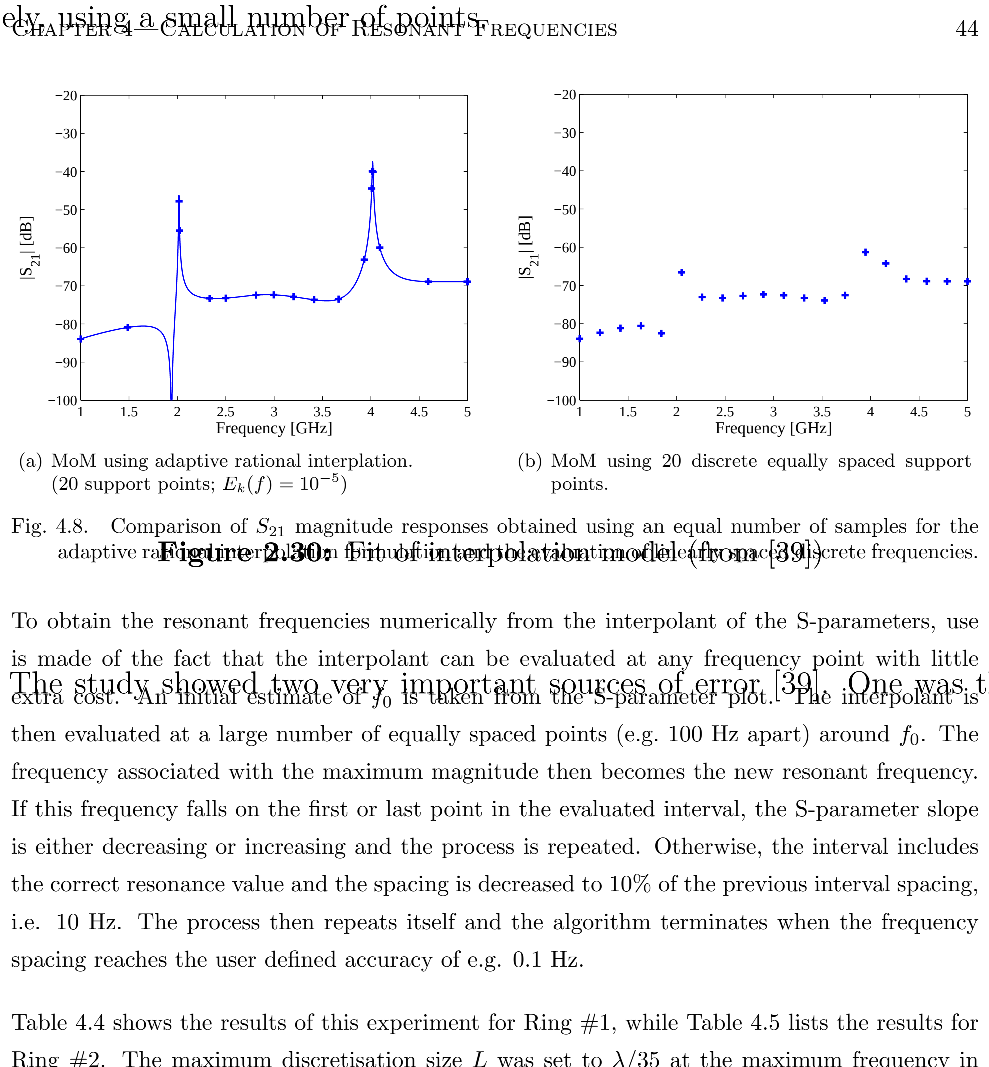
CHAPTER 4 — CALCULATION OF RESONANT FREQUENCIES 44

(a) MoM using adaptive rational interplation. (20 support points; $E_k(f) = 10^{-5}$)

(b) MoM using 20 discrete equally spaced support points.

Fig. 4.8. Comparison of S_{21} magnitude responses obtained using an equal number of samples for the adaptive rational interpolation formulation and the evaluation of linearly spaced discrete frequencies.

To obtain the resonant frequencies numerically from the interpolant of the S-parameters, use is made of the fact that the interpolant can be evaluated at any frequency point with little extra cost. An initial estimate of f_0 is taken from the S-parameter plot. The interpolant is then evaluated at a large number of equally spaced points (e.g. 100 Hz apart) around f_0. The frequency associated with the maximum magnitude then becomes the new resonant frequency. If this frequency falls on the first or last point in the evaluated interval, the S-parameter slope is either decreasing or increasing and the process is repeated. Otherwise, the interval includes the correct resonance value and the spacing is decreased to 10% of the previous interval spacing, i.e. 10 Hz. The process then repeats itself and the algorithm terminates when the frequency spacing reaches the user defined accuracy of e.g. 0.1 Hz.

Table 4.4 shows the results of this experiment for Ring #1, while Table 4.5 lists the results for Ring #2. The maximum discretisation size L was set to $\lambda/35$ at the maximum frequency in

Figure 2.30: Fit of interpolation model (from [39])

The study showed two very important sources of error [39]. One was the phenomenon of *mode splitting*, where one resonance is split into two apparent resonances due to the convergence error limit being set at too small a value, as shown in Fig. 2.31. The other is *masked modes*, where the close proximity of two adjacent modes causes one to become 'hidden' by the other, as shown in Fig. 2.32.

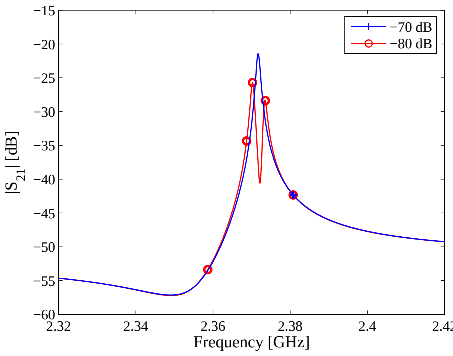

Figure 2.31: Split modes (from [39])

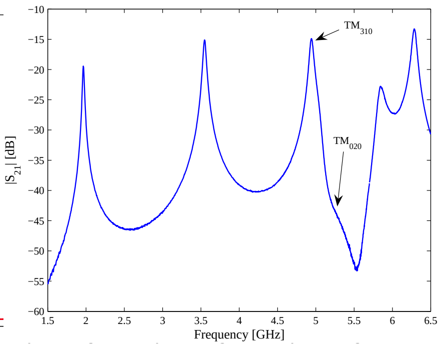

Figure 2.32: Masked modes (from [39])

For multiple modes on one structure, the identification of modes become important in addition to their resonance frequencies. To automatically recognise modes from field patterns requires a correlation between an 'ideal' field and the calculated field, at the exact resonant frequency. In the case of open ring resonators, the 'ideal' fields are calculated using magnetic wall boundaries on the outer circumference of the ring. Two sets of results are shown in Figs. 2.33 and 2.34, one set for a thin ring, and one for a thick ring. The result in Fig. 2.34 was particularly satisfactory, as both the CEM analysis and the meta-model have to be almost excact to achieve reliable recognition of higher order modes on thick rings.

Figs. 2.35 and 2.36 show the resonance frequencies for thin and thick rings as functions of ring diameter. Again, the algorithm could create these complete graphs in a fully automated way.

The next step was to calculate the Q-factors, using the interpolated curves. By a first order partial fraction expansion, it is simple to show that the form of any of the scattering parameters in the vicinity of a resonant peak, can be approximated as

$$S_{ij} = \frac{a_i t + a_2}{a_3 t + 1} \qquad t = \frac{2(f - f_L)}{f_L} \tag{2.9}$$

where f_L is the support point closest to the resonance point. In what is known as the *TQMF* method, the constants a_1 to a_3 are found using a least-squares fit of the analysis data in the vicinity of the resonant point to (2.9), from which the Q can be simply found as the imaginary part of a_3.

and the problem was discretised into 87 asymmetrically spaced triangles.

Fig. 4.10(a) shows the S-parameter response around the TM_{110} resonant frequency for a −70 dB and a −80 dB error in the interpolant. For the −80 dB error case, an unexpected mode splitting is observed, in this case traceable to a slightly assymetric MoM solution. However, this phenomenon is absent from the −70 dB error case, where the accuracy of the fit is only slightly worse. Using a finer symmetric discretisation of 200 triangles, mode splitting was eliminated and only a single mode was successfully excited.

The surface current magnitudes at first resonance were analysed and plotted along symmetrical lines around the ring. The currents, as shown in Fig. 4.10(b), are anti-metrical around the ring. Upon mirroring one set of data around the zero position, it was found that the currents indeed

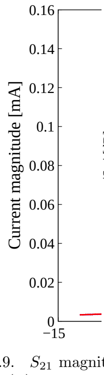

(a) Unwanted mode splitting visible at the first resonant mode, TM_{110}.

(b) Surface current magnitude along symmetrical lines around the ring.

Fig. 4.10. Mode splitting caused by slightly assymetric MoM solution.

CHAPTER 4 CALCULATION OF RESONANT FREQUENCIES 46

Fig. 4.9. S_{21} magnitude response of Ring #2 demonstrating the improbability of correctly identifying the TM_{020} mode frequency.

extracted from the S-parameter response as the TM_{310} and the TM_{020} modes were too closely spaced in frequency. This is shown in Fig. 4.9 where the TM_{020} mode disappears below the skirts of the more strongly coupled TM_{310} mode.

iv) Compared to the resonant frequencies read off the S_{21} magnitude responses measured and computed with FEKO Suite 4.2, the frequencies for Ring #1 were found to agree within 0.6% and 0.3% respectively. Also, compared to the natural frequencies found in Section 4.1.4 Table 4.2, results were within 0.4% of the MoM and 1.0% of the CST predictions.

v) For Ring #2, the comparisons yielded accuracies of better than 3.6% and 3.0% compared to the measured and FEKO simulated results. Larger discrepancies in the measured results may be a result of the finite size ground planes used in the practical structure. Compared to the natural frequencies found in Section 4.1.4 Table 4.3, results were within 0.7% of the MoM and 3.3% of the CST predictions.

Conclusion

Mode identification from an S-parameter response requires the finding of resonance peaks or maxima. Similar to the extraction techniques based on the solution of an eigenmode problem, resonance frequencies can be predicted accurately. However, finding multiple maxima using an automated algorithm poses a far more daunting task than to identify multiple zeros, as numerical noise effects can easily be misinterpreted as resonance frequencies. In addition, the technique can only identify those resonant frequencies of modes that are excited and do not disappear below the skirts of nearby modes that are more strongly coupled.

(Ring parameters: $R = 16.9$ mm, $w/R = 0.05$)

Resonant Mode	f_0 [GHz]	% Cross-Correlation	Band of Variance	2nd Highest % Cross-Correlation	Band of Variance
TM_{110}	2.0537	92.50	0.0235	83.83	0.0020
TM_{210}	4.0986	98.61	0.0237	83.94	0.0015
TM_{310}	6.1453	96.91	0.0224	81.28	0.0007
TM_{410}	8.1851	99.08	0.0229	84.08	0.0011
TM_{510}	10.2157	99.01	0.0219	81.06	0.0013

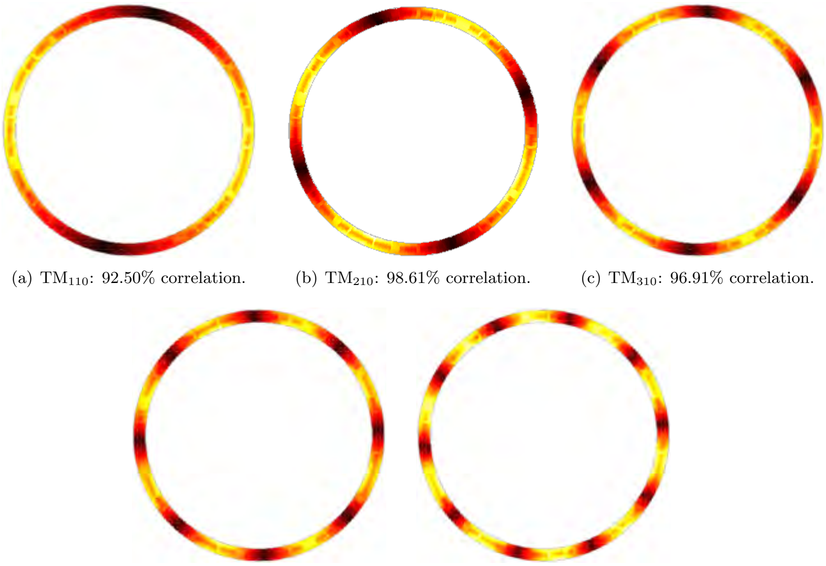

(a) TM_{110}: 92.50% correlation. (b) TM_{210}: 98.61% correlation. (c) TM_{310}: 96.91% correlation.

(d) TM_{410}: 99.08% correlation. (e) TM_{510}: 99.01% correlation.

Fig. 6.9. Resonant modes identified using cross-correlation and variance parameters. (Ring parameters: $R = 16.9$ mm, $w/R = 0.05$)

Figure 2.33: Identification of modes for thin ring (from [38])

percentage quite low (78.15%), but it is also worse than some of the other mode correlations achieved. Since none of these correlations are very good either (maximum of 89.30%), it was suggested to use the band of variance instead, which indeed identified the correct resonant mode. Figs. 6.9 and 6.10 verify the identified modes by plotting the current magnitude patterns at each of the resonant frequencies.

It was mentioned previously that the proposed technique is limited to the availability of an analytical field analysis model from which the ideal mode patterns can be computed. An example is the square or meander ring resonator. In fact, so far only the annular ring resonator has the field theory derivation for its frequency modes [74]. For square ring resonators, it is difficult

Referring to the formulation in the previous section [30], the full one-dimensional approximation function can be simplified in the vicinity of a resonant point [38],[39], to

$$R(f) = S_0 + \cfrac{f - f_0}{\varphi_1(f_1, f_0) + \cfrac{f - f_1}{\theta_N(f_L)}} \tag{2.10}$$

where f_L is the support point closest to the resonance point, S_0 ans S_1 the two other closest points, and $\theta(f_L)$ is the approximation function evaluated at f_L. It is clear that this form is the same as that of (2.9), and that the Q can therefore be obtained by simply equating the coefficients. No least-squares fit is however required, and the same interpolation function can be used for each resonant point. An example of this is shown in Fig. 2.37.

The results of an example ring resonator is shown in Fig. 2.38, where the interpolation-based method is compared to the TQMF method. Of note is the small number of support points required for good accuracy.

At this stage, another interpolation method known as *Vector-Fitting* became popular for microwave meta-models. In [40] and [41], this method was shown to compare very favourably to the rational function approach, especially for one variable, and for the modelling of resonance frequencies and Q-values. Extended procedures to accommodate noisy data, such as obtained from measurement, were also developed [42] and [43]. The use of Vector-Fitting was also shown to be applicable to the extraction of Spice models [44].

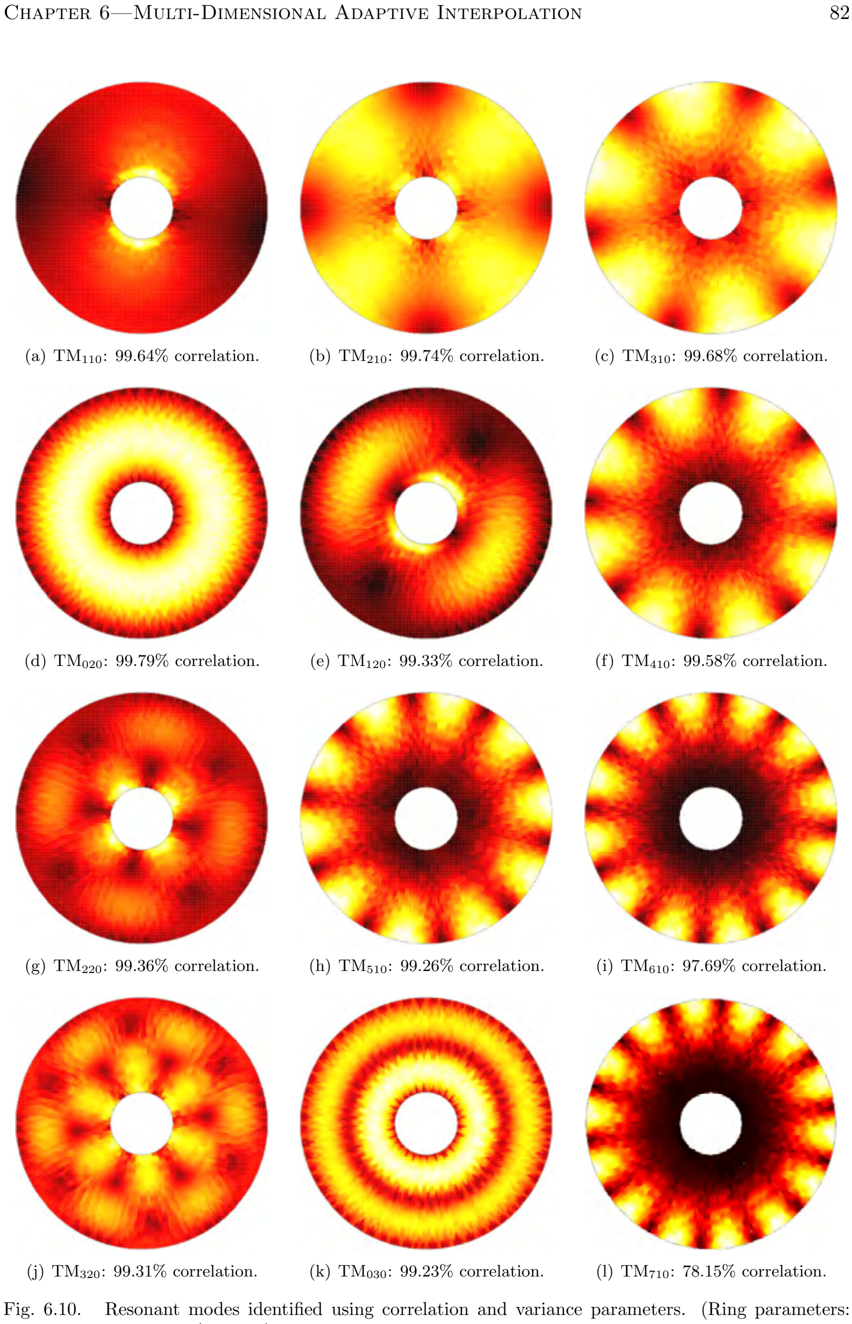

Figure 2.34: Identification of modes for thick ring (from [38])

As a final step, multi-variate models for resonance frequencies and Q-values were developed using the expanded multi-variate rational interpolation technique [37]. As before, this work is mathematically dense, and beyond the scope of this dissertation. The reader is referred to [37].

This follow-up work on meta-modelling was very valuable in terms of cementing the basic algorithms. To some extent, the capabilities of commercial EM-solvers have made parts of the work obsolete, but it is still used in-house the adaptive frequency sampling algorithm fails to identify some of the higher-order resonance frequencies. This was found to happen only when the resonance frequencies of two different modes are numerically close. However, this poses no significant problem, as the model for that mode is simply built using less data. A disadvantage, however, might be that the constrained region of interpolation ends up being more constrained than is actually the case (see TM_{020} and TM_{120}). Also, the algorithm might require selection of a few more geometrical samples with

recurrence formula

$$N_k(f_L) = \varphi_k(f_k, f_{k-1}, \cdots, f_0)N_{k-1}(f_L) + (f_L - f_{k-1})N_{k-2}(f_L) \qquad k = 4, 5, \cdots, N_s$$

$$D_k(f_L) = \varphi_k(f_k, f_{k-1}, \cdots, f_0)D_{k-1}(f_L) + (f_L - f_{k-1})D_{k-2}(f_L) \qquad k = 4, 5, \cdots, N_s \quad (5.18)$$

$$\Theta_k(f_L) = \frac{N_k(f_L)}{D_k(f_L)} \qquad k = 2, 3, \cdots, N_s$$

but with different starting conditions $N_2(f_L) = \varphi_2(f_2, f_1, f_0)$, $N_3(f_L) = \varphi_3(f_3, f_2, f_1, f_0)N_2 + (f_L - f_2)$, $D_2(f_L) = 1$ and $D_3(f_L) = \varphi_3(f_3, f_2, f_1, f_0)$.

Note that the interpolant passes through the point of resonance (f_L, H_L) and also the support points H_0 and H_1. For a best fit these are selected as the two support points closest to f_L. After transforming Eq. 5.17 to the form of Eq. 5.11†, the loaded quality factor is given by

$$Q_L = \mathrm{Im}\{a_3\} = \mathrm{Im}\left\{\frac{f_L}{2(\varphi_1(f_1, f_0)\Theta_N(f_L) - f_1 + f_L)}\right\}. \quad (5.19)$$

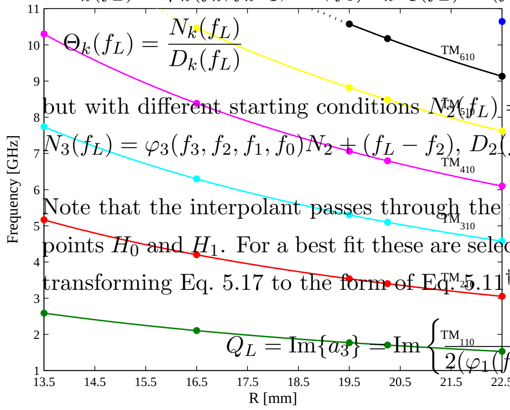

Fig. 6.14. Two-dimensional model of the resonance frequencies with R variable. (Ring parameters: R = [13.5 mm, 22.5 mm], w/R = 0.05; f = [1 GHz, 11 GHz])

Figure 2.35: Resonance frequencies of modes for thin ring (from [38])

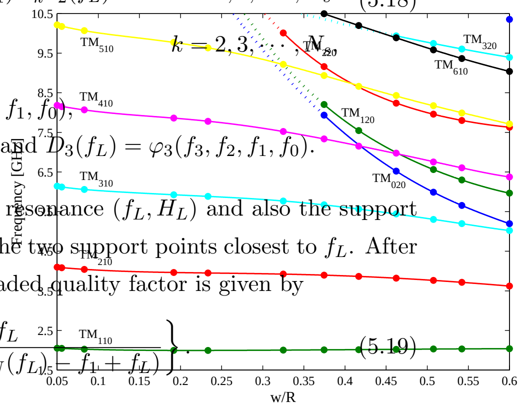

Fig. 6.15. Two-dimensional model of ring resonator with frequency and normalised ring width variable. (Ring parameters: R = 16.9 mm, w/R = [0.05, 0.6]; f = [1.5 GHz, 10.5 GHz])

Figure 2.36: Resonance frequencies of modes for thick ring (from [38])

Fig. 5.5 plots the improved three-point rational interpolation fit for the two test resonance frequencies discussed in Figs. 5.3 and 5.4. The method yielded Q-values of 1662.7 at $f_L = 2.0306$ GHz and 949.2 at $f_L = 4.0461$ GHz. These results are within 1.6% of the values predicted with the TMQF least-squares fit.

Fig. 6.14 plots the first six TM_{n10} mode frequencies that were successfully identified and approximated. Convergence of these models was reached within only 5 geometrical samples ($N_x = 5$), while the total number of CEM analyses added up to ... Upon further analysis it ... at $R = 22.5$ mm. Since ... not added to the output ... of the constrained inter... the extrapolated values ... example. However, in other situations these values cannot be trusted. Section 6.8 elaborates on this topic of accuracy in the interpolation and extrapolation models.

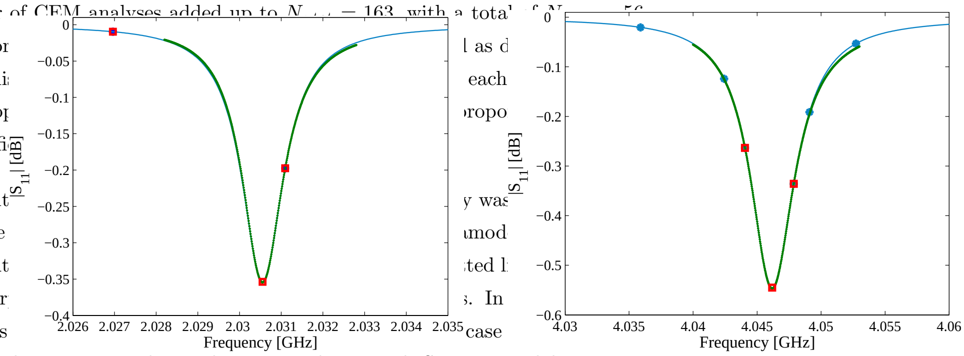

(a) $f_L = 2.0306$ GHz. (b) $f_L = 4.0461$ GHz.

Fig. 5.5. Improved three-point rational interpolation fit on S_{11} data.

Figure 2.37: Calculation of Q (from [38])

TABLE 6.6

NUMBER OF SAMPLES REQUIRED TO REACH CONVERGENCE IN EACH OF THE ADAPTIVE FREQUENCY SAMPLING LOOPS. (RING PARAMETERS: R = [13.5 mm, 22.5 mm], w/R = 0.05; f = [1 GHz, 11 GHz])

5.2.1 Study 1—Verification of the Three-Point Method

In this study, the three-point rational interpolation method is verified theoretically for both high-Q and low-Q values. The basic ring structure selected for this test study is that of Ring #1 (R = 16.9 mm, w/R = 0.1) described in Section 4.2.1, and supports only the TM_{n10} modes that are widely spaced in frequency. The three-point method computes the loaded quality factor of a resonator. To establish high values of Q_L, losses were suppressed by setting $\tan(\delta) = 0$, surface

† The result is obtained by a simple interchange from $\varphi_2(f_2, f_1, f_0)$ to $\Theta_N(f_L)$ in Eq. 5.15.

552 Schoeman and Meyer

TABLE III. Comparison of Q-Factors Calculated with the Transmission Mode Q-Factor (TMQF) Technique and the Three-Point Rational Interpolation Method. Substrate Parameters: h = 0.635 mm, ε_r = 10.2, $\tan(\delta)$ = 0; Ring Parameters: R = 7.475 mm, w/R = 0.1, g = 0.1 mm, W = 0.8 mm (Problem Discretised into 200 Symmetrically Spaced Triangles)

Interpolation Error [dB]	Support Points	TM_{110}: f = 2.3465 GHz, TMQF S_{21}	TMQF S_{11}	Three-Point Method S_{11}	TM_{210}: f = 4.6497 GHz, TMQF S_{21}	TMQF S_{11}	Three-Point Method S_{11}
−60	13	1172.0	1170.5	1249.1	1112.7	1121.9	1223.0
−80	17	1172.1	1170.6	1249.1	1129.1	1139.7	1146.1
−100	42	1173.5	1172.0	1174.7	1129.1	1139.6	1139.7

VI. CONCLUSION

In this article a rational interpolation model (Thiele-type continued fractions) was exploited to accurately predict the characteristics f_0 and Q of a microstrip ring resonator. Calculation of resonant frequencies was performed using two techniques: one predicting the natural frequencies of an unloaded resonator (eigenmode problem) and the other using the S-parameter response of a loosely coupled loaded resonator. For the calculation of Q-values, a new three-point rational interpolant function in the region of resonance was proposed. This technique utilises already known interpolant coefficients and provides a direct fit and solution to the Q-factors.

REFERENCES

1. T. Dhaene, J. Ureel, N. Faché, and D. de Zutter, Adaptive Frequency Sampling Algorithm for Fast and Accurate S-parameter Modeling of General Planar Structures, IEEE MTT-S Dig 3 (1995), 1427–1430.
2. R. Lehmensiek and P. Meyer, An efficient adaptive
5. R. Lehmensiek, Efficient adaptive sampling applied to multivariate, multiple output rational interpolation models, with applications in electromagnetics-based device modelling, Ph.D. dissertation, University of Stellenbosch, 2001.
6. I. Wolff and N. Knoppik, Microstrip ring resonator and dispersion measurement on microstrip lines, Electron Lett 7 (1971), 779–781.
7. S.G. Wu and F.J. Rosenbaum, Mode chart for microstrip ring resonators, IEEE Trans Microwave Theory Tech MTT-21 (1973), 487–489.
8. R.P. Owens, Curvature effect in microstrip ring resonators, Electron Lett 12 (1976), 356–357.
9. W. Sun, K.-M Chen, D.P. Nyquist, and E.J. Rothwell, Determination of the Natural Modes for a Rectangular Plate, IEEE Trans Antennas Propagat 38 (1990), 643–652.
10. Y. Long, Determination of the Natural Frequencies for Conducting Rectangular Boxes, IEEE Trans Antennas Propagat 42 (1994), 1016–1021.
11. C.A. Olley and T.E. Rozzi, Systematic characterisation of the spectrum of unilateral finline, IEEE Trans Microwave Theory Tech 34 (1986), 1147–1156.
12. V.A. Labay and J. Bornemann, Matrix singular value decomposition for pole-free solutions of homogenous matrix equations as applied to numerical modelling

Figure 2.38: Resonant frequency and Q results (from [39])

to characterise and optimise resonators, as it improves the accuracy of normal methods significantly. It also served to establish a two-decade relationship between my group and that of Profs Dhaene and Cuyt.

2.7 Conclusion

My work on modelling has constituted a significant part of my career, and has led to strong research cooperation with international groups. The principles involved in computational electromagnetic modelling, circuit model parameter extraction and meta-models also occur in a wide range of related fields, especially that of the design of passive circuits. All the methods discussed in this chapter represented state-of-the-art solutions at the time they were published, and together they served to establish my group internationally in the area of modelling.

The work has continued through the activities of my graduated students, both in academia and industry. In particular, Dr Lehmensiek (in his role at the company EMSS Antennas) and Prof de Villiers have applied these techniques to the design of the reflector array dishes of the Square-Kilometre-Array antenna in South Africa, the biggest electronic engineering and science project in the history of South Africa. Currently, Prof de Villiers has a large research programme in this field, with myself restarting efforts in this field - now in the area of statistical modelling as applied to manufacturing yield of microwave devices.

Chapter 3

Microwave Filters

3.1 Introduction

The design of microwave filters has been the most constant activity throughout my research and professional consulting career. From my very first reseach project, up to the writing of this dissertation, filters of varying form, frequency and type have permeated my work.

3.2 Bandpass filters utilising higher-order modes

The Mode-Matching codes developed in the first years of my research career naturally led me to filter structures which in some way utilised, or suffered from, higher order mode effects. While multiple modes exist on all guiding structures, dimensions for structures are normally chosen in such a way that all except one of these modes are below cut-off, as most design algorithms are based on single-mode transmission line models. A number of applications where multiple propagating modes were not only allowed, but used to good effect, have however been proposed through the years. Examples of this include the use of dual- and triple-mode cavities to reduce the size of waveguide filters, the improvement of aperture distributions in antenna feeds for reflector type antennas, and the shaping of power distributions in waveguides for spatial amplifier applications. Multiple propagating modes have also been utilised effectively to implement complicated designs elegantly, such as cross-coupled filters.

The design of devices utilising multiple propagating modes are complicated by a few problems. In general, a typical discontinuity separating two waveguides A and B is represented by an n x m scattering matrix, for which the equivalent circuit in Fig. 3.1 was proposed in [45]. Here, $W(n,m)$ represents a transformer ratio directly linked to the mode-matching method, and $Z_A(n)$

and $Z_B(m)$ the impedance of modes n and m in waveguides A and B respectively. In the case of single-mode propagation, only two of the terminating impedances are replaced by ports, resulting in a standard two-port network. All the other impedances are imaginary, and can be lumped together in one frequency dependant reactive element. For design purposes however, models that contain elements with non-linear frequency dependencies are virtually useless. In practice, the model in Fig. 3.1 is approximated for a specific structure and frequency range, by a few ideal elements like inductors, capacitors and sections of transmission line. This approach is inherently narrowband and approximate, although excellent models do exist.

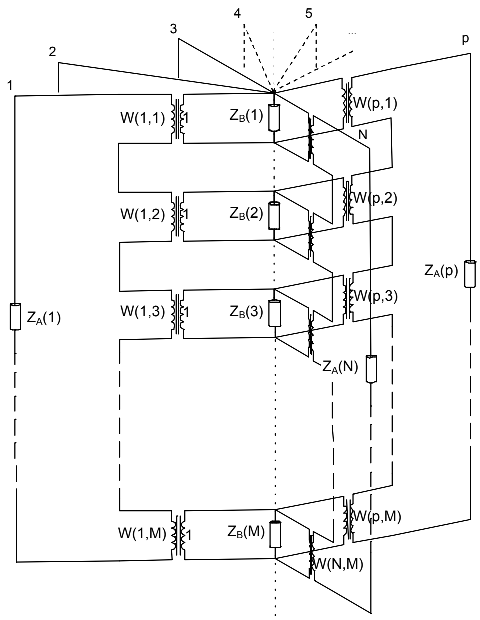

Figure 1: Circuit model of a general waveguide discontinuity

Figure 3.1: Circuit model for a mult-mode discontinuity (from [45])

In the case of multiple propagating modes, the equivalent circuit is a multi-port system with each mode represented by one port, and all the ports linked together through a complicated circuit. With the exception of the even- and odd-mode analysis which can be used for the two-mode case, no formal synthesis techniques exist for cascaded N-ports. Also, general optimisation techniques have great difficulty with these structures, as one dimensional change normally affects a number of output parameters, some positively and others negatively.

My first project focusing on devices which utilise higher order modes, was on improving the design of classical multi-mode coupled waveguide cavity filters, which had been used especially in space applications since the 1970's, but which were at the time still mostly designed using equivalent models from as far back as the 1940's, or experimentation.

the design of waveguide devices using multiple propagating modes

Petrie Meyer[1], Christopher A Vale[1], Werner Steyn[1]

paper presents a number of strategies which can designing waveguide devices with multiple des. Three types of devices are discussed by way mely bandstop filters for microwave heating arrow band coupled resonator filters, and nopulse feeds.

eguide, modes, bandstop filter, monopulse feed

I. INTRODUCTION

des exist on all guiding structures, but normally chosen in such a way that all except modes are below cut-off, as most design based on single-mode transmission line per of applications where multiple propagating t only allowed, but used to good effect, have proposed through the years. Examples of this of dual and triple mode cavities to reduce the de filters [1,2,3], the improvement of aperture antenna feeds for reflector type antennas [4,5], ntly, the shaping of power distributions in spatial amplifier applications [6,7]. Multiple odes have also been utilized effectively to mplicated designs elegantly, such as cross-Finally, the dimensions of a given problem are er the control of the designer, forcing him to modes.

f devices utilizing multiple propagating modes d by a few problems. In general, a typical separating two waveguides A and B is an nxm port scattering matrix, which can be s the equivalent circuit shown in Fig. 1 [8]. represents a transformer ratio directly linked to ching method, and $Z_A(n)$ and $Z_B(m)$ the modes *n* and *m* in waveguides *A* and *B* the case of single-mode propagation, only two ng impedances are replaced by ports, resulting vo-port network. All the other impedances are can be lumped together in one frequency tive element. For design purposes however, ontain elements with non-linear frequency re virtually useless. In practice, the model in ximated for a specific structure and frequency ideal elements like inductors, capacitors and nsmission line. This approach is inherently narrowband and approximate, although excellent models do exist.

In the case of multiple propagating modes, the equivalent circuit is a multiport system with each mode represented by one port, and all the ports linked together through a complicated circuit. With the exception of the even and odd mode analysis which can be used for the two-mode case, no formal synthesis techniques exist for cascaded n-ports. Also, general optimization techniques have great difficulty with these structures, as one dimensional change normally affects a number of output parameters, some positively and others negatively.

This paper will present a number of techniques that have been developed by the authors over the past few years to approach the design problem of devices with multiple propagating modes. The techniques are mostly a combination of synthesis and intelligent optimisation, and rely on the careful choice of structures (called functional blocks) which all contain a limited modal set, and can be cascaded to produce a required characteristic. These choices require good knowledge of the field patterns in different structures, and are very important, as they normally fall under the control of the designer, and as the wrong choices result in building blocks which are just too complicated to use.

with the Department of Electrical and Electronic versity of Stellenbosch, Private Bag X1, Matieland, ca, Email: pmeyer@sun.ac.za

The history of coupled waveguide cavity filters dates from 1948, when the description and implementation of a direct-coupled cavity filter by Fano and Lawson, consisting of a number of waveguide cavities separated by thin inductive irises, was proposed. The irises were designed using the small aperture theory derived by Bethe in 1944 and the measured polarisability data presented by Cohn in 1952. The possibilities of reducing filter size by allowing more than one mode to be resonant in the same cavity, were soon realised, and in 1951 Lin demonstrated a fifth order filter realised in a single cylindrical cavity. At this time prototypes were deemed to be impractical, since the authors could not achieve independent control of the wanted degenerate modes, as well as suppression of unwanted modes.

This was the state of coupled cavity filter design until the launch of the first commercial satellite communications systems in the late 1960s. New technology calling for reduction in filter size and weight was required, sparking new interest in the use of multi-mode coupled cavity filters. The first dual-mode cavity filter was developed by Atia and Williams at Comsat Laboratories in 1970 and showed that multi-mode cavity filters were indeed commercially viable, and could reduce the number of physical cavities (and thereby the size and weight) of standard coupled cavity filters by a factor of two. Another significant advantage of multi-mode cavities is that the structure allows coupling to non-adjacent resonators. This can be achieved by using cross-shaped irises or coupling screws. This cross-coupling between resonators results in transfer function zeros along the real or imaginary axis, thereby permitting the realisation of elliptical and linear phase filter functions. It was therefore possible to improve filter performance without increasing the physical dimensions, at the cost of increased design complexity. After dual-mode filters, the obvious step towards the design of triple-mode filters and even quad-mode filters was taken. For such filters, three or four inter-cavity coupling coefficients must be controlled uniquely and simultaneously by an iris containing more than one aperture.

At the time, numerical electromagnetic techniques had been introduced, but were still only viable for very simple structures. In 1999, myself and a PhD student Dr Werner Steyn, proposed a combination of the numerical Mode-Matching technique for cylindrical waveguides, adpatively sampled rational interpolation models, and the so-called *Space-Mapping* optimisation technique for the design of multi-mode waveguide filters [45],[46],[47].

The Mode-Matching analysis of cylindrical waveguides with off-centre irises coupling two cavities is very intensive, firstly due to the evaluation of Bessel functions for the calculation of the two-dimensional field distributions in each guide, and secondly as off-centre positioning requires the use of a high number of modes. It was therefore of high importance to reduce the number of EM-analysis steps as much as possible.

To solve the coupling factors for a coupled cavity system, the basic structure in Fig. 3.2 is modelled as shown in Fig. 3.3 for the case of a single mode in each cavity. Following equations developed by Conn, the coupling coefficient can be extracted from the two eigen-frequencies of the circuit when both ports are shorted. In terms of scattering parameters, this is illustrated in Fig. 3.4. For the multi-mode case, each mode is represented by a separate port, as shown in Fig. 3.5, and the eigen-frequencies must be solved from a characteristic equation of the full S-matrix. As numerical root-finding is also a numerical intensive process, the combination of this with the Mode Matching procedure proved to be almost intractable.

Figure 3.2: Basic waveguide discontinuity structure(from [45])

Figure 3.3: Basic waveguide discontinuity circuit (from [45])

Figure 3.4: Basic waveguide discontinuity structure(from [45])

Figure 3.5: Basic waveguide discontinuity circuit (from [45])

The first step in solving this problem was to reduce the S-matrix by an algorithm which identified uncoupled modes from the characteristic ideal two-dimensional field distributions. Instead of shorting all equivalent ports of the network, non-coupled ports were left unterminated, which reduced the number of zeros in the characteristic equation substantially. This reduced problem is however still very ill-behaved. Fig. 3.6 shows a typical cylindrical iris with two offset irises, and the characteristic equation of the reduced structure in Fig. 3.7. The root-finding problem is quite clear.

The second step was therefore to approximate the characteristic function using the adaptively sampled rational interpolation function theory developed by Dr Lehmensiek. This had the advantage of requiring only a few samples to determine a very accurate approximation function, and the even greater

This is the standard method for the calculation of coupling coefficients from the natural resonant frequencies of the structure. Very little information is available in literature on how resonant frequencies are linked to propagating modes. Accatino [76] uses symmetry properties of the iris structures to isolate coupling and natural resonant frequencies of specific propagating modes. This requires different mode sets for each propagating mode, which is impractical for general CAD procedures.

In the new CAD procedure, the natural resonant frequencies are determined by analysing the complete structure of figure 6.3. This is not usually done, because the complexity of the analysis is increased, but using the complete structure allows for the calculation of both natural resonant frequencies of a propagating mode in one analysis. Equation (6.5) then becomes:

$$\Re(f)=\det\left[\mathbf{S}^{c}+\mathbf{I}\right]=0 \qquad (6.6)$$

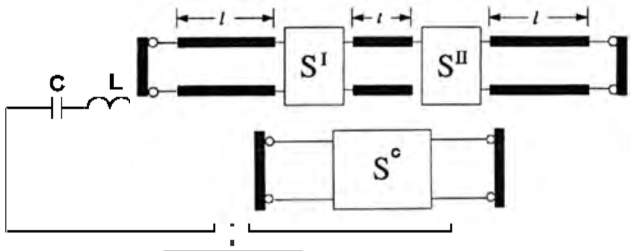

Figure 6.3: Mode-matching model of complete coupled cavity structure

basis of this technique is the measurement method whereby the coupling coefficients and resonant frequencies are determined from the phase of the reflection coefficient.

6.2 CAD PROCEDURE 1: IRIS DESIGN FOR IDENTICAL CAVITIES WITH NO CROSS-COUPLING

The derivation of the standard procedure follows from the analysis of the equivalent circuit of two identical coupled cavities as shown in figure 6.1.

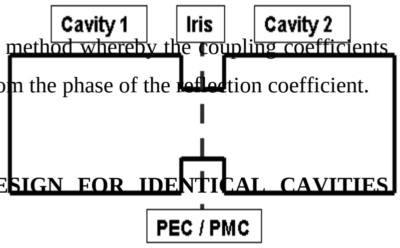

Figure 6.1: Equivalent circuit of two coupled cavities

Either a perfect electric (PEC) or magnetic conductor (PMC) in the centre of the symmetry plane of the structure, corresponds to either a short circuit or open circuit in the symmetry plane of the equivalent circuit. Solving for the resonant frequencies of the circuit with either the short or open circuit in place, results in the natural resonant frequencies of the coupled resonator structure.

$$f_e=\frac{1}{2\pi\sqrt{C(L-M)}}$$

$$f_m=\frac{1}{2\pi\sqrt{C(L+M)}} \qquad (6.1)$$

f_e corresponds to the electric wall or short circuit and f_m corresponds to the magnetic wall or open circuit. f_e is then slightly higher and f_m slightly lower than the resonant frequency of the unperturbed cavity. With the coupling coefficient defined as $K=\dfrac{M}{L}$, the equations in (6.1) can be manipulated to obtain a relation between the resonant frequencies and the coupling coefficient:

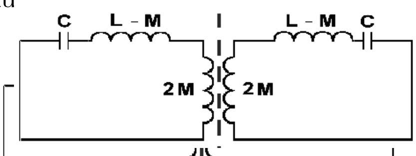

Figure 12: Equivalent Circuit for Coupled Cavities

The problem can be solved numerically by calculating the scattering matrix of the cavity-iris interface, and cascading it with the guides forming the cavities and the iris, as shown in Fig. 13. By shorting the end ports, the natural frequencies of the full system can be obtained by solving Eq. 1.

$$\Re(f)=\det\left[\mathbf{S}^{c}+\mathbf{I}\right]=0 \qquad (1)$$

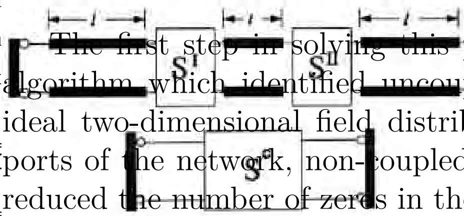

Figure 13: S-matrix Model of Coupled Cavities

For the short circuit and open circuit, two roots are obtained, and the coupling is given by Eq. 2, with f_e and f_m the two frequencies. This method is very standard and has been used for the iris design to obtain the coupling coefficient.

$$K=\frac{f_e^2-f_m^2}{f_e^2+f_m^2} \qquad (2)$$

In the case of multiple resonant modes, the numerical aspects of this procedure become difficult and time consuming. The roots of Eq. 1 becomes very close together, and the turning points of the function move to extremely close to the axis. This has the effect that many EM evaluations of the structure are necessary to find the required roots. Once this has been done, only one coupling value analysis has been completed. The next stage is to optimise the structure to give the required coupling values for all the modes, which requires a large number of coupling value analysis steps. For one complete design, the number of EM analysis points quickly become prohibitive.

To sole this problem, three techniques are combined, i.e. (a) reduction of the general scattering matrix (GSM) [11], (b) adaptive sampling interpolation [18] and (c) Agressive Space Mapping [19].

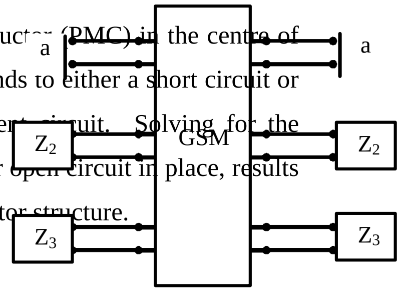

Figure 14: Reducing the Scattering Matrix

This has the result of reducing the generalised scattering matrix of the problem, and causing Eq. 1 to once again have only two roots instead of six.

(b) To limit the amount of EM evaluations needed to determine the roots, the function in Eq. 1 is first replaced by a rational interpolation model, created by an adaptive sampling algorithm. This algorithm is remarkably effective, and generates very accurate approximations to the function with typically 8-10 samples.

(c) The optimisation of the structure is performed by Agressive Space Mapping, using a coarse model derived from given by small aperture theory, and the full EM analysis the fine model.

D. Results

These three techniques combine to give excellent results, as shown in Fig. 15 for the design of a triple mode coupling iris in OKIE. The reduction in EM evaluations is marked.

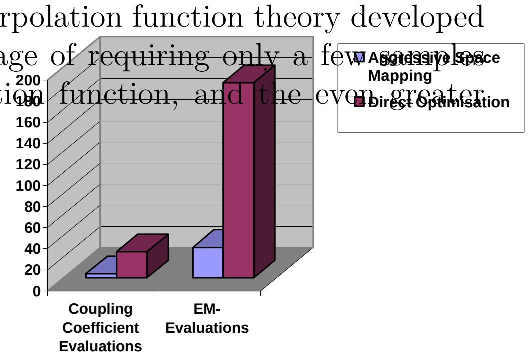

Figure 15: Reduction in EM Evaluations

With some extensions, these techniques were used to design a multimodal diplexer, consisting of three cavities which support three resonant modes each, and an input port which

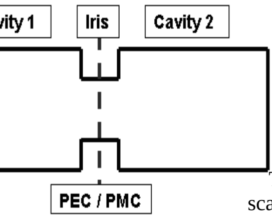

advantage that the roots of the rational function can be calculated almost directly due to the nature of the function [33].

Finally, analysis is of course only part of the design cycle. To obtain filter dimensions, an iris structure must be optimised to produce the correct coupling factors for multiple modes – a very difficult multi-parameter, multi-objective problem. This phase was implemented using the (then recently developed) Space-Mapping technique [46].

By combining all three these techniques, numerical design of irises for multi-mode couplings were made possible for the first time on a PC [47]. An example for a typical filter is shown in Fig. 3.7, where the number of analysis steps is shown for one design. The effect of the Space-Mapping was shown to be quite dramatic.

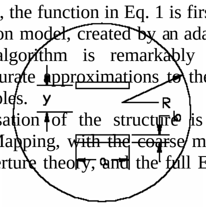

Figure 3.6: Typical cylindrical waveguide iris (from [45]).

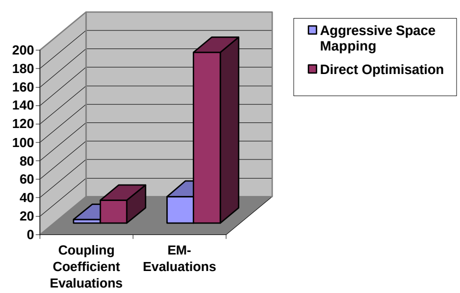

Figure 3.7: Performance of Space-Mapping optimisation (from [45]).

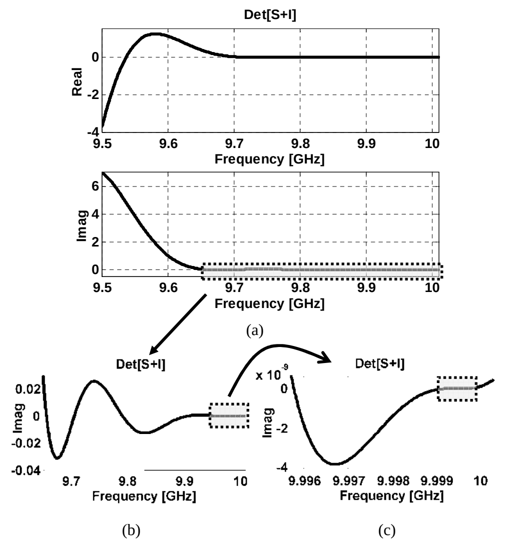

Figure 3.8: Typical characteristic polynomial (from [46]).

To illustrate the power of this integrated technique, a diplexer was designed which supported quadruple modes in the centre cavity, two at each frequency of the diplexer. The big advantage of this structure, was the orthogonal nature of the two input modes at the common port feed, which increased the isolation between channels substantially. At the time this was the first diplexer which made use of orthogonal field decoupling. The coupling diagram of the diplexer is shown in Fig. 3.9, with the actual manufactured structure shown in Fig. 3.10. The complexity of the structure is obvious.

The measured results of the diplexer is shown in Fig. 3.11. The excellent isolation in the lower passband is clearly visible, as well as the good pass-band

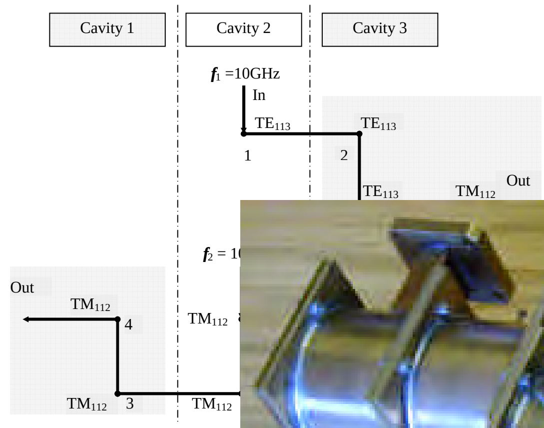

Figure 7.3: Basic coupling structure

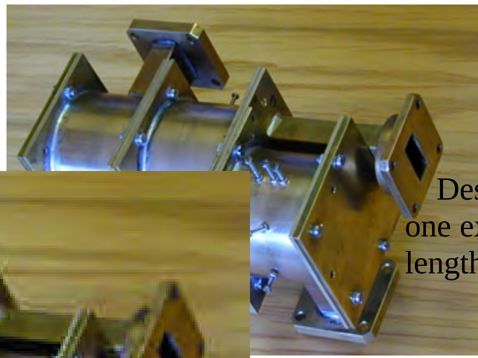

of constructed diplexer

Figure 3.9: Quad-mode diplexer modes (from [46])

The centre cavity is denoted as port one with the ports two and three respectively. The device were measured and the results ... 7.1.

relative bandwidth of 0.8% at 10GHz

reflection loss the coupling matrix re...

Designing a quarter wave ... one excitation, can therefore ... length for another mode.

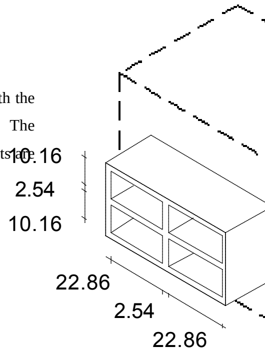

Figure 18: Mo...

return loss. This ... fabricated multi-mode waveguide structure ever published, and validated the design procedure very well.

Figure 16: Multimodal Diplexer

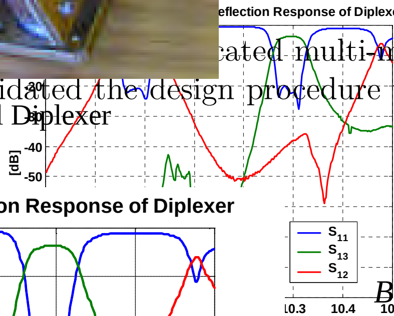

tion response of diplexer

A simulated transmission and reflection response of the diplexer is given in figure 7.4 where channel isolation of more than 70dB can be observed at the channel centre frequencies. The simulati... structure presented in figu... equivalent circuit allows f... channels. The remaining ... them.

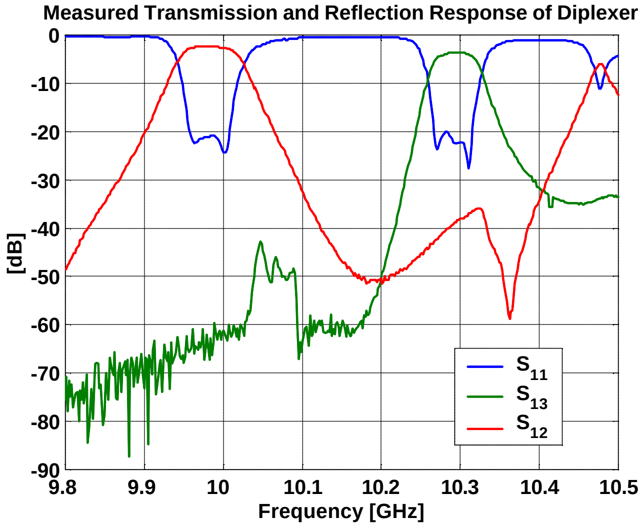

Figure 17: Measured results for Diplexer

Figure 3.11: Quad-mode diplexer results (from [46])

B. Choice of functional blo...

In this type of proble... determined by first using s... into three different problem... and odd mode symmetries ... as coupled lines. The symm... are shown in Fig. 19, wi... conductor and 'h' a perfect ...

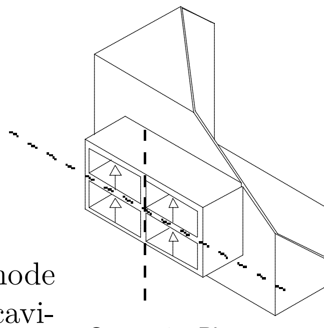

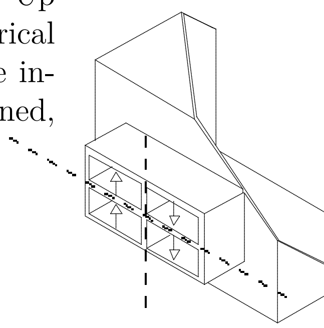

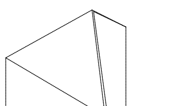

A second example of the integrated design technique, was a dual-mode cylindrical waveguide filter, using 90 degree spatially rotated rectangular cavities at both endpoints of a cylindrical resonator, as shown in Fig.3.12 [48]. Up to this point, cross-coupling between the two degenerate modes of a cylindrical waveguide was typically implemented using tuning screws at a 45 degree inclination to the electric field of both modes. This was typically not designed,

IV. Multimode Waveguide Antenna Feed for Monopulse Application

A. Introduction

In 1961, PW Hannan presented design objectives for optimum antenna feed systems for reflector type antennas in monopulse applications. The implementation of these ideas were found to be best achieved with multimode antenna feeds where, typically, a number of waveguide feeds are first combined into one overmoded waveguide, which terminates in the radiating aperture [20,5]. The basic problem is shown in Fig. 18. By exciting the four input waveguides in three different ways, three antenna patterns are obtained, called the plus, elevation and azimuth channels.

One of the problems with these types of feed, is the but simply tuned by hand after construction. In [48], thin, shallow, offset rectangular cavities called *shorted-stub couplings* are coupled to the main resonator on both endpoints, creating a controllable coupling between the two degenerate modes. The advantages of this were in the ability to accurately analyse and design these cavities, and the ability to realize a filter with no post-manufacturing tuning.

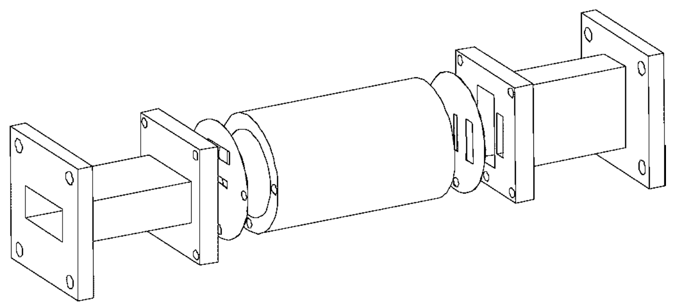

Fig. 7. Triple-mode single-cavity filter.

Figure 3.12: Shorted-stub filter (from [48])

Fig.3.13 shows the way the shorted stu modes, and Fig.3.14 shows the measured re bandwidth of the filter is very narrow (1% showed the power of the integrated design

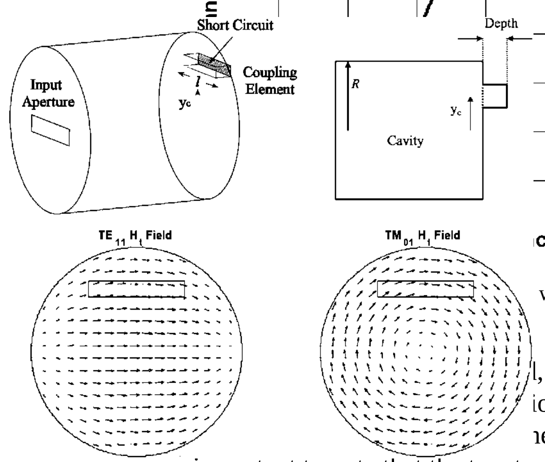

Fig. 3. Basic coupling element for triple-mode cavities.

Figure 3.13: Shorted-stub coupling (from [48])

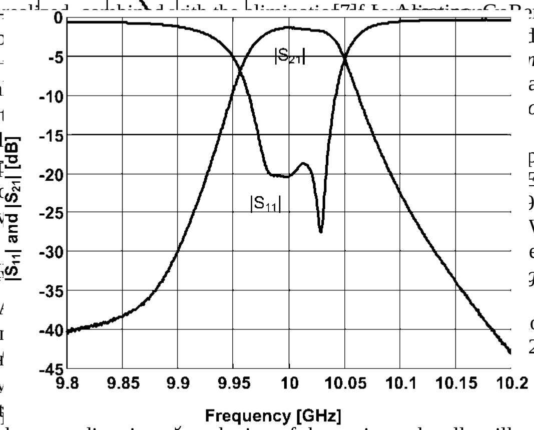

Figure 3.14: Shorted-stub filter re

This work the first time how powerful the combination of numerical techniques, model order reduction, and Space Mapping can be.

can be when applied to multi-modal waveguide filters. Most of these techniques have since been implemented into commercial software, and are used by designers without even realising. At the time, it served as the only way for us to design a umber of these filters for local industry, using fully in-house software.

3.3 Bandstop filters for microwave heating applications

In parallel with the work on bandpass filters which use higher order waveguide modes, my PhD student Dr Chris Vale and myself in 1999 embarked on a project to design bandstop waveguide filters for multiple propagating modes [49]. This worked stemmed from the research activity of colleagues Profs. Johann de Swardt and Howard Reader, on microwave dielectric heating.

The problem at the time was that many microwave heating facilities required conveyor belts passing through a microwave heating cavity, enforcing permanent large openings in the cavity sidewalls, through which dangerous levels of microwave energy can escape if not filtered. A typical system is shown in Fig. 3.15. The solution to this problem is the placement of bandstop filters (or *chokes*) on either side of the cavity to reflect and/or absorb any energy before it can do harm to people or equipment outside. These chokes must at the same time allow the free movement of product through the facility. The problem is of course that the object to be heated determines the aperture size, which is in general large enough to allow the propagation of multiple waveguide modes. A bandstop filter able to reflect a number of modes over a specified band was therefore required. This is a difficult problem for which no standard design techniques exist even at the time of writing, nearly two decades later.

Figure 3.15: Dielectric heating oven (from [45])

The proposed solution was an optimisation process using so-called *functional blocks* [50], [51]. Because the conveyor-belt channel cannot be blocked in

II. Bandstop Filters for Microwave Heating Applications [9]

A. Introduction

In many microwave heating facilities, conveyor belts passing through a microwave heating cavity enforce permanent large openings in the cavity sidewalls, through which dangerous levels of microwave energy can escape if not filtered. A typical system is shown in Fig. 2. The solution to this problem is the placement of 'chokes' on either side of the cavity to reflect and/or absorb any energy before it can do harm to people or equipment outside. These chokes must at the same time allow the free movement of product through the facility.

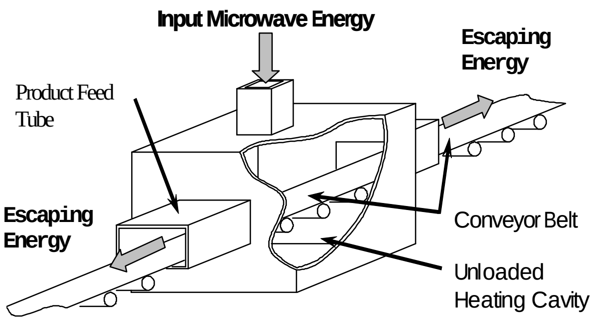

Figure 2: Microwave Heating Cavity with Conveyor Belt Feed

The preferred choke design solution is a reactive choke. This typically reflects the escaping energy back into the cavity using equivalent reactive elements, such as stub lines, in a similar fashion as would be used in a conventional bandstop filter design. Because of the complex nature of the microwave design problem, however, standard reactive choke designs typically enforce limitations on the aperture geometry, so as to apply single mode equivalent approaches. When such limited aperture geometries conflict with the physical requirements for aperture size set by the size of the product feed tube, the designer must resort to other solutions such as tunnels with absorbing walls, special arrangements of doors timed to open and close to admit product or 'maze openings' that force the product to 'meander through a folder corridor lined with absorbing walls' [10]. These approaches have many drawbacks, specifically since the use of absorbing materials requires bulky cooling and imposes power limitations, and the

which creates a null for one mode wi
other modes at the same frequency. A
null-creation with limited cross-couplin
functional blocks consisting of back-to-
separated by lengths of uniform guide, a
4. If the steps go from small to large t
size of the small waveguide is the sam
tubes discussed above, then such functi
would fulfill the requirements of a reac
terms of geometric limitations.

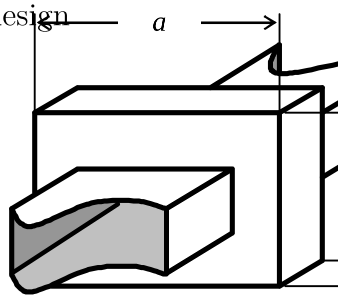

Figure 3: Functional Bl

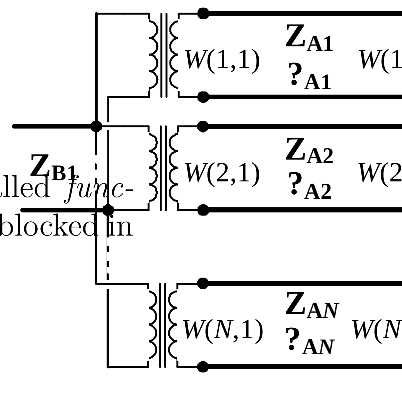

Figure 4: Functional Block Equi

The fundamental field activity in th
understood. In geometries which exhib
energy in the small guide is found to
between two modes of different propa

any way, the blocks are only allowed larger cross-sections, as shown in Fig. 3.16. The difficulty of a synthesis is clearly illustrated by the modal equivalent circuit for one such a block shown in Fig. 3.17, as a cascade of blocks is required to achieve the required levels of attenuation.

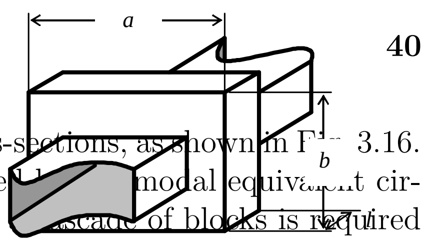

Figure 3.16: Bandstop filter functional block (from [45])

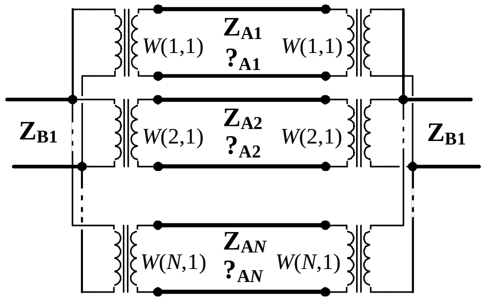

Figure 3.17: Functional block equivalent circuit (from [45])

The first step in the solution was the development of valid parameter spaces for the blocks, with one parameter space for each mode which propagates. Such a parameter space lists all the possible combinations of dimensions that would yield a block which would create a single null in the frequency band for a single mode. A typical parameter space is shown in Fig. 3.18. An the parameter spaces are then used as input to a genetic algorithm (which at that stage were just becoming popular in electromagnetic optimisation), and cascaded with variable lengths. A typical convergence graph is shown in Fig. 3.19.

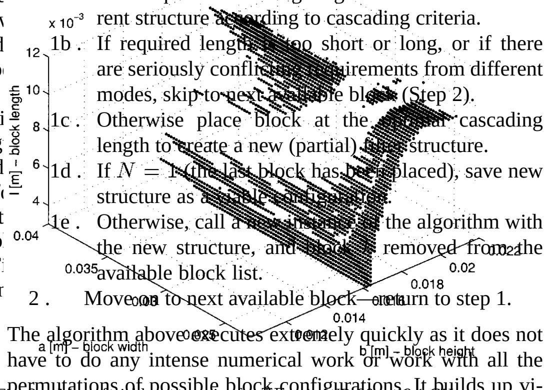

Figure 3.18: Functional block parameter space (from [45])

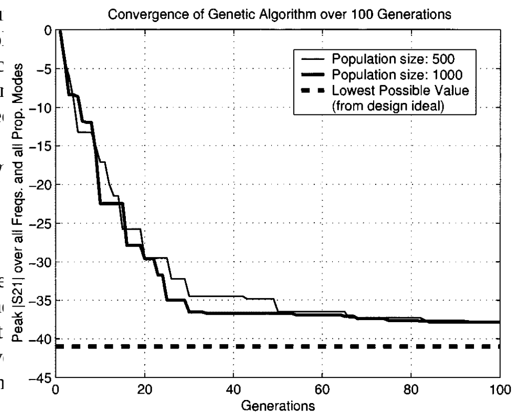

Figure 3.19: Bandstop filter convergence (from [45])

A prototype, scaled in frequency, was designed and measured. The measurement in itself is non-trivial, and required a completely new system making use of very lightly coupled probed-fed waveguides [49]. The filter is shown in Fig.3.20, with the measured results for a number of modes in Figs.3.21 to 3.23.

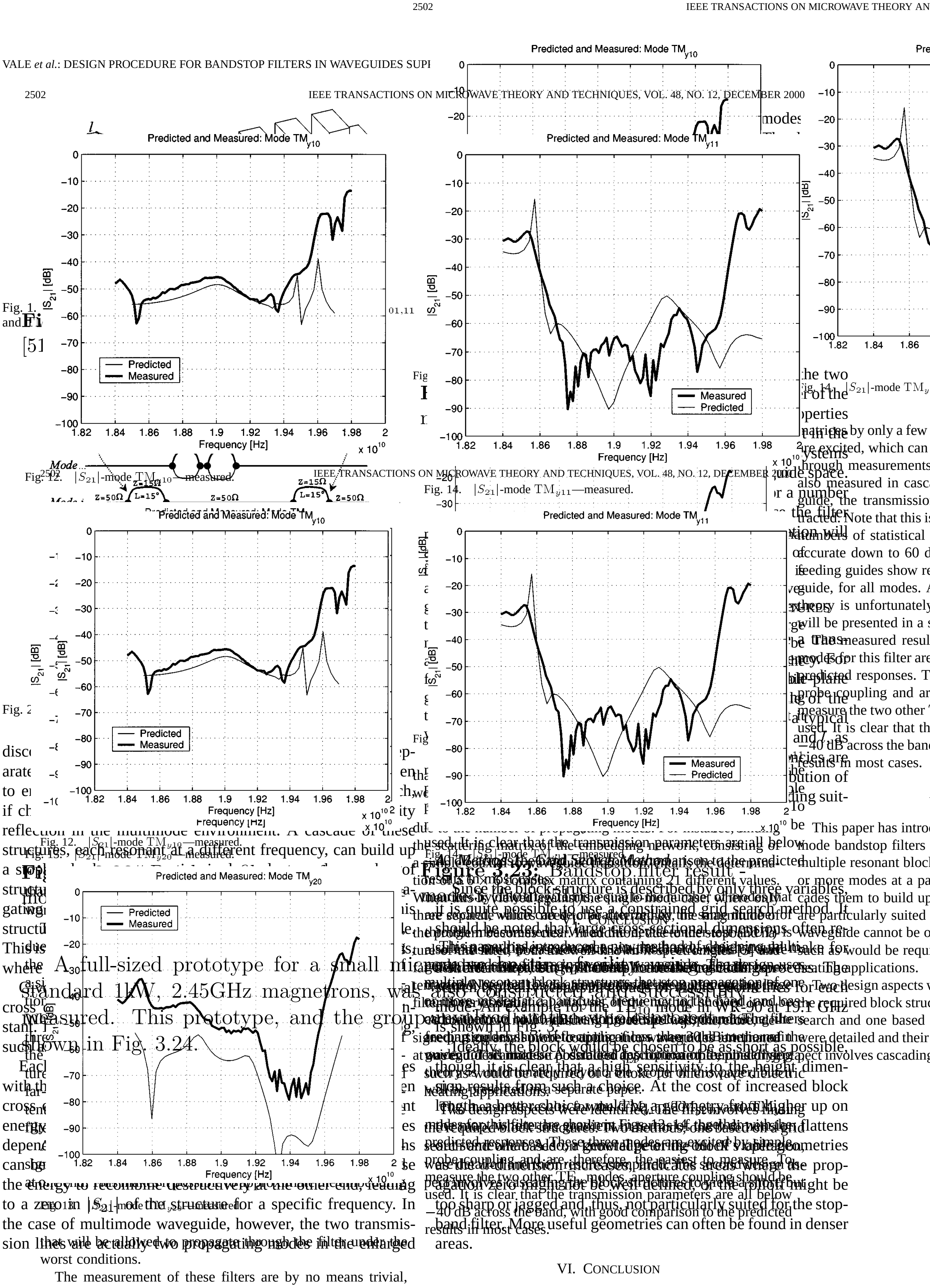

Figure 3.23: Bandstop filter result - [illegible]

A full-sized prototype for a small mi[illegible] standard 1kW, 2.45GHz magnetrons, was also constructed and successfully measured. This prototype, and the group[illegible] shown in Fig. 3.24.

-Filters-

5-mode bandstop filter

Figure 5.27 Photograph of the choke and its creators

Figure 3.24: Dielectric heating oven (from [45])

This work, even though it focused on a niche application, represented the first practical solution to the problem of multi-mode waveguide bandstop filters. It also presented the first tested solution for microwave heating applications requiring conveyor belts. The design approach using functional blocks was used in the group for a number of designs, and was the only solution available until the built-in optimisation capabilities of commercial software became so advanced as to render this work of mostly historical significance. The microwave heating system which was developed also served for many years as test bed for materials research.

3.4 Waffle-iron filters

An important part of high-power transmitter systems is the output filtering, which ensures that no signal harmonics are radiated. In waveguide systems, the standard solution for this filtering function has for almost seventy years been the so-called *waffle-iron* filter. In waveguide, due to the existence of higher order modes which have different field distributions and propagation constants at higher frequencies, filters with wide stopbands are difficult to design. Harmonic filters typically require stopbands of up to 1:6, and therefore need to provide an attenuation for up to 10 or 20 higher order modes in the upper stopband. The waffle-iron filter is a periodic structure with a periodicity of much less than a wavelength. From Floquet's work, it is known that such a structure exhibits periodic stopbands (or band-gaps). A classical waffle-iron filter is shown in Fig. 3.25, where the periodic structure is terminated at both ends with stepped transformers which reduce the waveguide height so as to suppress all modes with variation in the vertical direction.

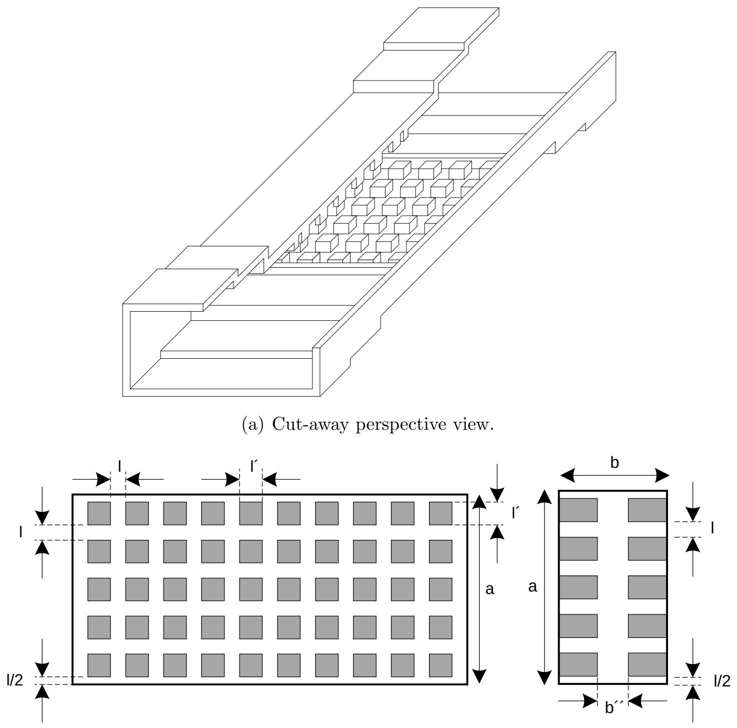

(a) Cut-away perspective view.

(b) Sectioned top view. (c) Sectioned front view.

Figure 3.1: Classical uniform waffle-iron filter.

Figure 3.25: Waffle-Iron filter (from [52])

CAD solutions have been developed in recent years [45, 46, 47]. The waffle iron structure is modeled by a series of general scattering problems, or solved utilising hybrid mode matching (MM) / finite element method (FEM), which allows transversal grooves to be optimised for both adequate stop-band response, as well as equiripple transmission across a defined frequency band. Traditional synthesis methods are, however, used for initial values [47].

This chapter will revisit the circuit model based synthesis of [25], but apply it to the non-uniform waffle iron filters proposed by [45], [46] and [47]. Secondly, this circuit model based approach will be used to investigate waffle-iron filters with bosses rotated for oblique incidence to the dominant TE_{10} mode propagation, in that way synthesising a phase path along the TEM propagation directions.

In addition to the wide stopband requirement, waffle-iron filters typically have to be able to handle very high power levels, as they are often used on Radar transmitters. The design of these filters stretches back to the early 1940's, to a method by Marcuvitz which relies on the basic model of a corrugated waveguide. This method is essentially only concerned with the filter passband, relying on rule-of-thumb dimensions for the lowest stopband cut-off, and the periodicity for the stopband width. No exact synthesis technique has ever been developed for these filters, and even the most recent work simply makes use of very intensive multi-parameter full-wave optimisation.

In 2010, due to a requirement from a local Radar company, my PhD student Dr Tinus Stander and myself started work on improved waffle-iron filter design [52]. In its standard form, the waffle-iron filter has a uniform spacing in both longitudinal and transverse dimensions, as the design approach by Marcuvitz is based on image parameter design, which essentially is the cascade of similar unit cells. Dr Stander proposed a variety of design approaches which allowed for non-uniform patterns, as well as uniform and non-uniform oblique patterns, as shown in Fig. 3.26 and Fig. 3.27. For the non-uniform rectangular and both

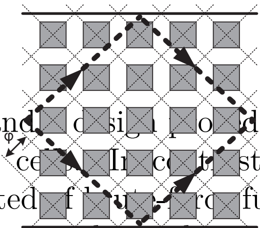

oblique cases, the Marcuvitz model was adapted, and a design procedure was developed to enable the use of non-identical unit cells. In contrast to the state-of-the-art solutions of the time, which consisted of lengthy full-wave electromagnetic optimisation, the proposed technique only used circuit-level optimisation, which is several orders of magnitude faster.

Figure 5: TEM phase path perturbation by uniform boss pattern with oblique angle of incidence.

stop-band than what is actually realised.

Table 3.13: Dimensions of four initial waffle-iron designs with $b'' \approx 2$ mm and $l_t \approx 2 \times a$.

	Corrugated	Marcuvitz	Non-uniform	Oblique
a	21.58	22.80	22.86	22.31
b	7.96	8.30	7.72	8.72
b_T	4.67	2.42	2.97	2.80
b''	1.79	1.92	2	1.79
l or l_i	2.78	2.10	2.34, 2.34, 2.09, 2.30, 2.42, 2.42, 2.30, 2.09, 2.34, 2.34	1.95, 1.87, 1.87, 1.95, 1.95, 1.87, 1.87, 1.95, 1.95, 1.87, 1.87, 1.95, 1.95, 1.87, 1.87, 1.95
l' or l'_i	2.62	1.70	1.38, 2.80, 2.74, 2.67, 2.67, 2.74, 2.76, 2.80, 1.38	2.76, 1.01, 2.24, 1.64, 2.24, 2.02, 2.24, 1.64, 2.24, 2.02, 2.24, 1.64, 2.24, 1.01
w or w_i	2.78	2.10	2.29	1.95, 1.87, 1.87, 1.95, 1.95, 1.87, 1.87, 1.95
w' or w'_i	2.78	1.70	2.29	1.95, 1.87, 1.87, 1.95, 1.95, 1.87, 1.87, 1.95,
l_t	43.16	45.60	50.39	44.62
n_t	[illegible]	[illegible]	10	16
n_l	[illegible]	7	6	[illegible]

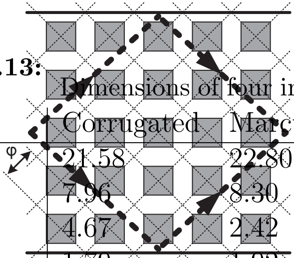

Figure 3.26: Waffle-iron filter with oblique pattern 1 (from [53])

Figure 3: TEM phase path perturbation by uniform boss pattern with oblique angle of incidence.

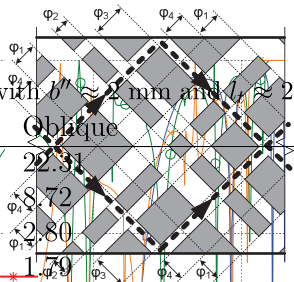

Figure 3.27: Waffle-iron filter with oblique pattern 2 (from [53])

Figure 4: TEM phase path perturbated by non-uniform boss pattern with oblique angle of incidence.

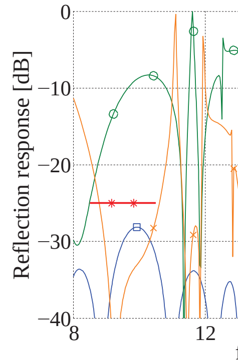

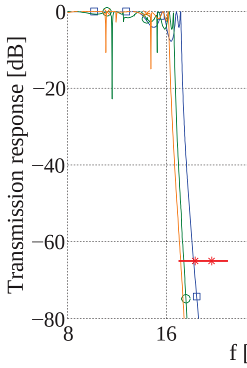

Figure 6: Simulated response of ... Filte...

A number of prototypes were designed, using the standard techniques as well as the proposed circuit-based optimisation, the latter being used for the design of non-uniform and oblique patterns. The simulated results of a variety of filters are shown in Fig. 3.28. Of importance here is the difference in return loss produced by the different designs, as well as the stopband roll-off. It is clear that the use of non-uniform patterns is advantageous, which makes standard design techniques obsolete. Either full-wave optimisation or the proposed circuit-based optimisation is therefore required, with the latter having a significantly shorter design time.

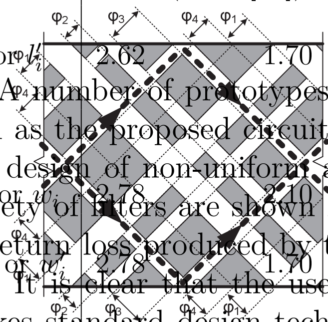

Figure 4: TEM phase path perturbated by non-uniform boss pattern with normal angle of incidence.

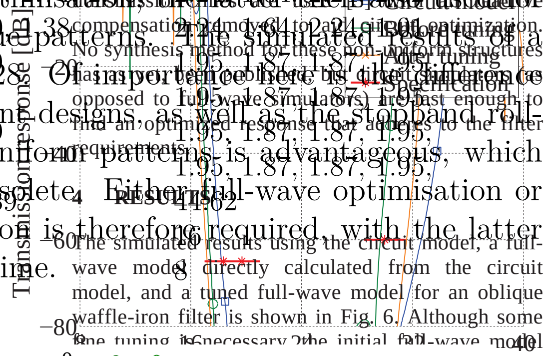

3 DESIGN

A very simple circuit model can be used for the design of these filters. As they are essentially TEM filters, the Marcuvitz model for shorted-stub-loaded transmission lines is used. The [?] model for [?] compensation is modified to a circuit optimization. No synthesis method for these non-uniform structures has as yet been published but circuit simulations (as opposed to full-wave simulators) are fast enough to find an optimized response that adheres to the filter requirements.

4 RESULTS

The simulated results using the circuit model, a full-wave model directly calculated from the circuit model, and a tuned full-wave model for an oblique waffle-iron filter is shown in Fig. 6. Although some fine tuning is necessary, the initial full-wave model (derived from the optimized circuit model) is established much faster than a model optimized in a full-wave solver. In addition, the filter can be shown to be more compact than normal waffle-iron filters. The spurious resonances excited inside the filter cavity are of concern, since these are unaccounted for in the circuit model. This aspect has to be evaluated with some scrutiny in any design.

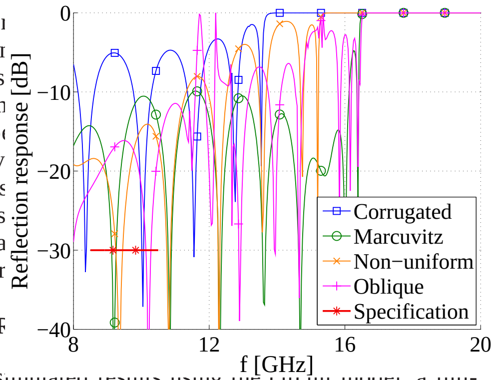

(a) Reflection response

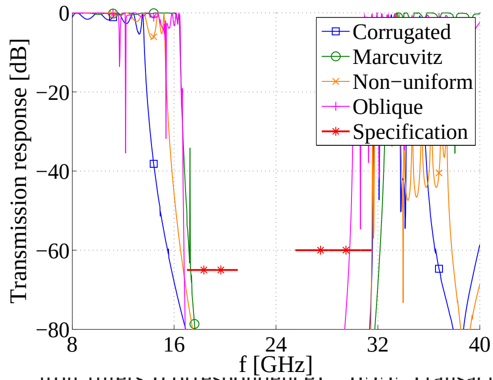

(b) Transmission response

Figure 3.28: Comparison of waffle-iron design approaches (from [52])

Figure 5: Comparison of four synthesis methods on the same specifications before full-wave tuning, $b'' \approx 2$ mm, $l_t \approx 2 \times a$.

Doubling the length of each filter, as is done in the second set, increases the roll-off (increased order) and the maximum stop-band attenuation, as shown in Fig. 3.28. To note from this example, is that three of the four models (Cohn's corrugated data, Marcuvitz data and oblique design) are increased in length by replicating existing dimensions. In the

References

[1] S.B. Cohn, E. M.T. ... Shimizu, B.M. Schi... "Research on design ... filters," Stanford Resear... – SRI Project 1331, June...
[2] L. Young, "Postscript ... iron filters (corresponde...)," IEEE Transactions on Microwave Theory and Techniques, vol. 11, no. 6, pp. 555 – 557, November 1963.
[3] G. L. Matthaei, L. Young, and E. M. T. Jones, Microwave Filters, Impedance-Matching Networks, and Coupling Structures. McGraw-Hill Book Co, 1964.
[4] F. Arndt and J. Brandt, "Direct EM based optimization of advanced waffle-iron and rectangular combline filters," in IEEE MTT-S International Microwave Symposium Digest, June 2002.

Using the proposed technique, a prototyp[e ...]le-iron filter was designed and tested, with the [...]he stopband attenuation shown in Fig. 3.29 and [...]ff, low return loss in the X-band, and good atte[...]nt.

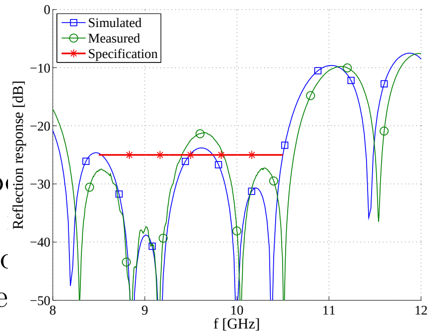

(a) Reflection response.

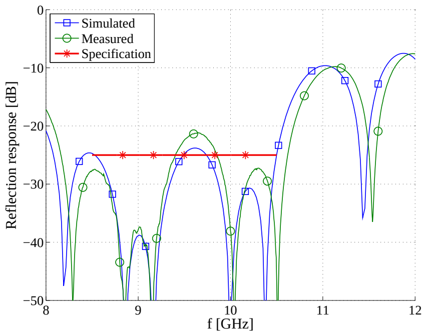

(a) Reflection response.

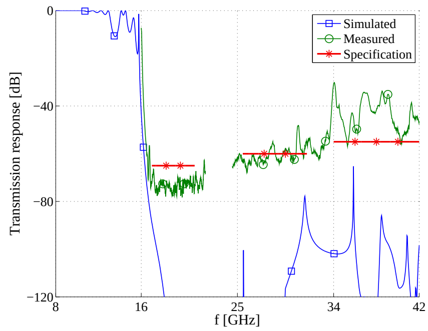

(b) Transmission response.

Figure 3.29: Waffle-Iron filter measured results S11(from [52])

Figure 3.30: Waffle-Iron filter measured results S21 (from [52])

Figure 3.39: Measured electrical response of waffle-iron filter.

Waffle-iron filters are traditionally all-metal filters, and especially for non-uniform patterns, the manufacturing is quite expensive. Recently, my PhD student Mrs Susan Maas and myself proposed the manufacturing of these filters in the medium of multi-layered circuit boards, using the so-called *Surface Integrated Waveguide (SIW)* structure as basis. Using substrate instead of air reduces the power-handling capability of the filters substantially, but yields significant reductions in size, weight, and cost. Especially the size and weight are of enormous importance in the very fast developing area of cube-sats, i.e. satellites not measuring larger than 10x10x10cm.

(b) Transmission response.

Figure 3.39: Measured electrical response of waffle-iron filter.

Manufacturing waffle-iron filters in this way poses significant challenges, as the inherent uncertainty in the etching and laminating processes of soft substrates is much higher that what can be achieved in high-quality milling. This causes for instance the posts in the filter to all have slightly different dimensions and spacings, as they are implemented using standard PC-board vias. The complexity of the structure mostly manifests in the multi-layer stackup, an example of which is shown in Fig. 3.33.

Two of these filters have been designed and manufactured - a shorter one covering a limited bandwidth shown in Fig. 3.31, and a longer one which includes multiple sections for improved stopband width, shown in Fig. 3.32.

Fig. 3.34 shows a few typical problems that arise in the manufacturing process, such as vias not perfectly aligned, not with the correct depth, and not making contact with the inner conductors. Despite this, the two filters were manufactured and tested, with the measured transmission results shown in Fig. 3.35 and Fig. 3.36. The good stopband performance, and the difference in stopband width between the two filters, are evident.

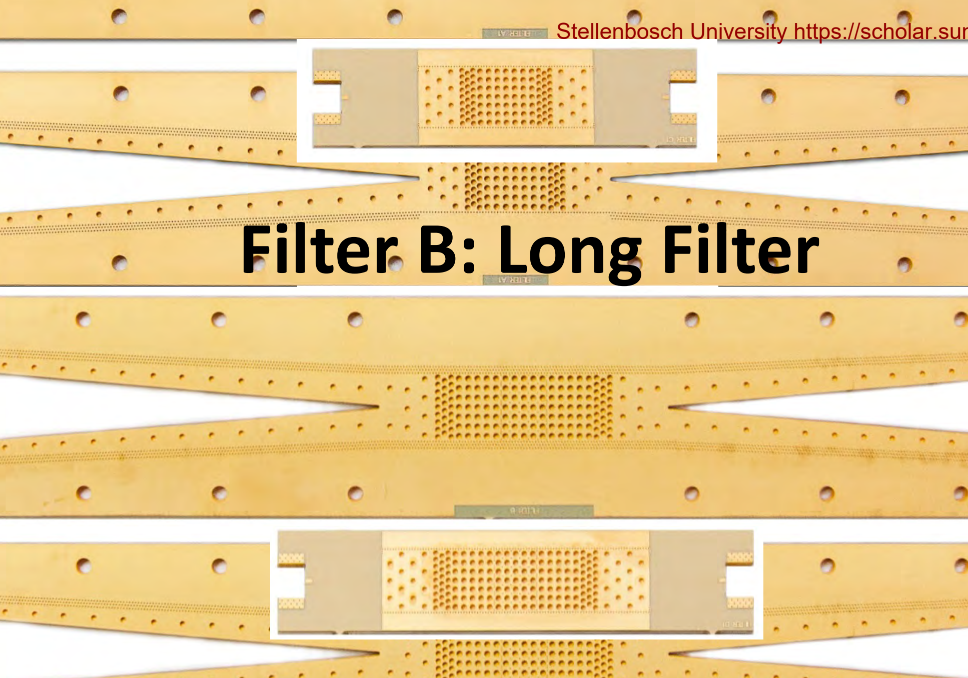

Figure 3.32: Planar waffle-iron filter 2 (from [54])

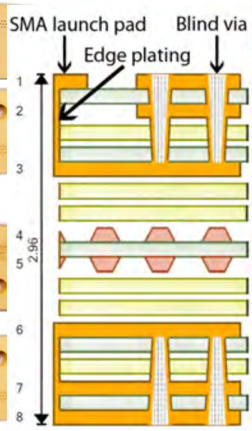

Figure 3.33: Planar waffle-iron stackup (from [54])

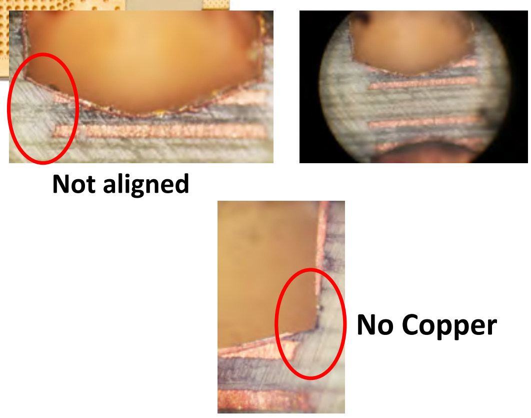

Figure 3.34: Typical planar manufacturing problems(from [54])

At the time of writing, these results are still unpublished and preliminary, but are included to give a complete picture of my work. The possibility to manufacture waffle-iron filters using standard PC-board techniques will be a completely new approach to the manufacturing of these filters, and will allow much more complicate patterns to be implemented. It will also open the door for the application of these very useful filters to small systems in which weight and size are overriding factors.

3.5 Absorbing filters

While by far the most microwave filters perform their filtering action by frequency selective reflection of energy, a small but important group selectively absorb energy in the stopband. The application of these filters is in any sys-

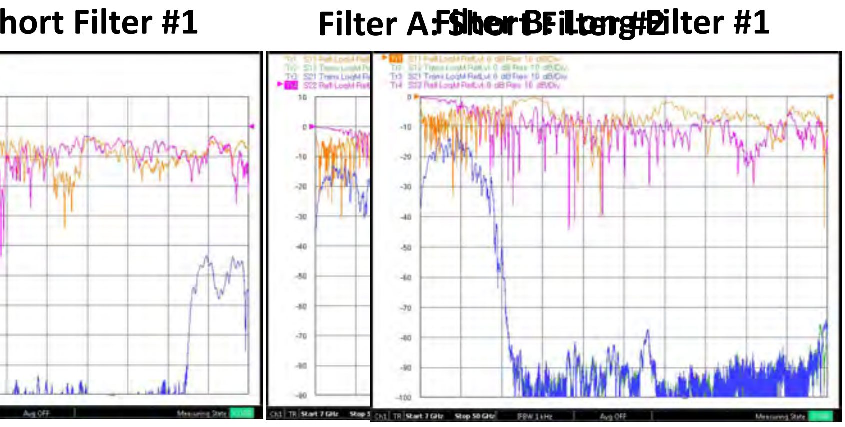

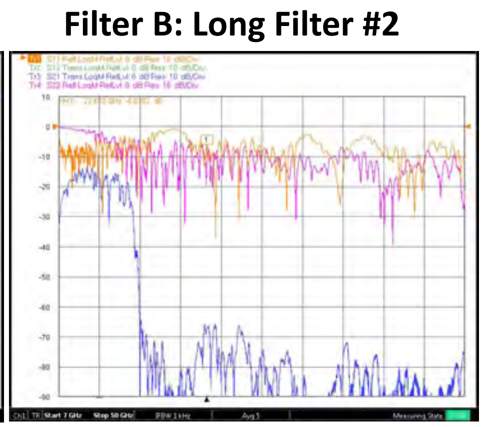

Figure 3.35: Planar waffle-iron filter 1 measurement (from [54])

Figure 3.36: Planar waffle-iron filter 2 measurement (from [54])

tem where reflected energy can become problematic, such as on the output of mixers, or high-power amplifiers. In the first, the reflection of spurious mixing products back into the mixer can lead to increased intermodulation problems, whereas in the latter, the power handling capability of the amplifiers can be exceeded.

For a filter to be aborbing, it has to have significant loss in the stopbands. Classical filter synthesis techniques however rely fundamentally on the network being exactly loss-less, and no design techniques have yet been developed for absorbing filters (note that some techniques, such as pre-distortion, do exist for low-loss filters, but these work on perturbation of the loss-less theory, and are not valid for high-loss filters).

In conjunction with the work on waffle-iron filters, the PhD of Dr Tinus Stander also focused on absorbing filters, especially on combining waffle-iron filters with absorbing structures [52]. A first attempt to implement such a filter was based on design techniques for slotted-waveguide array antennas, with each slot then replaced by an absorbing circuit [55]. The advantages to this are manifold, as slotted waveguide array theory is a mature field of research, with a solid body of design techniques, theory, and application examples.

For the equivalent 'absorbing slot', an etched ring resonator was proposed, as shown in Fig. 3.37. The ring is etched on a thin substrate, interrupted by small surface-mount resistors at two points, and placed transversely in a waveguide at the point where a slot would have been placed in a slotted-waveguide antenna. The length of the ring sets the resonance frequency of the absorber, while the resistors supply the loading.

To illustrate the procedure, a matched load was designed for the X-band, using three etched rings in an X-band waveguide. The measured return loss results are shown in Fig. 3.38, where the three resonant frequencies are clearly visible, as well as the low return loss from 9-12GHz.

While the etched-ring concept is a very useful design approach, the use of surface-mount resistors on a dielectric substrate places a significant limit on the

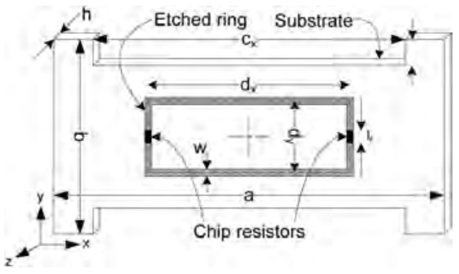

Figure 3.37: Etched ring absorber (from [55])

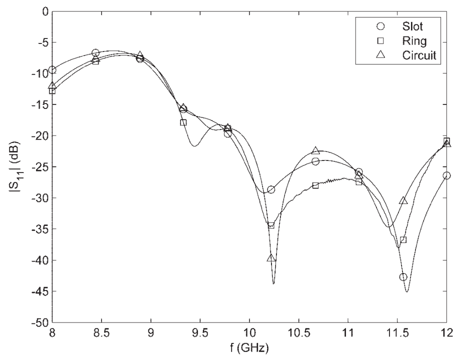

Figure 3.38: Etched ring filter results (from [55])

power-handling capabilities of the filter, as the thermal resistance from the resistor to ambient is very high. To allow for higher power levels, physically larger resistors are required, in some way thermally connected to a heat-dissipating structure. At high frequencies, this leads to higher reactive parasitics, and space problems. For high-power applications at high frequencies, the only solutions are to extract the power in the stopbands in some way from the main signal path, and then absorb it. This, the so-called *leaky-wave filter* has been doing successfully for decades. While an excellent solution, leaky-wave filters are unfortunately long and bulky.

Dr Stander proposed a very novel approach to the problem, namely to reflect the energy in the stopband with a wideband reflective filter, such as a waffle-iron filter, and then selectively absorb the reflected signal in aborbers tuned to the harmonic frequencies [56]. This principle is illustrated in Fig. 3.39.

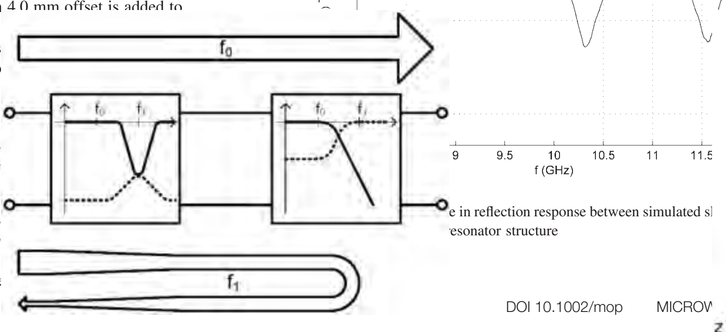

Figure 3.39: Principle of absorbing filter (from [52])

Using the principles of slotted-waveguide antennas, two slots can be placed in the waveguide in front of the plane of the reflective filter, at the point at which the standing wave for a specific harmonic is the largest. The energy which couples through theses slots, is transferred to two waveguides which are both loaded with absorbing material, thus absorbing the harmonic signal. The structure of one set of slots, and its equivalent circuit, are shown in Fig. 3.40 and Fig. 3.41.

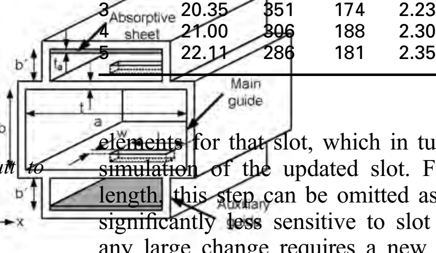

Figure 3.40: Basic absorbing slot structure (from [52])

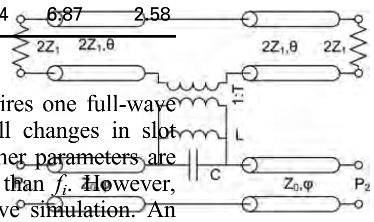

Figure 3.41: Absorbing slot equivalent circuit (from [52])

A full absorbing filter was designed to absorb the second harmonic of an X-band system, i.e. the band of 16-22GHz. The filter is shown in Fig. 3.42, where the terminating reflective waffle-iron filter is the one discussed before, and shown here as an S-parameter box. The measured results in Fig. 3.43 and Fig. 3.44 show the low return loss in the passband (8-11GHz) as well as in the second harmonic stopband (16-22GHz), the low insertion loss in the passband, and high attenuation in the second harmonic stopband.

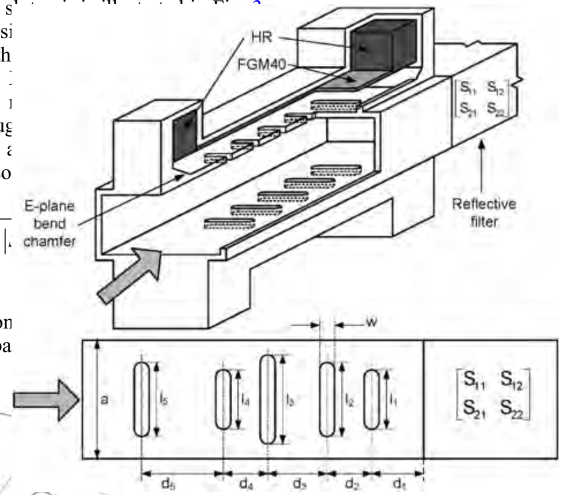

Figure 3.42: Absorbing slot filter (from [52])

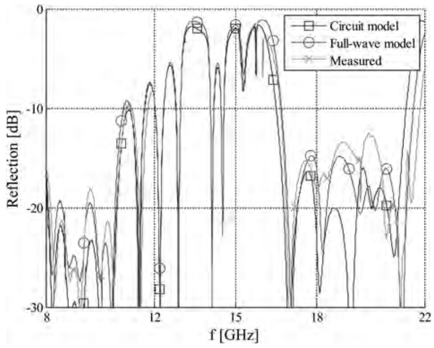

Figure 3.43: Absorbing filter S11 (from [52])

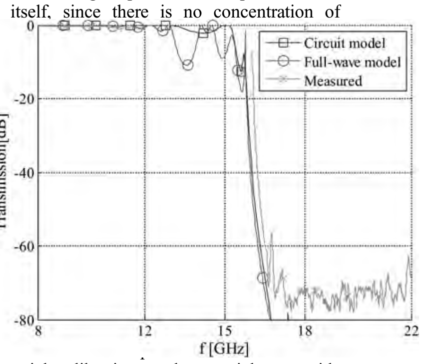

Figure 3.44: Absorbing filter S21 (from [52])

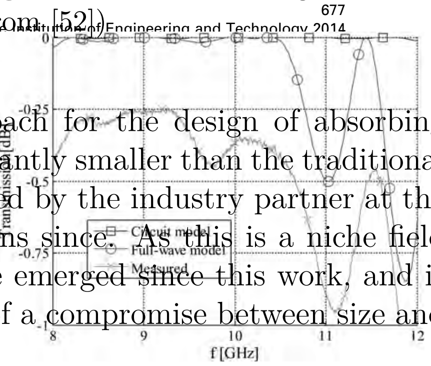

This work presented a very novel approach for the design of absorbing harmonic filters, and produced a filter significantly smaller than the traditional leaky-wave filters. It was immediately adopted by the industry partner at the time, and has been used in successive systems since. As this is a niche field of research, virtually no other solutions have emerged since this work, and it still represents the state-of-the-art in terms of a compromise between size and performance a decade later.

3.6 Tunable and Planar Filters

Planar filters, constructed using standard PC-board processes, have become increasingly popular over the last few decades as the quality and ability of the processes have developed. Especially the last decade has seen a huge surge in the development of multi-layer microwave circuits, using substrates such as RT-Duroid. At the same time, increases in affordable computing power, and in the capabilities of commercial full-wave electromagnetic analysis software, have removed most of the modelling restrictions on structures. Designers can now propose filter structures of almost arbitrary complexity, and solve it very accurately on machines as small as office laptops. This has lead to an explosion in filter topologies, resonating structures, coupling structures, and the incorporation of tuning elements into planar structures.

Over the last decade, my own filter work also shifted from mostly waveguide work, to mostly planar work. This was mainly driven by the needs of local industry, who in turn was reacting to a market which changed virtually overnight from almost completely defence orientated to almost completely commercially orientated.

3.6.1 Triple-mode filters

One of the areas in filter design which received significant international attention, was that of multi-frequency resonators. As a general goal, the emphasis on planar resonators has been on miniaturisation, and the possibility to achieve multiple resonances using a resonator with roughly the same footprint as a singly resonant circuit, was very attractive.

In cooperation with Prof Branka Jokanovic from Belgrade, and with a colleague Dr Riana Geschke, our first efforts in this direction was a triple-mode etched split-ring resonator [57] and [58]. This consisted of three very tightly coupled, concentric, split-ring resonators such as shown in Fig. 3.45. Having the three resonators so tightly coupled, reduces the total footprint by a huge margin, but makes the design quite complicated, as is quite clear from the complicated circuit model shown in Fig. 3.46. This especially becomes a problem when the resonator is to be used in a larger filter structure.

GESCHKE et al.: FILTER PARAMETER EXTRACTION FOR TRIPLE-BAND COMPOSITE SRRs AND FILTERS 1501

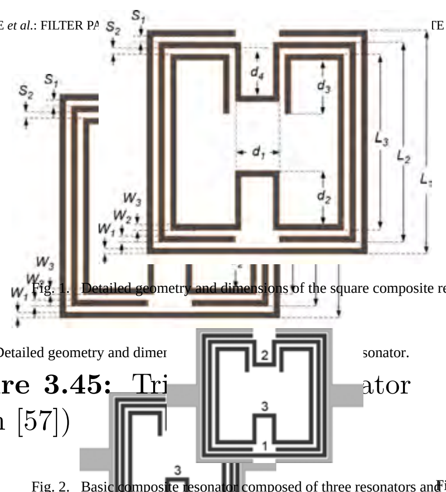

Figure 3.45: Tri[illegible]ator (from [57])

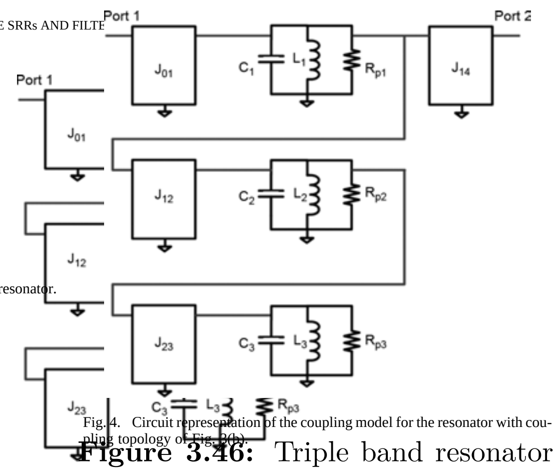

Figure 3.46: Triple band resonator equivalent circuit (from [57])

To enable a design process, we propose a systematic detuning system by which parts of the resonator could be detuned (instead of removed), leaving the structure to exhibit only the normal two resonances expected from a coupled resonator system. From these two frequencies, both the resonant frequencies can be extracted as well as the coupling factor. The main advantage of detuning instead of removing sections is of course that the structure only changes marginally when detuned. Fig. 3.47 shows two cases of detuning - one with the inner ring detuned, and the other with the outer ring detuned. The resulting curves in Fig. 3.48 show only two resonance peaks in each case, from which the relevant part of the full model can then be extracted.

The method of systematic detuning was used in the design of a sixth order filter with three passbands, consisting of two coupled triple-mode resonators,

Figure 3.48: Detuned resonance frequencies (from [57])

as shown in Fig. 3.49. Using the detuning [illegible] enabled [illegible] from a [illegible] instead of optimising [illegible] sation [illegible] to satisfy [illegible]. A photo [illegible] prototype is shown [illegible] sured S- [illegible] 3.50. For the sub[illegible] the foot[illegible] band filter is very [illegible] response.

Figure 3.49: Triple band filter (from [57])

Figure 3.50: Triple band filter measurements (from [57])

In conjunction with myself, the work was continued by Dr Jokanovic and her group, with the next phase being a reconfigurable, three-split-ring structure, called a *composite split-ring resonator* [59]. An example of the structure is shown in Fig. 3.51. Here, the ability to reconfigure the structure is made possible by the insertion of PIN-diodes at certain critical points, allowing DC bias signals to switch sections of the structure in and out of the circuit. Fig. 3.52 graphically shows (in yellow) the active sections (i.e. those contributing to the response) of the structure for five different states. As PIN-diodes are very inexpensive, and have very low loss as compared to varactor diodes, switching

Instead of tuning is an excellent option, and if designed correctly, can yield a set of transfer functions which also satisfy multi-band requirements.

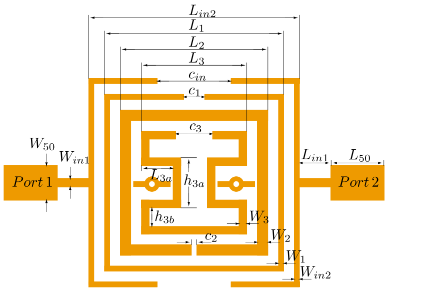

Figure 3.51: Composite split-ring resonator (from [59])

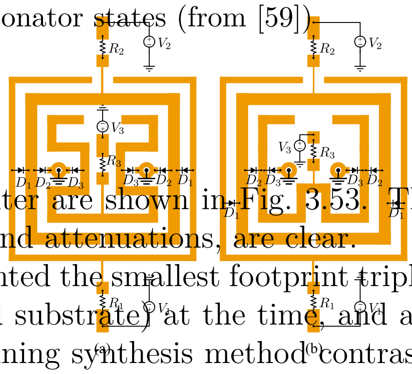

Figure 3.52: Composite split-ring resonator states (from [59])

The measured results for a seven-state filter are shown in Fig. 3.53. The variety of usable passbands, and inter-passband attenuations, are clear. The two structures presented here represented the smallest footprint triple-mode resonators (for a certain frequency and substrate) at the time, and are still among the smallest published. The detuning synthesis method contrasts strongly with a simple brute-force optimisation, which was the prevalent design method. In addition to shortening the design cycle, it also had the significant benefit of allowing a much more systematic design, in the normal way of filter synthesis.

3.6.2 Mixed-coupling multilayer filters

In another cooperation, this time with the group of Prof Jiasheng Hong from Heriot-Watt University in Edinburgh, and specifically with PhD students Dr Shilong Qian from Heriot-Watt, and Dr Gerdus Brand from Stellenbosch, the possibilities of multi-layer structures for the implementation of small filters was investigated [60]. In particular, the use of multiple layers to implement vertical coupling between resonators, and combinations of positive and negative couplings, were attempted. Vertical mixed coupling structures offer many advantages, and enables couplings to be made between non-adjacent resonators in a very simple manner. Fig. 3.54 for instance shows a standard coupling matrix resulting from a filter specification, which requires multiple cross-couplings. Using mixed-mode coupling (i.e. combined positive and negative coupling together), and circuit transformations, the complex coupling matrix can be implemented as the circuit in Fig. 3.55.

Using multi-layer manufacturing, the filter could then be implemented as the structure shown in Fig. 3.56, where the different patterns are shown for each layer, as well as the interconnects. The measured response of the filter is

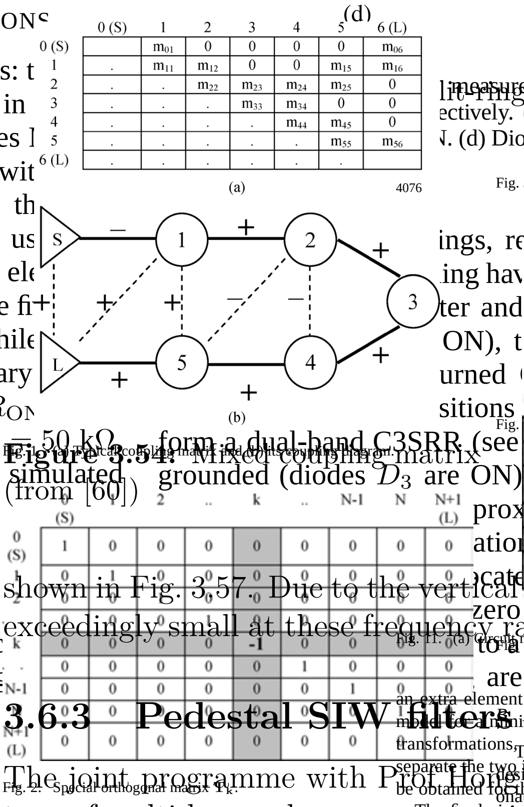

Figure 3.54: Mixed coupling matrix (from [60])

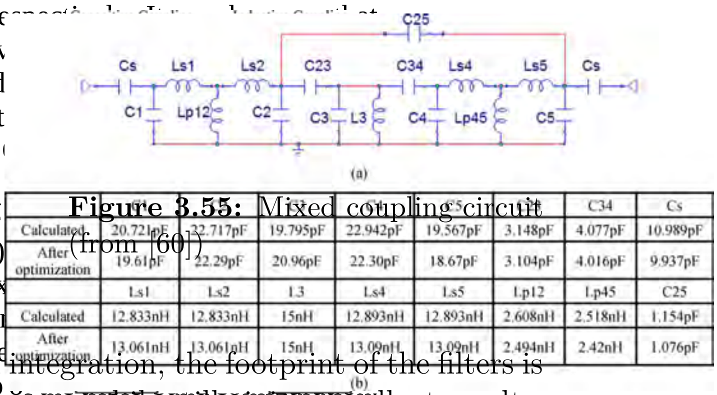

Figure 3.55: Mixed coupling circuit (from [60])

shown in Fig. 3.57. Due to the vertical integration, the footprint of the filters is exceedingly small at these frequency ranges, while still giving excellent results.

3.6.3 Pedestal SIW filters

The joint programme with Prof. Hong would serve as the seed for a new type of multi-layer, planar resonator known as the so-called pedestal resonator. This

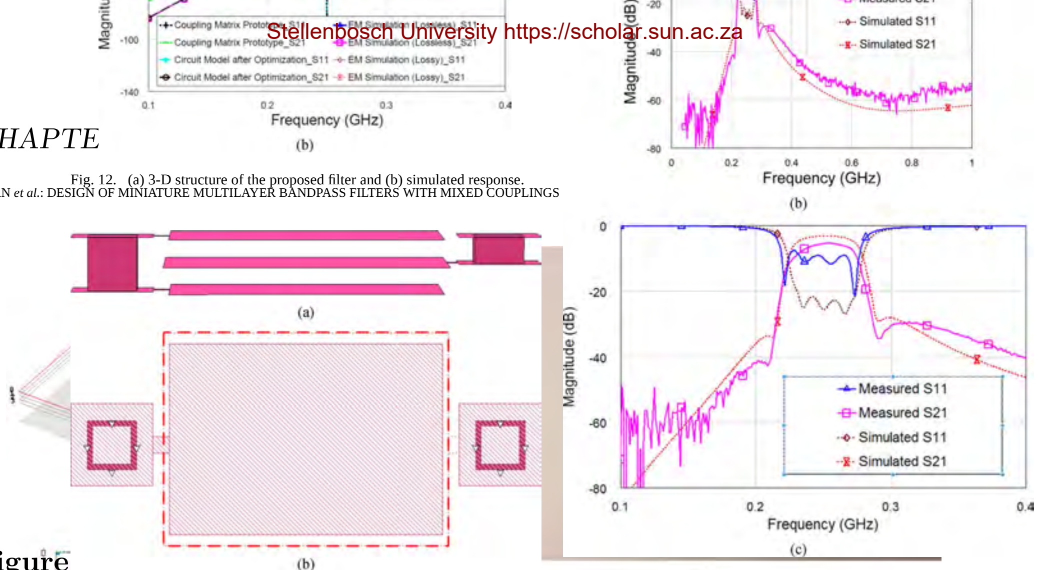

Figure ... layout (from [60])

Figure 3.57: Mixed coupling filter measurements (from [60])

concept was developed by my PhD student, Dr Shamim Nassar, and myself, as a structure to fill the gap between classical Surface Integrated Waveguide (SIW) resonators and other types of planar resonators, such as ring, split-ring, patch etc. [61]

SIW has become very popular over the last decade, as it is a very cost-efficient way of constructing dielectric filled waveguides. In SIW, the vertical 'walls' of the waveguide is implemented using closely spaced vias, running between the upper and lower ground planes of a double-sided microwave substrate. SIW resonators have higher Q-factors than other planar resonators, but due to the reduced height of the waveguide, and the introduction of a dielectric, typically an order of magnitude lower Q-values than standard metal waveguide. They are of course significantly smaller, as the height is set by the dielectric thickness, and the transverse dimensions by the permittivity of the dielectric.

As with normal waveguide, SIW suffers from the problem of spurious resonances due to the propagation of higher order modes. In standard waveguide, this problem is solved by the use of ridged waveguide, which increases the spacing between the cut-off frequencies of the first two modes by a factor of up to five or six. The pedestal resonator proposed in [62] can be viewed as a doubly folded ridge waveguide resonator as implemented in SIW, and retains to an extent the good modal separation of ridge waveguide. It can also be viewed as a loaded SIW resonator, with full control over the extent of loading. As in all waveguide, higher loading incurs smaller size and lower Q-values, but in the pedestal resonator, this compromise between Q-value, size and spurious resonance separation, can be chosen by the designer.

The pedestal resonator is constructed by a patch situated between the two ground planes of an SIW resonator, connected to the one ground plane through a via, or a set of vias. Two basic shapes are shown in Fig. 3.58.

The main characteristics of the pedestal resonator are shown in Fig. 3.59(a), which shows the resonance frequency of the second resonance as a function of the first resonance, for a set of typical resonators, and Fig. 3.59(b), which

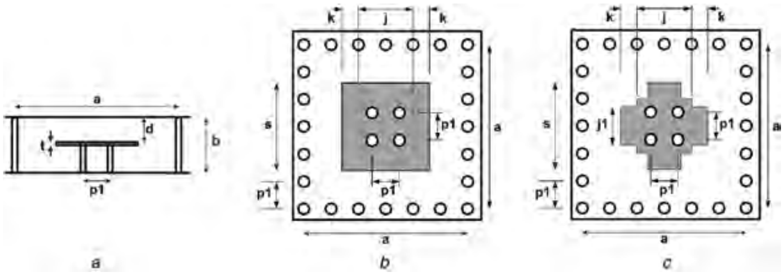

Figure 3.58: Pedestal resonator structure (from [62])

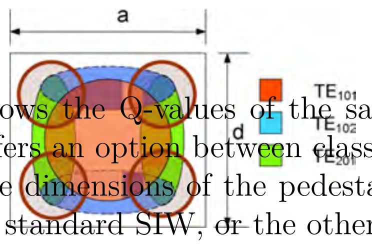

shows the Q-values of the same set. It is clear that the pedestal resonator offers an option between classical resonators, and standard SIW. By choosing the dimensions of the pedestal top, performance can be moved towards that of standard SIW, or the other way.

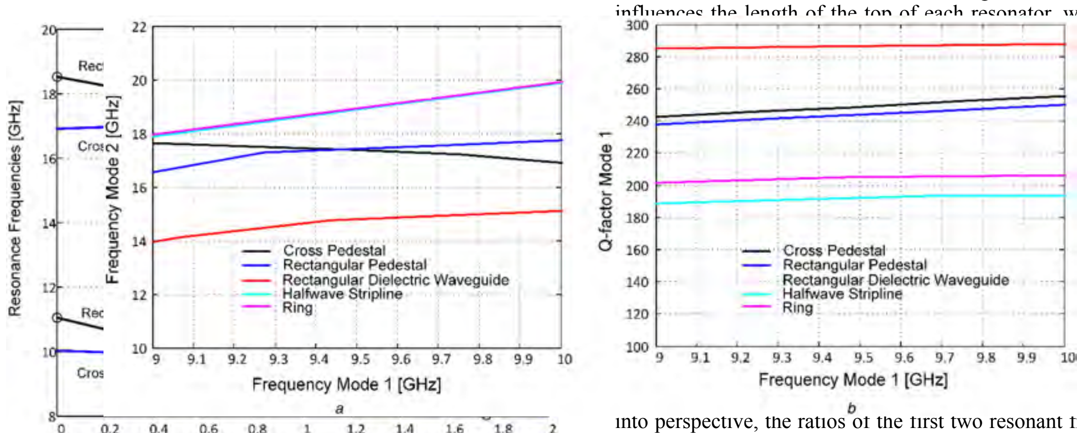

Figure 3.59: Pedestal resonator characteristics (from [62])

The first filters making use of the pedestal SIW resonator are shown in Figs. 3.60, where (a) and (b) show two layers of a filter using a cross-shaped pedestal top and inline magnetic coupling, and (c) and (d) show the two layers of a filter using square-topped pedestals, with magnetic coupling and electric cross-coupling. It should be noted that the very simple implementation of two types of coupling in this structure is one of the most favourable characteristics. Measurements of the two filters are shown in Fig. 3.61 and Fig. 3.62. Good performance in the pass-band is observed, with very good stop-band performance compared to normal SIW. The transmission zeros created by the electric coupling in the second filter are clearly visible.

Rectangular resonator: $a = 7.5$ mm, $s = 5.0$ mm

Cross-shaped resonator: $a = 7.9$ mm, $s = 5.4$ mm, $j1 = 3.2$ mm

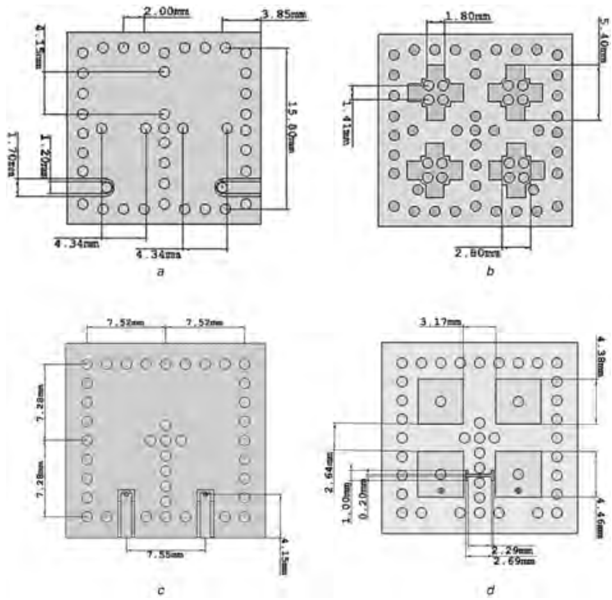

Fig. 7 *Two-layer implementation of the final structure of filter A*
(a) Filter A top layer, *(b)* Filter A internal layer, *(c)* Filter B top layer, *(d)* Filter B internal layer

Figure 3.60: Pedestal resonator filters (from [62])

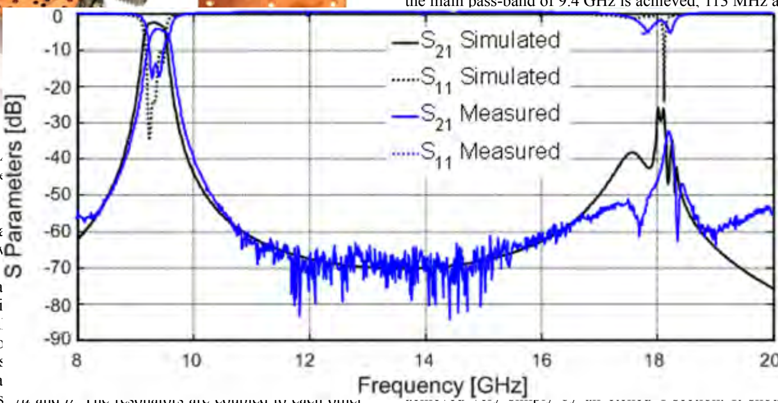

Fig. 9 *Broadband measurement results for filter A*

Figure 3.61: Pedestal resonator filter 1 measurements (from [62])

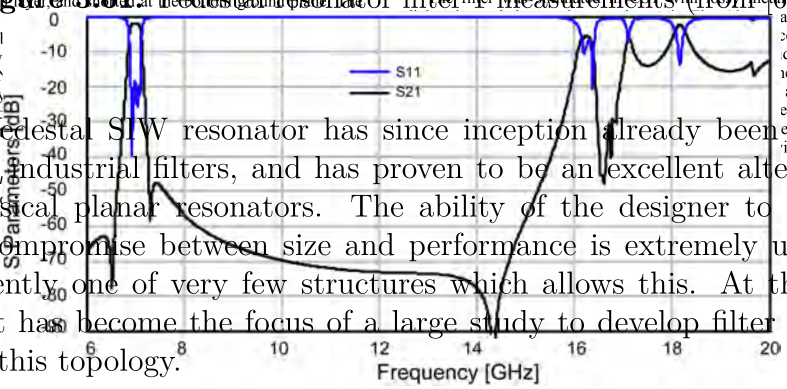

The pedestal SIW resonator has since inception already been used in a variety of industrial filters, and has proven to be an excellent alternative to more classical planar resonators. The ability of the designer to choose an optimal compromise between size and performance is extremely useful, and it is currently one of very few structures which allows this. At the time of writing, it has become the focus of a large study to develop filter structures based on this topology.

Fig. 10 *Broadband simulation results for filter B*

technology. A better than 40 dB spurious-free attenuation is predicted from 7.2 to 15.5 GHz, with the main second pass-band centred at 16.24 GHz, or 2.32f_0.

The results of the two filters can be compared with existing solutions. In [2], full-sized microstrip and coplanar waveguide resonators are loaded with complementary split ring resonators (CSRRs). Two third-order filters, one at f_0 = 1.8 GHz and one at f_0 = 2.4 GHz, both with 10% relative bandwidth, achieve stopbands of better than 20 dB over, respectively, 5 and 8 GHz. In [20], a so-called 'butterfly resonator' is used in a single resonator low-pass filter with a cut-off of 1 GHz. This resonator achieved a very small size of 0.1 of a wavelength, and attenuation of 17 dB from 2.37 to18 GHz. The author also provided a useful table of other planar resonators and their performance. While the stopbands of these filters are all very wide, they are all non-waveguide solutions, with

× 20 mm, with f_0 = 5 GHz, a 3 dB bandwidth of 320 MHz, insertion loss of 3.9 dB, and an attenuation of better than 40 dB from 5.5 to 6.5 GHz, and a filter with transverse dimensions of 45 × 12 mm, with f_0 = 5.45 GHz, a 3 dB bandwidth of 187 MHz, insertion loss of 5.8 dB, and an attenuation of better than 45 dB to up to 9 GHz. It should be clear that the proposed filters offer smaller footprints, similar insertion loss, and a wider stopband.

5 Conclusions

Pedestal SIW resonators are proposed which utilise the mode separation characteristics of ridge surface integrated waveguide, specifically T-ridge SIW guide. Two shapes of the pedestal resonator are compared with standard resonators, and are shown to offer a good compromise between size, Q-factor, and mode

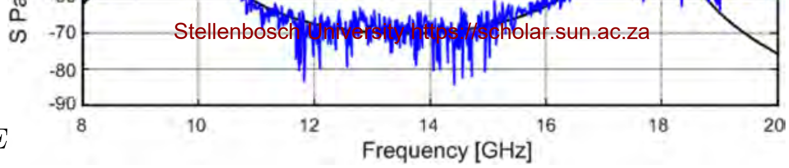

Fig. 9 *Broadband measurement results for filter A*

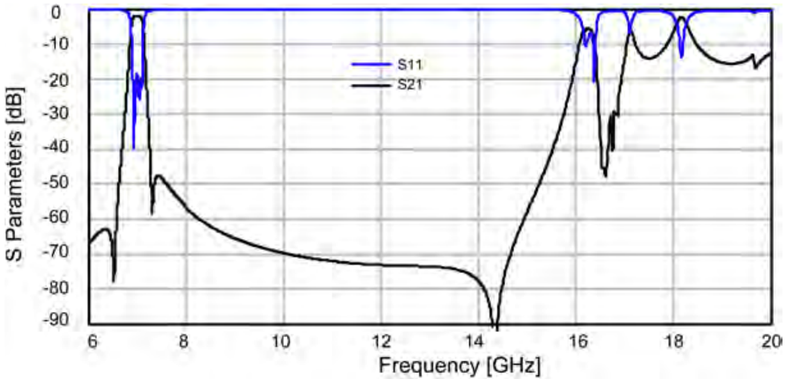

Fig. 10 *Broadband simulation results for filter B*

technology. A better than 40 dB spurious-free attenuation is predicted from 7.2 to 15.5 GHz, with the main second pass-band centred at 16.24 GHz, or $2.32f_0$.

The results of the two filters can be compared with existing solutions. In [2], full-sized microstrip and coplanar waveguide resonators are loaded with complementary split ring resonators (CSRRs). Two third-order filters, one at $f_0 = 1.8$ GHz and one at $f_0 = 2.4$ GHz, both with 10% fractional bandwidth, achieve stopbands of better than 20 dB over, respectively, 5 and 8 GHz. In [20], a so-called 'butterfly resonator' is used in a single resonator low-pass filter with a cut-off of 1 GHz. This resonator achieved a very small size of 0.1 of a wavelength, and attenuation of 17 dB from 2.37 to18 GHz. The author also provided a useful table of other planar resonators and their performance. While the stopbands of these filters are all very wide, they are all non-waveguide solutions, with lower Q-values than waveguide. In many cases, the resonators effectively approximate lumped elements, which accounts for the very wide stopbands. In terms of waveguide solutions, Salehi and Mehrshahi [14] uses dissimilar oversized SIW cavities with slot loading to design two filters at $f_0 = 10$ GHz and better than 30 dB attenuation stopbands of up to 19 GHz. In [21, 22], authors use cross-coupling of normal or higher-order modes to create transmission zeros distant from the pass-band, with, respectively, a 50 dB attenuation stopband achieved between 7.5 and 11.5 GHz for a fourth-order filter with a pass-band of 19.2 to 21.2 GHz, and a 50 dB attenuation stopband of 0–10 GHz achieved for a third-order filter with a 1 GHz bandwidth at $f_0 = 13$ GHz.

The most similar solutions to the structure proposed in this paper, are those in [23–25]. In [23], waveguides are loaded dielectrically to reduce size, achieving a fourth-order Chebyshev filter, measuring 40 × 40 × 12 mm, with $f_0 = 3.8$ GHz, a bandwidth of 3%, insertion loss of 0.4 dB, and better than 70 dB attenuation over the band 2.3–3.6 GHz and better than 20 dB attenuation over the band 4–5 GHz. Both [24, 25] use CSRRs to load SIW cavities, and, respectively, achieve a filter with transverse dimensions of 70 × 20 mm, with $f_0 = 5$ GHz, a 3 dB bandwidth of 320 MHz, insertion loss of 3.9 dB, and an attenuation of better than 40 dB from 5.5 to 6.5 GHz, and a filter with transverse dimensions of 45 × 12 mm, with $f_0 = 5.45$ GHz, a 3 dB bandwidth of 187 MHz, insertion loss of 5.8 dB, and an attenuation of better than 45 dB to up to 9 GHz. It should be clear that the proposed filters offer smaller footprints, similar insertion loss, and a wider stopband.

5 Conclusions

Pedestal SIW resonators are proposed which utilise the mode separation characteristics of ridge surface integrated waveguide, specifically ridge SIW guide. Two shapes of the pedestal resonator are compared with standard resonators, and are shown to offer a good compromise between size, Q-factor, and mode separation. Two fourth-order filters are designed in PCB multilayered technology and performance verified by both simulation and/or measurement. The results show improved performance over published filters employing similar miniaturisation techniques.

6 Acknowledgments

The authors thank Reutech Radar Systems (Pty) Ltd for financial support of this project, and CST GmbH for the use of CST Microwave Studio.

7 References

[1] Nassar, S., Meyer, P., Van der Walt, P.W.: 'An S-band combline filter with reduced size and increased pass-band separation'. 14th Conf. on Microwave Techniques (COMITE 2015), Pardubice, 2015
[2] García-García, J., Martín, F., Falcone, F., et al.: 'Microwave filters with improved stopband based on sub-wavelength resonators', *IEEE Trans. Microw. Theory Tech.*, 2005, **53**, (6), pp. 2104–2113
[3] Djerafi, T., Aubert, H., Wu, K.: 'Ridge substrate integrated waveguide (RSIW) dual-band hybrid ring coupler', *IEEE Microw. Wirel. Compon. Lett.*, 2012, **22**, pp. 70–72

Figure 3.62: Pedestal resonator filter 2 measurements (from [62])

3.6.4 Tunable staircase filters

Tunable planar filters have become a huge research field in the last few years. This effort is primarily driven by the personal communications market, where size is of prime importance. Tunable filters offer the possibility to have one filter structure which can be used for various frequency bands.

While a host of new types of tunable planar resonators, and tuning topologies, have emerged over the last five years, one of the oldest planar filters, i.e. the staircase filter, offers very attractive characteristics for the construction of tunable filters. This topology has therefore been at the focus of one of my research projects since 2015.

Tunable filters require a combination of resonators and tuning elements, the latter requiring biasing circuits. The humble, and very old, halfwave planar resonator, used in staircase filters, offers a very simple way to implement a tunable structure, with a varactor diode to ground being attached to each end, and a biasing circuit connected at some point on the resonator. The first step in our work on these filters was the development of a novel biasing circuit for such a tunable halfwave resonator, by my PhD student Dr Elmine Meyer and myself. This structure exploits the symmetry of fields, and the fact that the symmetry is unaffected by the change in resonant frequency [63], [64].

The basis of the biasing network is shown in Fig. 3.63, where the electric and magnetic fields on a resonant halfwave line are shown, together with the field orientations of a vertically connected biasing wire. Due to the orientation and the placing, the wire connects to a point of zero electric field on the line, with completely orthogonal magnetic fields. As neither of these fields change in position as the resonant frequency changes, the biasing line is *spatially decoupled* from the line for all frequencies. This is quite an advantage, as no extra circuitry is required, and the structure is theoretically of infinite bandwidth.

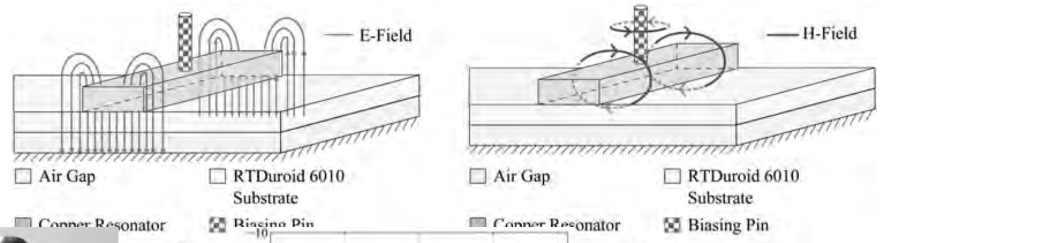

Figure 3.63: Spatially decoupled biasing principle (from [63])

The biasing structure was used to implement ... at 10GHz, as shown in Fig 3.64, where the varactors and the biasing lines, are shown as well as the ... uc-tion. Measured results for the filter, shown ... ing good insertion loss ...

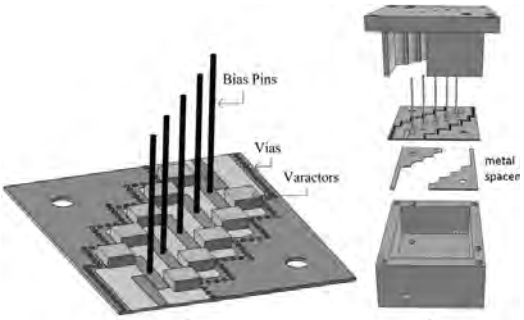

Figure 3.64: Tunable staircase filter using spatial decoupling (from [63])

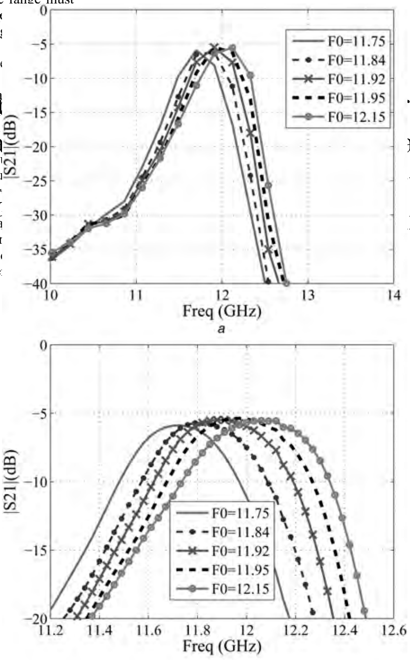

Figure 3.65: Filter measurements (from [63])

As filters are tuned over a frequency range, the bandwidth changes as well. For fixed absolute bandwidth systems, this is very undesirable, and an important part of tunable filter research has been focused on bandwidth control of these filters. The second phase of our work on tunable staircase filters was therefore a proposal for the control of the inter-resonator couplings. For this, my PhD student Dr Satyam Sharma and myself proposed a novel type of tunable inverter, based on a non-resonant-node (NRN) placed between resonators [65], [66].

The principle for this tunable NRN inverter is shown in Fig. 3.66, with the NRN realised by a short piece of line, terminated at both ends by a varactor diode to ground. The resulting equivalent circuit shows that a change in the varactor capacitance will result in change in the inverter value. As the coupling coefficient between resonators are directly controlled by this inverter constant, a tunable coupling is realised in this way.

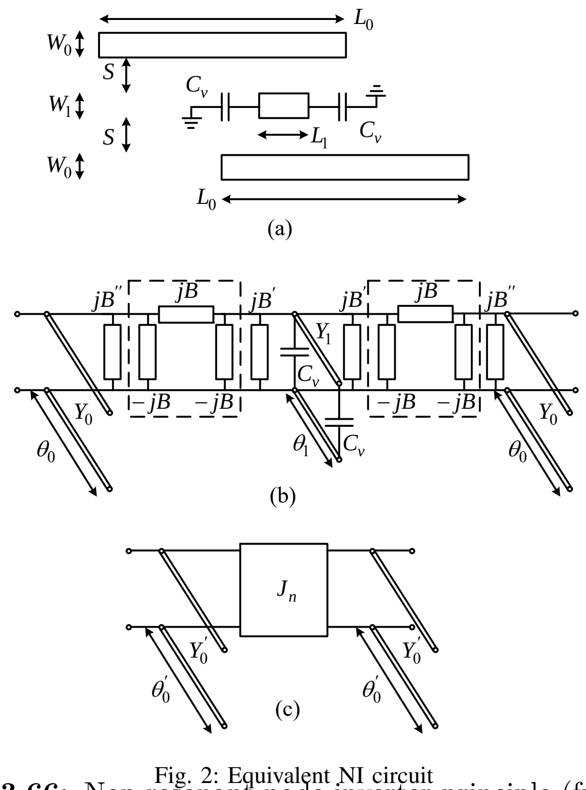

Figure 3.66: Non-resonant node inverter principle (from [65])

Fig.3.67 shows simulation results for the change in coupling coefficient as a function of the varactor capacitance, with very large range of coupling values clearly realizable. Unfortunately, such a structure will support a spurious resonance frequency as well, which will also be dependent on the varactor capacitance. This is shown in Fig. 3.68, and needs to be tightly controlled.

A set of tunable staircase filters, with tunable NRN inverters, and using the spatially decoupled biasing structure, was designed and tested, one of which is shown in Fig. 3.69. In order to compensate for the change in loaded q-values

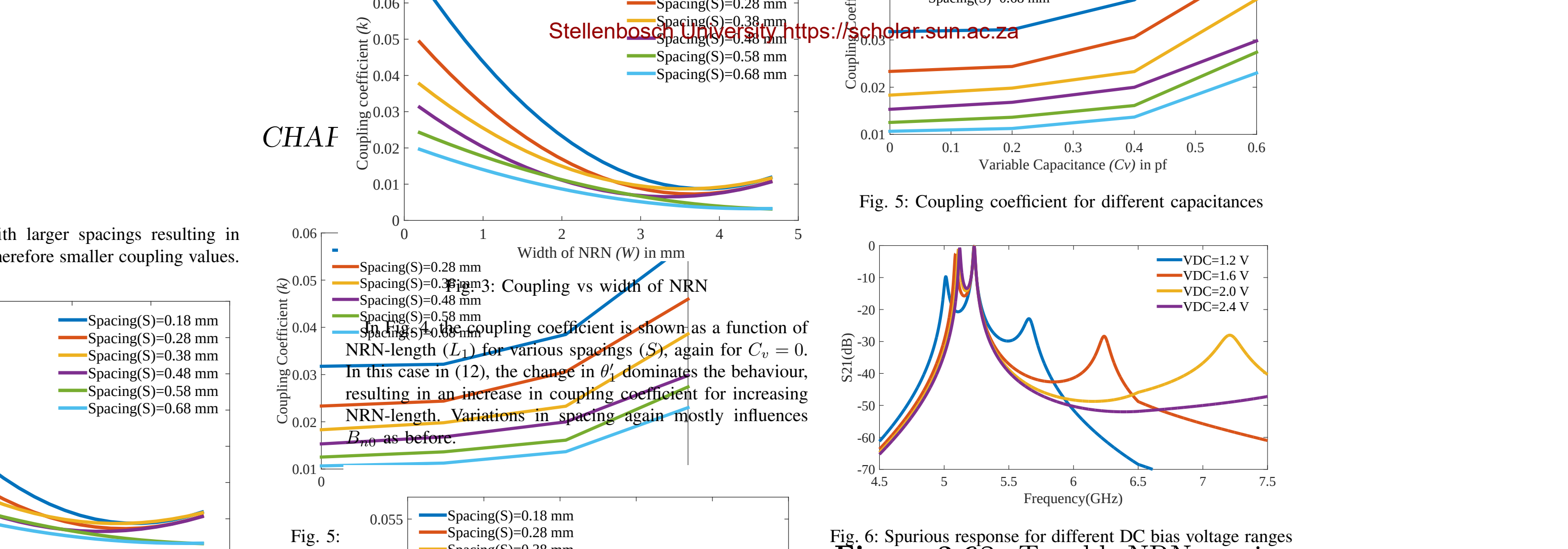

Figure 3.67: Coupling (

Figure 3.68: Tunable NRN spurious response (from [65])

at the input and output as frequency changes, these lines are also loaded with varactors. The measured results for a range of centre frequencies are shown in Fig. 3.70 and Fig.3.71. A tunable range of almost 1GHz is achieved, with a fixed bandwidth of 200MHz across the full tuning range. Insertion loss is on par for a filter of this nature, and return loss is acceptable across the whole tuning range. Fig. 3.72 shows the measurement if the centre frequency is kept constant, and only the bandwidth is tuned. A range of almost 1Hz can be achieved without spurious problems.

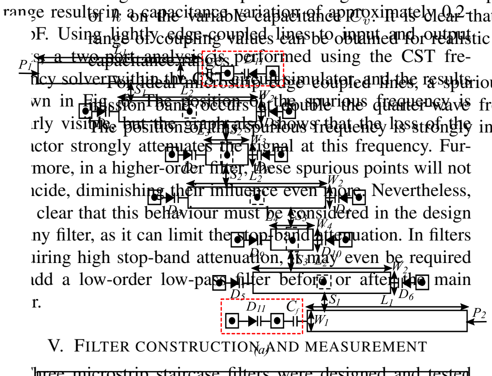

Figure 3.69: Tunable NRN Filter (from [65])

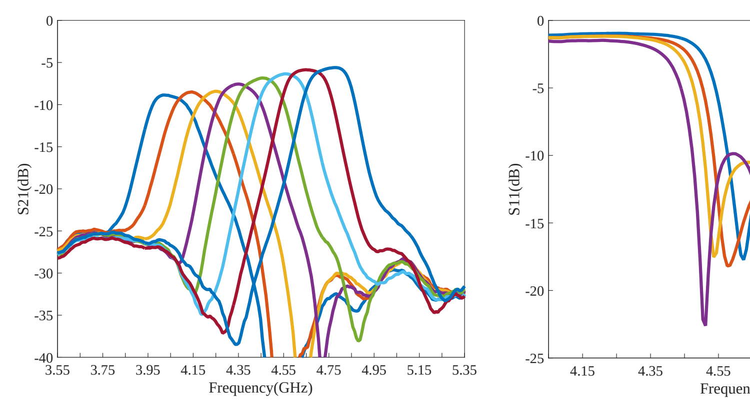

Figure 3.70: Tunable NRN filter measurements S21 (from [65])

This work showed that the classical staircase filter is an excellent candidate for tunable filter implementations. The symmetry of fields, and simple manufacturing possibilities for adding tunable components, as well as the very simple spatially decoupled biasing network, offer cost-effective manufacturing options. The tunable inverter based on an NRN represents the first implementation of such a structure, based on rigorous synthesis techniques.

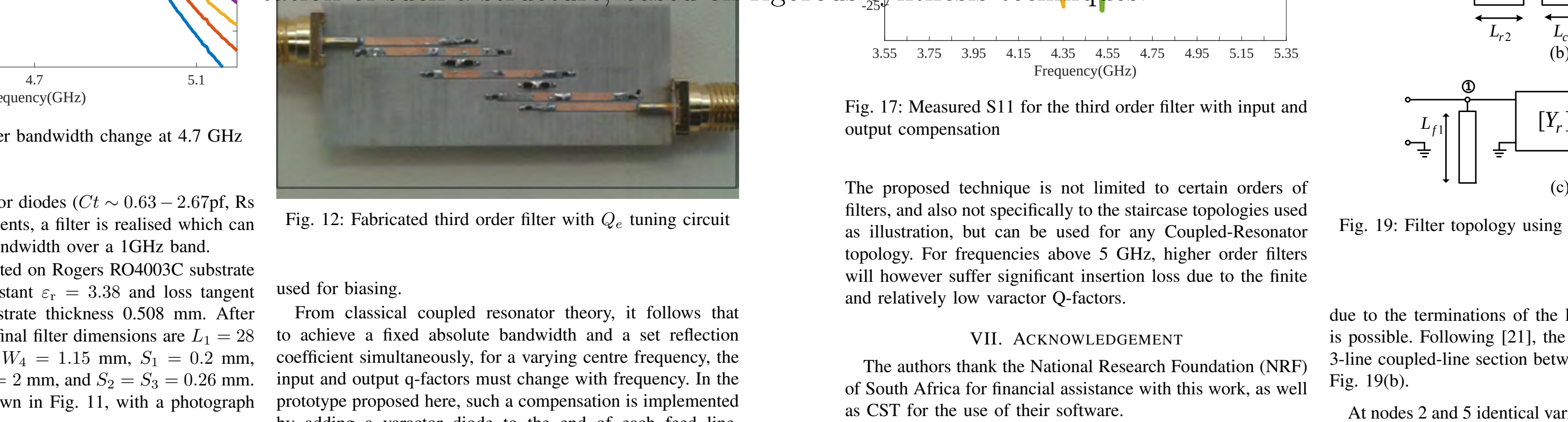

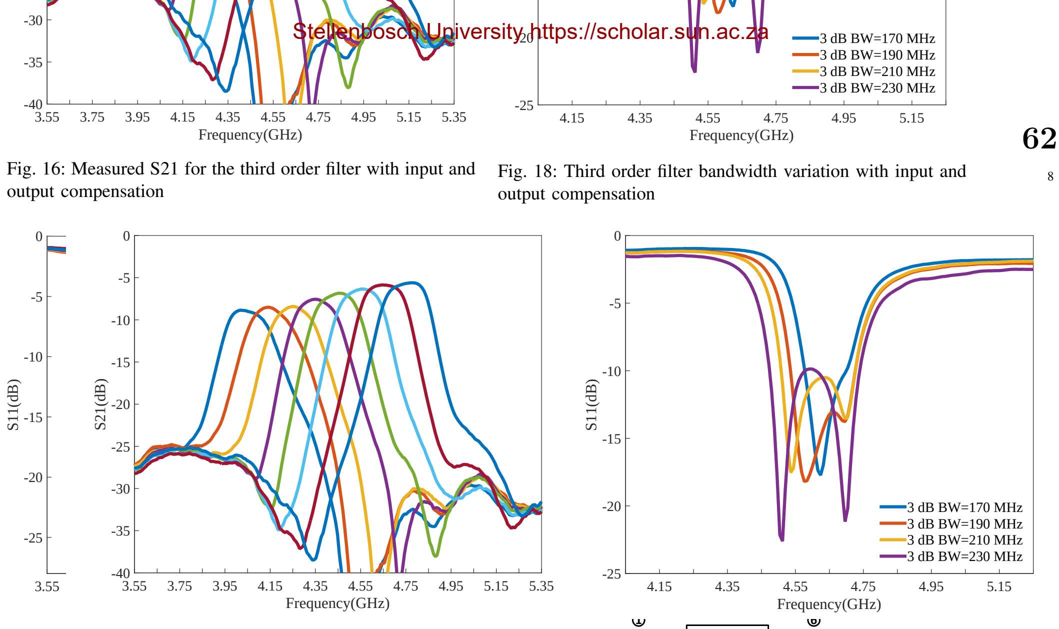

Figure 3.71: Tunable NRN filter meas

Figure 3.72: Tunable NRN filter measurements S11 (from [65])

3.7 Multi-band filters

Like tunable filters, multi-band filters have also received an enormous amount of attention in the filter research environment over the last decade, and for exactly the same reasons. However, whereas a tunable filter relies on a single-band design procedure, multi-band filters require a design approach which realises a number of pass-bands simultaneously. Three main approaches have been used to design these types of filters. Firstly, and also the simplest approach, is the interconnection of single-band filters. This approach typically results in larger structures, with performance degradation due to the interconnection structures. A second popular approach has been to use resonators with multiple resonances to create multiple pass-bands, with especially Stepped Impedance Resonators (SIR) proving to be quite popular. While centre frequencies can readily be controlled in this way, the control over pass-band bandwidths are challenging, especially for higher order filters. However, this technique has the advantages of small size and the ability to accommodate cases where there is a wide separation between the pass-bands.

The last, and most rigorous, methods to design multi-band filters are to either construct the approximation function to include multiple bands, and perform a standard synthesis, or to transform the approximation function and consequently the low-pass elements as well, to a multi-band one. The latter approach can also be viewed as an extension of the standard low-pass to band-pass transform. This approach makes it possible to design multi-band filters with pre-determined topologies and transfer functions, but has the disadvantage that the responses of all the bands are determined by the original prototype response.

In 2014, a rigorous theoretical background for the design of multi-band filters had not been established, and most designs relied on a mixture of approximate design and optimisation. Together with my PhD student Dr Gerdus

Brandt, we therefore set out to derive such a procedure. This led to a formal mathematical procedure to transform a low-pass transfer function of any form, to a multi-band one of arbitrary order, and with arbitrary bands, using no optimisation, and only exact transformations [67], [68].

The basic transformation problem is shown in Fig. 3.73, where a single-band, low-pass transfer function has to be transformed into a multi-band function with arbitrary band-edge frequencies.

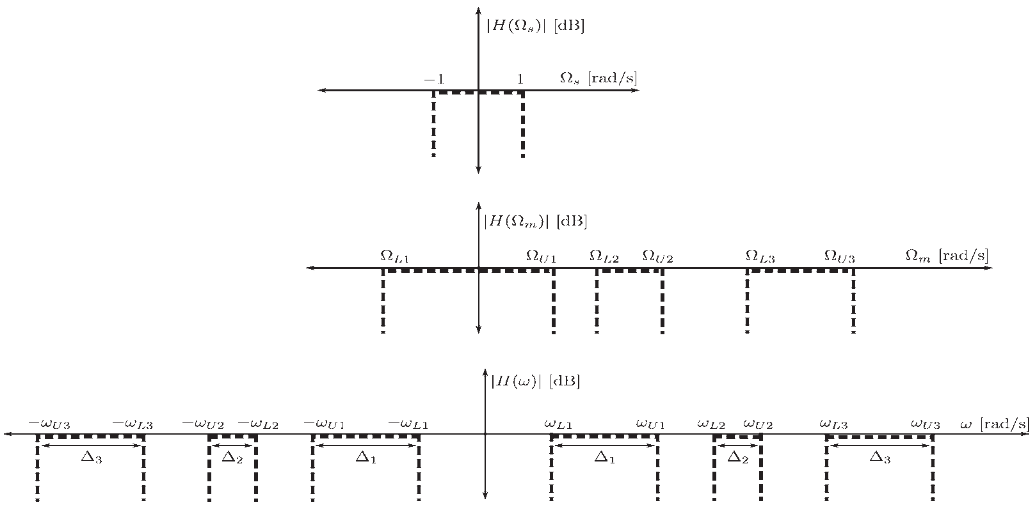

Figure 1 Low-pass to multiband response transformation using an unsymmetrical intermediate response.

Figure 3.73: Multiband frequency transform (from [68])

To find a function to do this is not trivial. For a pure polynomial, a minimum order Lagrange interpolation polynomial can for instance easily be constructed to map each band-edge as required. However, the behaviour of the function between these points can in this case not be specified, and the function can easily map parts of the low-pass stop-band into pass-bands. Both these aspects are significant drawbacks. To alleviate this, the order of the polynomial can be increased to create more degrees of freedom. This however becomes very difficult, as no new real-valued zeros are allowed. For higher order polynomials the behaviour of the function also becomes more complex, and the possibility of straying into forbidden regions becomes even higher. Optimisation of the polynomial coefficients therefore becomes necessary, and in many cases a solution does not exist.

In contrast, a rational fraction with poles and zeros offers a much improved mapping function, as the pole and zero positions can be specified separately. While an infinite number of rational functions can be constructed, we showed that the classical LC one-port reactance function can be used very effectively for this purpose, and is indeed an superb function to use, as it also maps

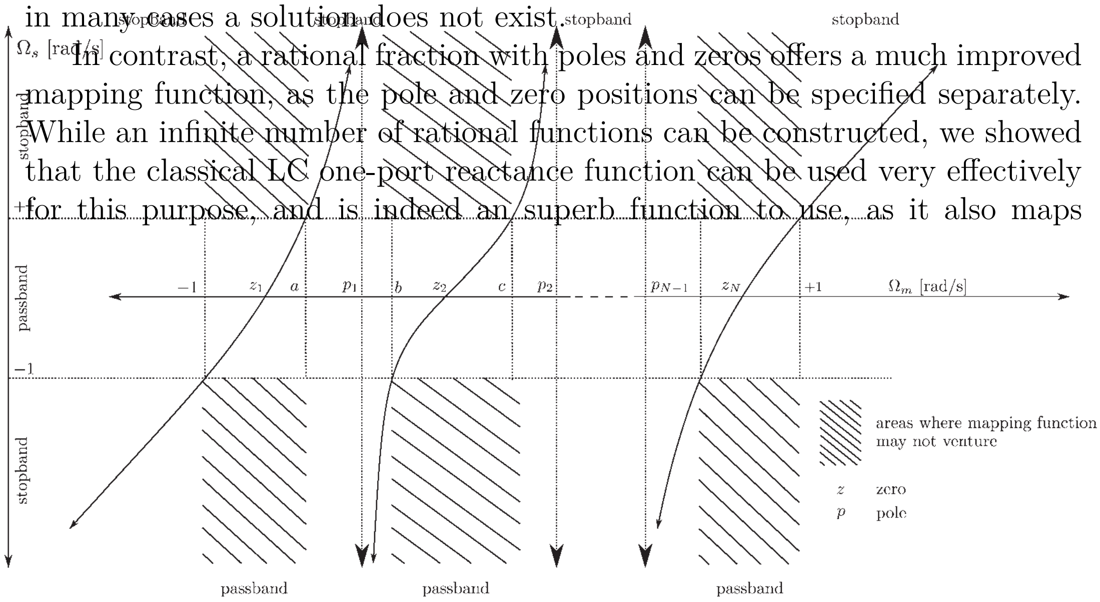

Figure 2 Graphical representation of the ideal frequency mapping function

reactive circuit elements only to other reactive circuit elements. Such a transformation function is shown in Fig. 3.74, with the corresponding element transforms in Fig. 3.75 and Fig. 3.76 and can be seen to be a high-order extension of the classical low-pass to band-pass transformation. The advantages of this transformation function are manifold, as discussed in [68].

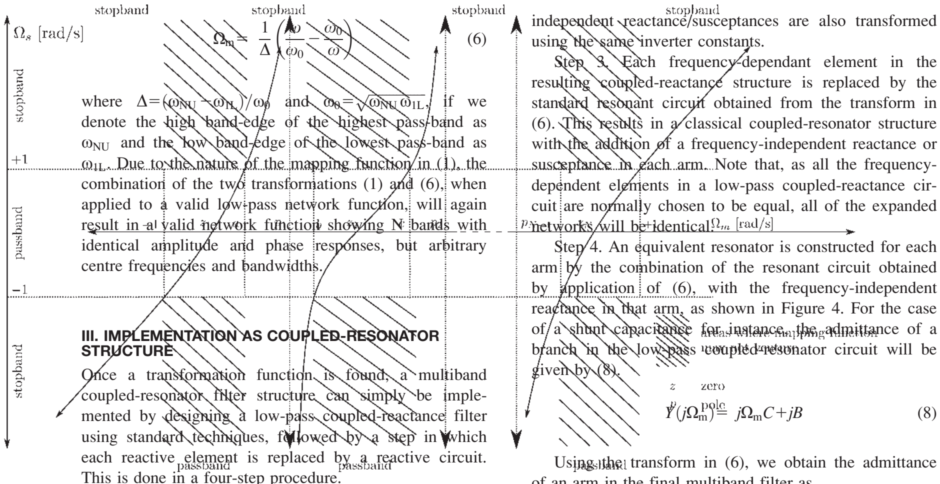

Figure 3.74: Multiband frequency transform function (from [68])

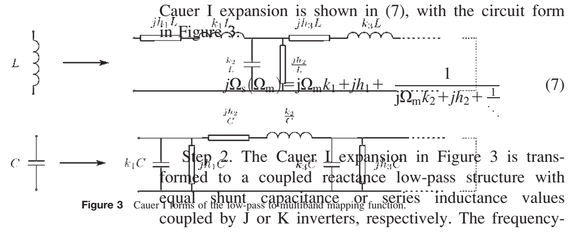

Figure 3.75: Multiband LC transform (from [68])

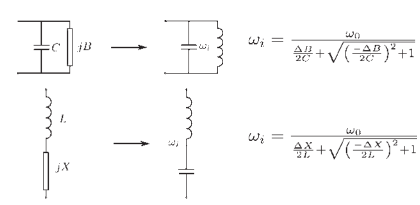

Figure 3.76: Multiband resonator transform (from [68])

The method was illustrated for various filters, with a triple-band one shown in Fig. 3.77, together with its ideal response in Fig. 3.78. As the transformation is exact, there is of course no theoretical limit on the number, or edge-frequencies, of the final network. The only limitation is that each band is an exact copy of the original low-pass transfer function.

The procedure was also applied to a triple-band waveguide filter, yielding the filter in Fig. 3.79, with simulated electromagnetic response shown in Fig. 3.80 [69].

As a practical example, a triple-band, twelfth-order filter, using coaxial resonators, was also designed and tested [67]. The filter layout and a photograph

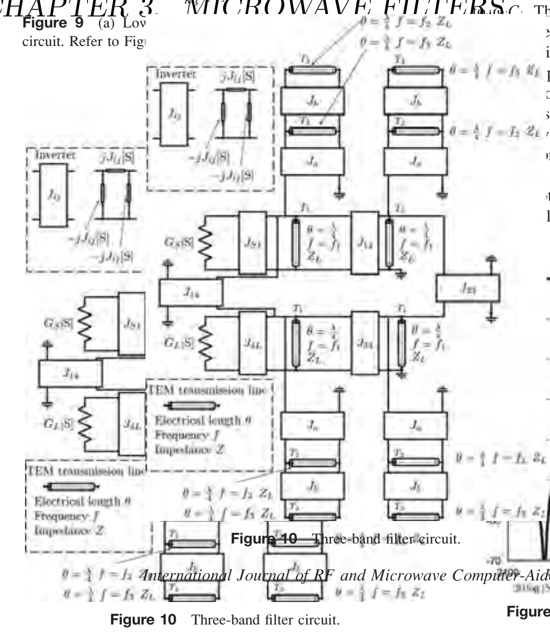

Figure 3.77: Multiband filter (from [68])

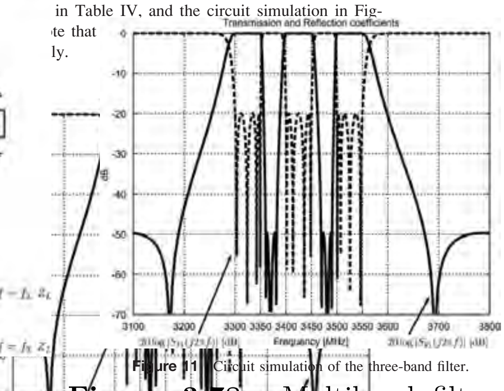

Figure 3.78: Multiband filter response (from [68])

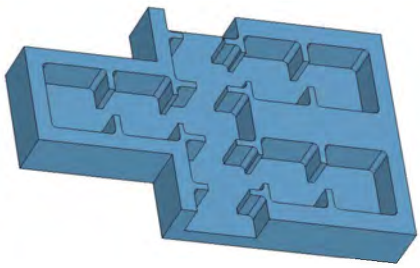

Figure 3.79: Multiband waveguide filter (from [69])

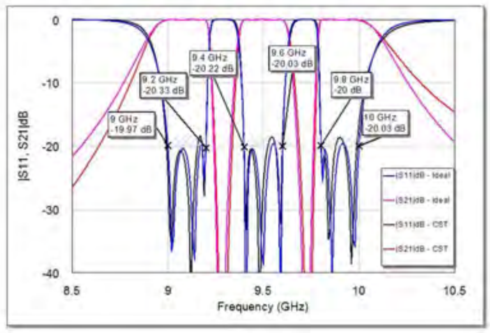

Figure 3.80: Multiband waveguide filter response (from [69])

is shown in Fig. 3.81 and Fig. 3.82, with the measured results in Fig. 3.83 and Fig. 3.84. One of the main drawbacks of these filters is clearly shown here, i.e. the effects of loss in at least one of the pass-bands. Another aspect which clearly emerged from the practical example, was the extreme difficulty in tuning such a multi-band filter, an issue which is largely ignored by the research community.

For me, the work on multi-band filters represents one of my best research efforts, as it provides a rigorous synthesis framework for a complete class of filters, and is inclusive of numerous published filters which were designed using partial versions of this theory. It is an elegant method, with virtually no theoretical limitations, and no special validity conditions beyond the normal ones of passivity and the absence of loss.

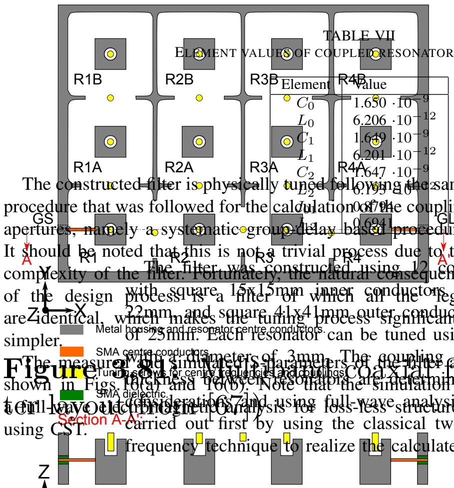

Figure 3.81: Multiband coaxial filter layout (from [67])

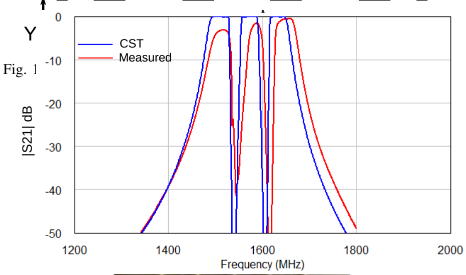

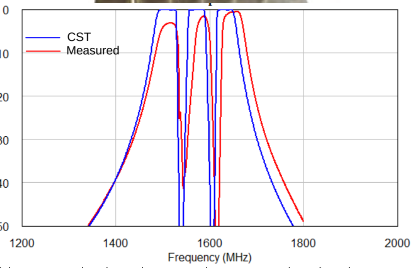

Figure 3.83: Multiband coaxial filter measurements(from [67])

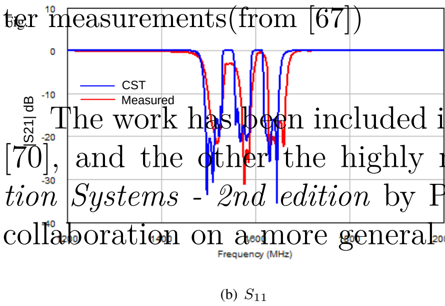

Figure 3.84: Multiband coaxial filter measurements (from [67])

The work has been included in two books: one as a chapter by the authors [70], and the other the highly regarded *Microwave Filters for Communication Systems - 2nd edition* by Prof Richard Cameron. The work also led to collaboration on a more general book chapter in multi-band filters [71].

3.8 Other Filters

Through the years, myself or myself with some students, designed a wide variety of filters which do not fit into any of the categories in this chapter. A few of them are discussed in this section (in no particular order), as they in some way present original ideas and concepts. While some of these have been published, a number was designed for commercial purposes, and therefore never published.

The first of these is a novel extension of the evanescent-mode PIN-diode switch from [72], using the same structure to create a tunable X-band evanescent-mode filter [64]. In principle, this is simply achieved by replacing the PIN-diodes with varactor diodes, as shown in Fig. 3.85. In practice however, a complete re-design is required, using a filter procedure instead of a switch design procedure. The measured results of a prototype filter are shown in

Fig. 3.86 ... nge is ... se frequenci... odes is ... loss mechanis... wave... in high inse... he lower end of the tuning range.

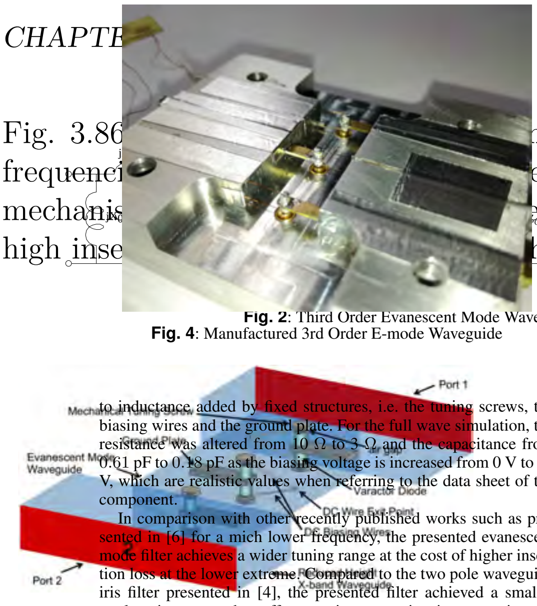

Figure 3.85: Tunable evanescent mode filter (from ...)

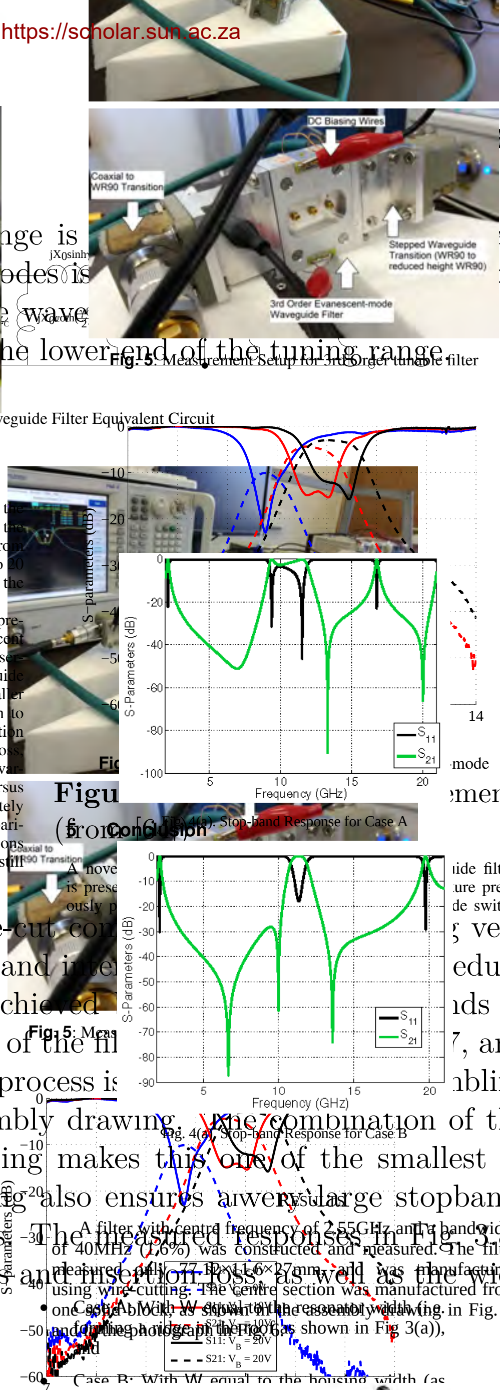

Figu... ments (fro...

A second interesting filter is a wire-cut co... very heavily end-loaded, square resonators, and inte... reduce the length [73]. The end-loading is achieved ... nds of the resonators into cut-outs in the roof of the fil... 7, and Fig. 3.88. The wire-cut manufacturing process is ... mbline filters, as shown in the exploded assembly drawing. The combination of the end-loading and inter-resonator shielding makes this one of the smallest S-band filters published. The end-loading also ensures a very large stopband, as compared to normal combline filters. The measured responses in Fig. 3.89 and Fig. 3.90 show the good return loss and insertion loss, as well as the wide stopband.

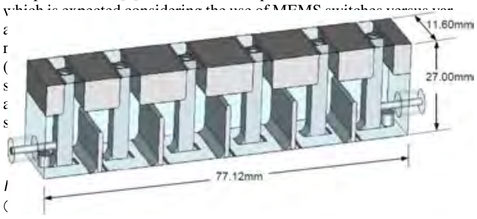

Fig. 2. Modified Combline Structure

Figure 3.87: Miniaturised combline filter structure (from [73])

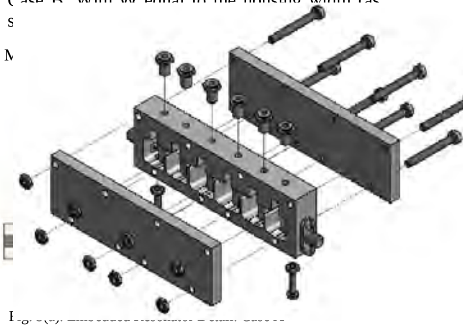

Fig. 5. Filter Construction

Figure 3.88: Miniaturised combline filter (from [73])

More importantly, the issue of pass-band separation is addressed. Combline filters are known for the favourable property of extending the stop-band by reducing the lengths of the resonators and loading it with end-capacitances. This is normally achieved by simply reducing the space between the housing and the ends of the resonators in Fig.1. However, for applications requiring very wide stop-bands, the line lengths have to be reduced by large fractions, and the end-gaps become so small that mechanical tolerances become a significant problem. For the filter presented here, the stop-band requirement called for resonators with electrical lengths of smaller than 40 degrees, resulting in end-gaps of smaller than 0.1mm. To alleviate this problem, the end of each resonator is 'inserted' into a lowered roof, as shown in Fig 2. This allows for significant increases in end-capacitance without any of the gap dimensions becoming too small.

While obvious, it is nevertheless worth noting that the advantages of the proposed changes would be difficult to achieve when using cylindrical resonators, as the end-capacitances will be reduced significantly for equivalent gap dimensions. The use of square resonators also enables the manufacturing process of wire-cutting to be utilized to good effect, allowing the complete central part of the structure to be cut from one piece of metal. This is shown in Fig 5, and is highly advantageous, as very high accuracy of the critical dimensions can easily be achieved.

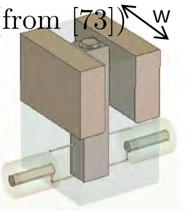

Fig. 3(b). Embedded Resonator Detail: Case B

For both cases, the resonator was coupled to input and output ports, and tuned to the same resonating frequency. Using CST Microwave Studio, wideband transmission responses were simulated, with the results shown in Figs. 4(a) and (b). The difference is quite marked. For Case A, the attenuation starts declining at frequencies just over 7GHz already, with the lower edge of a well-defined second pass-band occurring at 9.5GHz. For Case B, the lower edge of the second pass-band only occurs at 11.3GHz, an increase of

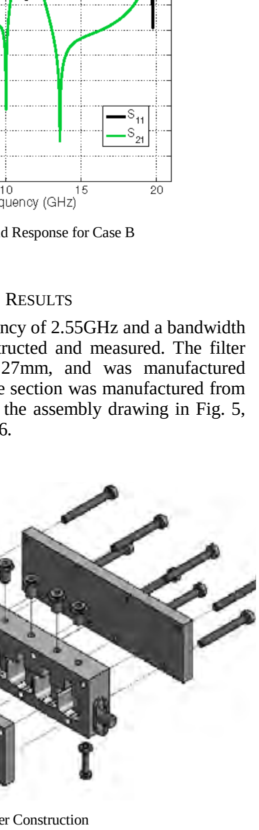

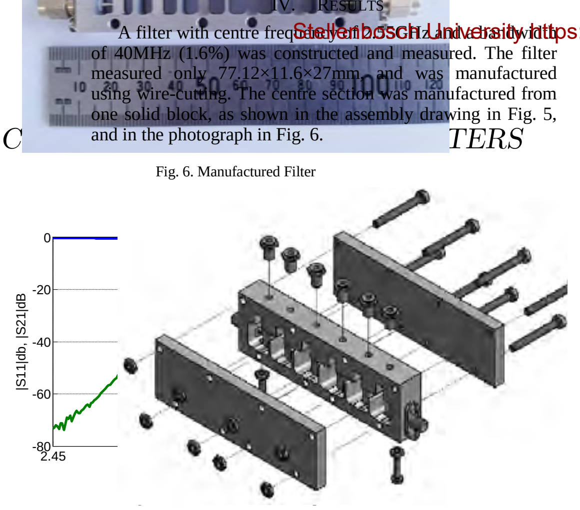

Figure 3.89: Miniaturised combline filter measurements (from [73])

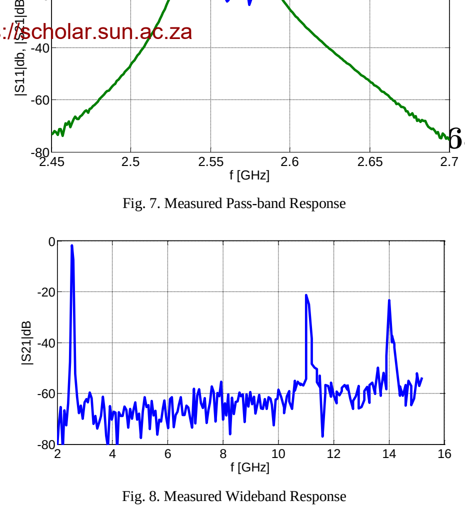

Figure 3.90: Wideband measurements (from [73])

One of the very interesting filter requirements in the last decade, stemmed from the receivers required for the Square Kilometre Antenna (SKA) project. As pre-cursor to the SKA, two smaller projects were first launched by the South African government, namely the Karoo Array Telescope (KAT), a one-dish, L-band demonstrator, and KAT7, a seven-dish extension of KAT. For both, the receivers required extreme magnitude flatness over frequency. As the filters in the receive chains have the strongest influence of overall system amplitude flatness, the required filters demanded very flat magnitude responses, in addition to wide bandwidths. The first solution for KAT is shown graphically in Fig. 3.91, and consisted of a basic combline filter with cylindrical rods, but tuned for insertion loss flatness at the expense of return loss. The measured results are shown in Fig. 3.92 and Fig. 3.93, where a 0.1dB insertion loss flatness was achieved over the band. The negative on the return loss, inherent to this type of design, is also clearly visible.

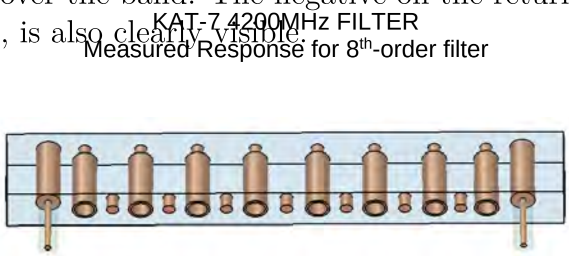

Figure 3.91: Combline filter for KAT receiver

For the second iteration of KAT, KAT7 had even more stringent specifications, with bandwidth, together with amplitude flatness, posing a very challenging problem. A very old structure, using parallel halfwave lines, spaced at half wavelengths, was used in this case, as shown in Fig. 3.94 and Fig. 3.95. Again, the measured results in Fig. 3.96 and Fig. 3.97 show the very flat amplitude response over the full band. In this case, as the filter was quite lossy due to the substrate, the return loss is significantly better, at the expense of insertion loss.

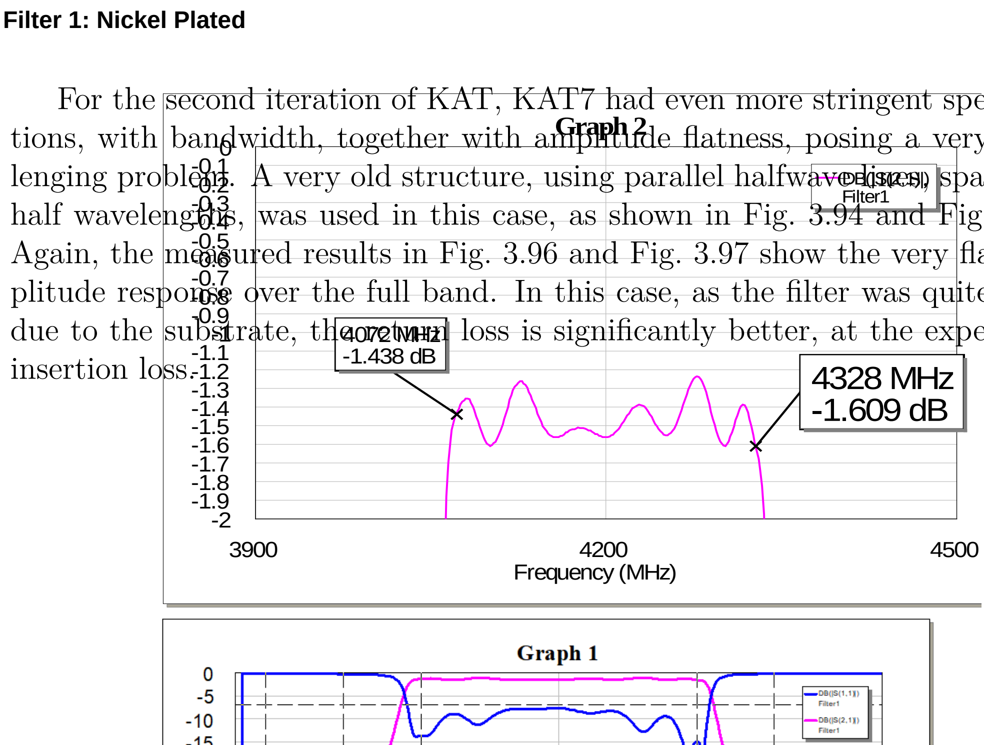

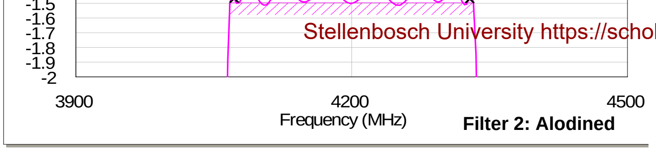

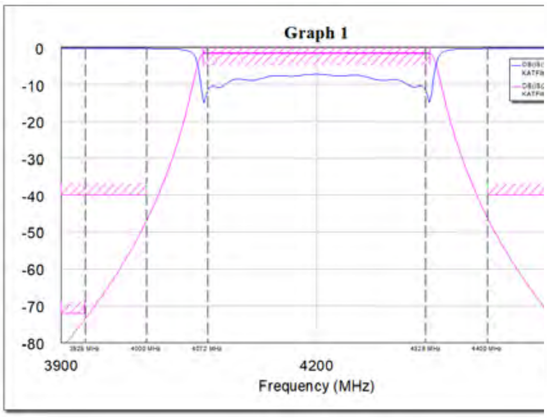

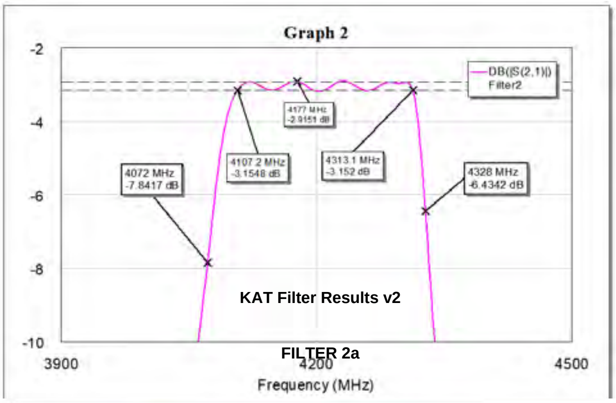

Figure 3.92: KAT combline filter measurements)

Figure 3.94: KAT7 filter photograph)

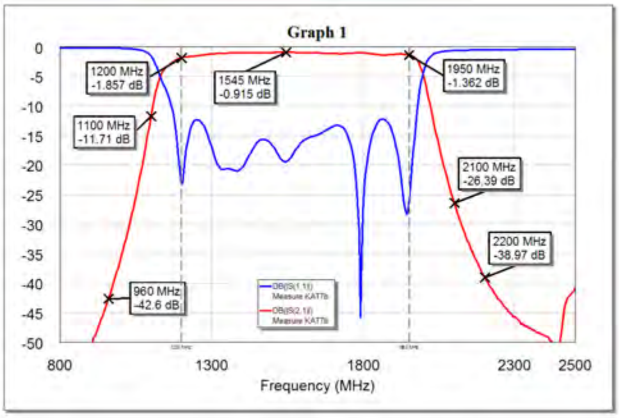

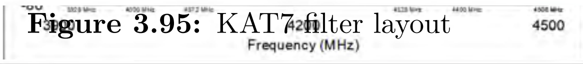

Figure 3.95: KAT7 filter layout

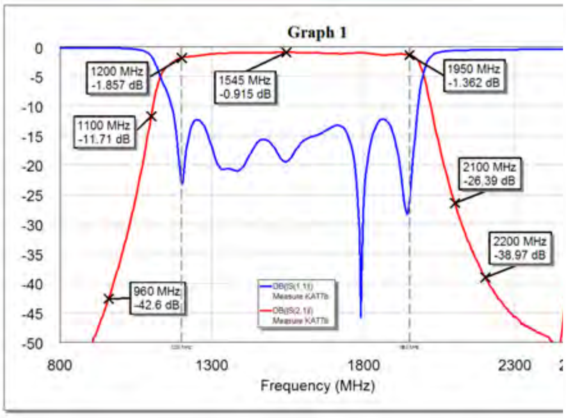

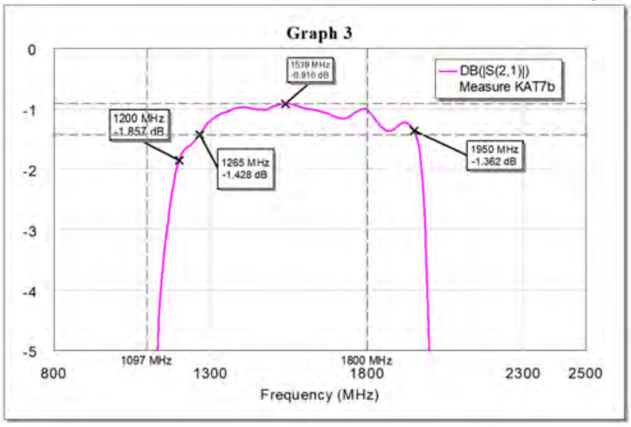

Figure 3.96: KAT7 combline filter measurements)

Figure 3.97: KAT7 filter measurements

I have also designed a wide variety of diplexers for commercial purposes, a few of which are discussed below. The first is a dual-mode cylindrical waveguide diplexer, using iris-coupled dual-mode resonators. The challenge here was the close proximity of the bands, and the sharp roll-off, which could only be achieved by waveguide. The filter and the measured performance are shown in Fig. 3.98.

The second diplexer is at a much lower frequency, and was interesting due

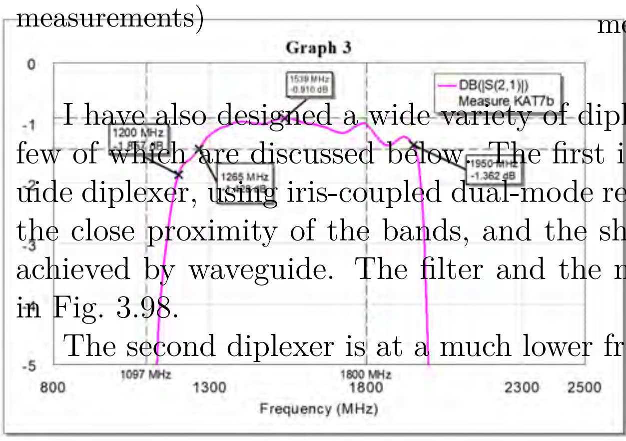

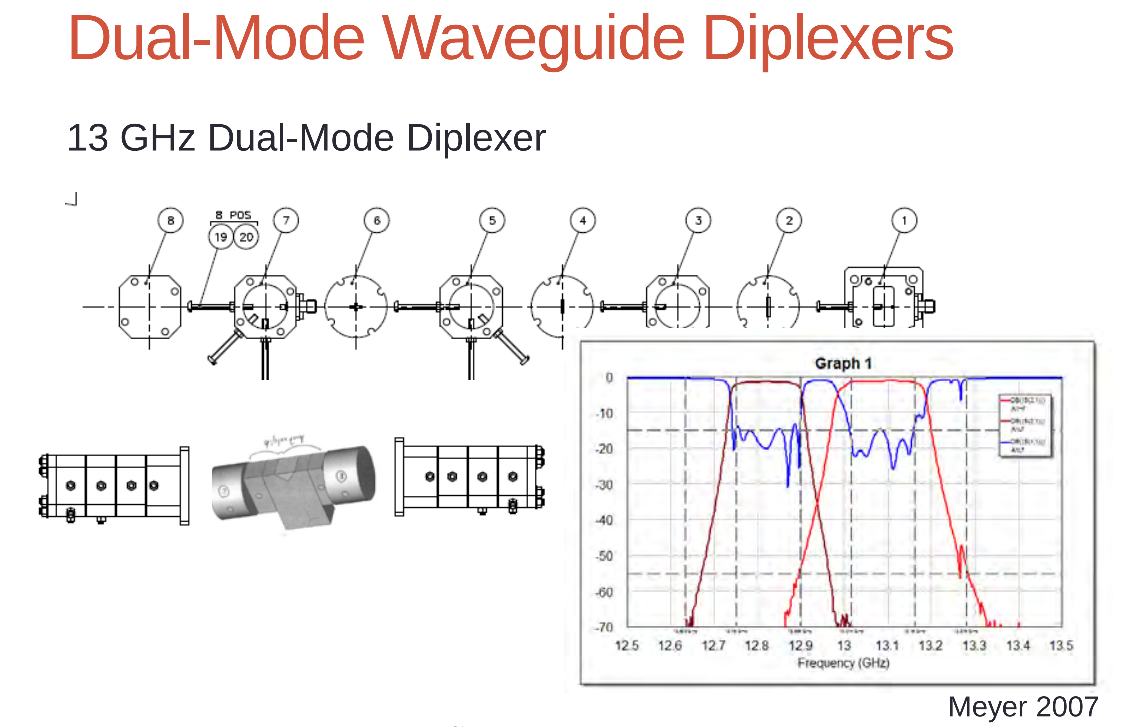

Figure 3.98: Cylindrical waveguide diplexer

to the specific space envelope available, which called for a shallow and wide design. The resulting diplexer consisted of two combline filters lying in the same plane next to each other, and coupled to a central port through one half-wave input line. The input coupling is quite novel, as it exploits the mirror arrangement of the combline filters. the filter is shown diagrammatically in Fig. 3.99, with the measured results in Fig. 3.100 and Fig. 3.101. A zoomed-in measurement shows the good insertion loss characteristics of the filter.

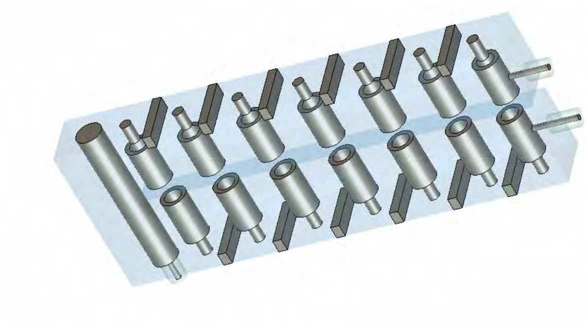

Figure 3.99: Combline diplexer

The final diplexer, and final filter in this chapter, represents the most challenging filter I have designed over my career. The filter consists of two 8th-order coaxial filters, each with three cross-couplings, which creates asymmetric transmission zeros on the high-band and low-band sides of the two filters respectively. The space envelope was extremely small, and the design pushes the

CBACS Diplexer Measurement

Measurement with light clamping on output ports

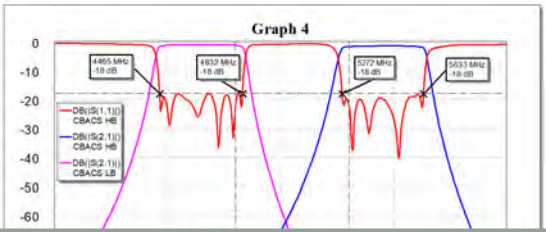

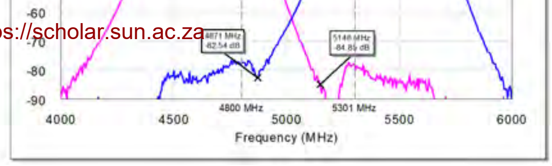

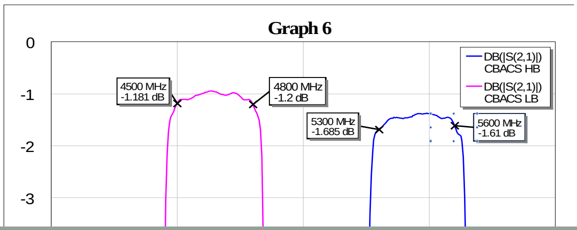

Coaxial Diplexer

4GHz Diplexer

2x 9th order with asymmetrical transmission zeros

Positive and Negative Triplets

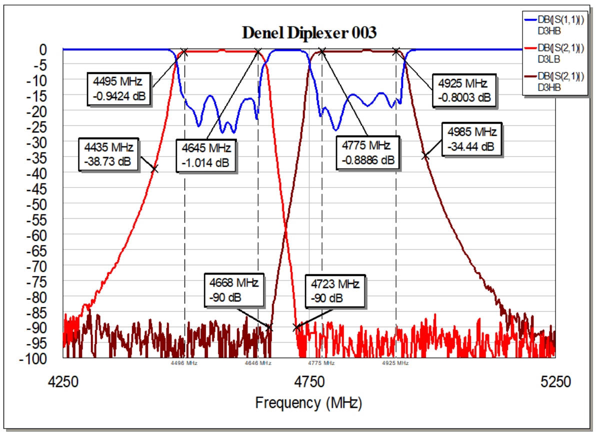

Meyer 2010

Figure 3.103: Coaxial diplexer measurements

My commercial filter work involved me in the local industry in a way that no research activity could do. It exposed me to a variety of projects and systems, and allowed me to work closely with extremely talented engineers with decades of experience. It also showed me that some of the toughest research problems originate in industry. In terms of technical aspects, whereas a research project needs only present proofs-of-concept, commercial prototypes need to work exactly to specifications. This is a significant difference, and has often exposed a lack of understanding of the subtleties or fundamentals of a particular piece of theory in my armoury of knowledge.

3.9 Conclusion

Microwave filters have been, and currently still are, one of the main pillars of my professional career, in terms of both research and industrial involvement. The combination of requirements on structural and electrical design, electromagnetic analysis, modelling, and optimisation, created numerous opportunities for innovation over the years. The explosion in personal communications over the last decade has increased the pressure on the available spectrum by orders of magnitude, making the role of filters more and more important. With the 5G-standard set to dominate communications for the next decade, the need for filters will increase even more. In addition, integration of antennas, amplifiers and filters is set to become one of the most important system requirements, calling for new design techniques and new measurement techniques. Massive integration will also in all likelihood more and more require non-traditional design and manufacturing techniques.

Due to our long history of development in this field, my group has established itself as the primary filter group in South Africa, with virtually all the filter designers in local industry being graduates from the group. Internationally, the group is involved with a number of other groups, and international companies. My activity on filters is therefore set to continue into the next decade, and in all likelihood until the end of my career.

Chapter 4

Passive Devices

4.1 Introduction

In terms of passive devices, microwave systems not only require filters, but a large variety of different signal control devices, such as switches, power dividers and combiners, couplers, matching networks and transitions between guiding structures. My work has included a number of these over the years, mostly as a result of requirements by the local Radar industry.

4.2 Matching networks

So-called *finline* structures became very popular in the 1990's as a way of inserting lumped components into waveguide. A typical single-sided finline is effectively a slotline on a substrate, which is inserted in the E-plane of a waveguide. As the substrate is typically quite thin, a very low-loss structure is obtained, but with the ability to add components across the slot.

For general applications, the use of finlines normally requires transitions between empty waveguide and the finline. As with normal planar structures, both stepped quarter-wave sections and smoothly tapered sections work well for finline. However, in waveguide these structures can become quite long. A classical exponentially tapered finline transition, also showing a stepped section created by cutting out a quarter-wave section of the substrate at the interface with the empty waveguide, is shown in Fig. 4.1.

I started work on the problem of finding optimal finline taper profiles in 1998 with the help of a Master's degree student, Mr JC Kruger (who qualified as a clinical psychologist after completion of his Master's degree, and is currently a practising professional psychologist). In this work, simple tapers such as exponential, linear, single circular arc and double circular arc tapers were experimentally investigated [74], [75]. This formed the starting point of work by myself and a student who was at that stage only an undergraduate final year student, Dr Chris Vale. The aim was to find an optimisation procedure

ICROWAVE THEORY AND TECHNIQUES, VOL. 47, NO. 12, DECEMBER 1999 2467

which would allow for almost completely arbitrary slot-width profiles, with the only restriction being that they be smooth. This type of structural optimisation typically uses a high number of unknowns, and is a common problem in any taper design. Furthermore, the numerical analysis of finline at that stage was still quite time-consuming, and when combined with the optimisation of 20-50 variables, became intractable very quickly.

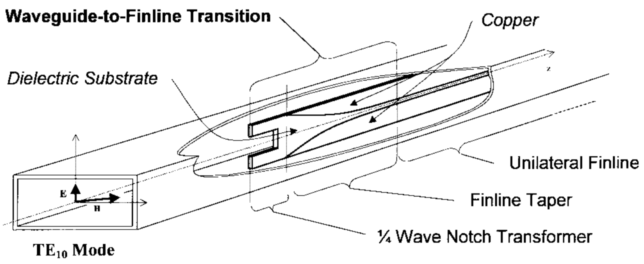

Fig. 1. Typical finline taper.

Figure 4.1: Waveguide to finline transition (from [76])

The proposed solution was a two-step process [76],[77]. For the inner process, a new optimising procedure which exploited a simplified form of the reflection coefficient, the so-called *VR-optimiser*, was proposed. For smoothly varying tapers, the theory of small reflections yields an integral of the form

$$\rho(\omega) = \frac{1}{2}\int_0^L \frac{\partial}{\partial z}\left[\ln[Z_0(z,\omega)]\right] \cdot e^{-2j\int_0^z \beta(\zeta,\omega)\,d\zeta}\,dz = \int_0^L M e^{j\theta+n\pi}\,dz \tag{4.1}$$

where $Z_0(z,\omega)$ is the impedance profile as a function of frequency and the distance along the line, and β the propagation constant. The integrand can clearly be viewed as a phasor (or vector). The proposed optimiser, instead of calculating the full integral, simply calculated a set of these vector values along the length of the line and then attempted to reduce the largest one during one iteration. This process is illustrated in Fig. 4.3.

For the outer optimisation loop, a process using progressively more variables, the so-called *focusing technique*, was proposed. With each variable a value of the slot-width at a certain distance along the line, the widths in between are calculated from spline interpolations between the points. Once a minimum for a set number of variables is reached, the number of variables, and thus the complexity of the taper, is increased. This is illustrated in Fig. 4.2.

The process worked extremely well, and yielded tapers significantly shorter than what was available at the stage. Two results are shown from the IEEE Transactions paper [76] in Fig. 4.4, which shows a taper just longer than a half-wavelength at 10GHz, and Fig. 4.5, which shows a taper of which the full length is shorter than one half wavelength.

This paper presents a novel two-step optimization algorithm for the design of finline tapers. The first step relies on a systematic increase of variables, similar to the method used by Kozak *et al.* [6], while the second step exploits the vector nature of the integral formulation of the reflection coefficient of smoothly varying tapers, as derived by Collin [7]. The algorithms are evaluated with respect to convergence and sensitivity to starting values, and are shown to be robust and to display stable minimization behavior for any number of variables. As examples, four X-band tapers are shown with their measured results: two very short tapers of $0.47\lambda_0$ and $0.67\lambda_0$ at 8 GHz (17.5 and 25 mm, respectively), and two tapers illustrating how the air–dielectric interface can be included in the optimization, with one taper compensating for the nonideal behavior of the notch transformer, and one taper compensating for a straight air–dielectric interface. The latter still displays a reflection coefficient of better than 30 dB across the 8.1–10.9-GHz band, despite having no notch transformer.

II. Two-Step Optimization Procedure

The taper shape is defined as the curve described by cubic interpolation between an arbitrary number of variable gap-width values spaced equally along the length of the taper. The more variables chosen to describe the taper shape, the more arbitrary the taper shape may become. A method of arbitrary taper analysis is therefore required which not only executes very quickly, but also provides accurate results. For the purposes of this paper, the standard formula for the reflection coefficient of smoothly varying tapers [7], shown in (1), is used with ρ, the reflection coefficient, Z_0 and β, the characteristic impedance and propagation constant, respectively, z the length along the taper, ℓ the total taper length, and ω the frequency in radians per second

$$\rho(\omega) = \frac{1}{2}\int_0^{\ell} \frac{\partial}{\partial z}\Big[\ln\left[Z_0(z,\omega)\right]\Big] \cdot e^{-2j\int_0^z \beta(\zeta,\omega)\,d\zeta}\,dz. \tag{1}$$

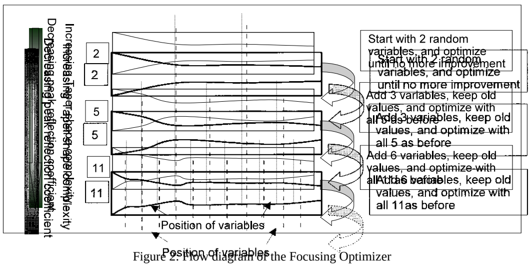

Figure 4.2: Focussing optimiser (from [76])

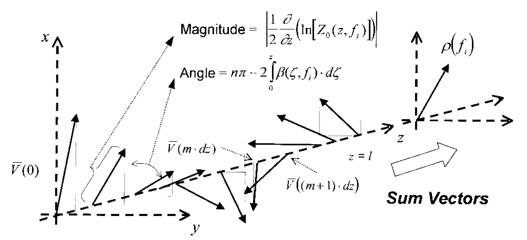

Figure 4.3: VR optimiser (from [76])

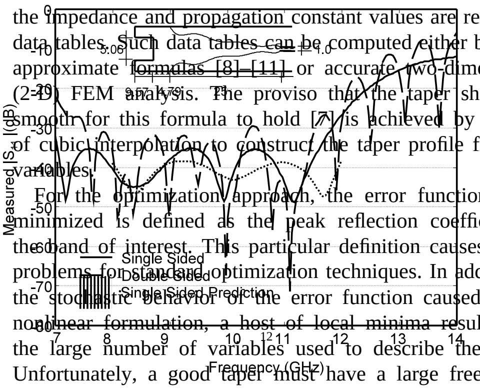

Figure 4.4: Finline taper measured results for a 25mm taper (from [76])

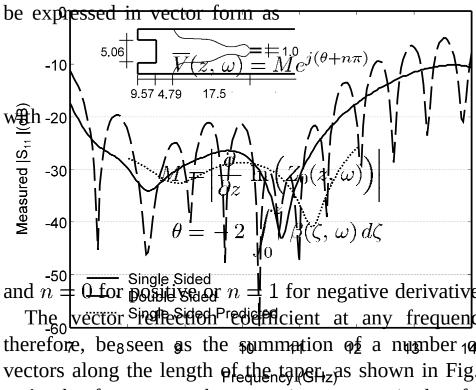

Figure 4.5: Finline taper measured results for a 17.5mm taper (from [76])

This work represented some of the first work on structural optimisation in microwave planar design, which allowed for continuously variable, random profiles. This would become very popular over the next decades as the capabilities of computer codes increased. It showed that the exploitation of mathematical forms can yield superior results, and proposed an approach for optimisation problems with high numbers of variables.

This project was particularly satisfying as it was the first and only IEEE MTT Transactions paper I published from undergraduate work. Dr Vale would subsequently do a PhD, at the completion of which he would be awarded the Stellenbosch University Chancellor's medal.

4.3 Directional Couplers

In addition to work on finline tapers, Mr Kruger's Master's work also included work on waveguide directional couplers [75]. By accident, I had discovered previously that traditional Bethe-hole couplers showed enormous improvements in coupling bandwidth when the waveguide roof was lowered. Mr Kruger investigated this in detail, using the classical Moreno crossed-slot, crossed guide coupler, as shown in Fig. 4.6. For analysis, we used one of the first versions of Ansys, an EM analysis software package which was derived from a FEM structural analysis package.

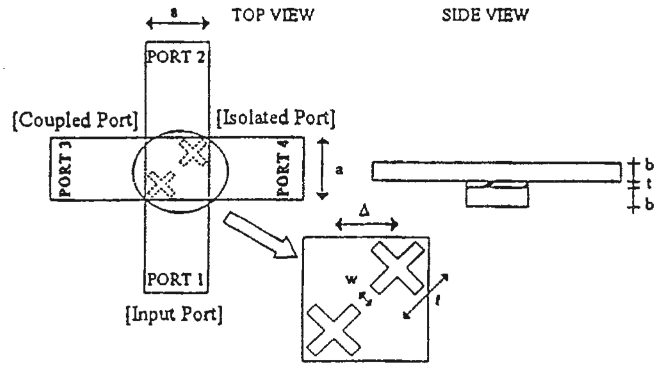

Figure 4.6: Moreno crossed-slot directional coupler (from [78])

Figure 1: Crossed-Guide Coupler with Dimensions

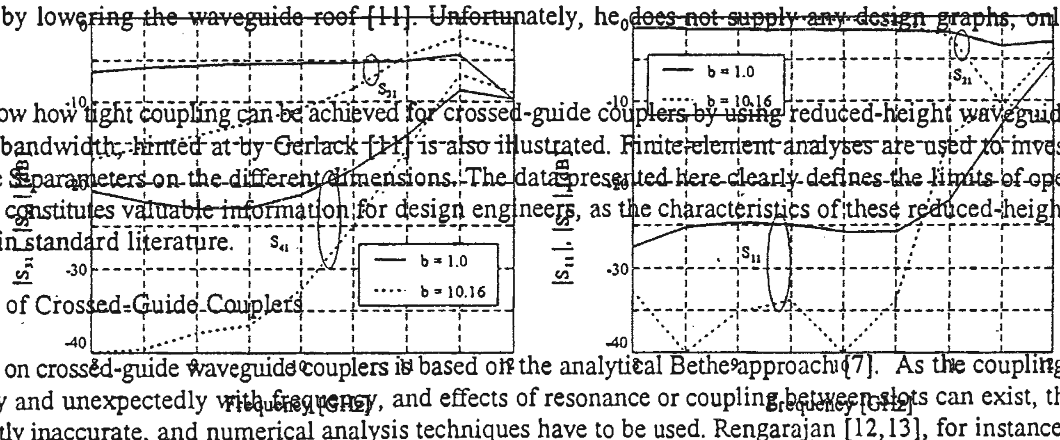

Figure 2: Effect of waveguide height: a=22.86, t=0, Δ=11.43, w=1.0, ℓ=12.0

Figure 4.7: Bandwidth comparisons for couplers with different roof heights. S_{11} is the reflection, S_{21} the through path, S_{31} the coupled path, S_{41} the isolated path, and b the waveguide height. (from [78])

What was singularly problematic of this software, was that no delete function was available in the drawing interface, which meant any mistake, or change in dimensions called for a redrawing of the complete structure!

Fig. 4.7 shows the simulated S-parameters for full-height and reduced-height crossed-slot, crossed-guide Moreno couplers [78]. It is evident that a coupler with a lowered roof (1mm height instead of the standard 10.16 mm for

1. Introduction

Directional couplers [1, 2] are finding increased usage in the design of dividers/combiners for distributed power amplifiers [3, 4, 5]. Waveguide couplers seem particularly attractive due to their low losses [6]. Unfortunately, these dividers utilize coupling values up to -3dB. The difficulties in achieving coupling values this high are evident from many of the referenced papers. In general, tight coupling is only achieved by the use of multi-aperture couplers.

A basic waveguide coupler consists of two waveguides joined by a mutual aperture, for instance a hole in the common broad wall. The most popular types are inline broadwall couplers, able to achieve coupling over large bandwidths. However, they are very bulky because of the large numbers of apertures needed. The crossed-guide coupler shown in figure 1 offers very compact size but smaller coupling values. Most couplers use crossed slots as coupling apertures due to the improved directivity [7].

Design data on waveguide crossed-guide couplers is readily available for coupling values of up to -15dB [8, 9, 10 and various engineering handbooks]. For higher values, no data exists in standard literature. Only one author describes a way of obtaining tighter coupling by lowering the waveguide roof [11]. Unfortunately, he does not supply any design graphs, only a single example.

This paper will show how tight coupling can be achieved for crossed-guide couplers by using reduced-height waveguide. A large improvement in bandwidth, hinted at by Gerlack [11] is also illustrated. Finite-element analyses are used to investigate the dependence of the S-parameters on the different dimensions. The data presented here clearly defines the limits of operation for these couplers and constitutes valuable information for design engineers, as the characteristics of these reduced-height couplers are not available in standard literature.

2. Characteristics of Crossed-Guide Couplers

Most existing data on crossed-guide waveguide couplers is based on the analytical Bethe approach [7]. As the coupling can vary quite considerably and unexpectedly with frequency, and effects of resonance or coupling between slots can exist, this type of analysis is frequently inaccurate, and numerical analysis techniques have to be used. Rengarajan [12,13], for instance, presents an analysis of resonant slot coupling, but no analyses are available for directional couplers. A Finite Element (FEM) technique (Maxwell Eminence from Ansoft) was used for this paper to accurately investigate the characteristics of these couplers.

A number of interesting properties will be illustrated in this paper, the most important being the influence of waveguide height shown in figure 2. For the same slot length, the coupling for the reduced height case changes by 1dB from 8 to 11 GHz, while for full-height the change is 15dB. In addition, the coupling value at 10GHz is approximately 7dB higher for the reduced height case. However, an increase in coupling forces an increase in reflection and a reduction in directivity. Other properties to be discussed in this paper are the effects of slot length, cross separation and wall thickness.

3. A Prototype Coupler - Analysis and Measurements

The results of a three-level coupler with guides crossing on both top and undersides of the main guide, is shown in fig... Measurements and predicted responses include a coaxial to waveguide transition at each port. Port 3 is the input port, ... and 5 the coupled ports, and ports 2 and 6 the isolated ports.

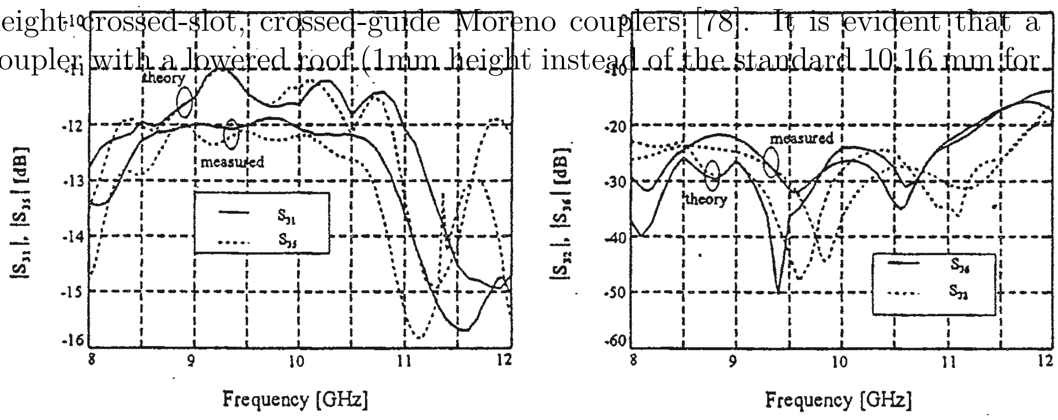

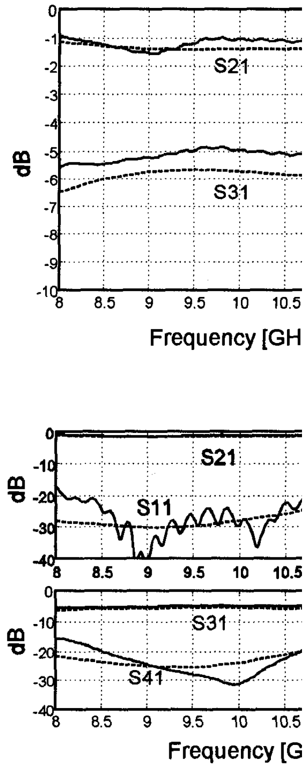

Figure 4.8: Two-layer measured results for 11mm (from [79])

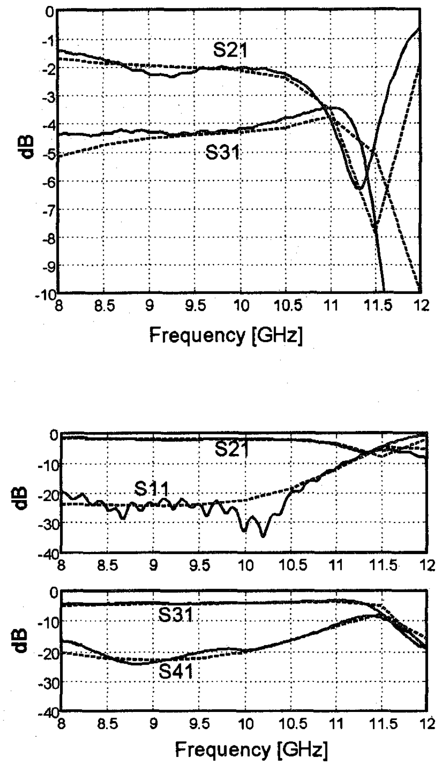

Figure 4.9: Two-layer crossed-slot measured results for 12mm slots (from [79])

X-band guide) creates a coupler with almost constant coupling over a 8-11.5 GHz band. (Note the coarse frequency interval of 0.5GHz – this was the finest interval for an analysis to fit into half a day.) A large set of experimental structures was constructed and tested, and reported at the 1998 IEEE IMS conference [79]. Some of the measured results are shown in Figs. 4.8 and 4.9.

Due to the excellent performance of the reduced-height coupler, the work was extended to that of a three-layered structure, with two reduced-height guides crossing a third reduced-height guide on both broadwalls. The results are shown in Fig. 4.10. Note that these results include coaxial to reduced-height waveguide transitions at all ports, which is the main reason for the variations.

This work was later extended to a full 10-way chain power divider for a local company. While it showed excellent coupling bandwidth, the losses were substantially higher than for normal height guide, which reduced the application of the principle substantially, especially for cascade couplers such as the chain divider. Nevertheless, it proved a valuable training ground for careful design of measurement experiments, and a first taste of commercial numerical electromagnetic analysis software.

paper are the effects of slot length, cross separation and wall thickness.

3. A Prototype Coupler - Analysis and Measurements

The results of a three-level coupler with guides crossing on both top and undersides of the main guide, is shown in fig

Measurements and predicted responses include a coaxial to waveguide transition at each port. Port 3 is the input port, p
and 5 the coupled ports, and ports 2 and 6 the isolated ports.

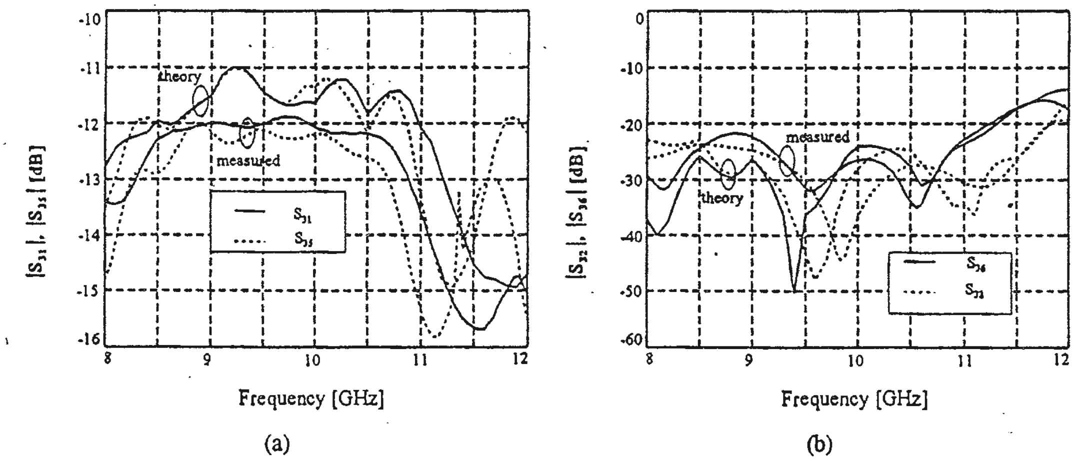

Figure 3: Measured and Predicted response of three-level coupler

Figure 4.10: Three-layer crossed-slot measured results. Port 3 is the input port, 1 and 5 the coupled ports, and 2 and 6 the isolated ports. (from [78])

It is clear that a wide-band coupler has been constructed with coupling value of 12 to 12.5 dB across a 2GHz bandwidth.
to 13dB across 2.5GHz. The coupling is equivalent to a two-level coupler with a coupling value of 9dB and is only made p
by the use of the reduced height waveguides.

4.4 Power dividers and combiners

4. Conclusions

A number of the characteristics of waveguide crossed-guide couplers will be discussed in this paper. Using this, design
can be derived for this kind of coupler. A prototype coupler showed good results and proved the validity of the FEM a
used. Complete agreement is however impossible because of the complexity of the problem and the inability to model
whole.

- 212 -

Pulsed search RADAR systems require the generation of short pulses of very high power, on the order of a few kilowatts typically. Historically, this was done using travelling wave tube (TWT) technology, but the late 90's saw a transition to the use of combined solid-state devices. This technology offered the very desirable characteristic of graceful degradation, as opposed to single point failure in TWT systems, but required low-loss combiners which could handle very high peak powers, and multiple inputs.

In 2005, myself and my PhD student Dr Dirk de Villiers started work on X-band combiners using a proposal by Prof PW van der Walt, a RADAR expert working in local industry, for a conical line combiner [80]. Conical line combiners look similar to radial combiners, but use conical lines instead of radial lines. While similar, the design and performance of conical line combiners are hugely different from radial combiners, as a conical line supports a TEM mode, with the line impedance defined by the angle between the two conductors. This offers a number of advantages, of which a wide spurious free frequency range, and the ability to use standard impedance matching techniques are the most important.

The first iteration of a ten-way conical line combiner was published in 2007 [81]. The basic structure of the combiner is shown in Fig. 4.11. Stepped impedance transformers were used on the input ports as well as the common output port - in the former case a very simple one using a cut-out of the dielectric surrounding the centre conductor of an extended dielectric SMA connector as shown in Fig. 4.12, and in the latter case a higher order stepped coxial line as shown in Fig. 4.13. A cross-section of the final combiner is shown in Fig. 4.14.

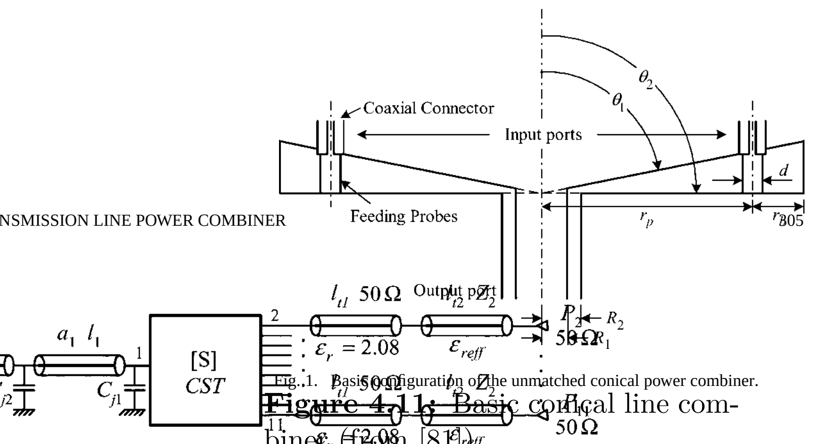

Figure 4.11: Basic conical line combiner (from [81])

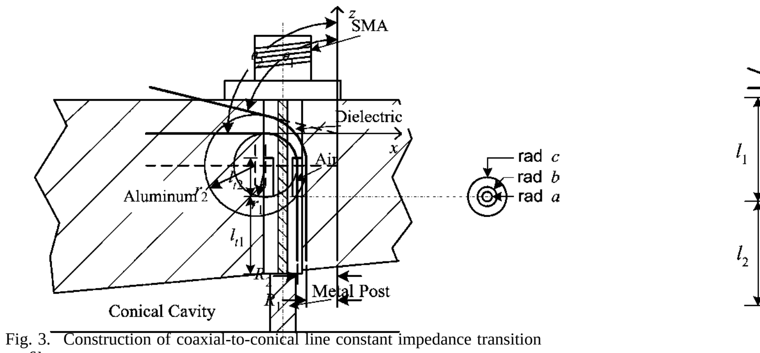

Figure 4.12: Conical combiner input port detail (from [81])

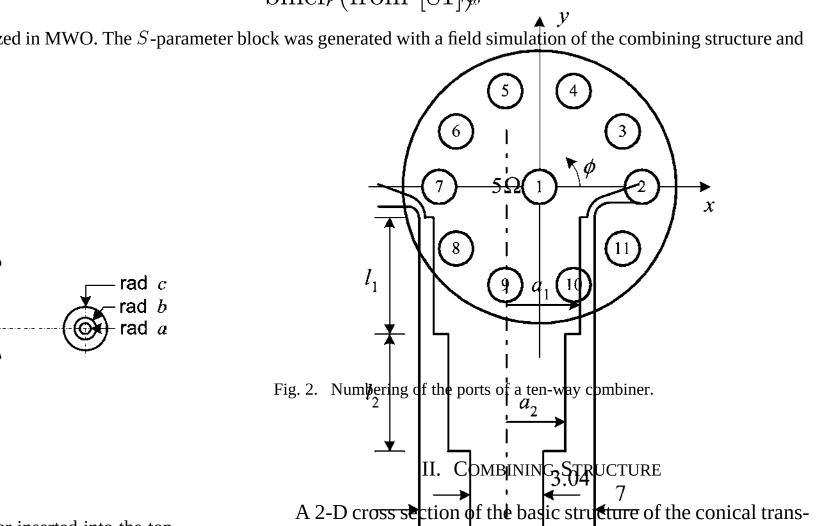

Figure 4.13: Conical combiner common port detail (from [81])

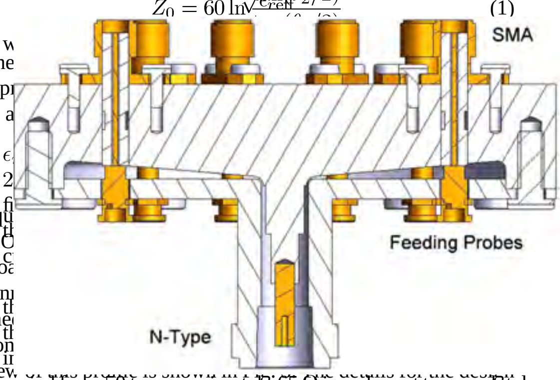

Figure 4.14: Conical combiner cross section (from [81])

The proposed combiner showed excellent wideband performance, as shown for the input reflection at the common port in Fig. 4.15, and the transmission responses between all input ports and the common port in Fig. 4.16. However, it had a very small gap at the transition from the common port coaxial line to the conical line, which called for high-accuracy manufacturing, and reduced the maximum power handling capability substantially.

To improve the design, a tapered impedance matching network wsa introduced in the common port coaxial line, as well as in the conical line [82]. This illustrated the advantages of a conical line very well, as the whole taper in both lines could be designed without optimisation. In comparison, attempting

Fig. 10. 2-D side view of the conical combiner structure showing all connectors, feeding probes, and fastening screws.

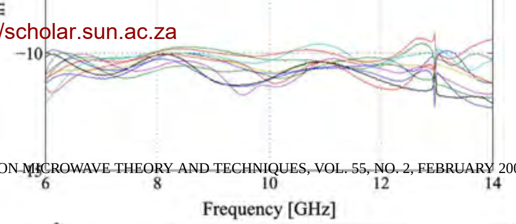

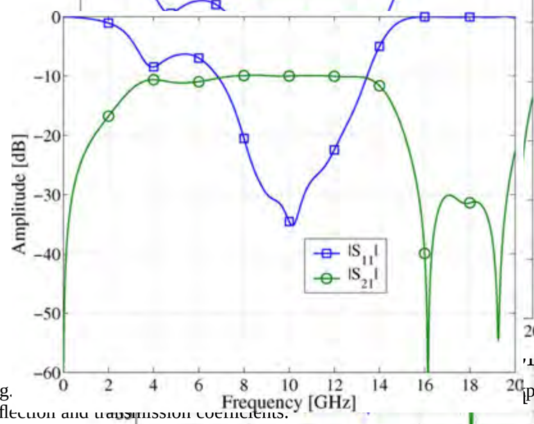

Fig. 5. Field simulation results of the combining structure central output port reflection and transmission coefficients.

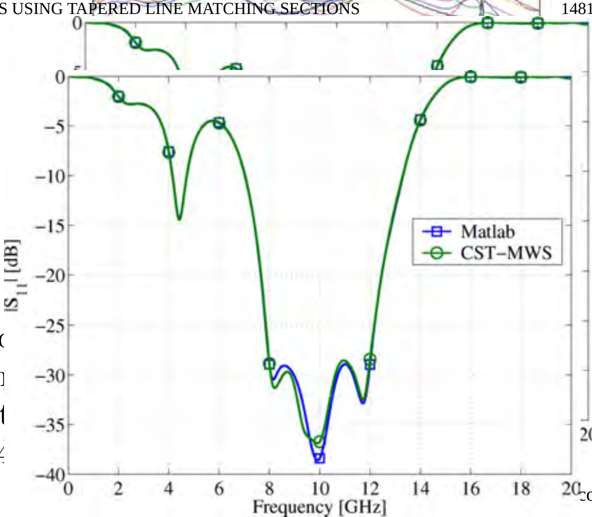

Fig. 7. Simulated reflection coefficient of a matched ten-way tapered line conical power combiner.

Fig. 11. Simulated and measured reflection coefficient at the central output port.

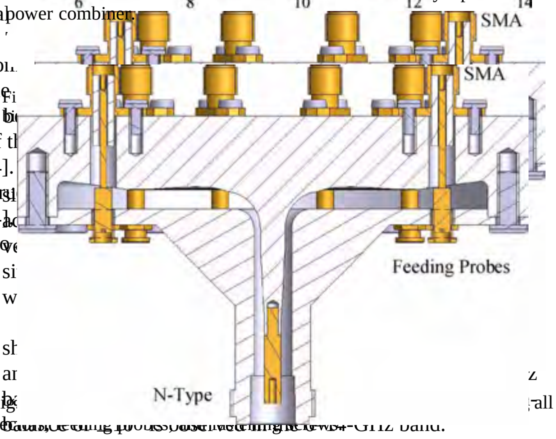

Fig. 8. 2-D section view of the tapered line conical combiner showing all connectors, feeding probes, and fastening screws.

Figure 4.17: Tapered line conical combiner common port detail (from [82])

Figure 4.18: Tapered line conical combiner cross section (from [82])

Fig. 6. 2-D profile of the coaxial taper showing optimization variables.

The measured results for the improved combiner show that a lower reflection coefficient was obtained, and an improved power balance to all ports. Most importantly, however, was the

III. CENTRAL OUTPUT PORT MATCHING DESIGN

To match the 25-Ω conical combining structure to a 50-Ω N-type connector across the entire X-band, with sharp edges in the matching network, an optimized taper is used in the feeding coaxial line. For simple construction, only the diameter of the coaxial line is adjusted. The optimization is done in MATLAB using transmission line models connected to the S-parameter box generated by a field simulation in Section II-C.

Since accurate construction of complex smooth profiles is difficult, even when a computer numerically controlled lathe is used, a taper consisting of several linear sections in the center conductor of the coaxial line is designed. Fig. 6 shows a 2-D profile of the taper with the definition of the optimization variables. The total length of the taper is ℓ_t and it consists of N sections defined by the diameters d_n and length $\ell_0 = \ell_t/N$.

The optimization routine written in MATLAB optimizes only the diameters d_n using a standard MATLAB function minimizer to yield a minimum S_{11} in the 8–12-GHz band. The length of

the diameters are constrained so that $d_{n+1} \leq d_n$ with $d_1 \geq 3.04$ mm and $d_N \leq 4.62$ mm. The number of sections N must also be kept to a minimum. A linear taper is used as the seed for the optimizer.

The reflection results of a five-section taper (increasing the number of sections does not significantly improve the reflection performance) are shown in Fig. 7. The final values of the optimization variables are $d_1 = 3.18$ mm, $d_2 = 3.74$ mm, $d_3 = 4.09$ mm, and $d_4 = 4.62$ mm. The length of each section is $\ell_0 = 4$ mm. The predicted reflection result from a CST-MWS simulation of the entire structure is also plotted in Fig. 7, and is in very good agreement with the MATLAB prediction. The return loss is better than −28 dB across the 8–12-GHz band.

IV. CONSTRUCTION AND MEASUREMENT

A 2-D section view of the entire manufactured aluminum structure with all the connectors, tuning posts, and fastening screws included, is shown in Fig. 8.

The simulated and measured reflection results of the common port of the constructed combiner is shown in Fig. 9. A matched

V. MEASURED RESULTS

A 2-D side view of the manufactured structure is shown in Fig. 10 showing all the components of the assembly. The aluminum structure was manufactured with a CNC lathe.

The simulated and measured reflection results of the common port of the constructed combiner is shown in Fig. 11. A matched bandwidth of 74% is achieved with a maximum return loss of −14.7 dB from 6.5 to 14.1 GHz.

reduction in the required manufacturing tolerances, and the increase in power handling capability.

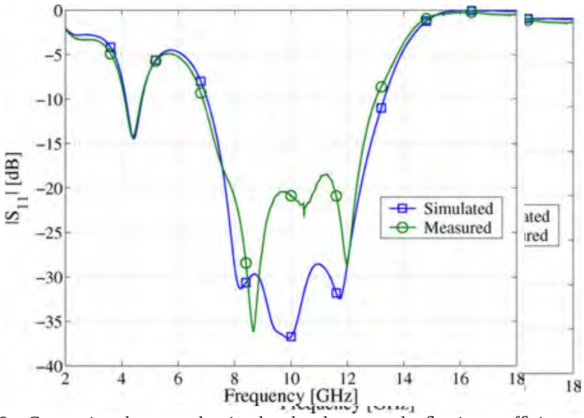

Figure 4.19: Conical combiner measured S11 (from [82])

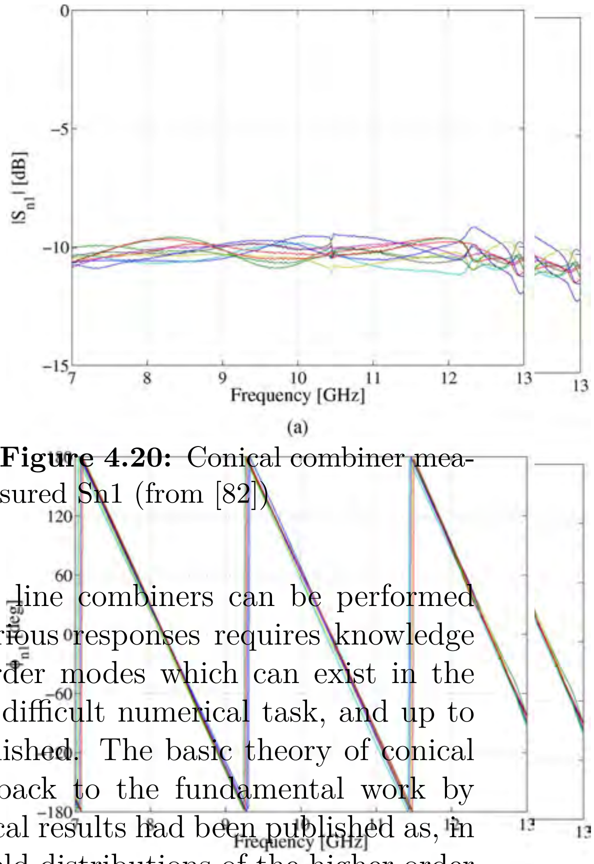

Figure 4.20: Conical combiner measured Sn1 (from [82])

While the pass-band design of conical line combiners can be performed using TEM line theory, designing for spurious responses requires knowledge of the higher order modes which can exist in the line. To calculate these is however a very difficult numerical task, and up to 2008, no such analysis had ever been published. The basic theory of conical lines goes back to the fundamental work by Schelkunoff. However, very limited numerical results had been published as, in order to obtain numerical results for the field distributions of the higher order modes, [illegible] to be solved. This requires accurate solutions of the nonnegative integer order associated Legendre functions up to very high positive real degrees (typically up to 100). Furthermore, to accommodate all conical lines, the argument of the functions should include all real values between −1 and 1.

In [83] we presented for the first time in open literature a detailed method to calculate the cut-off frequencies and field patterns of higher order modes in conical lines. A typical result for the cut-off frequencies is shown in Fig. 4.21 and an example of a modal field pattern in Fig. 4.22. Especially the field plots proved invaluable in the calculation of the limiting [illegible]

The final part of this work was then a systematic description of the design constraints in combiners using conical lines [84]. This paper derived very simple closed expressions for [illegible] especially [illegible] combiner to prevent higher order modes up to a given frequency. The approximated equations compared very well with the exact equations, and provided designers with a very simple way of designing these combiners.

tions in The Mathworks' MATLAB were compared to those found by *Mathematica* 4.1 for a wide range of the parameters. For the associated Legendre functions of the first kind, $P_\nu^m(x)$, results agree to at least 11 significant digits for all arguments in the range $-1 < x < 1$, real degrees up to $\nu = 1000$ and integer orders up to $m = 50$. The second kind functions,

was varied between 10° and 90° and θ_1 was chosen to give a 50 Ω line impedance, and also where $\theta_2 = 22.5°$ and θ_1 is varied to give line impedances of $Z_0 = 10, 25, 50, 75, 100$, and 125 Ω. Roots were also computed for $\theta_2 = 90°$ and $\theta_1 = 85.231°$ (5 Ω line impedance) for $m = 1{:}15$. All the results agree to at least five significant digits.

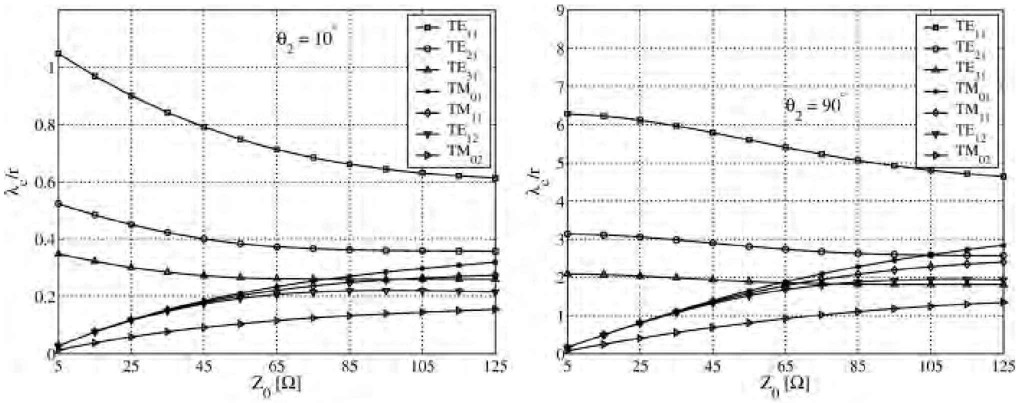

(a) $\theta_2 = 10°$ (b) $\theta_2 = 90°$

Figure 5. Normalized cutoff wavelength of higher order modes in a conical transmission line with θ_2 constant and Z_0 varied.

Figure 4.21: Conical line cut-off frequencies (from [83])

International Journal of RF and Microwave Computer-Aided Engineering DOI 10.1002/mmce

The work on conical line combiners and dividers showed for the first time that the conical line, which had up to this point mostly been used as theoretical model for dipole antennas, could be used very effectively in power combiners. The TEM characteristic of these lines makes it possible to use standard impedance matching techniques and profiles, which is a significant advantage. In addition, the frequency spacing between the fundamental mode cut-off (at DC) and that of the first higher order modes is much larger than for radial lines. The work on the calculation of the higher order modes by Dr De Villiers represented a high point of numerical mathematical algorithms in my career, with reviewers of the paper specifically pointing out the absence of work of this nature in literature, and the high quality of the mathematical and numerical innovation.

The research on conical line combiners also continued after completion of the work reported here, and formed one of the key research areas of Dr de Villiers and his research students.

4.5 Microwave Switches

One of the key components in a pulsed RADAR system is a microwave switch which can control the signal from the antenna to the receiver input port. For high power search RADAR, such a switch should in its off-state have a very large isolation to protect the high power transmitted signal from leaking through to the sensitive receiver. In its on-state, the switch should show a very low loss, as this loss directly impacts the detection range. Finally, the structure should be able to protect against power levels of several kilowatt.

To satisfy all these conditions, most high-power switches make use of waveguide technology due to its low loss and high power capability. However, to

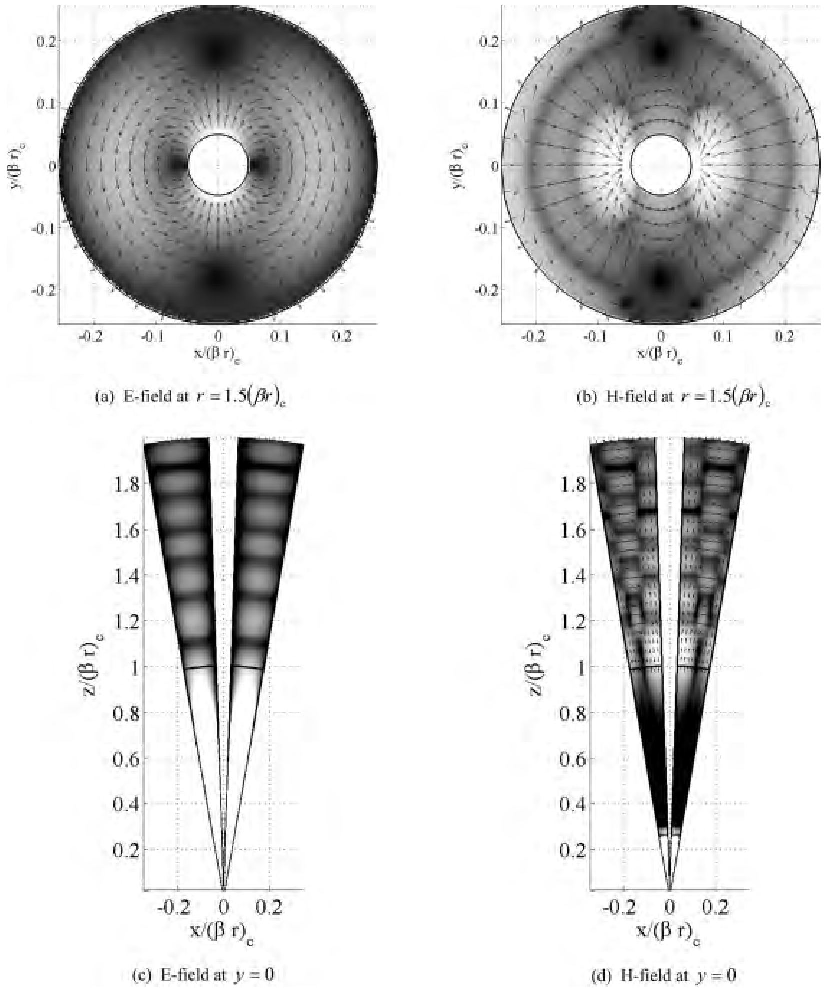

Figure 8. Normalized field patterns of the TE_{12} mode in a conical line with $\theta_2 = 10^\circ$ and $Z_0 = 100\ \Omega$. (See Fig. 1 for axis reference.)

C. Higher Order Modal Cutoff Plots

In this subsection plots are shown of the normalized cutoff wavelength of some of the higher order modes in conical transmission lines. The geometries of the lines are chosen to be consistent with the structures published in [3] ($\theta_2 = 10^\circ$ and $Z_0 = 100\ \Omega$) and [4] ($\theta_2 = 90^\circ$ and $Z_0 = 5\ \Omega$). The plots are shown with either θ_2 constant and varying Z_0, or Z_0 constant and varying θ_2.

The results in Figure 5 agree perfectly with those published in [3]. It can also be seen that for low impedance lines the TE_{m1} modes dominate. Also note in Figure 6a that this is no longer the case in high impedance lines with a large θ_2. These lines have a wider conductor spacing than low impedance lines with small θ_2. The dominance of the TE_{m1} modes for narrow lines will be explained by some modal field plots in the following subsection.

D. Modal Field Plots

Normalized field patterns for the TE_{11} and TE_{12} modes in a conical line with $\theta_2 = 10^\circ$ and $Z_0 = 100\ \Omega$, calculated from the equations in Section II.B., are shown in Figures 7 and 8.

The TE_{11} mode in Figure 7 is seen to have little θ variation of the θ-directed E-field and the φ-directed H-field. In the TE_{21} mode of Figure 8, the E-field is mainly φ-directed and the expected zeros of the tangential E-fields at the conductors are observed. TE_{mn} modes are similar to the modes shown here, but with

Figure 4.22: Conical line mode pattern (from [83])

achieve very high isolation in standard waveguide is difficult, as the signal simply 'leaks' around typical obstacles. In 2005, my PhD student Dr Thomas Sickel, together with myself and Prof PW van der Walt, proposed a PIN-diode switching structure in evanescent mode waveguide [72], [85]. Evanescent mode waveguide offers the significant advantage of having excellent isolation characteristics, but is much more difficult to work with than normal waveguide, as all the electrical parameters are strong non-linear functions of frequency.

At the core of the proposed switching structure was a novel PIN-diode mounting structure, shown in Fig. 4.23, with the equivalent circuit for the diodes in their off-state shown in Fig. 4.24. The mounting structure consists of two diodes mounted back-to-back on a thick, flat conductor which extends horizontally to the waveguide wall, where it is grounded. This plate is orthogonal to the electric field of the TE_{10}-mode, and therefore does not affect the signal path. The direct connections between the diodes, the grounding plate, and the waveguide wall creates a path of very low thermal resistance, which allows the diodes to dissipate high heat loads. This in turn allows the switch structure to protect against very high peak and average power levels. The bias to the diodes is supplied through two thin conductors running from the non-terminated side of each diode to a small hole in the waveguide wall. As these conductors are very thin, and approximately orthogonal to the electric field, they also disturb the signal path very little.

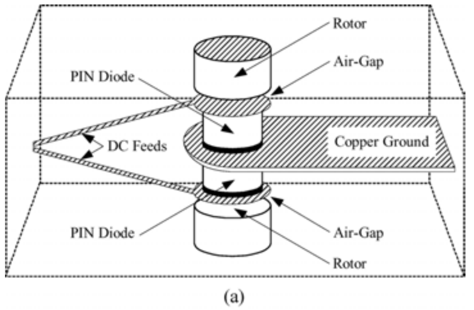

Figure 4.23: PIN diode mounting structure (from [72])

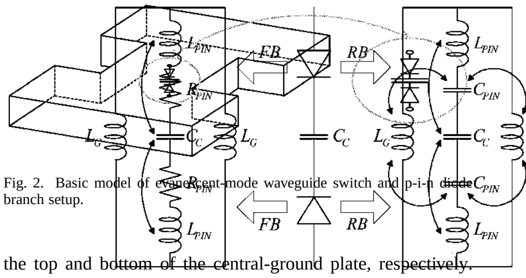

Figure 4.24: Embedded PIN diode model (from [72])

To achieve the high isolation necessary, the switch uses a section of waveguide operating below its cut-off frequency, forming what is called evanescent mode waveguide, as shown in Fig. 4.25. In the off-state, this structure is very accurately described by the circuit model in Fig. 4.26, where the strong non-linear dependency of the equivalent inductors on frequency is also shown. In the on-state, the diodes are forward biased and present as resistors of low value, almost short-circuits.

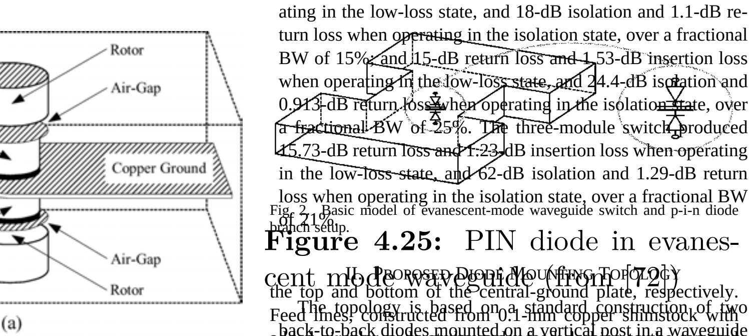

Figure 4.25: PIN diode in evanescent mode waveguide (from [72])

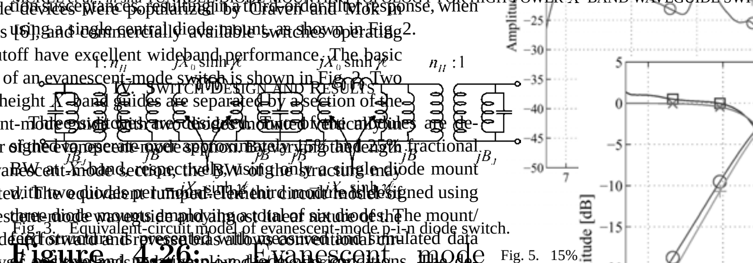

Figure 4.26: Evanescent mode waveguide model (from [72])

When the diodes are in their on-state, or forward-biased, the signal is shunted to ground through the effective resistors, and the two ports are isolated. In the off-state however, the diodes present as capacitances, and a signal can pass between the ports. It should be clear that careful design can

incorporate such capacitances into a filter
ate a pass-band with very low loss and low
response is very sensitive to the exact capa
diode mounting structures often create filter
as the structures are typically fixed, little t
aspects of the mounting structure proposed
above each diode, with a tuning screw the
gap presents as a series capacitor in the mou
manufacturing fine-tuning of each equivale
structure apart, a so-called *in-situ* tuning.
therefore be obtained.

The assembly drawing of a third order s
order filter was also constructed, and the me
graphs. Fig. 4.28 shows 60dB of isolation f
forward-biased, across the X-band. Such an
using standard waveguide.

IEEE TRANSACTIONS ON MICROWAVE THEORY AND TECHNIQUES, VOL. 55, NO. 2, FEBRUARY 2007

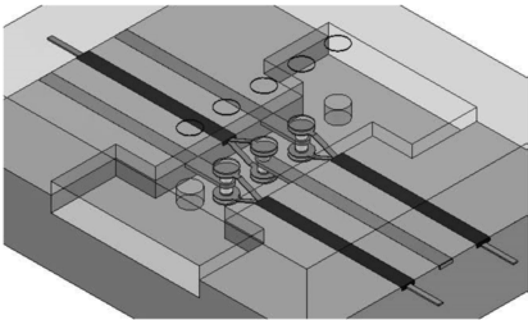

Fig. 7. Fifth-order switch.

Figure 4.27: Third order switch construction (from [72])

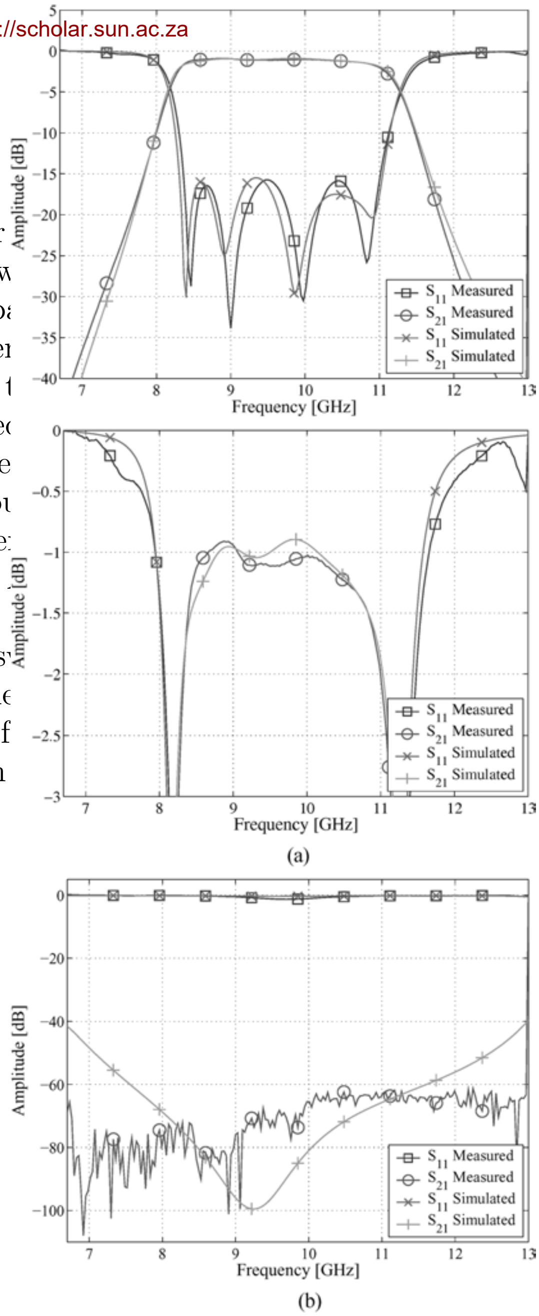

Figure 4.28: Fifth order switch attenuation (from [72])

Fig. 8. Fifth-order switch—measurement versus theory. (a) Switch transmission. (b) Switch isolation.

The performance of the switch as a filter, i.e. when the diodes are reverse-biased, is shown in Fig. 4.29 and Fig. 4.30. Note the excellent return loss characteristic, as well as the small pass-band loss. This was only possible due to the in-situ tuning capability of the switch.

An important part of the complete switch is the power handling capability. High power signals being shorted through the forward-biased diodes create large currents, which in turn create large amounts of heat in the diodes. A significant part of the design was therefore the development of an accurate thermal model, which not only includes thermal resistance, but also thermal capacitance. Especially the latter is of very high importance in pulsed systems. Such a model, together with both high and low power measurements, was published in [86]. Some of the results, showing model response and measured

used to build up accurate lumped-element models of diode mounts, evanescent-mode guide sections, and junctions between evanescent-mode and propagating guide sections. Sections are cascaded with dimensions determined by an optimized approach, where evanescent guide lengths, mount capacitances, and junction capacitances are tuned for optimal switch operation in low-loss and isolation states. The addition of junction tuning rotors on the input and output of the switch results in a fifth-order filter structure. The switch achieves a switch fractional BW of 21% with 15.73-dB return loss and 1.23-dB insertion loss with a ±0.155-dB amplitude flatness when operating in the low-loss state, and 62-dB isolation and 1.29-dB return loss when operating in the isolation state, as shown in Fig. 8.

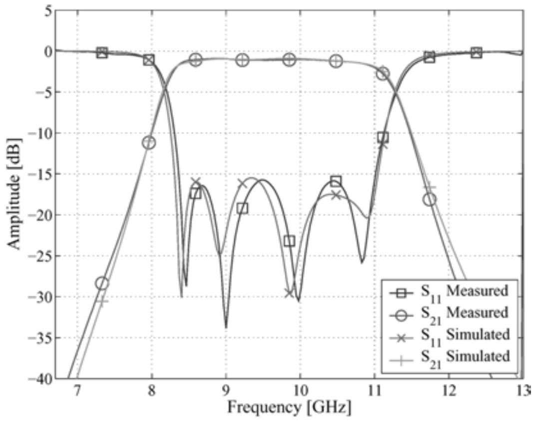

Figure 4.29: Fifth order switch in filter mode (from [72])

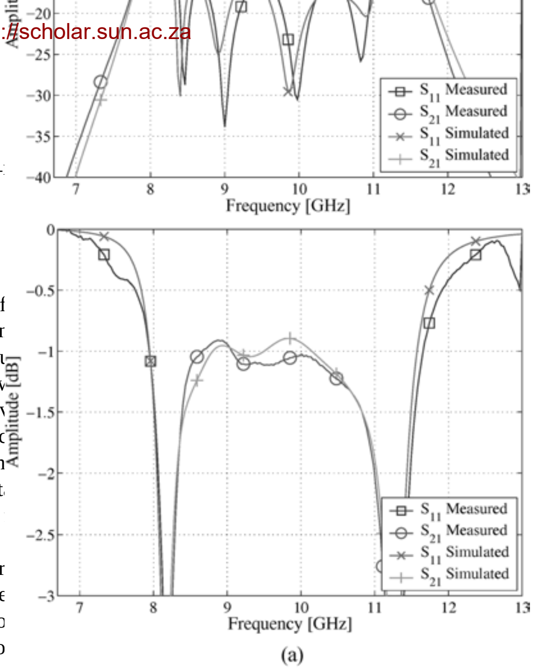

Figure 4.30: Fifth order switch attenuation in filter mode (from [72])

response, are shown in Fig. 4.31 for a low power, 1 microsecond pulse at a 10% duty cycle, and in Fig. 4.32 for an 8kW, 25 microsecond pulse at a 5% duty cycle. It is clear that the high power measurements show much higher peak temperatures for the model than in measurement. This can be attributed to a difficult-to-model increase of the I-region thermal capacitance at high peak powers. For the average temperature predictions however, the difference between the model and the measurements was only 11 degrees in the high power test. In all, the switch performed well at the 8kW peak power level.

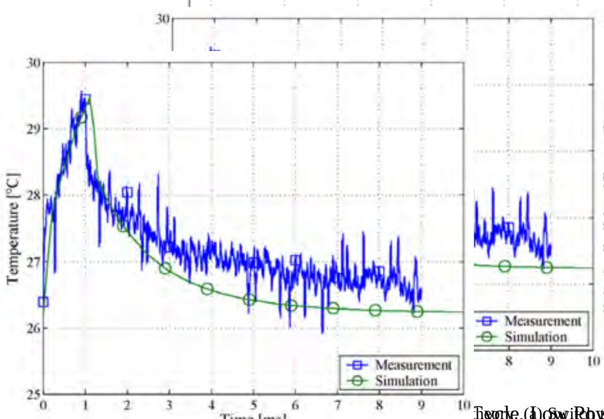

Figure 4.31: Evanescent mode switch low power test results (from

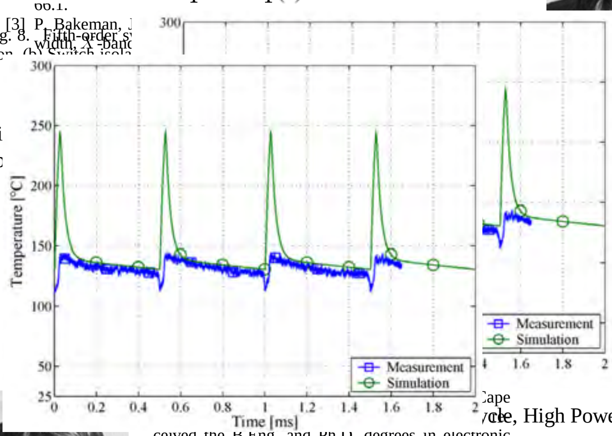

Figure 4.32: Evanescent mode switch high power test results (from

The mounting structure discussed above was ... tigated in [85]. A variety of mounting structures ... with an overview published in [87].

The temperatures and time constants of the low power measurements are predicted relatively accurately by the developed electric circuit analog of the PIN diode transient thermal heating model. Peak temperatures predicted by the thermal model for high input power levels are not observed in the measured junction temperature response. These peak values increase the average junction temperature considerably, resulting in an inaccurate peak power prediction ability of the simple thermal model. Refinements to the model using further high power measurement data, should improve the peak power prediction, resulting in accurate maximum power predictions for CW and pulsed switching conditions for waveguide mounted PIN diodes.

ACKNOWLEDGEMENT

The authors wish to thank the National Research Foundation (NRF) of South Africa, the Wilhelm Frank Trust and Reutech Radar Systems (RRS) for support during the period of research.

REFERENCES

The work on the evanescent mode waveguide switch was my first work on devices using high-power diode control elements. Commercially, these switches are produced in very low numbers, at high cost, and for the specific requirement this work was aimed at, only one company globally was prepared to quote at the time. The successful completion of this product, and its subsequent introduction into the RADAR systems of the local sponsoring company, made this research some of the most directly applicable industry-related work of my career.

4.6 Conclusion

My research on passive devices has formed a significant part of my overall work. Being very closely coupled to local industry and its requirements, this work also created the need for a number of other research topics over the years, such as my work on modelling, optimisation and so forth. Throughout my career I have found that some of the most challenging research topics stem from industry products, as commercial systems in most cases require the satisfaction of a huge number of requirements - not only electrical, but also mechanical and thermal, with spatial and weight constraints typically very important. As such, this research often calls for high levels of originality, combined with very practical constraints.

Chapter 5

Antennas, Antenna Feeds, and Mixed-Mode Formulations

5.1 Introduction

For most of my career, my work was primarily aimed at microwave receiver subsystems, and stopped short of antennas. Due to the close integration between the filtering subsystems and the antenna feed in typical receivers and transmitters, antenna feeds however also on occasion formed part of my work up to 2012. In 2013, my research focus took a quite dramatic turn towards actual antennas, through my involvement with the Square Kilometre Array (SKA) project. Especially my involvement in higher order modes on guided structures would prove to be very useful in this area, and lead to various projects utilising the modal characteristics of structures in antenna and antenna feed design.

5.2 X-band monopulse waveguide feed

My first project on antenna feeds stemmed directly from my work on Mode-Matching and waveguide filter design, and involved the design of a waveguide feed for an X-band reflector antenna system for monopulse RADAR in 1999. In these systems, a number of waveguide feeds are typically first combined into one overmoded waveguide, which terminates in the radiating aperture. Using three specific combinations of excitations at the four waveguide ports, a single mode is excited in the radiating aperture in each case. For the excitations shown in Fig. 5.1 for instance, the TE_{10}, TE_{20} and TE_{11} modes are respectively excited, which in turn radiate in what is called the plus, elevation and azimuth modes.

One of main the problems with the design of these types of feed in the late 1990's, was the achievement of good input match across a wide band for all three excitations. At the time, the state-of-the-art was a system with an input match of -18dB for all three excitations, over a bandwidth of only 10%.

The fundamental problem in reaching the objective of low input reflection, is of course that one physical structure, i.e. the overmoded waveguide, has to match three different terminating impedances to the impedance of the source guide - one for each mode. In addition, each excitation generates a different mode or set of modes in the overmoded guide, each of which has a different propagation constant. This is a classical optimisation problem, which, given the analysis software at the time, was simply intractable.

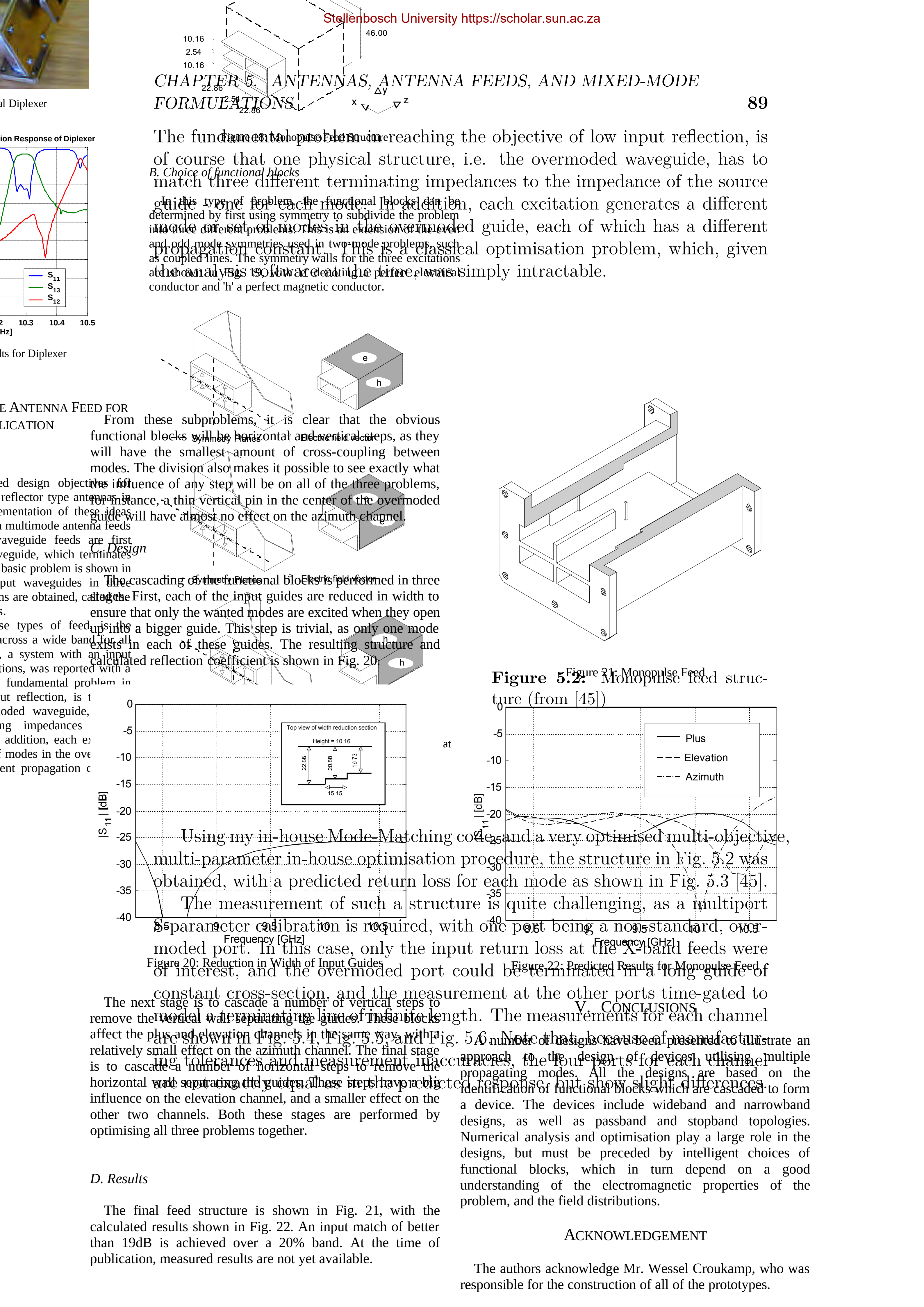

Figure 5.2: Monopulse feed structure (from [45])

Using my in-house Mode-Matching code, and a very optimised multi-objective, multi-parameter in-house optimisation procedure, the structure in Fig. 5.2 was obtained, with a predicted return loss for each mode as shown in Fig. 5.3 [45].

The measurement of such a structure is quite challenging, as a multiport S-parameter calibration is required, with one port being a non-standard, overmoded port. In this case, only the input return loss at the X-band feeds were of interest, and the overmoded port could be terminated in a long guide of constant cross-section, and the measurement at the other ports time-gated to model a terminating line of infinite length. The measurements for each channel are shown in Fig. 5.4, Fig. 5.5, and Fig. 5.6. Note that, because of manufacturing tolerances and measurement inaccuracies, the four ports for each channel are not exactly equal as in the predicted response, but show slight differences.

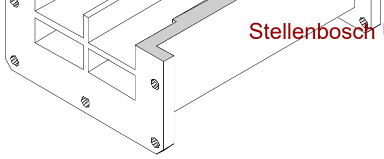

blocks is performed in three
ides are reduced in width to
s are excited when they open
is trivial, as only one mode
The resulting structure and
shown in Fig. 20.

Figure 21: Monopulse Feed

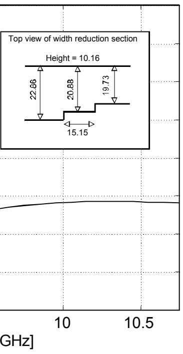

idth of Input Guides

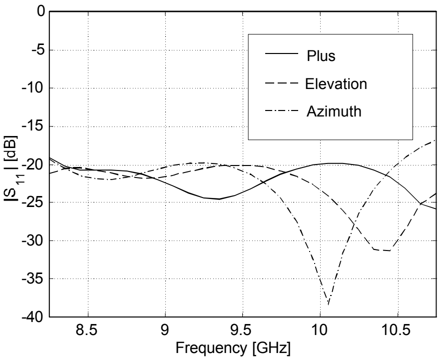

Figure 22: Predicted Results for Monopulse Feed

Figure 5.3: Monopulse feed predicted modal return loss (from [45])

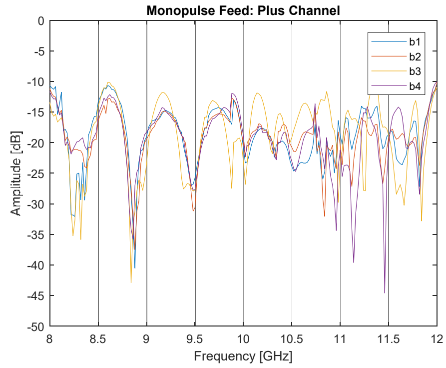

Figure 5.4: Monopulse feed plus channel return loss

number of vertical steps to
ng the guides. These blocks
nels in the same way, with a
uth channel. The final stage
zontal steps to remove the
ides. These steps have a big
l, and a smaller effect on the
stages are performed by
ther.

nown in Fig. 21, with the
22. An input match of better
20% band. At the time of
not yet available.

V. CONCLUSIONS

A number of designs have been presented to illustrate an approach to the design of devices utilising multiple propagating modes. All the designs are based on the identifica... form a device... band designs, ... gies. Numerica... the designs, ... s of functiona... good understan... the problem, ...

The au... was responsib...

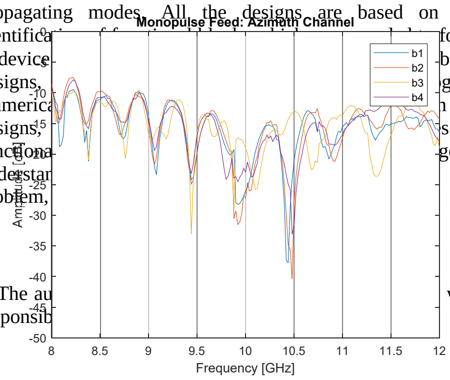

Figure 5.5: Monopulse feed azimuth channel return loss

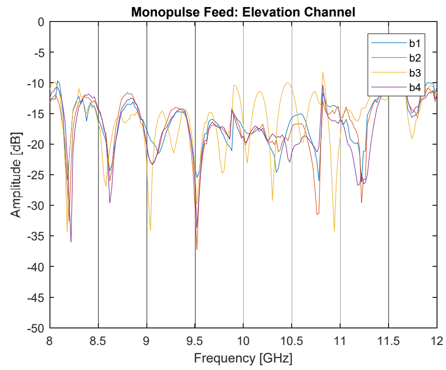

Figure 5.6: Monopulse feed elevation channel return loss

It is however clear that good return loss is measured for each port of each channel over the full X-band of 8-12GHz, or a 40% bandwidth.

These results represented a factor of four improvement in bandwidth over the state-of-the-art, and provided validation of the analysis and optimisation techniques developed in-house. This type of antenna, which has different radiation patterns for different excitation combinations, would later become part of a class of antennas which currently is called multi-mode antennas, and the expertise gained in this project would prove to be extremely useful two decades later.

5.3 The Square Kilometre Array Antenna

Many years would pass before I would become involved in antenna work again. The event which would trigger this was the SKA initiative which started in the early 2000's, with the aim of creating the world's largest radio-astronomy antenna - one with an effective receiving aperture of one square kilometre. Such a telescope would enable radio astronomy science at a completely new level of sensitivity.

The project was of particular interest to South Africa, as we have some of the most easily accessible radio-quiet zones in the world in a semi-desert region known as the Karoo. In order to convince the international SKA steering group of the viability of situating the antenna system in South Africa, the South African Department of Science and Technology (DST) approved the biggest funding for a single science project in the history of the country, with the aim of building a pathfinder antenna array on the proposed site. The name of the first phase of seven large dishes was proposed as the Karoo Array Telescope, or KAT-7. This phase was extended to 64 dishes, with the new name of MEERKAT. (In Afrikaans, 'meer' means more, thus literally 'more KAT', but a meerkat is also a small rodent which is unique to Africa.) Both KAT-7 and MEERKAT were fully designed and constructed locally, using local engineers, companies and universities.

At the time of writing, the main SKA site has been confirmed as the Karoo, and phase 1 of the SKA is starting construction. By some coincidence, on this day of writing, i.e. Friday 13 July 2018, the full MEERKAT array was inaugurated in a ceremony at the site close to Carnavon - a historic moment for South African engineering and science. The partially completed telescope has been in operation for science work for almost a year already, and the first science paper was published early in 2018. A recent photograph is shown in Fig. 5.7.

Figure 5.7: The MEERKAT antenna array

Alongside the actual technical project, the DST also launched an SKA focused human capital development programme, which currently supports on the order of 100 postgraduate students in the country. The SKA programme has had a significant influence on the research landscape in South Africa, and has been a focal point of government funding.

My own involvement in the SKA project has been substantial, both on the technical side with the development of receiver subsystems for KAT-7 and MEERKAT, and on the research side. Through my own efforts and that of my colleagues Profs David Davidson and Howard Reader, our department developed very strong ties with the South African SKA office, and currently have three staff positions funded in this way - one being a full research chair which forms part of the South African research Chairs' Initiative (SARCHI), a highly prestigious position.

The involvement with the SKA project caused me for the first time to broaden my research interest to include antennas and antenna systems. Two areas were of specific interest to SKA, namely wideband waveguide feeds for reflector antennas (SKA Phase 1 and 2), and small, inexpensive, lower frequency antenna elements which could be used as part of an array of thousands of fixed antennas (the SKA Mid-Frequency Aperture Array, or MFAA). In 2013, in cooperation with Profs Marianna Ivashina and Rob Maaskant from Chalmers University in Gothenburgh, I and two of my PhD students started on what would be my first serious antenna research.

5.4 Multi-mode antennas and mixed-mode systems

5.4.1 Dual-mode antennas

The first of these projects ran from 2013 to 2105 with my PhD student Dr David Prinsloo, co-supervised by the Chalmers group, and focused on developing a stationary antenna element to form part of the MFAA [88]. As stationary elements rotate with the earth, maximum observation times are directly dependent on the field-of-view of each element, with the ideal element having a $\pm 90°$ coverage from zenith. In radio astronomy, images are created by integrating for long periods (hours) while looking at a fixed point in the sky, therefore longer observation times yield better results. Antenna elements with fields-of-view approaching a full hemisphere are however very rare, with the quadrifilar helix being the best option at that time.

The first attempt at creating an element with a hemispherical field-of-view, was reported in [89], and is shown in Fig. 5.8. The antenna consists of a double-sided substrate, with on one side a narrow section of groundplane, connected to a single, open-circuited quarter-wave line. On the other side of the substrate, a balanced folded dipole structure is implemented. Only the two lines feeding the dipole are excited with respect to the narrow groundplane. Two possible orthogonal excitations can be used, i.e. a *common mode* and a *differential*

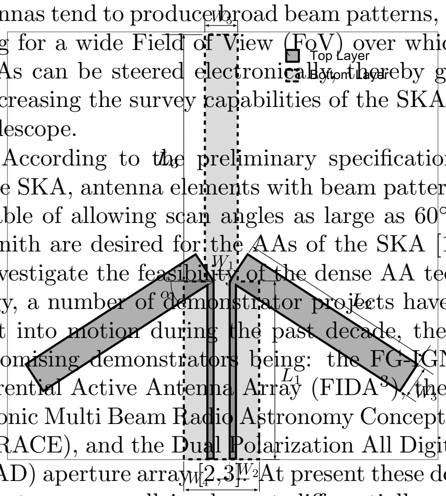

Figure 5.8: Dual mode antenna layout (from [89])

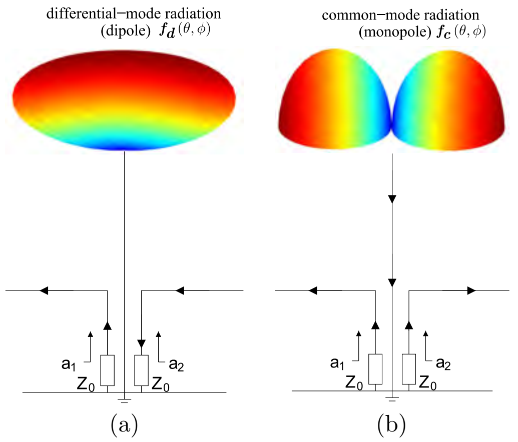

Figure 5.9: Modal radiation patterns (a) Even mode and (b) Odd mode (from [89])

mode, with the common mode exciting a monopole radiation pattern, and the differential mode exciting a dipole mode, as shown in Fig. 5.9. As it is designed to work for both modes, the antenna can be classified as a *dual-mode* antenna. At this time, modal antennas in waveguide had been used for decades, with the best examples that of monopulse RADAR antennas. However, the concept was rarely used for etched or wire antennas, where common modes were typically deemed to be undesired and therefore suppressed. The dual-mode antenna proposed here was amongst the first of a class of antennas which would become known as multi-modal antennas, which currently is an active field of research worldwide. The first prototype was built and successfully measured, as shown in Fig. 5.10.

What made the dual-mode concept very attractive, was the possibility of combining the differential and common mode excitations to create new patterns. One such a pattern is shown in Fig. 5.11 (indicated as DM+CM) together with the common ode and differential mode pattern cuts. This pattern combines the the dipole and the monopole patterns to give maximum gain at all angles, and good coverage up to the horizon.

An improved version of this antenna followed after the first prototype [90]. Here, as shown in Fig. 5.12, the groundplane is replaced with the ground sheath of a balanced coaxial line, while the monopole section is formed by folding the ground sheath back upon itself. This improved the ϕ variation of the pattern markedly, and reduced the size by half. The two orthogonal excitation modes at the feed port are shown in Fig. 5.13.

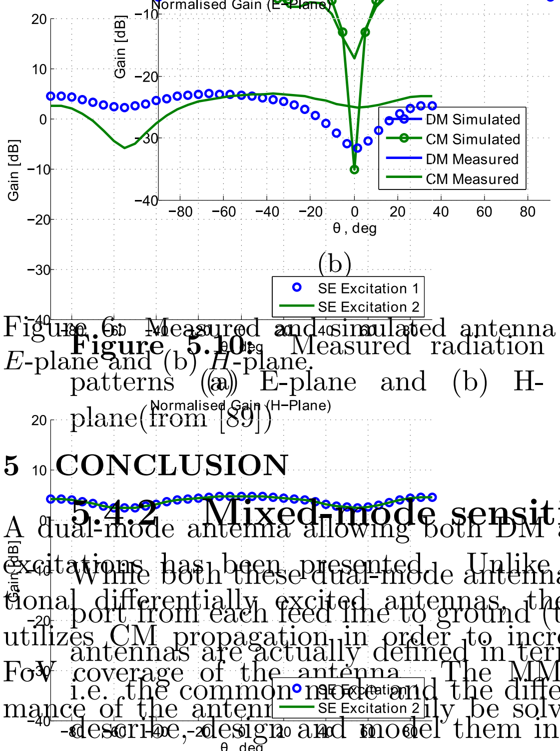

Figure 5.10: Measured radiation patterns (a) E-plane and (b) H-plane (from [89])

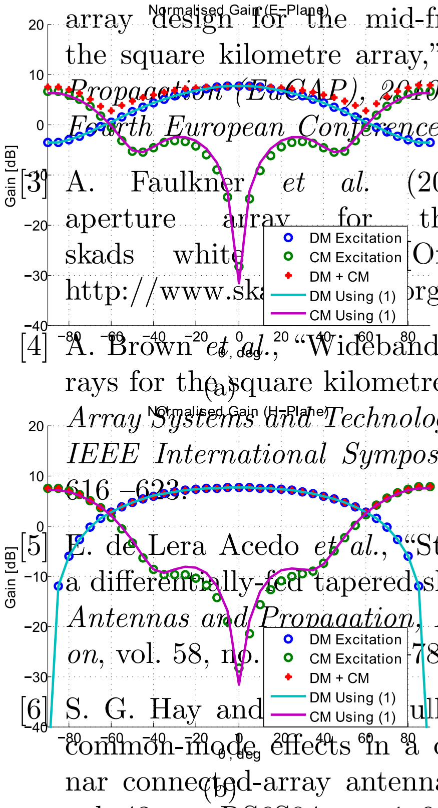

Figure 5.11: Combined common-mode patterns (a) E-plane and (b) H-plane (from [89])

5.4.2 Mixed-mode sensitivity analysis

While both these dual-mode antennas can be analysed as single-mode two-port from each feed line to ground (the so-called single-ended excitations), the antennas are actually defined in terms of the fundamental modes of the structure, i.e. the common mode and the differential mode. It therefore makes sense to describe, design and model them in terms of these modes, using for instance *mixed-mode* S-parameters, impedances, patterns, gains etc. However, the theory at the time for the analysis of receiver systems made no provision for this, being simply formulated in terms of single-ended ports.

In 2014, we therefore proposed a fully modal-based receiver analysis framework for analysing the dual-mode antenna, together with low-noise amplifiers and a beam-forming network, working fully in the mixed-mode domain. As in classical analysis of symmetrical circuits, such a treatment made many simplifications in the analysis possible. Fig. 5.14 shows the equivalent system for each of the modes in the dual-mode system analysis. For this analysis, standard mixed-mode S-parameter theory was available, but new mixed-mode

4 VERIFICATION RESULTS

4.1 Simulated Results

The antenna design described in Sec. 3 is analysed with an infinite ground plane in both the SE and MM excitation configurations, using CST MICROWAVE STUDIO®. Using (1), the equivalent DM and CM EEPs of the antenna can be determined from the SE EEPs shown in Fig. 3. The transformed E- and H-plane EEPs are compared to the MM EEPs, simulated with DM and CM excitations, in Figs. 4(a) and (b), respectively. It is clear from Fig. 4 that (1) provides a near exact solution for the MM EEPs of the antenna.

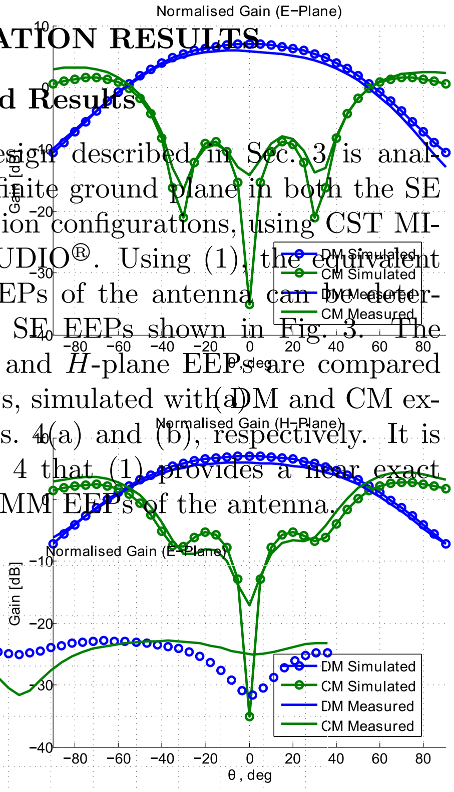

Figure 3: Simulated SE embedded element patterns (a) E-plane and (b) H-plane.

As illustrated conceptually in Fig. 1, Fig. 4 shows that DM and CM excitations realise dipole-over-ground and monopole beam patterns, respectively. The sharp decrease in gain of the DM EEP, seen for scan angles greater than 60°, can therefore be prevented by applying a CM excitation. By solving the respective MM complex beam forming weights the antenna gain (4) can be maximised for each scan angle. The optimally combined E- and H-plane gain (DM + CM), shown in Fig. 4, can be seen to follow the DM EEP for $0° \leq \theta \leq 60°$, from where the DM gain decreases significantly. For scan angles $60° \leq \theta \leq 90°$ the combined gain follows the CM EEP closely. Note that the combined E-plane gain shown in Fig. 4(a) is greater than either the DM or CM gains for scan angles larger than ±20° from zenith, whereas the combined H-plane gain in Fig. 4(b) follows the DM EEP from zenith up to the point of intersection with the CM EEP ($\theta = 60°$) after which the combined gain increases again along the CM EEP. The resulting gain variation of the combined DM and CM gain is shown to be less than 5 dB in both planes.

Figure 4: Simulated and transformed MM embedded element patterns (a) E-plane and (b) H-plane with maximized gain for scan angle.

4.2 Measured Results

To measure the S-parameters and gain, the antenna is fixed to a circular ground plane with a diameter of 500 mm. The S-parameters of the MM antenna are obtained by applying the transformation in (3) to the measured SE antenna S-matrix. Fig. 5 shows that the transformed (measured) DM and CM return loss of the antenna agrees well with the simulated MM return loss.

Gain measurements are performed by exciting each of the SE ports individually, while terminating the remaining port in a 50 Ω load. The MM EEPs of the antenna can then be solved from the SE measurements using the transformations in (1). Figs. 6(a) and (b) compare the measured E- and H-plane gain of the antenna to simulated results. The measured gains show good agreement with the simulated results, deviating by a maximum of 1.3 dB for scan angles from zenith to ±60°. Note that the loss in CM gain, seen when comparing Figs. 4 and 6, is due to the finite ground plane used for the physical antenna.

Figure 6: Measured and simulated antenna gain (a) E-plane and (b) H-plane.

5 CONCLUSION

A dual-mode antenna allowing both DM and CM excitations has been presented. Unlike conventional differentially excited antennas, the design utilizes CM propagation in order to increase the FoV coverage of the antenna. The MM performance of the antenna can easily be solved from

References

[1] R. T. Schilizzi *et al.* (2007, Dec.) Preliminary specifications for the square kilometre array. 100 Memo Schilizzi.pdf. [Online]. Available: http://www.skatelescope.org/PDF/memos/

[2] Garcia-Munoz *et al.*, "Fida3: A novel active array design for the mid-frequency range of the square kilometre array," in *Antennas and Propagation (EuCAP), 2010 Proceedings of the Fourth European Conference on*, pp. 1–4.

[3] A. Faulkner *et al.* (2010, Apr.) The aperture array for the ska: the skads white paper. [Online]. Available: http://www.skads-eu.org/publications

[4] A. Brown *et al.*, "Wideband planar phased arrays for the square kilometre array," in *Phased Array Systems and Technology (ARRAY), 2010 IEEE International Symposium on*, Oct., pp. 616 –623.

[5] E. de Lera Acedo *et al.*, "Study and design of a differentially-fed tapered slot antenna array," *Antennas and Propagation, IEEE Transactions on*, vol. 58, no. 1, pp. 68–78, Jan. 2010.

[6] S. G. Hay and J. D. O'Sullivan, "Analysis of common-mode effects in a dual-polarized planar connected-array antenna," *Radio Science*, vol. 43, no. RS6S04, pp. 1–9, Dec. 2008.

[7] "Common-mode resonances in dipole and connected arrays of dipoles: measurements from the demonstrator and exit strategy," in *Proc. Int. Conf. on Electromagn. in Adv. Applicat. (ICEAA)*, Torino, Sep. 2009, pp. 435–438.

[8] D. E. Bockelman and W. R. Eisenstadt, "Combined differential and common-mode scattering parameters: theory and simulation," vol. 43, no. 7, pp. 1530–1539, Jul. 1995.

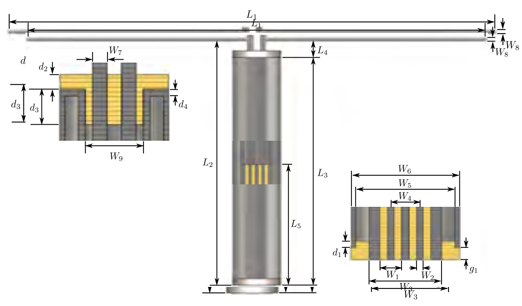

Figure 5.12: Dual mode antenna - second prototype (from [90])

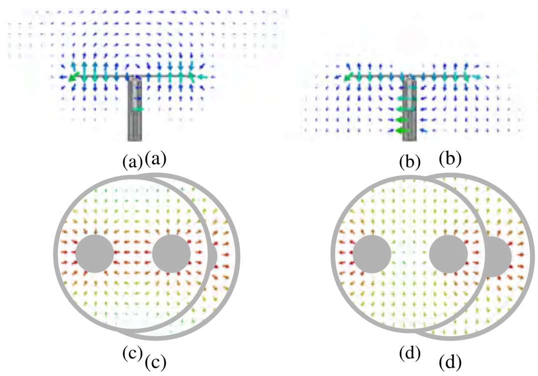

Figure 5.13: Modal excitations (a) Differential mode (b) Common mode (from [90])

treatments had to be developed for noise analysis, including concepts such as the noise correlation matrix. Finally, a full receiver sensitivity analysis was performed in the mixed-mode domain [90]. The results in Fig. 5.15 showed that, compared to a single differential mode dipole antenna, the mixed-mode usage of the proposed dual-mode antenna made huge increases in sensitivity possible towards the horizon.

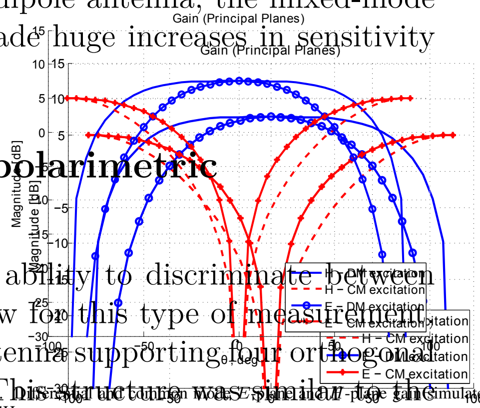

5.4.3 Quad-mode antennas for polarimetric measurements

For many radio astronomy applications, the ability to discriminate between polarisations is of prime importance. To allow for this type of measurement, the dual-mode concept was expanded to an antenna supporting four orthogonal modes, named the *quad-mode antenna* [91]. This structure was similar to the second iteration dual-mode antenna, but added a second dipole to form a crossed-dipole structure, with the whole antenna being fed by a quadraxial transmission line, as shown in Fig. 5.16. with a four-channel receiver and beam-forming network, can then be modelled in terms of the modes, as illustrated in Fig. 5.17. The orthogonal excitation modes and corresponding patterns are shown in Fig. 5.18.

The best figure of merit used to quantify polarimetric discrimination in radio astronomy, is the so-called *Intrinsic Cross-Polarisation Ratio (IXR)* as defined by Carozzi and Woan in 2011. In addition to the proposal of the improved antenna structure, [91] evaluated the performance of the antenna in terms of the IXR. For each scan angle, a set of beam-forming weights are calculated to optimise the IXR. These sets are different than those required for maximum gain in a specified scan angle, as is shown in Fig. 5.19, where the calculated gain is shown for each scan angle when beamforming for maximu gain, and maximum IXR respectively. Fig. 5.20 shows the difference in IXR

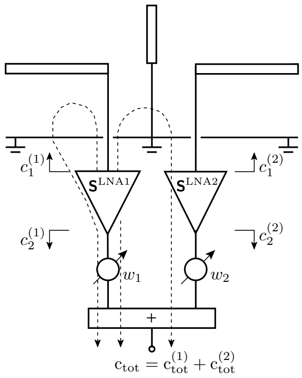

(a)

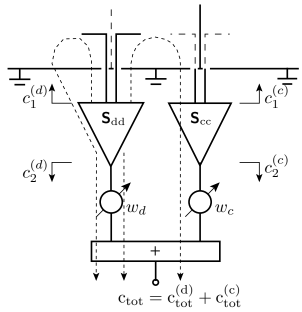

(b)

Figure 5.14: Dual mode receiver (a) Common mode (b) Differential mode (from [90])

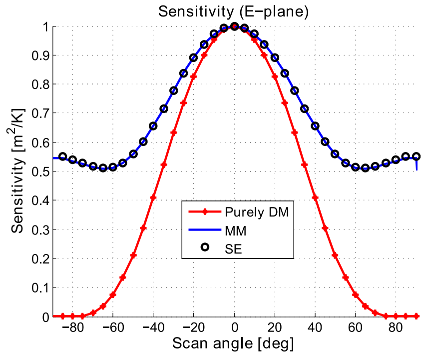

(a)

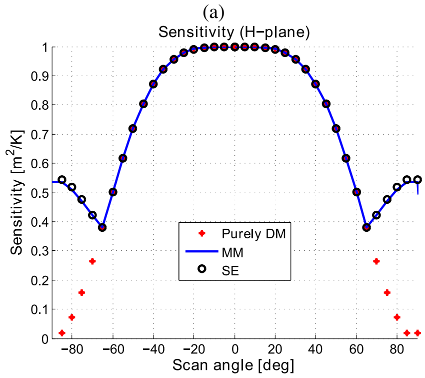

(b)

Figure 5.15: Sensitivity (a) E-plane (b) H-plane (from [90])

obtained by a normal crossed-dipole antenna, and the QMA. It is clear that the crossed-dipole only achieves a good IXR over a small region around zenith, whereas the QMA shows excellent IXR over a broad scan range.

5.4.4 Further improvements

The development of the QMA concept was to continue for a number of years in a quest for wider bandwidth, and to better control the matching of the fourth mode. Firstly, the crossed dipole was replaced by an etched, crossed bow-tie antenna, and the cylindrical sheath by a conical one, as shown in Fig. 5.21, and then a tapered-slot antenna was implemented in the gaps between the bow-ties, as shown in Fig. 5.23. From Figs. 5.22 and 5.24, it is clear that both modifications improved the matching bandwidth, but that the addition of the TSA was the final required step to create a QMA with all four modes matched over a wide bandwidth.

These antennas were evaluated for different beam-forming strategies in [94], manufacturability [92], and quality of IXR [93]. In terms of radio astronomy

the scattering parameters $\{S$, S $\}$ or $\{S_{dd}, S_{cc}\}$ for the SE and MM representations, respectively.

A. Receiver Noise

normalized sensitivity, in both the E- and H-planes, of the MM receiver is compared to the sensitivity of a conventional differential receiver in Figs. 13(a) and (b), respectively.

Fig. 13. Purely differential and dual-mode sensitivity (a) E-plane and (b) H-plane.

Fig. 13 indicates that, regardless of the increase in the equivalent noise temperature attributed to the CM present in the MM receiver, the utilization of CM propagation can result in an increase in the sensitivity over the entire FoV coverage when compared to the conventional receivers where CM is completely rejected. The variation in sensitivity of less than 50% in the E- and 60% in the H-plane. A comparison between the variation in sensitivity in Fig. 13 and the gain variation depicted in Fig. 11 shows that the variation in sensitivity corresponds to the gain variation in both planes.

As a final validation of the MM receiver model presented in this paper, Fig. 13 shows that the MM sensitivity analysis produces the same result obtained when analyzing the antenna and receiver using the equivalent SE S-matrix $\mathbf{S}_{SE}^{ant}$ and EEPs $f_1(\theta,\phi)$ and $f_2(\theta,\phi)$ with the corresponding SE complex beamforming vector $\mathbf{w} = [w_1 \; w_2]^T$ solved for maximum sensitivity at each scan angle.

VI. Conclusions and Recommendations

With the theoretical framework presented in this paper, single-polarized active receiving antennas can be modeled

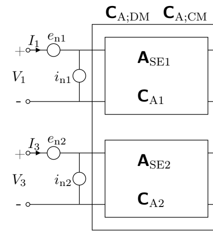

(a)

Fig. 14. Equivalent noise sour
isolated LNAs in (a) chain re

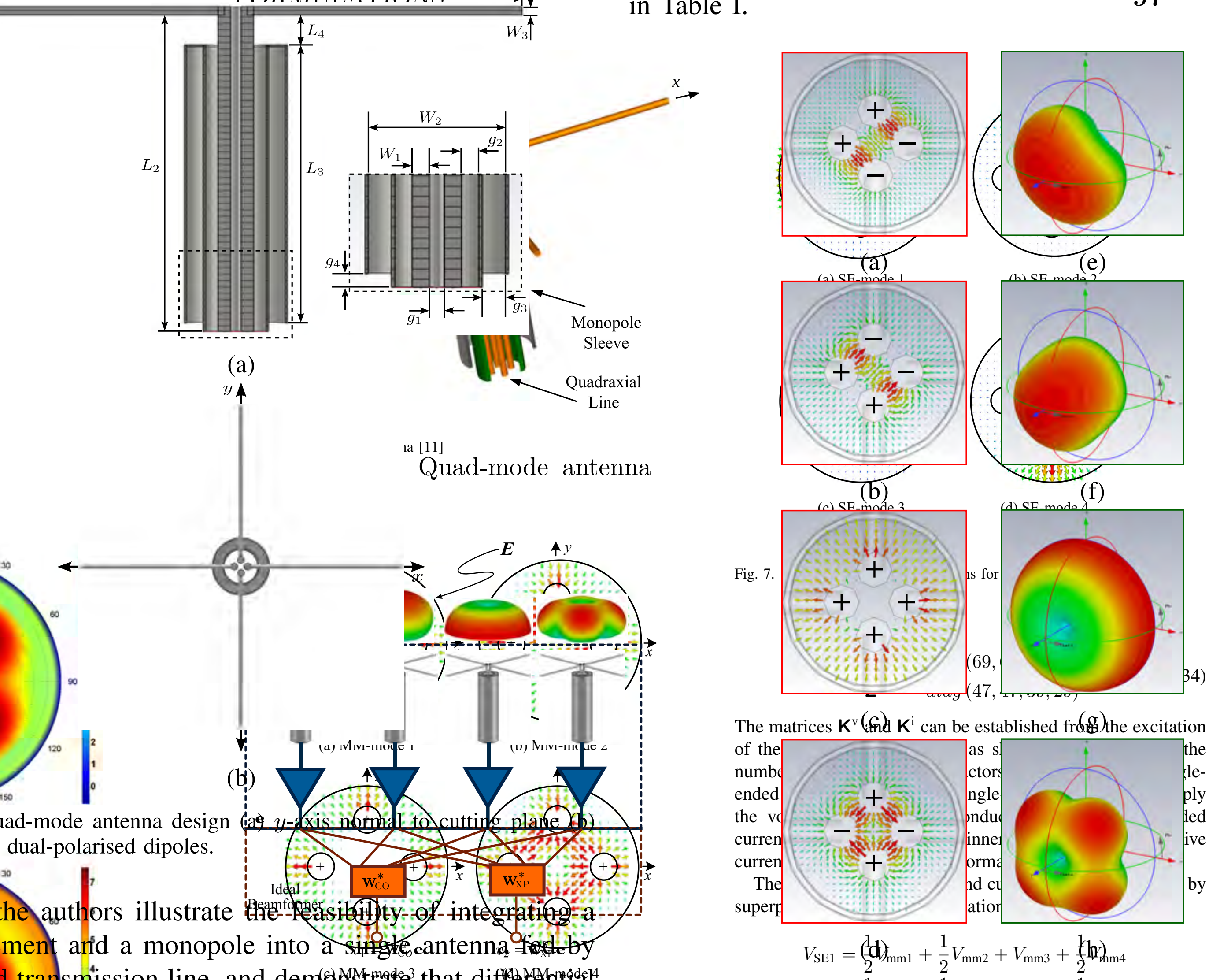

Figure 5.17: Quad-mode antenna (from [9]).

Figure 5.18: Quad-mode excitations and corresponding far-field radiation patterns (from [9]).

applications, the project reached its culmination in a theoretical study which compared a telescope station of the LOFAR array with an array of QMA-elements of exactly the same size and placement. (The LOFAR telescope consists of 48 stations containing two distinct arrays of 96 dual-polarized antenna elements each: an irregular array of inverted V-dipoles, referred to as Low Band Antennas (LBAs) which operates from 10 MHz to 90 MHz, and a more dense array of High Band Antennas (HBAs) operating from 110 MHz to 240 MHz.) The physical layout of the LOFAR LBA configuration at Onsala Observatory is shown in Fig. 5.25, and a comparison of the maximum possible array gains for the array using QMA-elements, LBA-elements and ideal point source radiators, in Fig. 5.26. It is clear that the use of QMA-elements results in significantly higher gain values towards the horizon.

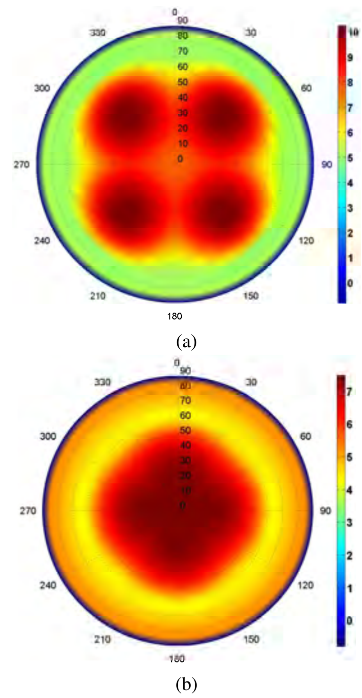

Figure 5.19: Quad-mode antenna gain when beamforming for (a) maximum gain and (b) optimum IXR at each scan angle (from [91]).

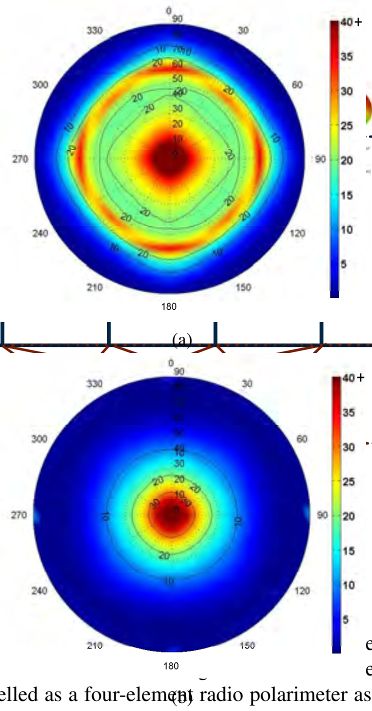

Figure 5.20: Simulated IXR at 1GHz over the hemispherical FoV of (a) quad- mode antenna and (b) conventional dual-polarised dipoles (from [91]).

5.4.5 Multi-mode antennas in communication systems

While the development of a multi-mode antenna was intended for radio astronomy purposes, the applications of such an antenna to wireless communications, especially the so-called *Multiple-Input-Multiple-Output* (MIMO) systems, soon became obvious. In MIMO, an effective system gain, called the *diversity gain*, is obtained by using diverse signal paths, and is optimal for completely independent paths. The QMA offers four fully orthogonal patterns and therefore satisfies this criteria optimally in some directions. Furthermore, the wide field-of-view of the QMA is a sought-after characteristic of small base-station antennas.

The first investigation into the cross-over from radio astronomy to wireless communications looked at the use of communications system analysis to evaluate radio astronomy antennas [96]. This paper aimed to illustrate that the techniques used to characterise the Random-Line-of-Sight performance of antenna elements in wireless systems, can readily be applied to the characterisation of antenna elements used in radio astronomy applications. This was followed by a full paper describing the characterisation of the QMA in MIMO

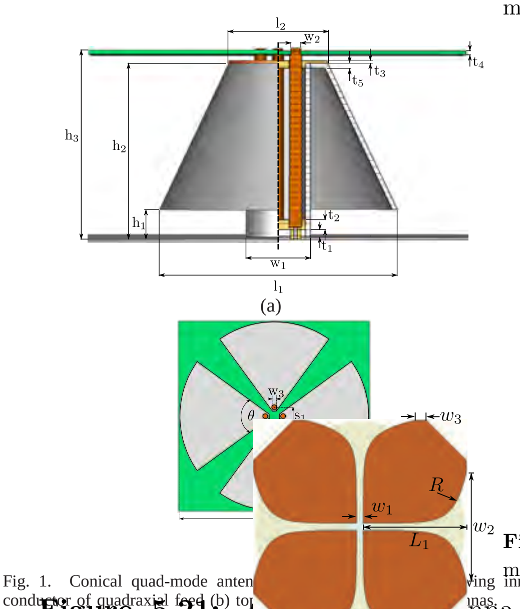

Figure 5.21: ... nna with bow-tie (from [92])

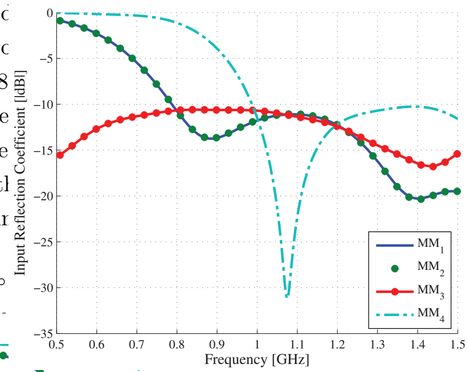

Figure 5.22: Matching of QMA with bow-tie (from [88])

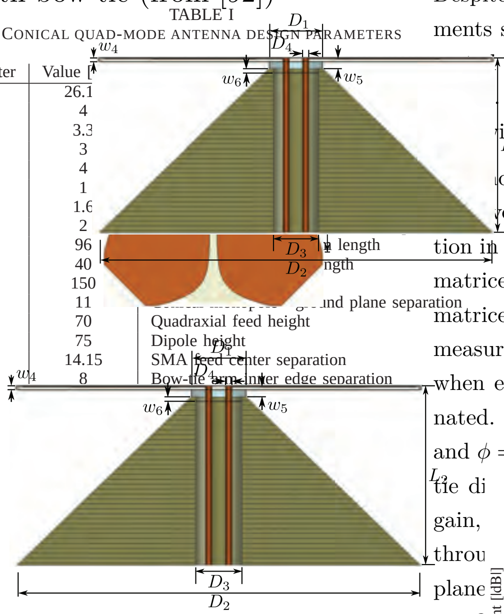

Figure 5.23: Quad-mode antenna with TSA (from [93])

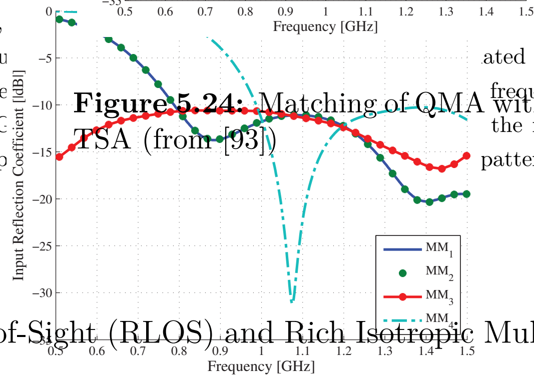

Figure 5.24: Matching of QMA with TSA (from [93])

scenarios [97], in both Random-Line-of-Sight (RLOS) and Rich Isotropic Multipath (RIMP) environments.

During the same period, both the crossed-bowtie and tapered-slot versions of the QMA were awarded patents [98][99]. This led to an award from the South African government's Technology Innovation Agency (TIA) seed fund, which supports the development of innovative ideas into commercial products,

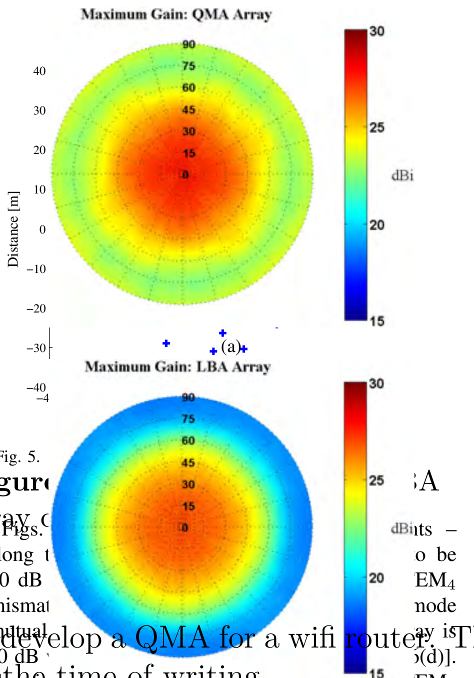

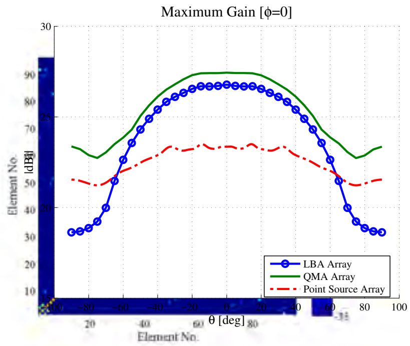

Figure 5.26: Comparison of the maximized gain of the QMA and LBA arrays with an array of hemispherically radiating point source elements (from [95]).

to develop a QMA for a wifi router. This work has been completed successfully at the time of writing.

5.4.6 General Scattering Parameter transformations applied to antennas

One of the unexpected outcomes of the work on multi-mode antennas was the development of circuit analysis formulations in terms of modes instead of ports. This can be classified under the general topic of mixed-mode formulations, and although a large body of work existed in this field prior to 2015, formulations for multi-mode antennas, general multi-mode networks, and networks with coupled ports did not exist at this time.

The mixed-mode sensitivity analysis discussed in section 5.4.2 formed the starting point of this work which, in addition to [90], led to work specifically on mixed-mode noise modelling. The first basic work for differential-mode LNA's was reported in [100] and [101] as a result of the Master's degree work of Dr [illegible]. Following [illegible] PhD work, this work was extended to full, general, mixed-mode systems [102]. Of particular significance in this last paper, is the development of a general mixed-mode noise correlation matrix, the first formulation of its kind in literature. This enables designers of mixed-mode systems to perform the full design and analysis, including noise, in the mixed-mode domain.

The culmination of this work however, was a general formulation named the *Generalized Multi-Mode Scattering Matrix Transformation*, which extended the network theory at the time to include completely general modal sets consisting of arbitrary combinations of coupled ports with arbitrary weighting. In addition, it showed that not only circuit parameters could be transformed, but also the radiation patterns of multi-mode antennas [103]. Especially the extension to general and coupled system is very powerful, as it allows any set of single-ended measurements, including antenna measurements, to be transformed to any set of mixed-mode parameters.

To perform a transformation, the port voltages and currents of one network (network B) must be expressed as linear combinations of any or all of the port voltages and currents of another network (network A). In terms of Fig. 5.27 the port voltages and currents become

$$V_n^B = k_{n1}^v V_1^A + k_{n2}^v V_2^A + \dots + k_{nN}^v V_N^A$$
$$I_n^B = k_{n1}^i I_1^A + k_{n2}^i I_2^A + \dots + k_{nN}^i I_N^A \qquad (5.1)$$
$$\text{for} \quad n = 1, \dots, N$$

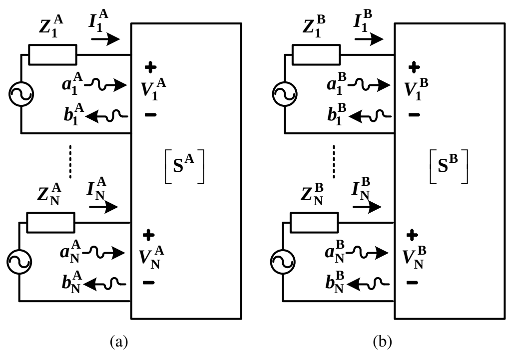

Figure 5.27: Muli-port Networks (from [103])

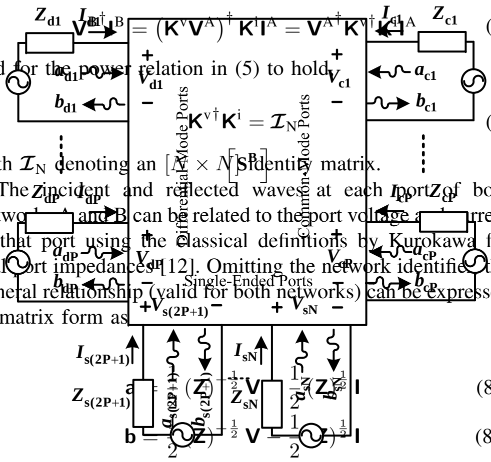

Figure 5.28: General mixed-mode network (from [103])

By defining matrices $\mathbf{M}_S$ and $\mathbf{M}_C$ in terms of matrix forms of the k-values and diagonal matrices containing the port impedances of each network, an expression for the incident and reflected waves can be derived.

$$\mathbf{M}_S = \frac{1}{2}\left(\mathbf{Z}^B\right)^{-\frac{1}{2}} \mathbf{K}^v \left(\mathbf{Z}^A\right)^{\frac{1}{2}} + \frac{1}{2}\left(\mathbf{Z}^B\right)^{\frac{1}{2}} \mathbf{K}^i \left(\mathbf{Z}^A\right)^{-\frac{1}{2}} \qquad (5.2a)$$
$$\mathbf{M}_C = \frac{1}{2}\left(\mathbf{Z}^B\right)^{-\frac{1}{2}} \mathbf{K}^v \left(\mathbf{Z}^A\right)^{\frac{1}{2}} - \frac{1}{2}\left(\mathbf{Z}^B\right)^{\frac{1}{2}} \mathbf{K}^i \left(\mathbf{Z}^A\right)^{-\frac{1}{2}} \qquad (5.2b)$$

$$\mathbf{a}^B = \mathbf{M}_S \mathbf{a}^A + \mathbf{M}_C \mathbf{b}^A \qquad (5.3a)$$
$$\mathbf{b}^B = \mathbf{M}_C \mathbf{a}^A + \mathbf{M}_S \mathbf{b}^A \qquad (5.3b)$$

nique is especially useful for the transformation of antenna far-fields. It is shown that the antenna far-fields generated by arbitrary multi-mode excitations can be successfully calculated from a set of far-fields generated by single-ended excitations of the transformed network using the same transformation as applied to the S-parameters. This makes it possible to determine multi-mode antenna far-fields from a set of single-ended measurements, such measurements being significantly easier to perform than multi-mode measurements.

II. S-Parameter Transformations

To develop the theory, consider an N-port network excited in two different ways to form two equivalent N-port networks A and B as shown in Fig. 1. Each network is described by an S-matrix $\mathbf{S}^{A,B}$, with port voltages $(V_n^{A,B})$, port currents $(I_n^{A,B})$, and port impedances $(Z_n^{A,B})$ indicated for both networks. In addition, the incident $(a_n^{A,B})$ and reflected $(b_n^{A,B})$ waves are also shown at each port. For the case where the port voltages and port currents of network B are linear combinations of the voltages and currents of network A, the aim is to establish a transformation from $\mathbf{S}^A$ to $\mathbf{S}^B$ for an arbitrary set of port impedances. A typical scenario would for instance be one where network A consists of N single-ended ports, each terminated by the same reference impedance, and network B of sets of differential ports and possible single-ended ports, each terminated by a different impedance.

Fig. 1. N-port networks with ports using (a) mode set A and (b) mode set B

For the completely general case, the port voltages and currents of network B can be expressed as linear combinations of any or all of the port voltages and currents of network A. That is,

$$V_n^B = k_{n1}^v V_1^A + k_{n2}^v V_2^A + \dots + k_{nN}^v V_N^A$$
$$I_n^B = k_{n1}^i I_1^A + k_{n2}^i I_2^A + \dots + k_{nN}^i I_N^A \qquad (1)$$
$$\text{for} \quad n = 1, \dots, N$$

or

$$\mathbf{V}^B = \mathbf{K}^v \mathbf{V}^A \qquad (2a)$$
$$\mathbf{I}^B = \mathbf{K}^i \mathbf{I}^A \qquad (2b)$$

where $\mathbf{V}^{A,B}$ and $\mathbf{I}^{A,B}$ denote $[N \times 1]$ matrices containing the port voltages and currents of networks A and B and $\mathbf{K}^{v,i}$ are $[N \times N]$ matrices as in (3) and (4).

$$\mathbf{K}^v = \begin{bmatrix} k_{11}^v & k_{12}^v & \cdots & k_{1N}^v \\ \vdots & \vdots & \ddots & \vdots \\ k_{N1}^v & k_{N2}^v & \cdots & k_{NN}^v \end{bmatrix} \qquad (3)$$

$$\mathbf{K}^i = \begin{bmatrix} k_{11}^i & k_{12}^i & \cdots & k_{1N}^i \\ \vdots & \vdots & \ddots & \vdots \\ k_{N1}^i & k_{N2}^i & \cdots & k_{NN}^i \end{bmatrix} \qquad (4)$$

While $\mathbf{K}^v$ and $\mathbf{K}^i$ can in general be chosen independently, a choice which guarantees the conservation of power under the transformation makes more physical sense, and will also be seen to reduce to the standard formulations in the case of differential and common-mode descriptions. In this case, the total complex power in networks A and B are set to be equal, requiring from Tellegen's theorem that the sum of the products of each port voltage and current remains constant under the transformation, as shown in (5).

$$\mathbf{V}^{A\dagger}\mathbf{I}^A = \mathbf{V}^{B\dagger}\mathbf{I}^B \qquad (5)$$

where † denotes the conjugate transpose. From (2a) and (2b)

$$\mathbf{V}^{B\dagger}\mathbf{I}^B = \left(\mathbf{K}^v\mathbf{V}^A\right)^\dagger \mathbf{K}^i\mathbf{I}^A = \mathbf{V}^{A\dagger}\mathbf{K}^{v\dagger}\mathbf{K}^i\mathbf{I}^A \qquad (6)$$

and for the power relation in (5) to hold

$$\mathbf{K}^{v\dagger}\mathbf{K}^i = \mathcal{I}_N \qquad (7)$$

with $\mathcal{I}_N$ denoting an $[N \times N]$ identity matrix.

The incident and reflected waves at each port of both network A and B can be related to the port voltage and current at that port using the classical definitions by Kurokawa for real port impedances [12]. Omitting the network identifier, the general relationship (valid for both networks) can be expressed in matrix form as

$$\mathbf{a} = \frac{1}{2}(\mathbf{Z})^{-\frac{1}{2}}\mathbf{V} + \frac{1}{2}(\mathbf{Z})^{\frac{1}{2}}\mathbf{I} \qquad (8a)$$
$$\mathbf{b} = \frac{1}{2}(\mathbf{Z})^{-\frac{1}{2}}\mathbf{V} - \frac{1}{2}(\mathbf{Z})^{\frac{1}{2}}\mathbf{I} \qquad (8b)$$

or alternatively as

$$\mathbf{V} = (\mathbf{Z})^{\frac{1}{2}}(\mathbf{a}+\mathbf{b}) \qquad (9a)$$
$$\mathbf{I} = (\mathbf{Z})^{-\frac{1}{2}}(\mathbf{a}-\mathbf{b}) \qquad (9b)$$

Fig. 4. N-port network with differential/common-mode ports and single-ended ports

any modification. For the combination treated by Ferrero, the port voltages and currents for the differential/common-mode ports of network B are defined as in (27) for $\mathbf{V}^B$ and $\mathbf{I}^B$, respectively, and $\mathbf{Z}$ is a diagonal matrix containing the characteristic port impedances as shown in (10).

$$\mathbf{Z} = \begin{bmatrix} Z_1 & \cdots & 0 \\ \vdots & \ddots & \vdots \\ 0 & \cdots & Z_N \end{bmatrix} \qquad (10)$$

$$\mathbf{V}^A = \begin{bmatrix} V_1 \\ \vdots \\ V_N \end{bmatrix} \mathbf{I}^A = \begin{bmatrix} I_1 \\ \vdots \\ I_N \end{bmatrix} \mathbf{V}^B = \begin{bmatrix} V_{d1} \\ \vdots \\ V_{dP} \\ V_{c1} \\ \vdots \\ V_{cP} \\ V_{s(2P+1)} \\ \vdots \\ V_{sN} \end{bmatrix} \mathbf{I}^B = \begin{bmatrix} I_{d1} \\ \vdots \\ I_{dP} \\ I_{c1} \\ \vdots \\ I_{cP} \\ I_{s(2P+1)} \\ \vdots \\ I_{sN} \end{bmatrix} \qquad (31)$$

The $\mathbf{K}$ matrices can simply be extended by the addition of a unity matrix to allow for this case, as in (32)

$$\mathbf{K}^v = \begin{bmatrix} \begin{matrix} 1 & -1 & \cdots & 0 \\ \vdots & \ddots & \ddots & \vdots \\ 0 & \cdots & 1 & -1 \\ \frac{1}{2} & \frac{1}{2} & \cdots & 0 \\ \vdots & \ddots & \ddots & \vdots \\ 0 & \cdots & \frac{1}{2} & \frac{1}{2} \end{matrix} & [\mathbf{0}] \\ [\mathbf{0}]^T & \begin{matrix} 1 & \cdots & 0 \\ \vdots & \ddots & \vdots \\ 0 & \cdots & 1 \end{matrix} \end{bmatrix} \quad \mathbf{K}^i = \left(\mathbf{K}^{v\dagger}\right)^{-1} \qquad (32)$$

where $[\mathbf{0}]$ denotes a $[2P \times (N-2P)]$ zero matrix. Finally, the diagonal port impedance matrices are given by (33).

$$\mathbf{Z}^A = diag\left(Z_1 \dots\right.$$
$$\mathbf{Z}^B = diag\left(Z_{d1} \dots\right.$$

In terms of scattering parameters, $\mathbf{b}^{\mathrm{A}} = \mathbf{S}^{\mathrm{A}}\mathbf{a}^{\mathrm{A}}$ and $\mathbf{b}^{\mathrm{B}} = \mathbf{S}^{\mathrm{B}}\mathbf{a}^{\mathrm{B}}$, and it follows that $\mathbf{S}^{\mathrm{B}}$ can be expressed in terms of $\mathbf{S}^{\mathrm{A}}$ by

$$\mathbf{S}^{\mathrm{B}} = \left(\mathbf{M}_{\mathrm{C}} + \mathbf{M}_{\mathrm{S}}\mathbf{S}^{\mathrm{A}}\right)\left(\mathbf{M}_{\mathrm{S}} + \mathbf{M}_{\mathrm{C}}\mathbf{S}^{\mathrm{A}}\right)^{-1} \tag{5.4}$$

A very important special case occurs when the port impedances of network B are related to the port impedances of network A by (5.5).

$$\mathbf{Z}^{\mathrm{B}} = \mathbf{K}^{\mathrm{v}}\,\mathbf{Z}^{\mathrm{A}}\,\left(\mathbf{K}^{\mathrm{i}}\right)^{-1} \tag{5.5}$$

In this case, $\mathbf{M}_{\mathrm{C}} = \mathbf{0}$, and the transformation in (5.4) simply becomes that shown in (5.6).

$$\mathbf{S}^{\mathrm{B}} = \mathbf{M}_{\mathrm{S}}\mathbf{S}^{\mathrm{A}}\left(\mathbf{M}_{\mathrm{S}}\right)^{-1} \tag{5.6}$$

where

$$\mathbf{M}_{\mathrm{S}} = \left(\mathbf{Z}^{\mathrm{B}}\right)^{-\frac{1}{2}}\mathbf{K}^{\mathrm{v}}\left(\mathbf{Z}^{\mathrm{A}}\right)^{\frac{1}{2}} \tag{5.7}$$

Note that this special case is the one most widely used for the transformation of single-ended S-parameters to mixed-mode S-parameters, often erroneously. The new formulation thus removed the restriction, and allowed for arbitrary impedances. In practice, the choosing of port impedances also allow for multi-line coupled-line networks to be used. A general example of transforming single-ended S-parameters to a mixed-mode set is shown in Fig. 5.28, where the mixed-mode network consists of differential ports, common-mode ports, and single-ended ports.

Figs. 5.29 and 5.30 show the effect of using this transformation on the four radiation modes of the quadraxial line feed of the QMA. In Fig. 5.29, each line of the quadraxial line is excited in turn, with the other three terminated, giving four single-ended radiation patterns. When transformed to four modal excitations, the patterns in Fig. 5.30 result.

This transformation of radiation patterns was used to experimentally verify various QMA's. As it is virtually impossible to apply modal excitations in a practical measurement setup, the antennas were measured using single-ended excitations on each conductor of the quadrixial line successively, and the full set of measurements could then be transformed to the modal case, and compared to the theoretical modal patterns. An example for one QMA is shown in Fig. 5.31.

5.4.7 General Scattering Parameter transformations applied to multi-conductor lines

The General Scattering Parameter transformation, once developed, was a promising technique to apply to networks. Multi-conductor transmission lines especially have been the focus of many modelling algorithms, as it forms part

$$\bar{\mathbf{F}}^{MM} = \begin{bmatrix} f_1^{MM}(\theta,\phi) \\ \vdots \\ f_N^{MM}(\theta,\phi) \end{bmatrix} = \left[\mathbf{M}_S + \mathbf{M}_C \mathbf{S}^{SE}\right] \bar{\mathbf{F}}^{SE}. \quad (40)$$

From these fields, the gain of the antenna for each multi-mode excitation can be calculated. Using the same simulated example as in section IV, the radiated electric far-fields for the four single-ended excitations are shown in Fig. 10, with the transformed multi-mode far-fields in Fig. 11.

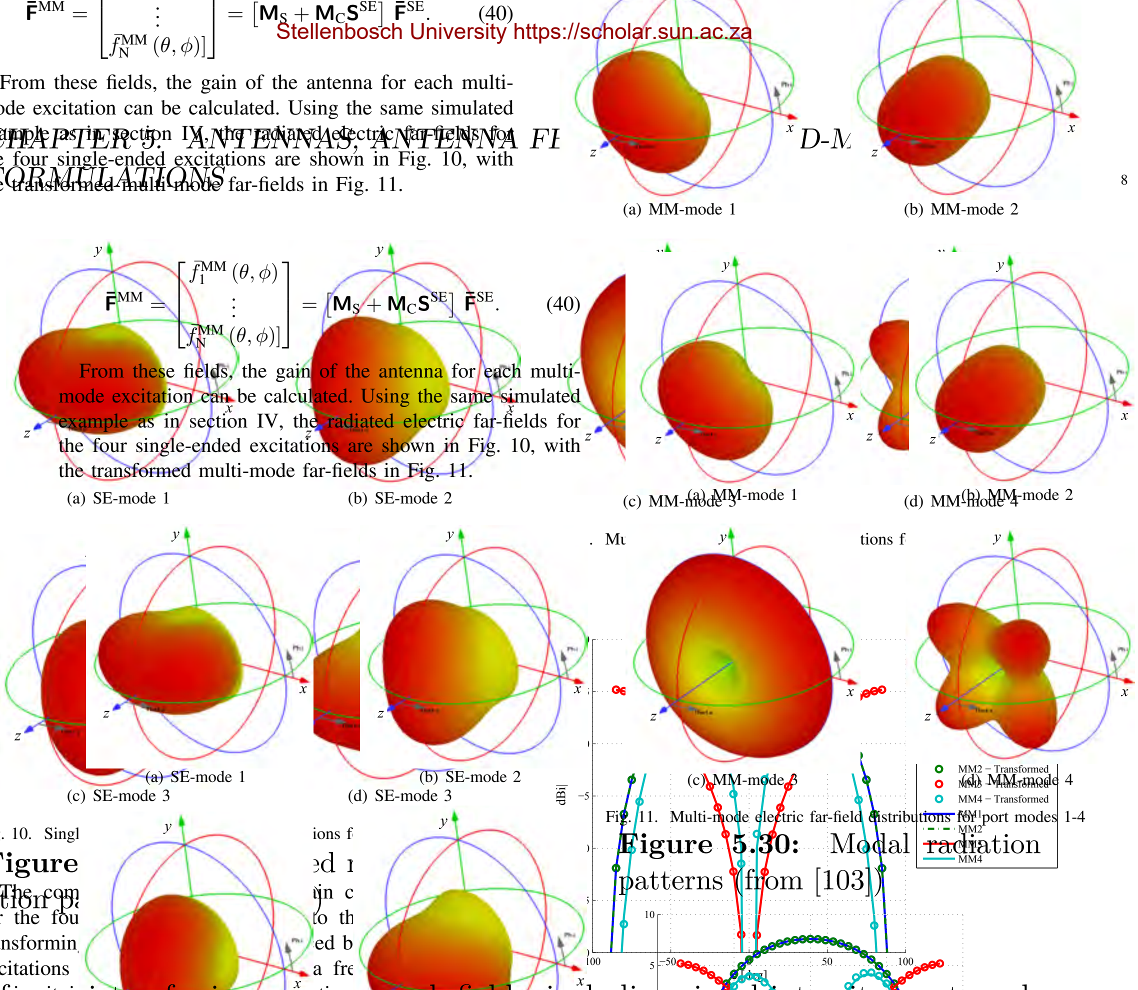

(a) SE-mode 1 (b) SE-mode 2 (c) SE-mode 3 (d) SE-mode 3

Fig. 10. Single-ended electric far-field distributions for port modes 1-4

(a) MM-mode 1 (b) MM-mode 2 (c) MM-mode 3 (d) MM-mode 4

Fig. 11. Multi-mode electric far-field distributions for port modes 1-4

Figure 5.30: Modal radiation patterns (from [103])

of a variety of microwave research fields, including signal integrity, port modelling, and cross-talk. In terms of the application to scattering parameters, only the simple transform of (5.6) has been used in literature. However, this breaks down quite quickly when multiple conductors are used in close proximity, such as ... Fi... the four conductors in very close proximity, creating a system of coupled lines. The electric fields of the four port ... are shown in Fig. 5.33, while the ... are shown in Fig. 5.34.

In ... using the simple transformation of (5.6) on this structure is shown ... S-parameters for the problem is calculated using single-ended port excitations. To obtain the mixed-mode S-parameters, both the simple and the full transformations are calculated, and then compared with the simulated results from CST. In Fig. 5.35, the simple transformation is shown to clearly give erroneous results, while the full transformation gives exactly the correct results.

It should be noted that, at the time of writing, even the CST result was only correct for symmetrical structures. For any other structure, the correct solution could at that stage only be obtained by the full transformation described above.

Using these transformations, one needs only perform one set of analyses of a structure, using single-ended port excitations. The S-parameters of any other combination of excitations can then simply be calculated using the transformation, instead of a new set of analyses. In such a way, a set of excitations

Fig. 12. Comparison of simulated transformed single-ended gains and multi-mode gains

The comparison of the antenna gain calculated by CST for the four multi-mode excitations to those calculated by transforming the four far-fields produced by the single-ended excitations is shown in Fig. 12 for a frequency of 1GHz. Again, it is clear that the transformation gives the correct results. As with the S-parameters, the proposed transformation thus allows for the far-field patterns of multiple sets of multi-mode excitations to be calculated from a single set of single-ended far-fields, without redoing the full electromagnetic analysis. In this case, it is however of even more importance, as antenna simulations are normally quite computationally intensive. The transformation also makes it possible to determine the multi-mode far-fields of the antenna from a set of simple single-ended measurements.

To show this, the procedure was also applied to the measurement of a manufactured quad-mode antenna shown in Fig. 13 [14]. Figs. 14(a) and 14(b) respectively show the comparison between the E-plane and H-plane cuts of the antenna gain of a quad-mode antenna at 1GHz for each of the four fundamental modes. Here, graphs denoted as *CST* are the direct CST time-domain analyses using the fundamental modes of an ideal waveguide port which terminates the quadraxial line, while *Measured* denotes the gain calculated by doing a set of single-ended far-field measurements in an antenna chamber and transforming it to the multi-mode case using (40). For the transformation, the multi-mode characteristic impedances were set to be the same as those used by CST. It is clear that, except for some discrepancy towards the horizon for mode 3 excitation, the two methods agree very well. It should be noted that the measured results are of course affected by any non-idealities in the manufactured antenna, whilst the CST results are for an ideal antenna.

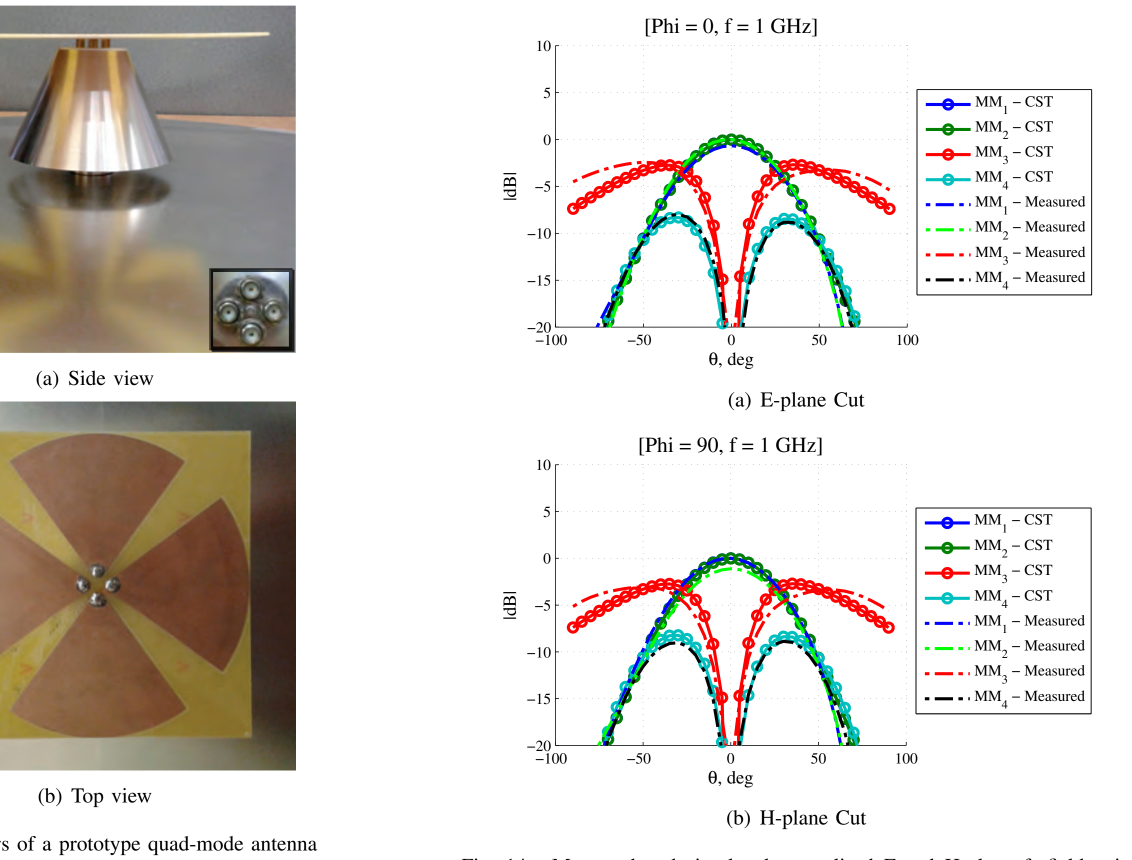

Figure 5.31: Transformed measured pattern cuts (from [103])

which yields optimally low levels of cross-talk can for instance be calculated very quickly by optimising the transformation constants, instead of running full-wave optimisations of the full structure.

The inverse procedure is also possible, and can be used to good effect to simplify problems. In Chapter 2, it was shown that mathematical interpolation models can be used efficiently to model the S-parameters of a network, as a function of one or more variables. For multi-line (or multi-port) networks, this quickly becomes prohibitive, as an N-port network is described by an $N \times N$ S-matrix, requiring N^2 functions to be modelled in general. Using the transformation technique, a set of excitations can however be derived which will ensure that many mixed-mode S-parameters become negligible, requiring no models.

This was illustrated in [105]. In Fig. 5.37, a six-conductor transmission line is shown, running through a thin section of dielectric. The electric fields at the ports are shown in Fig. 5.38 for all single-ended modes, and a set of mixed-modes in which every pair of lines is excited with differential and common modes respectively.

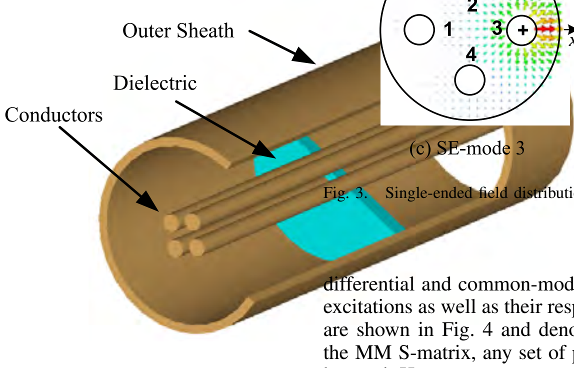

Figure 5.32: Four conductor transmission line (from [104])

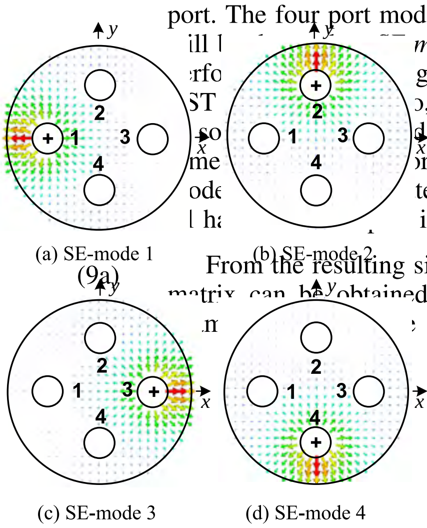

Figure 5.33: Single-ended port electric fields (from [104])

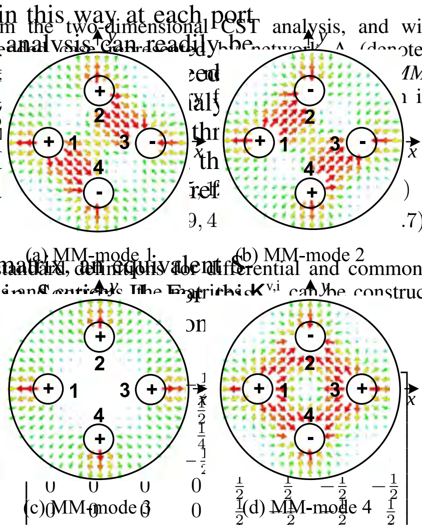

Figure 5.34: Mixed-mode port electric fields (from [104])

The two sets of S-parameters which result are shown in Fig. 5.39, clearly showing that in the second case, the number of S-parameters with magnitudes large enough to be important, has been reduced substantially. For certain cases, a set of excitations can indeed be calculated which would result in a fully orthogonal system, with zero cross-talk between pairs of lines.

5.4.8 Assessment

The 2014 paper ([90]) holds special significance for me, as it was my first paper in the IEEE Transactions on Antennas and Propagation, and as such marked my first move into the antenna arena after almost exactly 20 years of working on microwave circuits. It also made use of a number of concepts from

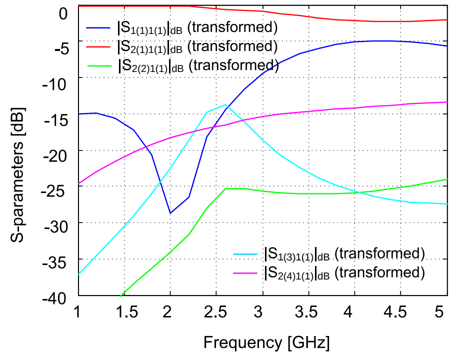

Fig. 7. Comparison of simulated transformed single-ended S-parameters and simulated multi-mode S-parameters using simple transformation

Figure 5.35: S-parameters using simple transformation (from [104])

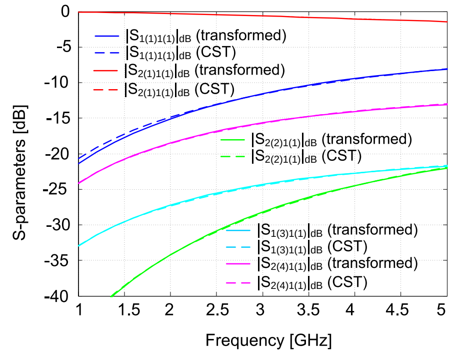

Fig. 6. Comparison of simulated transformed single-ended S-parameters and simulated multi-mode S-parameters

Figure 5.36: S-parameters using full transformation (from [104])

Petrie Meyer

ACKNOWLEDGMENT

The authors thank CST for providing software and support, as well as the NRF for financial assistance.

pin separately, with all the other pins connected to terminated transmission lines. This measurement can then be used instead of the single-mode analysis. In practice, a standard 50 ohm line can be used and de-embedded from the measurement. Also, as no restrictions were placed on the voltage transformation matrix, it should be evident that the transformation makes ...e one set of single-ended S-parameters to ...arameters for any set of modes, without re-...ctromagnetic analysis.

IV. CONCLUSION

...hows how the generalized multi-mode scat-... transformation can be used for the analysis ...r transmission lines. A four-port example is ...ate the technique, but the technique is not ...c numbers or lines, or any specific sets of ...shown that the S-parameters for multi-mode ...sily be calculated from a single set of single-...s.

REFERENCES

[1] D. Bockelman and W. Eisenstadt, "Combined differe... mode scattering parameters: theory and simulation," ...crowave Theory Tech., vol. 43, no. 7, Jul. 1995, pp. ...
[2] P. Meyer and D. Prinsloo, "Generalized Multi-Mode ... eter and Antenna Far-Field Conversions," IEEE Tra... Propagation, submitted December 2014.
[3] A. Huynh, P. Hakansson, and S. Gong, "Mixed-... conversion for networks with coupled differential ... European Microwave Conference, Munich, Oct. 2007
[4] D. Prinsloo, P. Meyer, R. Maaskant, and M. Iva... an active dual-mode antenna with near hemispheri... coverage," Int. Conf. on Electromagnetics in Adva... (ICEAA), Sep. 2013, pp. 1064-1067.
[5] D. Prinsloo, P. Meyer, M.V. Ivashina, and R. Ma... mode antenna for accurate polarimetric measureme... wide field-of-view," 8th European Conf. on Antenna... (EuCAP), April 2014, pp. 3794-3797.
[6] T.S. Beukman, M. Ivashina, R. Maaskant, P. Meyer, C. Bencivenni, "A quadraxial feed for ultra-wide bandwidth quadruple-ridged flared horn antennas", 8th European Conference on Antennas and Propagation (EuCAP 2014), The Hague, The Netherlands, 6-11 April 2014.
[7] D. Prinsloo, R. Maaskant, M.V. Ivashina, and P. Meyer, "Mixed-mode sensitivity analysis of a combined differential and common mode active receiving antenna providing near-hemispherical field-of-view coverage," IEEE Trans. Antennas and Propagation, vol. 62, no. 8, August 2014, pp. 3951-3961.
[8] K. Kurokawa, "Power waves and the Scattering matrix," IEEE Trans. Microwave Theory Tech., vol. MTT-13, no. 3, pp. 194-202, Mar. 1965.

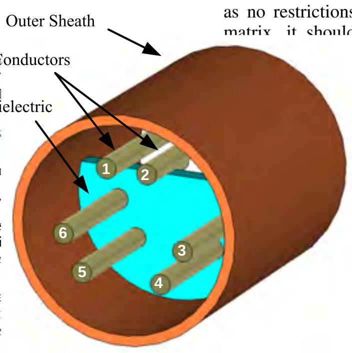

Figure 2: Six-conductor transmission line

Figure 5.37: Six conductor transmiaasion line (from [105])

the circuit world. Such equivalent sets of non-physical ports, noise analysis, and mixed-mode S-parameters. Personally I therefore view this is a landmark paper in my research career. The work also led to my first joint patents, which was a milestone of a different nature.

I believe the work itself established and developed a number of concepts which will become part of the basic theory used to treat the more general class of multi-mode antennas, and multi-mode networks. Especially the improved transformation techniques, the transformations on antenna patterns, and the demonstration of improvements in various metrics in both the radio astronomy world and the communications world, are important concepts for not only the QMA, but any antenna or system making use of multiple sets of excitations.

An infinite number of sets of S-parameters can be calculated for this structure. For the purposes of this paper, only two will be shown. Firstly, each conductor can be excited at each of its ports, with all the others terminated in 50 ohm loads. Such an analysis can readily be performed using a single-ended multi-pin waveguide feed in CST Microwave Studio, with a fast two-dimensional analysis to solve the port impedance for each mode, and a full three-dimensional analysis for the S-matrix. The six port modes established in this way at each port will be denoted as *SE-modes*. The electric field patterns for this set are shown in Fig. 3(a). For six lines at each of two ports, this results in a 12x12 complex S-matrix. For simplicity, only a dependence on frequency will be used here. To model this problem using surrogate models, 144 one-variable models are therefore required. While this can be reduced substantially using reciprocity and symmetry in the longitudinal direction, the dielectric disc reduces the number of symmetries in the transverse plane.

Using the generalized multi-mode S-parameter transformation, various other sets of S-parameters can be computed from the single-ended set, without any additional full-wave analyses. A typical set for this structure is the one obtained by exciting each set of two conductors with both common-mode and differential-mode signals at each port. These excitations as well as their respective electric field distributions are shown in Fig. 3(b) and denoted as *MM-modes*. To calculate the MM S-matrix, any set of port impedances can in principle be used. Here, the port impedance calculated for each MM-mode by a fast two-dimensional analysis in CST is used. For this analysis, each mode of the set is excited using a multi-pin feed with the indicated polarity.

From the two-dimensional CST analysis, and with the single-ended case represented by network A (denoted *SE*) and the multi-mode case by network B (denoted *MM*), the impedance matrices necessary for the transformation in (10) are shown in (14).

$$\begin{aligned} \mathbf{Z}^{\mathrm{SE}} &= diag\,(50) \\ \mathbf{Z}^{\mathrm{MM}} &= diag\,(138, 138, 138, 138, 138, 138, 70, 70, 70, 70, 70, 70) \end{aligned} \tag{14}$$

From standard definitions for differential and common-mode voltages and currents, the matrices

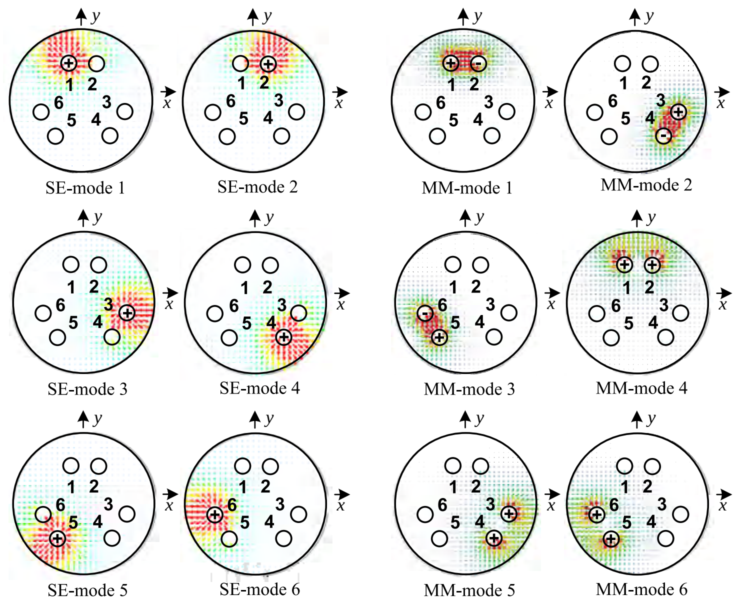

Figure 3: Electric field distributions for port modes

Figure 5.38: Six conductor transmission line port electric fields (from [105])

Petrie Meyer

$\mathbf{K}^{v,1}$ can be constructed as in (15)

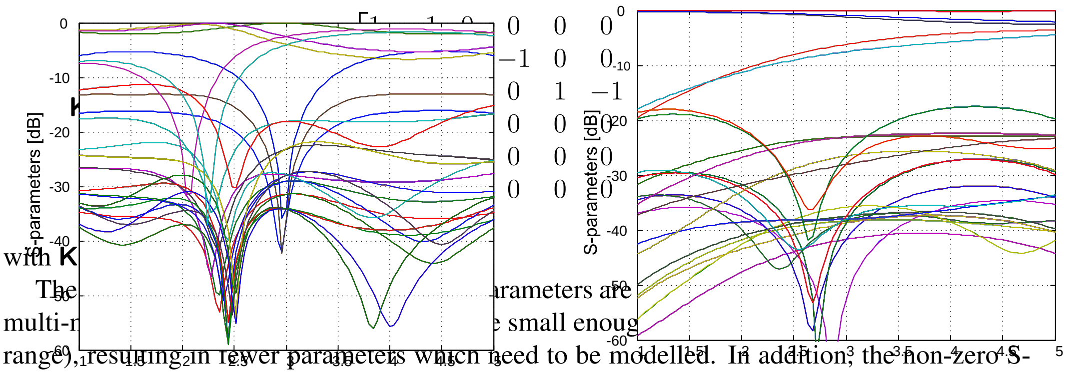

Figure 4: Single-ended and multi-mode S-parameters

Figure 5.39: Six conductor transmission line S-parameters (from [105])

with $\mathbf{K}$

The ... parameters are ... multi-... small enough range), resulting in fewer parameters which need to be modelled. In addition, the non-zero S-parameters frequently occur in identical sets, and in general show less variation as functions of frequency than the single-ended set. This requires lower order surrogate functions for a similar modelling accuracy. Taken in combination, the change in the choice of excitation functions will result in a significant simplification of the required multiport surrogate model.

The given multi-mode set is of course only one example, and in general, each problem can be analyzed in order to find the optimum transformation matrix which will result in the smallest S-parameter set which can be modelled with the lowest order functions. The transformation technique has very few limitations mathematically, and can be included into most surrogate algorithms very easily as a data pre-conditioning step.

5.5 Reflector antenna feeds

In parallel with the work on the multi-mode antennas, 2013 also saw a second of my PhD students, Dr Theunis Beukman, also co-supervised by Profs Marianna Ivashina and Rob Maaskant at Chalmers University, start work on the other main SKA topic, that of very wideband waveguide feeds for reflector antennas

4 CONCLUSION

This paper shows how the generalized multi-mode scattering parameter transformation can be used to reduce the required number and order of modelling functions required to create an accurate surrogate model. A twelve-port, six-line transmission line problem is used here as an example, but the technique is not limited to specific numbers of lines, or any specific sets of excitations.

ACKNOWLEDGEMENT

The authors thank CST for providing software and support.

REFERENCES

[1] P. Meyer, D.S. Prinsloo, Generalized Multi-Mode Scattering Parameter and Antenna Far-Field Conversions. *IEEE Trans. Antennas and Propagation*, **63**, 4815-4825, 2015.

[2] P. Meyer, Multi-Conductor Transmission Line Analysis Using the Generalized Multi-Mode S-parameter Transformation. *19th IEEE Workshop on Signal and Power Integrity*

[106].

For radio astronomy, bandwidth is normally of very high importance, and for the SKA a frequency range of 1-20 GHz is envisaged for the reflector array. This is an exceedingly complex problem, as not only does the input reflection match have to be sufficiently good over a 1:20 bandwidth, but the illumination of the reflector has to ideally be constant in terms of beam width and phase centre over this whole band. The *quadruple-ridged flared horn (QRFH)* antenna is one of the best candidates to achieve bandwidths approaching this, as it offers unique abilities to control the beamwidth over very wide frequency ranges, using combinations of higher order waveguide modes at the feed aperture. The control of these modes is however very difficult, and most QRFH antennas suffer from certain problems caused by uncontrolled modes.

The basic structure of a QRFH is shown in Fig. 5.40, with a cross-section of the flared ridges in Fig. 5.41. Virtually all design procedures at the time approximated the flare curve using exponential curves, and simply optimised the whole structure. As such an optimisation should ideally include the reflector, these optimisations ran for weeks at a time.

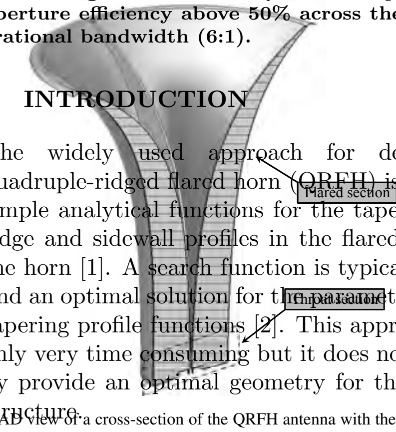

Figure 5.40: QRFH structure (from [107])

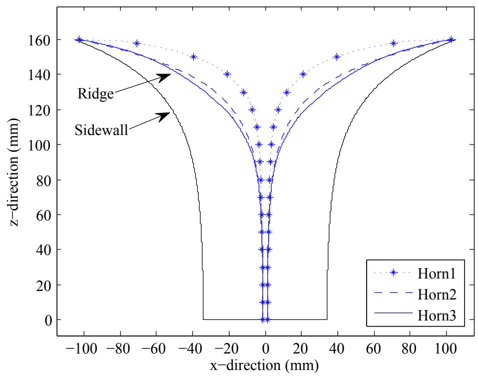

Figure 5.41: Cross-section of flared ridges (from [108])

Our first work on this problem was actually an extension of a standard orthomode transducer for a quad-ridge waveguide, using a novel offset coaxial feed. This work was undertaken by my post-doctoral fellow of the time, Dr du Villiers, and my colleague Prof Keith Palmer [109], [110]. This proposal, however, resulted in a very long structure. The classical flared TEM horn was also investigated, but again, this results in long structures, and in this case, very difficult to extend to two polarisations [111].

For Dr Beukman's PhD, we followed a whole philosophy centred on the control of the aperture field modal content, and the design of the structure in terms of modes at every cross-section, instead of optimisation. In the initial phase, the problem of the coaxial-to-waveguide transition was addressed. In standard QRFH-antennas, this is done by running a very thin coaxial line cross-wise through one of the (thin) ridges, and extending the centre conductor across the gap, as shown in Fig. 5.42(b). Such a transition however generates multiple modes right at the base of the horn, requiring the control of all these modes throughout the whole length of the horn. To solve this problem, the structure in Fig. 5.42(a) was proposed [107], [112]. This structure used a novel *quadraxial feed*, where a four-line transmission line (a quadraxial line) feeds directly via four lines into each of the four ridges.

The advantage of the quadraxial feed is that a very pure single-mode excitation can be applied by simply exciting the four pins correctly. The effect of this is quite dramatic, as shown in Fig. 5.43, where Fig. 5.43(a) shows the magnitudes of the modes excited at the base of the horn using the conventional feed, with Fig. 5.43(b) showing the same when the quadraxial feed is used. It is evident that, especially at higher frequencies, the quadraxial feed generates significantly fewer modes. In this first paper, the aim was to simply create a pure TE_{11}-mode, which was shown to give a significantly better beamwidth performance over frequency. A follow-up paper presented a very simple circuit model for the proposed quadraxial feed, which made it possible to design such a feed without numerical electromagnetic analysis [113].

Once a way was established to guarantee an almost pure TE_{11}-mode at the base of the horn, the design of the tapered section of the horn could be addressed. This was performed in two steps: firstly, the aperture plane modal content which would produce a desired illumination pattern was calculated using the procedure by Ludwig, and secondly, the taper is designed to generate these modes. This procedure was presented in [108].

Fig. 5.44 show the relative TE-mode magnitudes which will produce an optimal aperture field over frequency for a feed intended to work in an unshaped offset Gregorian system, with an F/D ratio of 0.55, and main and sub-reflectors having diameters of 15m and 5m respectively. The difference between the required relative magnitude of the TE_{11}-mode at low and high frequencies is quite substantial, requiring careful control. To achieve such a control, a taper design based on the cut-off frequencies of the different modes at various points in the taper were used as design parameters, where it is assumed that a mode below cut-off does not contribute to the aperture field. An example for three different horns is shown in Fig. 5.45.

The full technique was presented for a possible solution to the SKA Phase 2 antennas in 2016 in an IEEE Transactions paper [114]. The manufactured prototype is shown in Figs. 5.46 and 5.47, where Fig. 5.46 shoes the whole structure, milled from Alumnium, and Fig. 5.47 the quadraxial feed and the transition to four coaxial ports. This design included a number of improvements, including a stepped outside cylinder at the base of the horn to improve matching.

The measured results are shown in Figs. 5.48 and 5.49. A significant im-

The 8th European Conference on Antennas and Prop

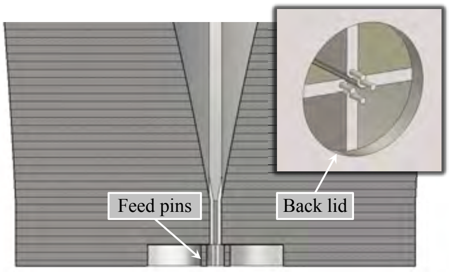

(a)

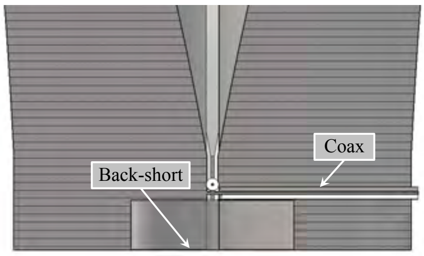

(b)

Fig. 2. CAD views of the cross-sections of two feed networks for the QRFH antenna in Fig. 1. (a) The quadraxial feed with centre conductors connected to the ridges, with the inset showing the back of the QRFH. (b) The conventional feed with a back-short section and ridge-to-coax transition.

Figure 5.42: QRFH feeds (a) quadraxial transition (b) conventional transition (from [107])

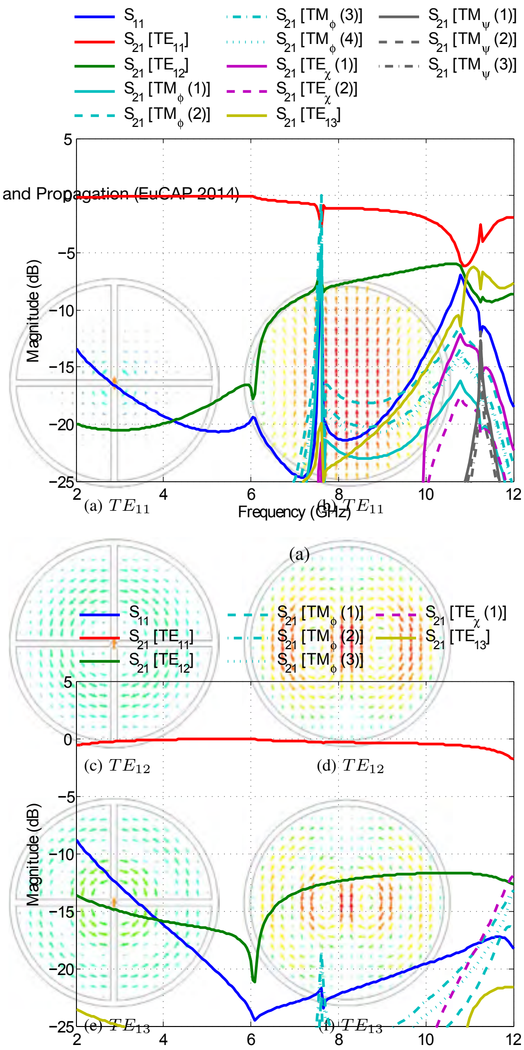

(a)

(b)

Fig. 3. The E-field distributions of the TE_{11}, TE_{12} and TE_{13} modes in circular waveguides with and without ridges.

differential impedance of the twinaxial line is the diameter of the cylinder in the back lid of the QRFH, shown in Fig.2(a). This diameter should be small enough in order for the higher-order modes to be below cut-off in the band of operation.

A unique feature of the QRFH antenna is that it can easily be separated into two independent sections as indicated in Fig. 1, reducing simulation time for design purposes. Here the throat section refers to the uniform waveguide terminated by the feeding network, while the flared section is the radiating part of the antenna. The flared section therefore serves as a good matching network between free-space and the fundamental TE_{11} mode in the throat.

In order to compare the performance of the proposed feed with the conventional balun consisting of a back-short section and ridge-to-coax transition as shown in Fig. 2(b), a QRFH antenna operating from 2 to 12 GHz is designed. The values of the throat dimensions (i.e. cylinder diameter, ridge thickness, gap width, etc.) are taken from an existing QRFH design for a coax-feed with a characteristic impedance of 100 Ω. The dimensions of the flared section (i.e. horn length, aperture size and taper) are optimised for constant beamwidth over the frequency range, while the horn is excited with a pure TE_{11} mode. The product is an antenna capable of being fed by either the coax- or twinax-feed.

III. MODAL CONTENT ANALYSIS

As illustrated in [1] through a simplified analytic approach, the TE_{11} mode should be dominant in the aperture field distribution of a QRFH over a large bandwidth in order to achieve the required radiation. The subordinate modes should be in declining order of power TM_{11}, TE_{12}, TM_{12}, TE_{13}, etc. In Fig. 3 the field distributions of the first three TE modes are shown for clarity. Furthermore, due to the two-fold symmetry of the aperture field distribution [1] all even-order modes are undesired (i.e. TE_{mn} and TM_{mn} where $m = 0, 2, 4, \ldots$).

The modal content of the QRFH antenna is investigated through full-wave simulations using Computer Simulation Technology's Microwave Suite software (CST-MWS). For this purpose a waveguide port is placed at the plane where the flared section of the complete QRFH model would begin. The simulated S-parameters of the throat section with either a coax- or twinax-feed are shown in Fig. 4(a) and 4(b), respectively. These results only include the significant excited modes.

As expected, the TE_{11} mode is most strongly excited over

Fig. 4. The simulated S-parameters of the throat section of the QRFH, excited by either the (a) coax- or (b) twinax-feed. In both these configurations port 1 is connected to the feed terminals while port 2 is a waveguide port terminating the quad-ridged circular waveguide. The following modes are representative of a superposition of cylindrical modes: $\{TM_{01}, TM_{11}, TM_{21L}\} \subset TM_\phi$; $\{TE_{22U}, TE_{32}, TE_{42L}\} \subset TE_\chi$; $\{TM_{21U}, TM_{12}, TM_{41L}\} \subset TM_\psi$. Note that the notations U and L refer to the upper and lower modes, respectively.

Figure 5.43: Comparison of excited modes for (a) the conventional transition and (b) quadraxial feed (from [108])

the wide frequency band ($|S_{2,1}[TE_{11}]|$ is close to 0 dB) for both feeds, whereas the contents of the higher-order modes are rather different. Interestingly enough, the second strongest mode is TE_{12} and is excited significantly higher with the coax-feed than with the twinax-feed for the majority of the frequency band. Although this mode is one of the desired subordinate aperture modes, its presence in the throat section is not beneficial. The purpose of the flared section is to excite the higher-order modes required in the aperture from the dominant

TE_{11} mode
the throat, u
aperture. Fu
at the lowe
imbalance o
is evanescen
Another i
a cut-off fre
strong reso
$|S_{2,1}|$ of the
not present
of TE_{13} an
range in Fig
at 7.6 GHz
The TM_ϕ
modes. In ri
specific cyli
between the
tions as a s
to its own c
cylindrical
superpositio
modes repre
represent T
U and L re
which is the
capacitive lo
Fig. 4 refer
It is clear
excited in t
feed substan
higher-order
the QRFH,

Although
in the litera
with about
(typically de
a factor of
results from
where the c
the coaxial f
mode. This
cannot be co
sion techniq
was introdu
suppress the
to improve
in the H-pla
To illustra
band soluti
the E, H an
antenna whe
feed. Each g

provement was obtained for the aperture illumination pattern, especially in terms of an absence of the pattern breakup at high frequencies, while achieving good matching over a very wide band. Using these measured results, predictions could be made for the efficiency of the full system and it was shown that a better than 50% efficiency could be achieved.

In an environment where optimisation is used increasingly as a first design option, and a field where optimisation is virtually the only technique used by designers, the work on the QRFH-antennas showed that intelligent use of

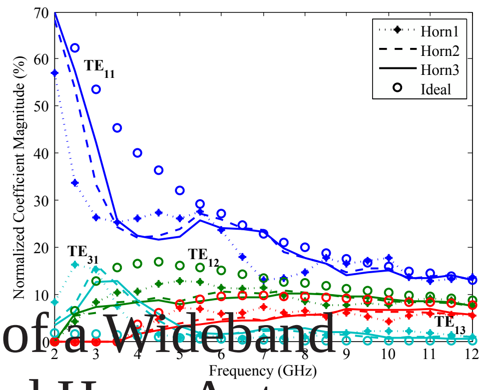

Figure 5.44: Aperture modes (from [108])

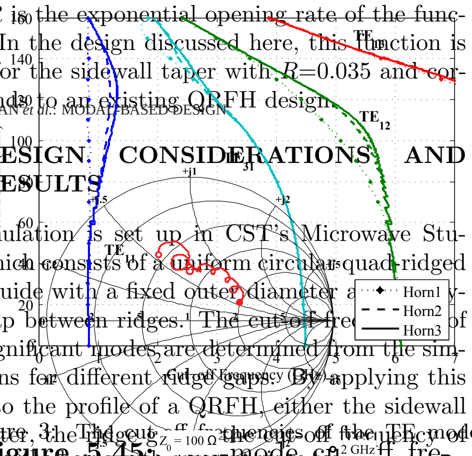

Figure 5.45: Input mode cut-off frequencies in taper (from [108])

Figure 5.46: QRFH antenna prototype (from [114])

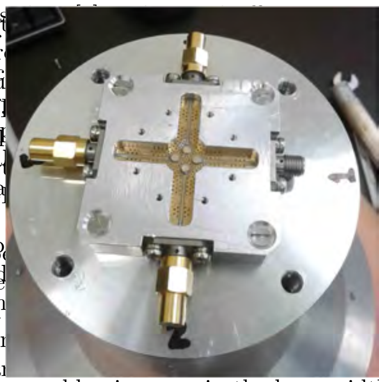

Figure 5.47: Prototype quadraxial feed (from [114])

5.6 Conclusion

The work on antennas constituted a turning point in my career at a fairly late stage, and is set to continue. My knowledge of multi-mode networks, waveguides and passive structures proved invaluable when applied to the field of antennas, especially the work presented in this chapter. South Africa is set

1622 IEEE TRANSACTIONS ON ANTENNAS AND PROPAGATION, VOL. 64, NO. 5, MAY 2016

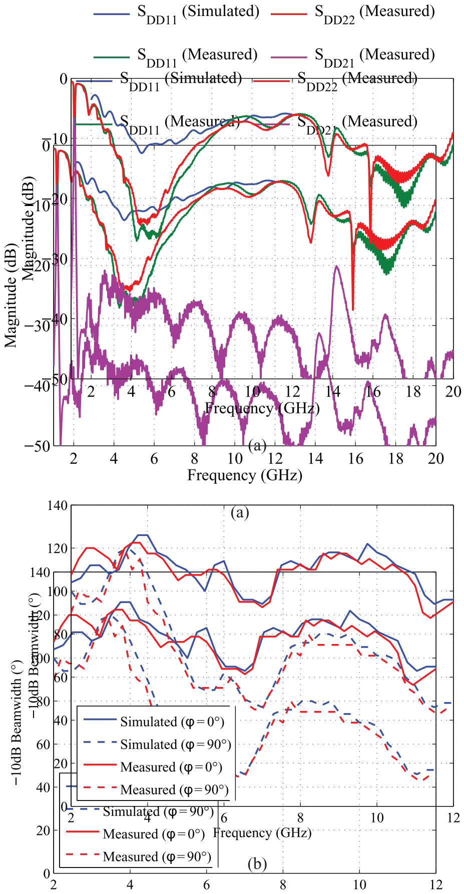

Fig. 12. Simulated and measured (a) S-parameters of the differential mode; and (b) the −10-dB beamwidths in the E- and H-planes.

Figure 5.48: Measured results of the QRFH prototype (a) S-parameters of the differential mode; and (b) the −10dB beamwidths in the E- and H-planes. (from [114])

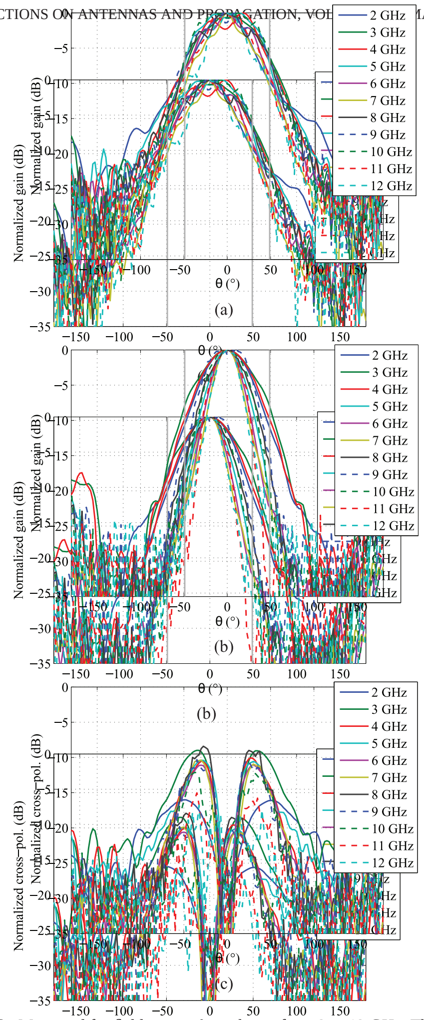

Fig. 13. Measured far-field patterns are shown from 2 to 12 GHz. The copolar results are given for the (a) E-plane and (b) H-plane cuts, while the cross polar results are given for the (c) $\phi = 45^\circ$ plane.

Figure 5.49: Measured results of the QRFH prototype (a) E-plane cuts (b) H-plane cuts (c) cross polar results for the (c) ϕ=45 degree plane. (from [114])

The far-field radiation of the manufactured prototype was measured in an anechoic chamber using dual-ridged horns. In Fig. 12(b), the −10-dB beamwidth results are shown for the E- and H-planes, where it is clear that the measured results agree well with the simulations. The H-plane beamwidth narrows between 3 and 5 GHz relative to E-plane beamwidth but then maintains a near-constant difference over the rest of the band, with an overall elliptic shape.

The measured far-field patterns are given in Fig. 13 for different cut planes across the frequency range. It is clear that no breakup of the main beam occurs in either of the principle planes, even at the normally problematic higher frequencies. This is due to the careful control of the modal content in the horn and is an improvement over even heavily optimized state-of-the-art horns. The normalized cross-polarization patterns in the $\phi = 45^\circ$ are given in Fig. 13(c). Note that the measured cross-polarization levels are slightly lower than in the simulated results, due to the difficulty in positioning the horn with a 45° orientation with respect to the probe antenna.

The close agreement found between the simulation and measured results is evidence of the reduction in sensitivity to manufacturing tolerances, which the quadraxial feed gives. Not only does it pose a simple assembling solution, but the quadraxial feed also allows an oversized throat section without compromising the modal purity. This is contrary to the coaxial feed solution, where the coaxial line needs to feed through a very thin ridge and is highly sensitive to the excitation of higher order modes.

C. Performance in Reflector System

As this paper focuses on the design of a QRFH for a reflector antenna, the performance of the QRFH within the full reflector

on a path to develop radio astronomy as a strategic research area over the next decades, and I foresee that antenna work, especially large arrays, will remain a priority.

Chapter 6

Conclusions

This is the conclusion.

Appendices

Appendix A

Postgraduate Students

A.1 DEng Graduates

The DEng is the highest degree awarded by the Faculty of Engineering at Stellenbosch University. It is a lifetime award based on contributions over a full career.

1. D.B. Davidson - Contributions to Engineering Electromagnetics - (2017)
2. W.J. Perold - From High-Speed Superconducting Devices to Nanosensors (2017)

A.2 Postdoctoral Fellows

1. E. Knox-Davies - Scanning mm-wave antenna (2006-2007)
2. M. Schoeman - Meta-Modelling of Microwave Structures (2006-2007)
3. T. Sickel - X-band Limiters (2006-2007)
4. D. Prinsloo - Quad-Mode Antenna Arrays (2015-2016)

A.3 PhD Graduates

1. C. van Niekerk - Multi-Bias Decomposition-Based Optimisation for the Extraction of Small-Signal GaAs FET Models (1999)
2. R. Lehmensieck - Efficient Adaptive Sampling Applied to Multivariate, Multiple Output Rational Interpolation Models, with Applications in Electromagnetic-Based Device Modelling (2001)
3. W. Steyn - CAD-Based Iris Design Procedures for Multimode Coupled Cavity Devices (2002)

4. C.A.W. Vale - Growth-Based Computer Aided Design Strategies for Multimode Waveguide Design with the Aid of Functional Blocks (2001)
5. R.H. Geschke - Application of an Extended Huygens's Principle to Scattering Discontinuities in Waveguide (2004)
6. T. Sickel - Tuneable Evanescent Mode X-Band Waveguide Switch (2005)
7. M. Schoeman - Interpolation-Based Modelling of Microwave Ring Resonators (2006)
8. D.I.L. de Villiers - Analysis and Design of Conical Transmission Line Power Combiners (2007)
9. T. Stander - High-Power Broadband Absorptive Waveguide Filters (2009)
10. D.M.P. Smith - Aspects of Small Airborne Passive Millimetre-Wave Imaging Systems (2010)
11. S.O. Nasser - Miniaturised Multilayer RF and and Microwave Circuits (2016)
12. D.S.vd M.Prinsloo - Multi-Mode Antennas for Hemispherical Field-of-View Coverage(2015)
13. T.S. Beukman - Modal-Based Design Techniques for Circular Quadruple-Ridged Flared Horn Antennas (2015)
14. T.G. Brand - Synthesis Methods for Multiband Coupled Resonator Filters (2014)
15. E. Meyer - Tunable Narrow-Band X-Band Bandpass Filters (2018)
16. S.K. Sharma - Variable Bandwidth Planar Coupled Resonator Filters

A.4 Current PhD students - 2018

1. R. Kenned - Optimum noise matching of very large connected antenna arrays
2. S. Maas - SIW Waffle-Iron Filters

A.5 Master's students upgraded to PhD

1. C.A.W. Vale
2. T. Sickel

3. D.I.L. de Villiers
4. T. Stander
5. E. Meyer (prev Botes)
6. R. Kenned

A.6 Master's Graduates

1. J.E. van Zyl - A Calibration Procedure for Superconducting Microwave Measurements Using One Calibration Standard (1994)
2. C. Smit - Die Ontwikkeling en Evaluasie van 'n Progressiewe Korrelasie kodesluitlus vir 'n Strekspektrum Kommunikasiestelsel (1995)
3. C. van Niekerk - An Investigation into the Manufacturing and Measurement of Superconducting Microwave Devices (1995)
4. J.C. Kruger - Design of Wideband, Low Loss, High Power Waveguide Couplers and Transitions for Implementation in Power Combiners and Dividers (1998)
5. W.J.A. van Brakel - Solving Three-Layer Planar Microwave Structures with the Method-of-Lines (1998)
6. W. Steyn - A Room Temperature X-Band Receiver Front End Optimised for Introduction of High Temperature Superconductor Technology (1998)
7. J.D. Theron - Die Ontwikkeling van 'n Koaksiale Resoneerder Filter vir Implementering in L-Band Dipleksers (1999)
8. M. MÃ¼ller - Neural Network Models of Slotted Waveguide Directional Couplers (2001)
9. A.P.E. van der Colff - Rekenaargesteunde Instelling van Gekoppelde-Resoneerder Filters deur die gebruik van Modelgebaseerde Parameterontrekking (2002)
10. K.H. Cherenack - Modelling of Layered Cylindrical Dielectric Resonators with reference to Whispering Gallery Mode Resonators (2002)
11. L. Sam - The Design of a Coupled Coaxial Resonator Filter for Low Earth Orbit Satellites working at Microwave Frequencies (2002)
12. M. Schoeman - Mixed-Potential Integral Equation Technique for Hybrid Microstrip-Slotline Mutli-Layered Circuits with Horizontal and Vertical Shielding Walls (2003)

13. M.L. Strydom - Design of Equal Division Microwave Power Dividers (2003)
14. N. Coetzee - Asymmetrical S-band Coupled Resonator Filters (2005)
15. V.P. Netshifhire - The Design and Implementation of Microwave Receiver Front End Components (2005)
16. E.M Hansmann - An Investigation of Coupling Mechanisms in Narrowband Microwave Filters (2009)
17. S. Maas - Coaxial Resonator Filters (2011)
18. S. Otto - A Study of Radio Astronomy Principles and SKA Pathfinder System Designs with Pulsar Science (2011)
19. M. van der Walt - A Design Environment for the Automated Optimisation of Low Cross-Polarisation Horn Antennas (2010)
20. K. Schoeman - Waveguide Antenna Feed for the Square Kilometre Array (2011)
21. D.S.vd M. Prinsloo - Characterisation of L-band Differential Low Noise Amplifiers (2011)
22. S.O. Nasser - An Investigation of the Equivalence between Combline and Evanescent-Mode Waveguide Filters and Aspects related to Reduction of Manufacturing Costs for Combline Filters (2011)
23. P. Terblanche - Electronically Adjustable Bandpass Filter (2011)
24. D.A. Botes - Wideband, Low-Noise Amplifiers for the Mid-Range SKA (2014)
25. M. van Wyk - The Ribbon Microphone: A Multi-Physics Educational Aid (2017)
26. G. van Tonder - Beamforming Techniques for a Quad-Mode Antenna Array (2016)
27. P.L. Benson - Tunable Lumped Element Notch Filter for UHF Communications Systems (2017)

A.7 Current Master's students

1. L. Johnson - Tunable Pedestal SIW Filters
2. A. Bester - Evaluation of the SU Antenna Range

Bibliography

[1] W. Perold, “From High-Speed Superconducting Devices to Nanosensors,” Ph.D. dissertation, Department of Electrical and Electronic Engineering, Stellenbosch University, 2017.

[2] D. Davidson, “Contributions to Engineering Electromagnetics,” Ph.D. dissertation, Department of Electrical and Electronic Engineering, Stellenbosch University, 2017.

[3] R. Holemans, P. Van Der Walt, W. Rencken, P. Meyer, and P. Steyn, “Accurate procedures for the exact synthesis of high order narrow band distributed filters,” in *Second Joint Symposium on Antennas & Propagation and Microwave Theory and Techniques*, Pretoria, 1988, pp. 32.1–32.11.

[4] R. Holemans, P. Van der Walt, W. Rencken, P. Meyer, and P. Steyn, “Accurate procedures for the exact synthesis of high order narrow band distributed filters,” *Transactions of the SAIEE*, vol. 80, no. 1, pp. 12–15, 1990.

[5] P. Meyer and P. Van Der Walt, “Design of narrowband E plane waveguide filters,” in *Second Joint Symposium on Antennas & Propagation and Microwave Theory and Techniques*, Pretoria, 1988, pp. 26.1–26.11.

[6] P. Meyer, “The design of E-plane waveguide filters with a pocket calculator,” *Joint Symposium on Antennas & Propagation and Microwave Theory and Techniques*, 1991.

[7] P. Meyer and P. Van der Walt, “Design equations for narrow-band E-plane waveguide filters,” *Transactions of the SAIEE*, vol. 84, no. 3, pp. 226–229, 1993.

[8] P. Meyer, “The design and analysis of waveguide E-plane filters with multiple round inductive posts using a Moment-Method approach,” in *IEEE AFRICON Conference 1996*, vol. 1, Stellenbosch, 1996, pp. 532–535.

[9] ——, “A comined Mode-Matching and Method-of-Lines procedure for the analysis of planar microwave structures,” PhD, Stellenbosch, 1995.

[10] ——, "Solving microstrip discontinuities with a combined Mode-Matching and Method-of-Lines procedure," *Microwave and Optical Technology Letters*, vol. 8, no. 1, pp. 4–8, 1995.

[11] P. Meyer and P. Van Der Walt, "Closed-form expression for implementing the method of lines for two-layer boxed planar structures," *Electronics Letters*, vol. 30, no. 18, pp. 1497–1498, 1994.

[12] P. Meyer, "Analysis of microstrip filters with a combined Mode-Matching and Method-of-Lines procedure," in *IEEE MTT-S International Microwave Symposium Digest 1995*, vol. 2, Orlando, 1995, pp. 837–840.

[13] R. Geschke, "Application of an Extended Huygens's Principle to Scattering Discontinuities in Waveguide," Ph.D. dissertation, Department of Electrical and Electronic Engineering, Stellenbosch University, 2004.

[14] R. Geschke, R. Ferrari, D. Davidson, and P. Meyer, "Application of extended Huygens' principle to scattering discontinuities in waveguide," in *2002 IEEE AFRICON Conference*, vol. 2, 2002, pp. 555–558.

[15] ——, "Application of extende Huygens' Principle to scattering discontinuities in waveguide," *Transactions of the SAIEE*, vol. 94, no. 2, pp. 28–31, 2003.

[16] ——, "Application of extended Huygens' principle to dielectric posts in waveguide," in *Proceedings of the IASTED International Conference on Antennas, Radar, and Wave Propagation*, 2004, pp. 107–110.

[17] ——, "The solution of waveguide scattering problems by application of an extended Huygens formulation," *IEEE Transactions on Microwave Theory and Techniques*, vol. 54, no. 10, pp. 3698–3705, 2006.

[18] C. Vale and P. Meyer, "Automated intelligent mode selection for fast mode matching analysis of waveguide discontinuities," in *IEEE MTT-S International Microwave Symposium Digest 2001*, vol. 1, Phoenix, 2001, pp. 1949–1952.

[19] M. Schoeman, "Mixed-Potential Integral Equation Technique for Hybrid Microstrip-Slotline Mutli-Layered Circuits with Horizontal and Vertical Shielding Walls," Master's thesis, Department of Electrical and Electronic Engineering, Stellenbosch University, 2003.

[20] M. Schoeman and P. Meyer, "On the structure and packing of the Moment matrix in problems supporting simultaneous electric and magnetic surface currents," *Microwave and Optical Technology Letters*, vol. 41, no. 6, pp. 500–505, 2004.

[21] D. De Villiers and P. Meyer, "An efficient grid placing technique for 2-D Method of Moments analysis of coupled line structures," in *2007 IEEE AFRICON Conference*, Windhoek, 2007, pp. 1–6.

[22] J. van Zyl, "A Calibration Procedure for Superconducting Microwave Measurements Using One Calibration Standard," Master's thesis, Department of Electrical and Electronic Engineering, Stellenbosch University, 1994.

[23] J. Van Zyl, P. Meyer, and C. van Niekerk, "Simplified calibration procedure for cryogenic microwave measurements," in *IEEE MTT-S International Microwave Symposium Digest 1996*, vol. 3, 1996, pp. 1403–1406.

[24] C. van Niekerk and P. Meyer, "The development of a simple TRL microstrip calibration and test fixture suitable for measurements at cryogenic temperatures," in *IEEE AFRICON Conference 1996*, vol. 2, Stellenbosch, 1996, pp. 919–922.

[25] C. Van Niekerk, "Multi-Bias Decomposition-Based Optimisation for the Extraction of Small-Signal GaAs FET Models," Ph.D. dissertation, Department of Electrical and Electronic Engineering, Stellenbosch University, 1999.

[26] C. Van Niekerk and P. Meyer, "A new approach for the extraction of an FET equivalent circuit from measured S parameters," *Microwave and Optical Technology Letters*, vol. 11, no. 5, pp. 279–281, 1996.

[27] ——, "Performance and limitations of decompositionbased parameter-extraction procedures for FET small-signal models," *IEEE Transactions on Microwave Theory and Techniques*, vol. 46, no. 11, pp. 1620–1627, 1998.

[28] C. Van Niekerk, D. Schreurs, and P. Meyer, "Recent developments in non-linear device modelling techniques," in *IEEE AFRICON Conference 1999*, vol. 2, Cape Town, 1999, pp. 1105–1110.

[29] C. Van Niekerk, P. Meyer, D. Schreurs, and P. Winson, "A robust integrated multibias parameter-extraction method for MESFET and HEMT models," *IEEE Transactions on Microwave Theory and Techniques*, vol. 48, no. 5, pp. 777–786, 2000.

[30] R. Lehmensiek, "Efficient Adaptive Sampling Applied to Multivariate, Multiple Output Rational Interpolation Models, with Applications in Electromagnetic-Based Device Modelling," Ph.D. dissertation, Department of Electrical and Electronic Engineering, Stellenbosch University, 2001.

[31] R. Lehmensiek and P. Meyer, “An efficient adaptive frequency sampling algorithm for model-based parameter estimation, as applied to Aggressive Space Mapping,” *Microwave and Optical Technology Letters*, vol. 24, no. 1, pp. 71–78, 2000.

[32] ——, “Using efficient model-based parameter estimation for pole-free solutions of modal propagation constants, as applied to shielded planar structures,” *ACES Journal*, vol. 16, no. 1, pp. 1–10, 2001.

[33] P. Meyer, R. Lehmensiek, and W. Steyn, “On the application of rational interpolation to root-finding problems in microwave engineering,” in *International Conference on Numerical Analysis and Applied Mathematics (ICNAAM) 2004*, Greece, 2004, pp. 265–268.

[34] R. Lehmensiek and P. Meyer, “Creating accurate multivariate rational interpolation models of microwave circuits by using efficient adaptive sampling to minimize the number of computational electromagnetic analyses,” *IEEE Transactions on Microwave Theory and Techniques*, vol. 49, no. 8, pp. 1419–1430, 2001.

[35] ——, “Using efficient multivariate adaptive sampling by minimizing the number of computational electromagnetic analysis needed to establish accurate interpolation models,” in *IEEE MTT-S International Microwave Symposium Digest 2001*, vol. 1, Phoenix, 2001, pp. 1749–1752.

[36] R. Lehmensiek, P. Meyer, and M. Müller, “Adaptive sampling applied to multivariate, multiple output rational interpolation models with application to microwave circuits,” *International Journal of RF and Microwave Computer-Aided Engineering*, vol. 12, no. 4, pp. 332–340, 2002.

[37] M. Schoeman, “Interpolation-Based Modelling of Microwave Ring Resonators,” Ph.D. dissertation, Department of Electrical and Electronic Engineering, Stellenbosch University, 2006.

[38] M. Schoeman and P. Meyer, “On the use of adaptive rational interpolation for the calculation of resonator characteristics from MoM analysis,” in *International Conference on Adaptive Modeling and Simulation (ADMOS) 2005*, Barcelona, 2005, pp. 317–320.

[39] ——, “On the use of adaptive rational interpolation for the calculation of resonator characteristics from EM analysis,” in *International Journal of RF and Microwave Computer-Aided Engineering*, vol. 16, no. 6, 2006, pp. 545–553.

[40] ——, “Prediction of microwave resonator frequencies using 1D adaptive vector fitting,” in *International Conference on Numerical Analysis and Applied Mathematics (ICNAAM) 2006*, Greece, 2006, pp. 472–475.

[41] ——, "A comparative study on adaptive rational macromodels of highly resonant structures," *International Journal of RF and Microwave Computer-Aided Engineering*, vol. 17, no. 2, pp. 281–285, 2007.

[42] D. Deschrijver, M. Schoeman, T. Dhaene, and P. Meyer, "Experimental analysis on the relaxation of macromodeling methods," in *2007 IEEE AFRICON Conference*, Windhoek, 2007, pp. 1–5.

[43] ——, "Rational approximation of noisy frequency responses," in *23rd International Review of Progress in Applied Computational Electromagnetics (ACES 2007)*, no. 3, Verona, 2007, pp. 1439–1444.

[44] M. Schoeman, T. Dhaene, and P. Meyer, "Vector fitting and state equation transformations to extract SPICE models," in *International Conference on Numerical Analysis and Applied Mathematics (ICNAAM) 2006*, no. 1, Greece, 2006, pp. 462–465.

[45] P. Meyer, C. Vale, and W. Steyn, "On the design of waveguide devices using multiple propagating modes," in *6th International Conference on Telecommunications in Modern Satellite, Cable and Broadcasting Service, TELSIKS 2003 - Proceedings*, vol. 1, 2003, pp. 329–338.

[46] W. Steyn, "CAD-Based Iris Design Procedures for Multimode Coupled Cavity Devices," Ph.D. dissertation, Department of Electrical and Electronic Engineering, Stellenbosch University, 2002.

[47] W. Steyn, R. Lehmensiek, and P. Meyer, "Integrated CAD procedure for iris design in a multi-mode wave guide environment," in *IEEE MTT-S International Microwave Symposium Digest 2001*, vol. 2, Phoenix, 2001, pp. 1163–1166.

[48] W. Steyn and P. Meyer, "A shorted waveguide-stub coupling mechanism for narrow-band multimode coupled resonator filters," *IEEE Transactions on Microwave Theory and Techniques*, vol. 52, no. 6, pp. 1622–1625, 2004.

[49] C. Vale, "Growth-Based Computer Aided Design Strategies for Multimode Waveguide Design with the Aid of Functional Blocks," Ph.D. dissertation, Department of Electrical and Electronic Engineering, Stellenbosch University, 2001.

[50] C. Vale and P. Meyer, "A design procedure for co-existing multi-mode waveguide bandstop filters," in *IEEE MTT-S International Microwave Symposium Digest 2000*, vol. 2, Boston, 2000, pp. 1189–1192.

[51] C. Vale, P. Meyer, and K. Palmer, "A design procedure for bandstop filters in waveguides supporting multiple propagating modes," *IEEE*

Transactions on Microwave Theory and Techniques, vol. 48, no. 12, pp. 2496–2503, 2000.

[52] T. Stander, "High-Power Broadband Absorptive Waveguide Filters," Ph.D. dissertation, Department of Electrical and Electronic Engineering, Stellenbosch University, 2009.

[53] T. Stander, P. Meyer, P. Van Der Walt, and W. Steyn, "Waffle-iron filters with oblique boss patterns," in *Proceedings of the 2012 International Conference on Electromagnetics in Advanced Applications, ICEAA'12*, Cape Town, 2012, pp. 1256–1257.

[54] S. Maas and P. Meyer, "Multilayer SIW Waffle-Iron filters," *IEEE Transactions on Microwave Theory and Techniques (submitted)*, 2018.

[55] T. Stander and P. Meyer, "Etched ring absorbing waveguide filter based on a slotted waveguide antenna response," *Microwave and Optical Technology Letters*, vol. 50, no. 4, pp. 977–981, 2008.

[56] T. Stander, P. Meyer, and P. Van der Walt, "Compact high-power broadband absorptive filters using slotted waveguide harmonic pads," *IET Microwaves, Antennas and Propagation*, vol. 8, no. 9, pp. 673–678, 2014.

[57] R. Geschke, B. Jokanovic, and P. Meyer, "Filter parameter extraction for triple-band composite split-ring resonators and filters," *IEEE Transactions on Microwave Theory and Techniques*, vol. 59, no. 6, pp. 1500–1508, 2011.

[58] ——, "Compact triple-band resonators using multiple split-ring resonators," in *European Microwave Week 2009, EuMW 2009: Science, Progress and Quality at Radiofrequencies, Conference Proceedings - 39th European Microwave Conference, EuMC 2009*, Rome, 2009, pp. 366–369.

[59] M. Ninic, B. Jokanovic, and P. Meyer, "Reconfigurable multi-state composite split-ring resonators," *IEEE Microwave and Wireless Components Letters*, vol. 26, no. 4, pp. 267–269, 2016.

[60] S. Qian, T. Brand, J. Hong, and P. Meyer, "The design of miniature multilayer bandpass filters with mixed couplings," *IEEE Transactions on Microwave Theory and Techniques*, vol. 61, no. 12, pp. 4072–4078, 2013.

[61] S. Nassar, "Miniaturised Multilayer RF and and Microwave Circuits," Ph.D. dissertation, Department of Electrical and Electronic Engineering, Stellenbosch University, 2016.

[62] P. Meyer and S. Nassar, “Pedestal substrate integrated waveguide resonators and filters,” *IET Microwaves, Antennas & Propagation*, pp. 1–8, 2017.

[63] E. Botes and P. Meyer, “Spatially decoupled varactor biasing for a tunable staircase filter,” *IET Microwaves, Antennas and Propagation*, vol. 11, no. 1, pp. 10–16, 2017.

[64] E. Meyer, “Tunable Narrow-Band X-Band Bandpass Filters,” Ph.D. dissertation, Department of Electrical and Electronic Engineering, Stellenbosch University, 2018.

[65] S. Sharma, “Variable Bandwidth Planar Coupled Resonator Filters,” Ph.D. dissertation, Department of Electrical and Electronic Engineering, Stellenbosch University, 2018.

[66] S. Sharma and P. Meyer, “Variable bandwidth coupled resonator filters utilizing tunable non-resonant node inverters,” *IEEE Transactions on Microwave Theory and Techniques (submitted)*, 2018.

[67] T. Brand, “Synthesis Methods for Multiband Coupled Resonator Filters,” Ph.D. dissertation, Department of Electrical and Electronic Engineering, Stellenbosch University, 2014.

[68] T. Brand, P. Meyer, and R. Geschke, “Designing multiband coupled-resonator filters using reactance transformations,” *International Journal of RF and Microwave Computer-Aided Engineering*, vol. 25, no. 1, pp. 81–92, 2015.

[69] P. Meyer and T. Brand, “Design equations for multi-band coupled-resonator filters using reactance mapping,” in *2015 IEEE Asia-Pacific Microwave Conference Proceedings, APMC*, vol. 1, Nanjing, 2016, pp. 1–4.

[70] P. Meyer, T. Brand, and R. Geschke, “Techniques for the synthesis of multi-band transfer functions,” in *Recent Advances in Multi-Band Microstrip Filters*, Cambridge University Press, Ed., 2015, pp. 67–109.

[71] N. Jankovic, V. Crnojevic-Bengin, P. Meyer, and J. Hong, “Design methods of multi-band filters,” in *Recent Advances in Multi-Band Microstrip Filters*. Cambridge University Press, 2015, pp. 5–66.

[72] T. Sickel, P. Meyer, and P. Van der Walt, “An in situ tunable diode mounting topology for high-power X-band waveguide switches,” *IEEE Transactions on Microwave Theory and Techniques*, vol. 55, no. 2, pp. 281–285, 2007.

[73] S. Nassar, P. Meyer, and P. Van Der Walt, "An S-band combline filter with reduced size and increased pass-band separation," in *Proceedings of 14th Conference on Microwave Techniques, COMITE 2015*, Pardubice, 2015, pp. 1–4.

[74] J. Kruger and P. Meyer, "Finline and coaxial line to waveguide transitions at X-band," in *Proceedings of the South African Symposium on Communications and Signal Processing, COMSIG*, Cape Town, 1998, pp. 401–406.

[75] J. Kruger, "Design of Wideband, Low Loss, High Power Waveguide Couplers and Transitions for Implementation in Power Combiners and Dividers," Master's thesis, Department of Electrical and Electronic Engineering, Stellenbosch University, 1998.

[76] C. Vale and P. Meyer, "Designing high-performance finline tapers with vector-based optimization," *IEEE Transactions on Microwave Theory and Techniques*, vol. 47, no. 12, pp. 2467–2472, 1999.

[77] P. Meyer and C. Vale, "Designing high-performance finline tapers with vector-based optimization," in *IEEE MTT-S International Microwave Symposium Digest 1999*, vol. 2, Anaheim, 1999, pp. 707–710.

[78] P. Meyer, "Characteristics of tightly coupled crossed-guide waveguide directional couplers," in *1997 International Miteko Conference*, 1997, pp. 211–213.

[79] P. Meyer and J. Kruger, "Wideband crossed-guide waveguide directional couplers," in *IEEE MTT-S International Microwave Symposium Digest 1998*, vol. 1, Baltimore, 1998, pp. 253–256.

[80] D. De Villiers, "Analysis and Design of Conical Transmission Line Power Combiners," Ph.D. dissertation, Department of Electrical and Electronic Engineering, Stellenbosch University, 2007.

[81] D. De Villiers, P. Van der Walt, and P. Meyer, "Design of a ten-way conical transmission line power Combiner," *IEEE Transactions on Microwave Theory and Techniques*, vol. 55, no. 2, pp. 302–308, 2007.

[82] ——, "Design of conical transmission line power combiners using tapered line matching sections," *IEEE Transactions on Microwave Theory and Techniques*, vol. 56, no. 6, pp. 1478–1484, 2008.

[83] D. De Villiers and P. Meyer, "Numerical calculation of analytic solutions for higher order modes in conical lines," *International Journal of RF and Microwave Computer-Aided Engineering*, vol. 19, no. 1, pp. 99–109, 2009.

[84] D. De Villiers, P. Van der Walt, and P. Meyer, "Design constraints in conical line power combiners," in *2010 10th Mediterranean Microwave Symposium, MMS 2010*, Guzelyurt, 2010, pp. 148–151.

[85] T. Sickel, "Tuneable Evanescent Mode X-Band Waveguide Switch," Ph.D. dissertation, Department of Electrical and Electronic Engineering, Stellenbosch University, 2005.

[86] T. Sickel, P. Meyer, and P. Van Der Walt, "A waveguide PIN diode mount with thermal model for high-power applications," in *2014 18th IEEE Workshop on Signal and Power Integrity, SPI 2014 - Proceedings*, Ghent, 2014, pp. 1–4.

[87] ——, "Diode mounting topologies for X-band waveguide switches," in *2007 IEEE AFRICON Conference*, 2007, pp. 1–7.

[88] D. Prinsloo, "Multi-Mode Antennas for Hemispherical Field-of-View Coverage," Ph.D. dissertation, Department of Electrical and Electronic Engineering, Stellenbosch University, 2015.

[89] D. Prinsloo, P. Meyer, R. Maaskant, and M. Ivashina, "Design of an active dual-mode antenna with near hemispherical Field of View coverage," in *Proceedings of the 2013 International Conference on Electromagnetics in Advanced Applications, ICEAA 2013*, Turin, 2013, pp. 1064–1067.

[90] D. Prinsloo, R. Maaskant, M. Ivashina, and P. Meyer, "Mixed-mode sensitivity analysis of a combined differential and common mode active receiving antenna providing near-hemispherical field-of-view coverage," *IEEE Transactions on Antennas and Propagation*, vol. 62, no. 8, pp. 3951–3961, 2014.

[91] D. Prinsloo, P. Meyer, M. Ivashina, and R. Maaskant, "A quad-mode antenna for accurate polarimetric measurements over an ultra-wide field-of-view," in *8th European Conference on Antennas and Propagation, EuCAP 2014*, The Hague, 2014, pp. 3260–3263.

[92] D. Prinsloo, P. Meyer, R. Maaskant, and M. Ivashina, "Quad-mode antenna for wide-scan sparse arrays," in *IEEE Antennas and Propagation Society, AP-S International Symposium (Digest)*, vol. 2015-Octob, Vancouver, 2015, pp. 1516–1518.

[93] ——, "Conical quad-mode antenna with integrated tapered slot antennas for wide-field polarimetry," in *Proceedings of the 2015 IEEE-APS Topical Conference on Antennas and Propagation in Wireless Communications, IEEE APWC 2015*, Turin, 2015, pp. 1235–1238.

[94] D. Prinsloo, M. Ivashina, R. Maaskant, and P. Meyer, "Beamforming strategies for active multi-mode antennas: Maximum gain, Signal-to-Noise ratio, and polarization discrimination," in *Proceedings - 2014 International Conference on Electromagnetics in Advanced Applications, ICEAA 2014*, Aruba, 2014, pp. 507–510.

[95] D. Prinsloo, P. Meyer, R. Maaskant, and M. Ivashina, "Irregular quad-mode antenna array: Field-of-View comparison with the swedish LOFAR station," in *2015 9th European Conference on Antennas and Propagation, EuCAP 2015*, Lisbon, 2015, pp. 1–5.

[96] D. Prinsloo, R. Maaskant, M. Ivashina, A. Glazunov, and P. Meyer, "Synergy in design of phased array antennas for modern radio astronomy and wireless communication systems," in *2016 10th European Conference on Antennas and Propagation, EuCAP 2016*, Davos, 2016, pp. 1–5.

[97] D. Prinsloo, A. Glazunov, R. Maaskant, M. Ivashina, V. Kukush, and P. Meyer, "Design of a quad-mode antenna with near-hemispherical gain coverage and its characterization in MIMO scenarios," *IEEE Transactions on Antennas and Propagation (submitted 2018)*, 2018.

[98] D. Prinsloo, R. Maaskant, M. Ivashina, and P. Meyer, "Multi-mode composite antenna," 2015.

[99] ——, "Tapered slot quad-mode antenna," 2015.

[100] D. Prinsloo, "Characterisation of L-band Differential Low Noise Amplifiers," Master's thesis, Department of Electrical and Electronic Engineering, Stellenbosch University, 2011.

[101] D. Prinsloo and P. Meyer, "Noise figure measurement of three-port differential low-noise amplifiers," *Electronics Letters*, vol. 48, no. 10, pp. 578–580, 2012.

[102] ——, "Multi-mode noise parameters for multi-port networks," *IET Microwaves, Antennas and Propagation*, vol. 10, no. 3, pp. 333–338, 2016.

[103] P. Meyer and D. Prinsloo, "Generalized multimode Scattering parameter and antenna far-field conversions," *IEEE Transactions on Antennas and Propagation*, vol. 63, no. 11, pp. 4818–4826, 2015.

[104] P. Meyer, "Multi-conductor transmission line analysis using the generalized multi-mode S-parameter transformation," in *SPI 2015 - 19th IEEE Workshop on Signal and Power Integrity*, Berlin, 2015, pp. 1–4.

[105] ——, "On the use of S-parameter transformations to improve surrogate model behaviour ofmultiport networks," in *ECCOMAS Congress 2016 -*

Proceedings of the 7th European Congress on Computational Methods in Applied Sciences and Engineering, vol. 2, Crete, 2016, pp. 1–5.

[106] T. Beukman, "Modal-Based Design Techniques for Circular Quadruple-Ridged Flared Horn Antennas," Ph.D. dissertation, Department of Electrical and Electronic Engineering, Stellenbosch University, 2015.

[107] T. Beukman, M. Ivashina, R. Maaskant, P. Meyer, and C. Bencivenni, "A quadraxial feed for ultra-wide bandwidth quadruple-ridged flared horn antennas," in *8th European Conference on Antennas and Propagation, EuCAP 2014*, The Hague, 2014, pp. 3312–3316.

[108] T. Beukman, P. Meyer, M. Ivashina, R. Maaskant, and D. De Villiers, "Modal considerations for synthesizing the tapering profile of a quadruple-ridged flared horn antenna," in *Proceedings - International Conference on Electromagnetics in Advanced Applications, ICEAA 2014*, Aruba, 2014, pp. 488–491.

[109] D. De Villiers and P. Meyer, "Broadband offset quad-ridged waveguide orthomode transducer," *Electronics Letters*, vol. 45, no. 1, pp. 60–62, 2009.

[110] D. De Villiers, P. Meyer, and K. Palmer, "Design of a wideband orthomode transducer," in *2009 IEEE AFRICON Conference*, Nairobi, 2009, pp. 1–6.

[111] K. Schoeman, P. Meyer, and D. De Villiers, "Exponential TEM horn with a convex triangular arc," in *2013 IEEE AFRICON Conference*, Mauritius, 2013, pp. 1–4.

[112] M. Ivashina, T. Beukman, C. Bencivenni, O. Iupikov, R. Maaskant, P. Meyer, and M. Pantaleev, "Design of wideband quadruple-ridged flared horn feeds for future radio telescopes," in *Antenna EMB Symposium, Swedish Microwave Days, 11-12 March, Gothenburg, Sweden*, 2014.

[113] T. Beukman, P. Meyer, R. Maaskant, and M. Ivashina, "Equivalent circuit of a quadraxial feed for ultra-wide bandwidth quadruple-ridged flared horn antennas," in *2015 9th European Conference on Antennas and Propagation, EuCAP 2015*, Lisbon, 2015, pp. 1–5.

[114] T. Beukman, P. Meyer, M. Ivashina, and R. Maaskant, "Modal-based design of a wideband quadruple-ridged flared horn antenna," *IEEE Transactions on Antennas and Propagation*, vol. 64, no. 5, pp. 1615–1626, 2016.